Mid-IR Waveguide Lasers in Transition Metal Doped II-VI Semiconductors

Adam Lancaster MPhys (Hons.)

Submitted for the degree of Doctor of Philosophy

Institute of Photonics and Quantum Sciences

School of Engineering and Physical Sciences

Heriot-Watt University

May 2017

Abstract

This thesis focuses on the development of compact Mid-IR waveguide laser systems in transition metal doped II-VI semiconductors. These waveguide lasers have been developed to produce high brightness and compact sources in the Mid-IR.

The wavelength tuneable operation of Cr:ZnSe waveguides was investigated. The waveguides were fabricated using ultrafast laser inscription. The waveguide laser demonstrated a tuning range of 2080 - 2883 nm, with more than 15 mW of output power across the full range. This resulted in a tuneable bandwidth of 39 THz, which is the widest range demonstrated by a Mid-IR waveguide laser. Modelocking of a Cr:ZnSe waveguide laser was investigated using a SESAM. This resulted in the demonstration of a CW modelocked laser with a PRF of 308 MHz, pulse energy of 0.3 nJ and a pulse width of 638 fs. In addition, a CW modelocked laser was demonstrated with a PRF of 1.03 GHz, this is the fastest PRF of any Cr:ZnSe laser demonstrated.

Other transition metal doped II-VI semiconductors were investigated. Waveguides were developed in Cr:ZnS because of its improved thermal properties compared with Cr:ZnSe for future power scaling applications. The Cr:ZnS waveguide laser emitted 97 mW at a central wavelength of 2333 nm. Waveguide laser operation was investigated in Fe:ZnSe for laser operation in the 3.7 to 5 μm spectral band. Firstly, low-loss laser waveguide parameters were investigated in Fe:ZnSe. The passive characterisation found the waveguide propagation losses to be as low as 0.4 dB/cm, which is much lower than those demonstrated in other ULI cladding waveguides in Cr:ZnSe and Cr:ZnS. The low-loss waveguides were inserted inside a cryostat for CW laser operation. A free running CW laser operation with an Fe:ZnSe waveguide laser was demonstrated. An output power of 76 mW was produced at 4122 nm with a pump power of 908 mW. This work highlights the operational wavelength versatility of ULI fabricated depressed cladding waveguides.

Acknowledgements

I would like to thank my supervisor Ajoy K. Kar, for his support and encouragement throughout my PhD.

I thank the Engineering and Physical Sciences Research Council (EPSRC) for my studentship which provided the means for me to undertake this work.

I would like to than all the members of the Nonlinear Optics Group over the past four years. In particular, I thank John Macdonald and Stephen Beecher for training me in ULI and Mid-IR waveguide laser characterisation. Equally, I would like to thank James Morris and Mark Mackenzie for the discussions on all things ULI throughout my PhD. I extend my gratitude to Fiona Thorburn for her collaborations with me at the end of my thesis and wish her the best of luck in continuing the project.

Sincere thanks to Gary Cook and Sean McDaniel at the Air Force Research Laboratory, the Wright-Patterson Air Force Base (WPAFB), USA for the many discussions on TM:II-VI lasers. I am grateful for the research visits they made to Heriot-Watt, where I learned many skills from them, without which most of my thesis would not exist. I thank Gary for letting me tap into his vast knowledge of all things related to photonics, and for his excellent photographs which always encourage me to pick up my own camera. I would also like to thank Sean for inscribing waveguides in Cr:ZnSe for my work and introducing me to Laphroaig whisky.

I would like to thank my family Paul, Morag and Kirsty for their continued support.

Finally, I would like to extend my eternal gratitude to my fiancée Eilidh Francis for her support and patience throughout my PhD. In particular, I would like to thank her for her eagle-eyed editing to ensure the removal of all farm animals from this thesis.

Contents

1. Introduction 1

1.1. Mid Infrared Laser Sources 1

1.2. Ultrafast Laser Inscription 3

1.3. Summary of the Thesis 6

1.4. Thesis Outline 7

2. Review of ULI waveguides in Transition Metal doped II-VI Semiconductors 9

2.1. Spectroscopy of Transition Metal doped II-VI Lasers 9

2.2. Ultrafast Laser Inscription Absorption Processes 12

2.3. Implementation of Ultrafast Laser Inscription 14

2.3.1. ULI Inscription Geometry 14

2.3.2. Multi Element Waveguide Schemes 17

2.4. Ultrafast Laser Inscription in ZnSe Substrates 19

2.4.1. Mitigating Nonlinear Effects for ULI in ZnSe 22

2.4.2. NIR Waveguides in ZnSe 30

2.4.3. Mid-IR Waveguides in ZnSe 31

2.4.4. Ultrafast Laser Inscription in Cr:ZnSe 33

2.5. Conclusion 36

3. Cr:ZnSe tuneable waveguide laser 38

3.1. Introduction 38

3.2. Tuning Methods 39

3.2.1. Blazed gratings tuning 39

3.2.2. Prism tuning 41

3.2.3. Theoretical comparison of grating and prisms tuning extended cavities 42

3.3. Cr:ZnSe wavelength tuning with blazed grating 46

3.4. Modelling of diffraction grating 52
3.5. Cr:ZnSe Wavelength Tuning with Silicone Prism 54
3.6. Conclusion 63
4. Modelocking of Cr:ZnSe waveguide laser 64
4.1. Introduction 64
4.2. Background Theory of Modelocked Lasers 65
4.3. Measurement of Ultrafast Laser Pulses 72
4.4. Modelocking of Cr:ZnSe Waveguide Laser 74
4.5. Power Scaling of Modelocked Cr:ZnSe Waveguide Laser 82
4.5.1. Pump Laser Characterisation 82
4.5.2. Waveguides and Cavity Setup 86
4.5.3. Modelocked Laser Results of 300 MHz Cavity 87
4.5.4. Modelocked Laser Results of Gigahertz Cavity 91
4.5.5. Conclusion of Modelocked Power Scaling 96
4.6. Conclusion 97
5. Cr:ZnS Waveguide Laser 99
5.1. Introduction 99
5.2. Waveguide Fabrication in Cr:ZnS 103
5.3. Cr:ZnS Waveguide Laser 105
5.4. Conclusion 111
6. Fe:ZnSe Waveguide Laser 113
6.1. Introduction 113
6.2. Waveguide Fabrication and Passive Guiding Characterisation 115
6.2.1. Waveguide Fabrication in Fe:ZnSe 115
6.2.2. Mid-IR Passive Characterisation of Fe:ZnSe Waveguides 121
6.3. Fe:ZnSe Waveguide Laser 124
6.3.1. Optical Pumping of Fe:ZnSe and its Limitations 124

6.3.2. Fe:ZnSe Waveguide Laser Operation 125
6.3.3. Fe:ZnSe Waveguide Laser Loss Analysis 132
6.4. Bulk Fe:ZnSe Laser 139
6.5. Conclusion 145
7. Conclusions and Future Work 147
7.1. Conclusions 147
7.2. Future Work 148
7.2.1. Monolithic Wavelength Tuned Waveguide Laser 148
7.2.2. Monolithic Dispersion Compensated Modelocked Waveguide Laser 150
7.2.3. Monolithic Optical pumping of TM:II-VI Waveguide Laser 153
References 155
Appendix 173

List of Abbreviations

Acoustic Optic Modulator - AOM

Cerium - Ce

Continuous Wave - CW

Erbium Doped Fibre Amplifier - EDFA

Frequency-Resolved Optical Gating - FROG

Gallium Lanthanum Sulphide - GLS

Gradient-Index - GRIN

Graphene Saturable Absorber Mirror - GSAM

Group Velocity Dispersion - GVD

Hot Isostatic Pressing - HIP

Integrated Circuits - IC

Iron-doped ZnSe – Fe:ZnSe

Mode Field Diameter - MFD

Multicore Fibre - MCF

Optical Parameter Oscillators - OPO

Optical Spectrum Analyser - OSA

Photonic Integrated Circuits - PIC

Polydimethylsiloxane - PDMS

Pulse Repetition Frequency - PRF

Pulsed Laser Deposition - PLD

Q-Switched Modelocking - QML

Quantum Cascade Lasers - QCL

Rare Earth - RE

Room Temperature - RT

Saturable Absorber - SA

Scandium - Sc

Semiconductor Saturable Absorber Mirror - SESAM

Silicon-On-Insulator - SIO

Strontium Barium Niobate - SBN

Transition Metal - TM

Ultrafast Laser Inscription - ULI

Zinc - Zn

List of Publications by the Author

Journal Papers

1. J. R. Macdonald, S. J. Beecher, **A. Lancaster**, P. A. Berry, K. L. Schepler, S. B. Mirov and A. K. Kar, "Compact Cr:ZnS channel waveguide laser operating at 2333 nm," Optics Express **22**, 7052-7057 (2014).

2. J. R. Macdonald, S. J. Beecher, **A. Lancaster**, P. A. Berry, K. L. Schepler, and A. K. Kar, "Ultrabroad Mid-Infrared Tunable Cr:ZnSe Channel Waveguide Laser," Selected Topics in Quantum Electronics, IEEE Journal of **21**, 375-379 (2015).

3. **A. Lancaster**, G. Cook, S. A. McDaniel, J. Evans, P. A. Berry, J. D. Shephard, and A. K. Kar, "Mid-infrared laser emission from Fe:ZnSe cladding waveguides," Appl. Phys. Lett. **107**, 031108 (2015).

4. S. A. McDaniel, **A. Lancaster**, J. W. Evans, A. K. Kar, and G. Cook, "Power scaling of ultrafast laser inscribed waveguide lasers in chromium and iron doped zinc selenide," Optics Express **24**, 3502-3512 (2016).

5. S. McDaniel, F. Thorburn, **A. Lancaster**, R. Stites, G. Cook, and A. Kar, "Operation of Ho:YAG ultrafast laser inscribed waveguide lasers," Applied Optics **56**, 3251-3256 (2017).

Conference Papers

1. Y. Y. Ren, S. J. Beecher, G. Brown, A. Rodenas, **A. Lancaster**, F. Chen and A. K. Kar, "Q-switched mode-locking of a mid-infrared Tm:YAG waveguide laser with graphene film," in *Lasers and Electro-Optics Pacific Rim (CLEO-PR), 2013 Conference on*, 2013), 1-2.

2. **A. Lancaster**, G. Cook, S. McDaniel, J. Evans, P. Berry, J. Shephard and A. Kar, "Fe:ZnSe Channel Waveguide Laser Operating at 4122 nm," in *CLEO: 2015*, OSA Technical Digest (online) (Optical Society of America, 2015), SM2F.5.

3. G. Demetriou, F. Thorburn, **A. Lancaster**, C. Craig, E. Weatherby, D. W. Hewak and A. Kar, "Fluorescence in Erbium Doped Gallium Lanthanum Sulphide: Potential for mid-IR Waveguide Laser," in *CLEO: Science and Innovations*, (Optical Society of America, 2015), STh1G. 2.

4. **A. Lancaster**, A. Choudhary, J. S. Nitin, R. Mary, D. P. Shepherd and A. K. Kar, "1.94 GHz CW Modelocked Ytterbium-Doped Bismuthate Glass Waveguide Laser," in *Advanced Solid State Lasers*, OSA Technical Digest (online) (Optical Society of America, 2015), AM5A.22.

5. J. Morris, G. Demetriou, **A. Lancaster**, A. Kar and H. Bookey, "3D Optical Waveguides in Ge22As20Se58 Glass - a Highly Nonlinear Material for the Mid-IR," in *Conference on Lasers and Electro-Optics*, OSA Technical Digest (2016) (Optical Society of America, 2016), JTh2A.82.

6. S. A. McDaniel, **A. Lancaster**, R. W. Stites, F. Thorburn, A. K. Kar and G. Cook, "Cr:ZnSe guided wave lasers and materials," in SPIE Photonics West/LASE, 2017), paper 10082-10012.

ACADEMIC REGISTRY

Research Thesis Submission

Name:	Adam Lancaster		
School:	School of Engineering and Physical Sciences		
Version: *(i.e. First, Resubmission, Final)*	Final	Degree Sought:	PhD Physics

Declaration

In accordance with the appropriate regulations I hereby submit my thesis and I declare that:

1) the thesis embodies the results of my own work and has been composed by myself
2) where appropriate, I have made acknowledgement of the work of others and have made reference to work carried out in collaboration with other persons
3) the thesis is the correct version of the thesis for submission and is the same version as any electronic versions submitted*.
4) my thesis for the award referred to, deposited in the Heriot-Watt University Library, should be made available for loan or photocopying and be available via the Institutional Repository, subject to such conditions as the Librarian may require
5) I understand that as a student of the University I am required to abide by the Regulations of the University and to conform to its discipline.
6) I confirm that the thesis has been verified against plagiarism via an approved plagiarism detection application e.g. Turnitin.

* *Please note that it is the responsibility of the candidate to ensure that the correct version of the thesis is submitted.*

Signature of Candidate:		Date:	

Submission

Submitted By *(name in capitals):*	
Signature of Individual Submitting:	
Date Submitted:	

For Completion in the Student Service Centre (SSC)

Received in the SSC by *(name in capitals):*			
Method of Submission *(Handed in to SSC; posted through internal/external mail):*			
E-thesis Submitted ***(mandatory for final theses)***			
Signature:		Date:	

Please note this form should be bound into the submitted thesis.
Academic Registry/Version (1) August 2016

List of Figures

Figure 2.1. Energy level diagram showing weak and strong electron-phonon coupling in (a) RE and (b) TM ions respectively. This diagram has been reproduced from Petermann [60]. 10

Figure 2.2. Schematic of the elongation of an octahedral crystal field arising from the Jahn-Teller effect, resulting in a splitting of the energy levels. This process is also present in a tetrahedral crystal field. This schematic has been reproduced from Lancashire [64]. 11

Figure 2.3. Normalised absorption and emission spectra of Cr^{2+} and Fe^{2+} doped into (i) ZnS, (ii) ZnSe, (iii) CdSe and (iv) CdMnTe. This graph has been reproduced from Mirov et al. [68]. 12

Figure 2.4. Diagram of ULI, initial absorption process is from (a) Multiphoton ionisation or (b) Tunnelling ionisation. These processes seed Avalanche ionisation which consists of (c) Free carrier absorption leading to (d) Impact ionisation. 13

Figure 2.6. Schematic of (a) longitudinal and (b) transverse inscription geometry. 15

Figure 2.7. Schematic of waveguides fabricated with a femtosecond laser viewed from the end facet of the waveguide. Red represents a localised increase in refractive index. Black modification represents a reduction in refractive index. 17

Figure 2.8. Refractive index profile of (a) step-index waveguide and (b) W-type waveguide. This diagram has been reproduced from Hu and Menuk [89]. 19

Figure 2.9. Transmission of 4.81 mm thick polycrystalline ZnSe sample. Transmittance has not been Fresnel corrected. This graph has been reproduced from Berry et al. [92]. 21

Figure 2.10. Schematic of self-focusing of a collimated Gaussian laser beam showing the Kerr effect as predicted by Fermat's principle. Reproduced from Boyd [94] 22

Figure 2.11. Schematic of self-trapping of light when $P = P_{cr}$. Reproduced from Boyd [94]. 23

Figure 2.12. (a) Schematic of self-focusing followed by filamentation leading to defocusing and then repeating. This has been reproduced from Couairon and Mysyrowicz [96]. (b) Transmission microscope image of ZnSe end facet shows a filamentation structure formed after ULI. The field of view of the image is 90 μm by 100 μm. The

inscription laser had a pulse width of 500 fs at 1047 nm. This image has been reproduced from MacDonald et al. [23]. 24
Figure 2.13. Nonlinear refractive index of ZnSe in the visible to NIR. Figure reproduced from M. Balu et al. [95]. 25
Figure 2.14. Group velocity dispersion (GVD) of ZnSe for 0.7–1.2 μm. Values calculated for Sellmeier coefficients of ZnSe given in [101] using equations detailed in [97]. 28
Figure 2.15. Modelling of Gaussian pulse width after propagating through 300 μm of ZnSe. The initial pulse width was 10 fs. Calculations were based on Sellmeier coefficients for ZnSe given in Table 1. 29
Figure 2.16. Modelling of Gaussian pulse width after propagating through 300 μm of ZnSe. The initial pulse width was 100 fs. Calculations were based on Sellmeier coefficients for ZnSe given in Table 1. 29
Figure 2.17. Modelling of Gaussian pulse width after propagating through 300 μm of ZnSe. The initial pulse width was 1000 fs. Calculations were based on Sellmeier coefficients for ZnSe given in Table 1. 30
Figure 2.18. (a) is a transmission microscope image of a ZnSe multiscan waveguide end facet.The waveguide structure was inscribed with a 1.5 ps laser pulse width. (b) Near-field mode image of the waveguide output at 1550 nm. The field of view of (a) and (b) is 50 μm x 50 μm. This figure has been reproduced from MacDonald et al. [23]. 31
Figure 2.19. Schematic of cladding waveguide structures in ZnSe viewed from the end facet. Left is a negative index change element. Centre is a box section multiscan cladding waveguide. Right is a circular depressed cladding waveguide. 33
Figure 2.20. Multiscan structure inscribed in (a) ZnSe and (b) Cr:ZnSe with identical inscription parameters. Reproduced from MacDonald [52]. 34
Figure 2.21. Schematic of double cladding waveguide in Cr:ZnSe. Diagram (a) shows the entire waveguide sample, (b) is a zoomed in image of the end facet. The blue inner cladding is inscribed with less than 500 nJ pulse energy. The orange outer cladding was inscribed with 1 μJ pulse energy. Reproduced from MacDonald et al. [53]. 34
Figure 3.1. Spectral tuneability range of Cr^{2+} lasers and spectral positions of trace gas absorption lines with minimum detectible concentrations. This graph has been reproduced from Sorokina and Sorokin [106]. 38
Figure 3.2. Schematic of extended cavity wavelength tuning designs using a blazed grating (a) is the Littrow configuration and (b) is the Littman-Metcalf configuration ... 40

Figure 3.3. Schematic of extended cavity wavelength tuneable waveguide laser cavity using a single stationary prisms and rotating output coupler 42
Figure 3.4. Acceptance bandwidth of grating and tuneable elements. The grating used for the Littrow (blue) and Littman-Metcalf (red) has 600 grooves per mm. The angle of incidence on the gratings is set to sin(θ) = λ/2d. For this calculation the prisms are arranged in the Littrow configuration. The prism materials examined are ZnSe (yellow), CaF_2 (purple) and Si (green). 44
Figure 3.5. Efficiency curve for Littrow configuration of Thorlabs GR25-0616 grating. The incident laser light polarised perpendicular (blue) and parallel (red) to the lines of the grating are shown. The graph has been reproduced from the Thorlabs specification sheet. 45
Figure 3.6. Efficiency curve for Littrow configuration of Thorlabs 1325-45031 grating. The incident laser light polarised perpendicular (blue) and parallel (red) to the lines of the grating are shown. The graph has been reproduced from Thorlabs' specification sheet. 46
Figure 3.7. Absorption cross-section of Cr:ZnS (green) and Cr:ZnSe (red). The emission wavelength of Er and Tm doped fibre lasers have been superimposed on top of the graph to show their overlap with Cr:II-VI materials absorption. This graph has been reproduced from Sorokina et al. [106]. 47
Figure 3.8. Transmission microscope image of the Cr:ZnSe waveguide end facet used in the wavelength tuneable experiments. A x20 microscope lens was used to image the end facet. Horizontal diameter of waveguide is 80 µm. 49
Figure 3.9. Schematic of extended cavity Littman-Metacalf grating configuration wavelength tuneable Cr:ZnSe waveguide lasers. Lenses 1 and 2 are D coated 50 mm focal length plano-convex CaF_2 lens. Wavelength tuning of the cavity is achieved by rotating the silver mirror as shown above. 50
Figure 3.10. Littman-Metcalf tuneable grating Cr:ZnSe waveguide laser performance. The wavelength was tuned by rotating the tuning mirror. The pump power for these measurements was set to 1.4 W. Black dots show the measured output power of the laser for a corresponding wavelength. The red and blue lines show the normalised absorption and emission cross-section of Cr:ZnSe. 51
Figure 3.11. Wavelength spectra of grating tuned extended cavity Cr:ZnSe waveguide laser. Measurements were taken with Yokogawa AQ6375 with a resolution of 0.05 nm. 52

Figure 3.12. Cr:ZnSe tuneable waveguide laser experimental results and numerical model overlaid. The black dots represent the experimental data. The red line is the numeric model. 54
Figure 3.13. Experimental arrangement of the wavelength tuneable Cr:ZnSe external cavity waveguide laser using a Si prism. The output coupler is rotated to tune the lasing wavelength. Lens 1 and 2 are 50 mm and 20 mm focal length lenses respectively, which are D coated CaF_2 plano-convex lenses. 55
Figure 3.14. Wavelength tuneable Cr:ZnSe laser performance using a Si prism. The short wavelength mirror set (black squares) used a pump mirror with reflectance > 99.9 % for a range of 2000-2500 nm and an output coupler with reflectance 80 ± 5 % for a range of 1700-2700 nm. The long wavelength mirror set (red dots) used a pump mirror with reflectance > 99.6 % for a range of 2500-3000 nm and an output coupler with reflectance 89 ± 1 % for a range of 2800-3070 nm. 57
Figure 3.15. Normalised intensity spectrum of Si prism wavelength tuned Cr:ZnSe waveguide. Measurements taken with Zolix Omni-λ 300 monochromator. Spectra taken with a short mirror set are black. Spectra taken with a long mirror set are red. 58
Figure 3.16. Typical spectra of Si prism tuned Cr:ZnSe waveguide laser with short wavelength mirror set. Green line is a Gaussian fit to the data. From the fit the peak was found to be centred at 2275.7 nm with a FWHM of 2.6 nm. 59
Figure 3.17. Typical spectra of Si prism tuned Cr:ZnSe waveguide laser with long wavelength mirror set. Purple line is a Gaussian fit to the data. From the fit the peak was found to be centred at 2690.6 nm with a FWHM of 1.7 nm. 59
Figure 3.18. Red dots are experimental measurements of FWHM linewidth of Si prism tuned Cr:ZnSe waveguide laser. Blue line is the acceptance bandwidth of a Si prism tuned cavity expected form the model. The beam radius was to 2 μm for the model. Sellmeier coefficients used for calculating dn/dλ are detailed in Table 3. 61
Figure 3.19. Bulk Cr:ZnSe lasers tuned with CaF_2 prism. Red dots are output powers at a given wavelength for 5 W of pump incident on the sample. Grey line represents the intra cavity transmission of a resonator with a round trip length of 120 cm with the room at 40 % r.h.. The absorption is from water vapour. This graph has been reproduced from Sorkin et al. [17]. 62
Figure 4.1. Model cavity design showing the optical elements needed for a modelocked laser cavity. This has been reproduced from Keller [59]. 66

Figure 4.2. Schematic of loss modulation in an active modelocked laser. This has been reproduced from Keller [59]. 67
Figure 4.3. Schematic of passive modelocking showing the interaction of the loss induced by an SA and a circulating laser pulse. This has been reproduced from Keller [59]. 68
Figure 4.4. Schematic of modelocked laser in the time domain, where I is the intensity of the laser pulse and φ is the phase. This has been reproduced from Keller et al. [59]. ... 69
Figure 4.5 Schematic of modelocked laser operation in frequency space, note the constant phase. This has been reproduced from Keller et al. [59]. 69
Figure 4.6. Schematic of interferometric autocorrelator experimental setup, with nonlinear crystal. 73
Figure 4.7. Interferometric autocorrelation of modelocked Ti- Sapphire laser. This graph has been reproduced from Yuqiang et al.[141]. 74
Figure 4.8. Schematic of modelocked Cr:ZnSe waveguide laser. M1 is a 45º AR coated at 1.9 μm and HR coated at 2.3 - 3 μm dichroic mirror. M2 is a dichroic mirror with AR at 1.9 μm and 98 % reflecting at 2 - 3μm coatings. L1, L2 and L3 are 50 mm plano-convex lenses AR coated from 1.65 to 3.0 μm. LP is a 2000 nm longpass filter. 75
Figure 4.9. RF spectrum of CW modelocked Cr:ZnSe waveguide laser operating with 1.3 W of pump power. The graph has a span of 9 MHz and the measurement was taken with a resolution bandwidth of 1 kHz. 77
Figure 4.10. RF spectrum of CW modelocked Cr:ZnSe waveguide laser operating with 1.3 W of pump power. The graph has a span of 100 kHz and the measurement was taken with a resolution bandwidth of 1 kHz. 77
Figure 4.11. Power performances of modelocked Cr:ZnSe waveguide lasers with PRF of 295 MHz. Slope efficiency of laser was calculated from a linear fit of the black data points where the laser was found to be modelocked from the RF spectrum. The red data points are when the laser is operating in pure CW operation. 78
Figure 4.12. MFD of Cr:ZnSe modelocked laser. Imaged with a 500 mm lens with the laser pumped with 1.3 W of pump power. 79
Figure 4.13. Full wavelength spectra of modelocked Cr:ZnSe waveguide laser 80
Figure 4.14. Expanded view of main spectral emission peak of modelocked Cr:ZnSe waveguide laser. 81
Figure 4.15. Plot of IPG laser beam waist along the z axis for M^2 measurement. The collimated output of the IPG laser was focused with a 50 mm lens. The IPG laser was set to 40% diode power for this measurement. 84

Figure 4.16. Plot of beam waist squared against propagation in the z axis. The IPG laser was operated at 40% diode power. This plot was fitted with Equation 23 using Matlab's lense squared curve fitting tool. This fit found the free parameters to be w_o= 19.11 μm, z_0 = 10.86 mm, θ = 0.0432 rad and M^2 of 1.361. 85
Figure 4.17. Power control system for IPG pump laser 86
Figure 4.18. Schematic of modelocked Cr:ZnSe waveguide laser. M1 is a 45° AR 1.9 μm and HR 2.3 - 3 μm dichroic mirror. M2 is a dichroic mirror that is AR at 1.9 μm and 98%, reflecting at 2 - 3 μm. L1, L2 and L3 are 50 mm CaF_2 plano-convex lenses AR coated from 1.65 - 3.0 μm. 87
Figure 4.19. RF spectrum of CW modelocked Cr:ZnSe waveguide laser operating with 5 W of pump power. The graph has a span of 4 MHz and the measurement was taken with a resolution bandwidth of 300 Hz. 88
Figure 4.20. Wavelength spectrum of modelocked Cr:ZnSe waveguide laser. A Gaussian fit was applied to the data. From the fit, the central wavelength was found to be 2508 nm with a FWHM of 6 nm. The laser was operated with PRF of 308 MHz at a pump power of 5W. 89
Figure 4.21. Schematic of 2-photon interferometric autocorrelator 90
Figure 4.22. Autocorrelation of Cr:ZnSe waveguide laser with PRF of 308 MHz with pump power of 5 W. Light blue line is the autocorrelation trace. Dark blue dots are smoothed data setup using the nearest neighbour method. Red line is a $sech^2$ fit of the autocorrelation trace. From the fit, the pulse width was calculated to be 638 fs. 91
Figure 4.23. RF spectrum of CW modelocked Cr:ZnSe waveguide laser operating with a PRF of 961 MHz. The laser was pumped with 5 W. The graph has a span of 10 MHz and the measurement was taken with a resolution bandwidth of 300 Hz. 92
Figure 4.24. Wavelength spectra of modelocked Cr:ZnSe waveguide laser. The laser was operated at 961 MHz with a pump power of 5 W. 93
Figure 4.25. Autocorrelation of Cr:ZnSe waveguide laser with PRF of 961 MHz with pump power of 5 W. Light blue line is the autocorrelation trace. Dark blue dots are the nearest neighbour smoothing of the autocorrelation trace. Red line is a $sech^2$ fit of the autocorrelation trace. From the fit, the pulse width was calculated to be 1477 fs. 94
Figure 4.26. Wavelength spectra of modelocked Cr:ZnSe waveguide laser. The laser was operated at 1.03 GHz with a pump power of 5 W. 95
Figure 4.27. Autocorrelation of Cr:ZnSe waveguide laser with PRF of 1.03 GHz, operated with a pump power of 5 W. Light blue line is the autocorrelation trace. Dark blue dots are

the nearest neighbour smoothing of the autocorrelation trace. Red line is a $sech^2$ fit of the autocorrelation trace. From the fit, the pulse width was calculated to be 2024 fs. 96
Figure 5.1. Absorption cross-section of (i) Cr:ZnS and (ii) Cr:ZnSe. Emission cross-section of (iii) Cr:ZnS and (iv) Cr:ZnSe. Figure reproduced form Mirov et al. [70].... 100
Figure 5.2. Temperature dependent upper state lifetime of vibronically-broadened gain media. Green dots are Cr:ZnS, red dots are Cr:ZnSe and pink dots are Ti:Sapphire. This graph has been reproduced from Sorokina et al. [106]. 102
Figure 5.3. Diagram viewing from the end facet of a depressed cladding waveguide inscribed in Cr:ZnS. Conventions used for waveguide depth, diameter and element are given. 104
Figure 5.4.(a) Schematic of depressed cladding waveguide, red elements represent the irradiated area of the Cr:ZnS. (b) transmission microscope image of waveguide viewed from the end facet. This waveguide had a diameter of 60 μm and was made up of 40 elements..... 105
Figure 5.5. Schematic of Cr:ZnS waveguide laser used in the CW laser operation investigation. Lenses 1 and 2 are AR coated CaF_2 lenses with 50 mm focal length. LP is a 2000 nm longpass filter to remove any non-absorbed pump light. 106
Figure 5.6. Characterisation of Cr:ZnS waveguide laser output power for different output coupler reflectance. The pump power has been compensated for a Fresnel reflection at the input of the air-Cr:ZnS surface. The output power of a 99% reflective (black squares), 80% reflective (red circles), 70% reflective (blue triangle) and 60% reflective (pink triangle) output couplers have been fitted with a linear fit. The green data points were near or at threshold and have been removed for the fitting..... 107
Figure 5.7. Findlay-Clay analysis of Cr:ZnS waveguide laser. From the linear fit the total cavity loss was is 6.4 dB. 108
Figure 5.8. Output mode image of Cr:ZnS waveguide lasers. Image taken with 30 mm focal length lens and Mid-IR camera (FLIR SC7000). 110
Figure 5.9. Normalised wavelength spectra of Cr:ZnS waveguide laser using Zolix Omni-λ 300 monochromator. The measurement was taken with a 60% reflective output coupler. From the Gaussian fit, the laser peak was calculated to be 2332.6 nm with a FWHM of 2.2 nm..... 111
Figure 6.1. Luminescence lifetime of Fe doped ZnSe and ZnS. This graph has been reproduced from Myoung et al. [174]. 114

Figure 6.2. Transmission microscope image of waveguides fabricated in Fe:ZnSe. Inscription parameters are given in Table 11, waveguides are numbered from 1 to 11, left to right respectively. Field of view of image is 3.2 mm by 0.7 mm. 118
Figure 6.3. Absorption cross-section of Cr:ZnSe (red line) and Fe:ZnSe (blue line). Insert shows an expanded view of the absorption at the inscription laser wavelength 1047 nm. This graph has been reproduced from McDaniel et al. [24]. 120
Figure 6.4. Photograph of the copper cold finger. Note the image was taken with a wide angle lens (phone camera) hence has strong optical distortions. The diameter of the cold finger was 10 mm. 122
Figure 6.5. Passive waveguide test setup for Fe:ZnSe waveguides at 77 K. L1 is a non-AR coated 100 mm focal length CaF_2 lens. L2 and L3 are AR coated CaF_2 lenses with focal lengths of 50 mm. W1 and W2 are non-AR coated CaF_2 windows. 123
Figure 6.6. Schematic of Fe:ZnSe waveguide laser in a cryostat cooled by liquid nitrogen. L1 is a 100 mm focal length CaF_2 lens used to collimate the pump laser. L2 and L3 are AR coated intra cavity CaF_2 lenses with a focal length of 50 mm. W1 and W2 are CaF_2 windows. Longpass Filter is a 3000 nm longpass filter used to remove residual pump light. 126
Figure 6.7. Waveguide 3: Input power vs. output power of Fe:ZnSe waveguide lasers. This waveguide had an inscription diameter of 150 μm. 127
Figure 6.8. Waveguide 4: Input power vs. Output power of Fe:ZnSe waveguide lasers. This waveguide had an inscription diameter of 200 μm. 127
Figure 6.9. Normalised spectra of Fe:ZnSe waveguide laser under 908 mW of pump power. Waveguide 4: output coupler was 80% reflecting. 129
Figure 6.10. Near field mode imagining setup for Fe:ZnSe waveguides. L1 is a 35 mm AR coated CaF_2 lens. L2 is a 50 mm AR coated CaF_2 lens. LP filter is a 3000 nm longpass filter. The signal and pump guide modes where image with the setup. For pump guide mode imaging, the LP filter was removed. 130
Figures 6.11(a) and (b)are transmisson microscope images of Waveguides 3 and 4 respectively. Images (c) and (b) are mode images of the pump mode from Waveguides 3 and 4 respectively. Images (e) and (f) are the mode images of the lasing signal mode of Waveguides 3 and 4 respectively. 131
Figure 6.12. Findlay-Clay analysis of Fe:ZnSe waveguide laser. The blue lines are a linear fit for Waveguide 3 data points, as the black lines are for Waveguide 4. The dotted lines

include all data points and the solid lines omit the lasing for the end facet data points. 133
Figure 6.13. Schematic of intra cavity loss contributions in Fe:ZnSe waveguide laser. L1 and L2 represent the transmission loss the of the AR coated CaF_2 lens. W1 and W2 represent the transmission loss of the CaF_2 windows. F1 and F2 are the loss contributions from Fresnel reflections. WG is the propagation loss of the Fe:ZnSe waveguide.....134
Figure 6.14. Schematic of experimental setup of scattering loss measurements using a Mid-IR imaging camera positioned transverse to the waveguide propagation direction 136
Figure 6.15. Scattering loss of Waveguide 4 measured by the scattering imaging method. The blue line is the measured data and the red dotted line is fit to that data. The inset shows the image captured by the Mid-IR camera. The arrow indicates the input facet. 137
Figure 6.16. Emission spectrum of diffusion doped polycrystalline Fe:ZnSe bulk laser, red line. Insert shows an expanded view of the laser emission. Emission cross-section is shown by the black dotted line. This graph has been reproduced from Evans et al. [180]. 140
Figure 6.17. Fe:ZnSe bulk laser cavity for CW operation. L1 is a non AR coated CaF_2 lens used for collimation of the pump laser. L2 is a 35 mm focal length AR coated CaF_2 lens. W1 and W2 are non-coated CaF_2 flat windows. L3 is a 45 mm focal length AR coated CaF_2 lens. F2 and F3 size is the same as the focal lengths of lens L2 and L3 respectively. 141
Figure 6.18. Output power of Fe:ZnSe bulk laser black triangles and waveguide laser red squares. For both cases the laser had a 90% reflective output coupler at the signal wavelength. The pump power has been reduced by the first Fresnel reflection on the input facet. 142
Figure 6.19.(a) Pump mode of bulk laser cavity. (b) Pump mode image of waveguide laser. (c) Waveguide laser mode image at 4122 nm imaged at end facet when lasing from Fresnel reflection at output facet. (d) Bulk laser output mode centered at 4123 nm lasing from Fresnel reflection at output facet. 143
Figure 6.20. Normalised wavelength spectra of Fe:ZnSe lasers. The resolution of the spectra are 0.4 nm. Red dotted line is a bulk cavity configuration. Black solid line is a waveguide cavity configuration. 144

Figure 7.1. Schematic of electro-optic tuned Bragg grating for monolithic wavelength tuning of Cr:ZnSe waveguide lasers. 149
Figure 7.2. Holographically recorded reflection filters in $LiNbO_3$:Ti:Cu channel waveguides. (a)Geometry for recording and read-out of the grating, and (b)typical transmission spectrum T(λ) of a 15 mm-long filter. The c-axis referred to in the report is the z-axis in this schematic. These figures have be reproduced from Gunter and Huignard [193]. 150
Figure 7.3. Schematic of CW modelocked Cr:ZnS bulk laser operating with a pulse width of 41 fs at a PRF for 108 MHz. FL is the pump focusing lens (f= 40 mm), M2 and M3 are HR dielectric mirrors, CM is a concave chirped mirror, GSA is a graphene-based saturable absorber mirror, DC is the YAG prism pair and OC is the output coupler. This diagram has been reproduced from Tolstik et al. [194]. 151
Figure 7.4. Diagram of CW modelocked Ytterbium doped bismuthate glass waveguide laser with GVD compensation from adjusting the gap Δx. 152
Figure 7.5. Schematic of cavity design for a monolithic passively modelocked Cr:ZnSe waveguide laser. GVD control is managed with a ULI inscribed waveguide in CaF_2. Passive modelocking is achieved using a SESAM or multilayer layer graphene saturable absorber. 153
Figure 7.6. Proposed design of fully monolithic Cr:ZnSe waveguide laser system. 154
Figure 7.7. Proposed design of fully monolithic Fe:ZnSe waveguide lasers system.... 154

1. Introduction

1.1. Mid Infrared Laser Sources

The first laser was demonstrated in 1960 by T. H. Maiman [1] with a flash lamp pumped ruby laser. In the following years, the race was on to find and characterise new potential sources for laser emission [2]. This resulted in the discovery of a Nd:YAG laser by J. E. Geusic et al. [3] in 1964, which is still widely used today. The first application of a laser was in range-finding; it works by a time of flight measurement of a pulsed laser beam. Initial range-finders used a ruby laser, but with the factor of 10 efficiency improvement offered by Q-switched Nd:YAG it quickly became the standard source for this application [2]. For long range stand-off sensing applications, it is important to choose a laser with its emission wavelength in the atmospheric transmission window. Care must also be taken to ensure that the laser is eye safe when operating in open air conditions. There are two methods of achieving this. The first is to limit the output power of the laser, less than a few mW in the visible region, by using only Class 1 or 2 lasers. The second is to use radiation at a longer wavelength, > 1.4 μm, in the eye safe range. The signal to noise of detected reflected light may not be sufficient for a successful measurement using Class 1 or 2 lasers. This has led to the development of Mid-IR lasers for remote sensing applications.

Initially, very few laser sources existed that operated in the Mid-IR, 2 − 5 μm, part of the electromagnetic spectrum. The reason for this was the lack of semiconductor diode lasers operating in the Mid-IR. However, gas and lead salt lasers were available. Arguably the most well known laser, the HeNe gas laser commonly used for 633 nm emissions also offers laser emission at 3.39 μm. CO and CO_2 gas lasers output at wavelengths of 4.8 – 8.3 μm and 9.4 or 10.6 μm respectively. Wider wavelength tuneablity was achieved with lead salt based lasers. An example is the PbSnTe which has demonstrated laser emission over the range of 8.5 – 15.9 μm, operating over a cryogenically cooled temperature range of 12 – 114 K [4]. A wide wavelength tuneable operation is also available by taking advantage of nonlinear properties of light in a dielectric medium such as in optical parameter oscillators (OPO). This system requires a high irradiance pumping with relatively long coherence lengths, which normally requires a diode-pumped solid-state laser source such as a Modelocked Ti-Sapphire laser system. This makes the system large

and it becomes very sensitive to slight alignment changes; thus making it unsuitable for many applications. The invention of quantum cascade lasers (QCLs), first demonstrated by Faist et al., [5], replaced many of the lead salt lasers and nonlinear systems. QCLs now cover a vast wavelength range of 3 – 25 μm [6]. Their performance peaks at 5 μm, with wall plug efficiencies of 50% [7] and a continuous wave (CW) laser operation of 5.1 W at room temperature [8].

Interest in the development of new laser sources in the Mid-IR (2 – 5 μm) has grown in recent years. The reason for this is that the atmospheric transmission window and molecular absorption lines both lie in the Mid-IR. Potential uses for these lasers include: breath analysis [9], laser surgery [10], remote sensing and military applications, among others. Many of these applications require small footprint devices which operate at room temperature (RT) to make them practical. This means that the commonly used lead salt lasers are not suitable because of the requirement for cryogenic cooling for effective operation [11]. Availability of non-cryogenically cooled quantum cascade lasers in the 2 – 3 μm range is very limited [6]. OPOs are also unsuitable because of the large optical setup needed to take advantage of the frequency splitting by use of nonlinear materials and gratings. Transition metal doped II-VI (TM:II-VI) semiconductors, first introduced to the optics community by DeLoach et al., [12], offers one solution to the lack of laser sources in the Mid-IR spectral region. TM:II-VI semiconductors with chromium 2+ ions as the dopant in ZnSe, ZnS and CdSe bases have many desirable properties such as large absorption and gain bandwidths, large emission cross-sections, no excited state absorption and room temperature operation [12-15]. Cr:ZnSe lasers have demonstrated room temperature operation with CW output powers of 139 W using a rotating disk cavity [16] and a continually tuneable CW laser operation from 1973-3339 nm [17]. Iron-doped ZnSe (Fe:ZnSe) is another promising broadband gain medium with luminescence from 3.5 to 5.2 μm at room-temperature [18]. This lines up well with the second Mid-IR atmospheric transmission window.

The limitations in further power scaling of TM:II-VI-based lasers has been attributed to thermal lensing caused by the material's high thermo-optic coefficient ($\partial n/\partial T$), which is 70×10^{-6} K^{-1} and 46×10^{-6} K^{-1} in ZnSe and ZnS respectively. One method of overcoming the issue of thermal lensing is to use a waveguide geometry, since this will maintain a plane wavefront throughout the gain medium and so mitigate the issue [19, 20]. ZnSe waveguides have been demonstrated in fibre, thin film and ultrafast laser inscription

(ULI) waveguide from [21-23]. The only fabrication method to demonstrate a waveguide laser with output powers greater than a few mW is the ULI fabricated depressed cladding structure [24]. The reason for ULI fabricated waveguides' success is their ability to use the high quality polycrystalline samples which have been developed for bulk lasers [18, 24].

1.2. Ultrafast Laser Inscription

Waveguide technology, in this case optical fibres, is at the heart of the modern high speed internet. In order to support the ever-increasing demand for more bandwidth, it was clear early on that the copper cable would not be suitable. Optical fibres have become synonymous with high speed internet connections. The reason for this is the low propagation loss of 1550 nm light in an optical fibre, allowing for communication over large distances without the need for as many amplification stages as would be needed for a copper system. This was not always the case, since the first generation of fibres had high propagation losses of more than 20 dB/km from absorption of impurities in the bulk glass [25]. Researchers at Corning © were the first to develop optical fibres with losses of less than 20 dB/km, needed for telecoms applications, in the early 1970s. Today, the company offers optical fibre with propagation losses of ≤ 0.2 dB/km [26]. Amplification is also performed using waveguide technology, in this case the Erbium Doped Fibre Amplifier (EDFA), first developed in D. N. Payne's research group at Southampton University [27]. Using an all optical amplification method eliminates the use of electrical signal converters, facilitating larger bandwidths. Optical fibre can be functionalised to create many devices such as gyroscopes, optical splitters, filters and strain sensors, among others. With these devices, minimising package size is important; this results in packaging the fibre in a loop and having the input and output fibre end facets located next to each other. Optical fibres have a minimum bend radius that is defined by fundamental mechanical properties and optical loss, creating a limit on the final device size. This is where the photonic integrated circuits (PIC) come to the fore.

PICs are used to bridge two giants of technology: the optical fibre and CMOS-constructed integrated circuits (IC). With this in mind, a key driver for PICs' development is for them to be fabricated using the current CMOS methods that are commonplace in IC fabrication facilities around the world. Planar Silicon-on-insulator (SIO) waveguides are CMOS-compatible, so are the lowest cost and highest volume method for fabricated

optical interconnects which are needed to support today's data bandwidth requirements [28, 29]. However, SIO has limited 3D fabrication capability and for active devices the efficiency is low [28]. A hybrid system is therefore needed to combine CMOS compatible waveguides with efficient waveguide laser sources. There are a number of fabrication methods for thin film waveguides, suitable for active applications, such as Pulsed Laser Deposition (PLD), Chemical Vapour Deposition (CVD) and lithographic methods [30]. These methods, however, are all limited to 2D fabrication.

ULI is an established technique of waveguide fabrication in dielectrics that are linearly transparent to the inscription laser. The output beam of a modelocked laser with a pulse width of 0.1 – 2 ps is focused below the surface of the substrate. The energy is absorbed in the focal volume of the lens by a number of nonlinar processes, leaving the rest of the sample unmodified [31]. In 1996, Davis et al. [32] showed that, with a careful choice of laser parameters, a change in refractive index could be induced in the modified region [31]. Translating the sample on an xyz stage allows a waveguide of any geometric design to be easily drawn out. This method has many advantages such as sub-diffraction limited feature sizes, no requirement for a clean room environment or mask, and, what's more, it is fully 3D-compatible. ULI has been shown to be effective in fabricating waveguides, with sub-1 dB/cm propagation losses, in a number of doped and non-doped crystals, glasses and polymers with only relatively small changes in pulse parameters, making it a very versatile method [33].

ULI versatility has resulted in applications spanning many different fields such as telecommunications, data storage, astrophotonics, biology and laser physics [31, 34-36]. The refractive index change induced by ULI is typically in the order of 10^{-3} which results in a physical core size and mode field diameter at 1550 nm similar to those of SMF28 fibre. These properties result in low coupling loss between the optical fibres and waveguides, an important metric for the PIC industry. By arranging multiple cores in a shared cladding of the same dimensions as SMF28, multicore fibre (MCF) has the ability to increase the bandwidth of optical fibre without an increase in diameter. The issue with integrating MCF with current PIC technology is PIC tends to be 2D wafer- based and thus need the fibre cores to be arranged in a linear array to couple into the chip. ULI's 3D capability is an effective way of solving this geometric problem, first demonstrated by R. R. Thomson et al. [37] with their fan-out device. Based on this device, a spinout company called Optoscribe from Ajoy K. Kar's Nonlinear Optics (NLO) group at Heriot-Watt was

formed. A recent division multiplexing experiment using the fan-out technology combined with the ability to control the number of supported modes demonstrated a throughput of 255 Tbit per second [38].

Using a higher energy pulse, 150 – 500 nJ for a 100 fs pulse at 800 nm focused with a 0.6 NA lens, than would be used for ULI waveguide fabrication in fused silica, substrates can form nanograting at the focus of the laser [39]. The irradiated area can be selectively removed with wet chemical etching to form a microfluidic channel. These channels can be fabricated into intricate Lab on chip devices useful for applications in the field of biology [40]. Microfluidics fabricated in polymers such as Polydimethylsiloxane (PDMS) are commonly used owing to their low cost and ease of fabrication by embossing or moulding [41]. The limitation of PDMS is its absorptive nature. PDMS has been shown to absorb small hydrophobic molecules such as commonly used fluorescent markers Nile red and Rhodamine B [42, 43]. Fused silica microfluidics do not have this issue and have the added advantage of being fully 3D-compatible. Examples of ULI fabricated microfluidics in fused silica are a cell separator [44] and imaging flow cytometer [45]. The combination of waveguides and microfluidics channels to create an optofluidic in one fabrication step is where ULI can create a truly lab-on-chip device. Without a waveguide to deliver the light to the desired location on a chip, a microscope set-up would normally be used which increases cost and reduces portability. Osellame et al. [46] and Keloth et al. [47] demonstrated the use of ULI fabricated optofluidic chips for fluorescence imaging and optical tweezer experiments respectively.

For active devices such as lasers and amplifiers, the propagation losses of the ULI waveguide are a critical factor in creating a useful device. The optical gain must be greater than the parasitic loss induced by the waveguide and bulk material. The first ULI inscribed waveguide with net gain was fabricated in Er:Yb co-doped phosphate glass by Osellame et al. [48] in 2003. The following year, a waveguide laser was demonstrated in this material with a maximum output power of 1.7 mW at 1533.5 nm with 300 mW of pump power [49]. Since this initial work, fabrication parameters with sufficiently low propagation losses have been developed to achieve laser action in many different doped substrates such as YAG, Bismuthate glass, ZBLAN, ZnS and ZnSe [34, 35]. The emission wavelengths of ULI inscribed waveguide lasers span the visible [50] to the Mid-IR range [51], this is testament to the flexibility of the ULI fabrication process. Recent power scaling investigations have reached CW output powers of up to 5.1 W in ULI waveguides

fabricated in Cr:ZnSe [24]. Waveguide laser geometries' advantages over bulk laser systems include increased pump and single overlap, compact cavities a few centimetres in length and vibrational insensitivity [34, 51]. These benefits can also be found in fibre lasers but, critically, ULI can add waveguides to bulk material, such as crystals, that cannot be fabricated into optical fibres [34]. A fully monolithic waveguide laser can be achieved by directly coating of the waveguide end facets with the input and output coupler to form a laser cavity [24]. This forms a vibrational insensitive laser system which can be used outside the laboratory with minimal post-fabrication alignment, which is paramount to future applications.

1.3. Summary of the Thesis

The long term goal of my work as part of Ajoy K. Kar's research group at Heriot-Watt University - in close collaboration with G. Cook's Novel Laser Technologies research group at Wright-Patterson Air Force Base USA - was to develop a black box that emits laser light from 2 – 12 μm with no free space optics. My PhD focuses on developing the waveguide laser sources in the 2 – 5 μm spectra region. ULI waveguides lasers in Cr doped ZnS/ZnSe and Fe doped ZnSe are demonstrated. These sources were chosen because they cover the atmospheric transmission windows in the 2 – 5 μm spectral band. Initial work by J. R. Macdonald during his PhD developed the first waveguides in Cr:ZnSe, demonstrating an efficient CW laser [52]. Our work built on this by power scaling the lasers by an order of magnitude [24] and demonstrating modelocked operation. Fabrication and laser demonstration of waveguides in Cr:ZnS were investigated as a potential path for future power scaling by taking advantage of the materials' improved thermal properties over those of ZnSe [53]. The first Fe:ZnSe waveguide laser was developed [51] and then power-scaled to output powers of 1 W at 4 μm [24]. The next stage of our work moved to developing monolithic waveguide laser components such as wavelength tuning elements. To achieve this, ULI waveguides were developed in Strontium Barium Niobate (SBN) to take advantage of its strong electro-optic coefficients and Bragg gratings were fabricated in Gallium Lanthanum Sulphide (GLS).

Chapter 2 provides a review of the underlining absorption phenomena that take place in ULI waveguide fabrication. Inscription geometries and waveguide types will be discussed. The main focus of this chapter will detail the steps required for successful fabrication of a waveguide in II-VI semiconductors, particularly ZnSe. Finally, the laser levels of TM:II-VI Semiconductors will be detailed.

Chapter 3 examines the CW wavelength tuning range of extended cavity Cr:ZnSe waveguide lasers. Tuning with a diffraction grating in a Littman-Metcalf-configured cavity demonstrated a narrow linewidth of 53 pm. The tuning range of this laser was 2077 – 2777 nm with output powers of more than 15 mW available across the full range. Computer modelling of the laser showed the optical loss of the grating, particularly at longer wavelengths, was limiting the tuning range. The grating was removed and then replaced with a prism. This cavity change resulted in the CW tuning range being increased to 2080 – 2883 nm. This resulted in a Tuneable bandwidth of 39 THz, which is the widest range demonstrated by a Mid-IR waveguide laser.

Chapter 4 advances the applications of a compact TM:II-VI laser by demonstrating a modelocked Cr:ZnSe laser. The laser was passively modelocked using a semiconductor saturable absorber. A CW modelocked laser with a PRF of 300 MHz and a pulse width of 638 fs, is demostrated assuming a sech^2 pulse shape,.

Chapter 5 investigates a potential alternative to a ZnSe laser host ZnS. This material has improved thermal characteristics over ZnSe and so presents a path for further power scaling. Fabrication of depressed cladding waveguide in Cr:ZnS is present. CW laser operation is demonstrated with pump limited output powers of 97 mW at 2333 nm.

Chapter 6 transfers the knowledge of waveguide fabrication discovered in Cr:ZnSe and Cr:ZnS to the 3.7 – 5 μm wavelength band with a Fe:ZnSe waveguide laser. Waveguide fabrication of depressed cladding waveguides are detailed. CW output power of 76 mW were demonstrated at 4122 nm. This work highlights the operational wavelength versatility of ULI fabricated depressed cladding waveguides.

Chapter 7 concludes the work. It also discusses the future work on what is required to achieve our research goal of a black box that emits laser light from 2 – 12 μm with no free space optics.

In summary, this thesis details waveguide fabrication and laser action in TM:II:VI semiconductor laser materials. These laser crystals have CW tuneable ranges that span the two atmospheric transmission window in the Mid-IR. The incorporation of waveguide geometry will facilitate the out of the laboratory operation paramount to practical applications within this wavelength range.

2. Review of ULI waveguides in Transition Metal doped II-VI Semiconductors

ULI is an established additive manufacturing technology for processing dielectric materials transparent to the laser wavelength. This chapter outlines the key processes behind refractive index modification induced by a femtosecond laser in transparent dielectric media. The focus of this chapter is to detail the challenges in fabricating Mid-IR waveguides in ZnSe using ULI. An initial report by Okhrimchuk et al. [54] concluded that ULI modification of ZnSe was not feasible even with pulse energies greater than 10 µJ. However, with careful consideration of inscription laser wavelength and pulse width, nonlinear effects can be mitigated to induce permanent refractive index modification in ZnSe [55]. Mid-IR waveguides were not realised with the standard ULI positive index change methods in ZnSe [56], due to micro-cracking of the sample when scaling the waveguides size to support Mid-IR light [57]. This limitation can be mitigated in doped and undoped ZnSe by implementing negative index change depressed cladding waveguides. ULI fabricated depressed cladding waveguide in Cr:ZnSe have demonstrated a waveguide laser with a slope efficiency of 45% at 2486 nm [58].

Furthermore, the spectroscopy of transition metal doped II-VI semiconductors in relation to laser applications will be discussed. These materials have very broad absorption and emission bands due to a combination of vibration broadened transitions with additional broadening from Jahn-Teller effects [11]. This chapter outlines the challenges and solutions to successful waveguide fabrication in Cr:ZnSe for laser applications. This knowledge was applied to other materials of the TM:II-VI family, and this is discussed in later chapters of this thesis.

2.1. Spectroscopy of Transition Metal doped II-VI Lasers

Transition metals (TM) are elements that have stable ions and only partially filled *d* orbitals, located along the top of the periodic table between Scandium (Sc) and Zinc (Zn). When Cr^{2+} or Fe^{2+} ions are doped into binary or tertiary II-VI compounds such as ZnSe, ZnS, ZnTe, CdSe and CdS, the result is vibronically broadened laser transitions. Vibronically broadened lasers are characterised by strong homogeneous broadening, resulting in wide emission and absorption bands which makes them particularly well

suited to wavelength tuneable and modelocked applications. The most well known example of a vibronically broadened laser is the Ti:Sapphire laser emitting in the Near IR spectral region. It is widely used in research because of its wavelength tunable laser output spanning 680 to 1100 nm and its ability to generate less than 10 femtosecond pulses [59].

TM lasers based on the 3d-3d transitions are sensitive to the crystal environment because of the strong electron-phonon interaction. This is in contrast to the rare earth (RE) ions such as Er, Tm and Ho, which are based on shielded inner 4f electron shell transitions, resulting in similar absorption and emission peaks in different host materials. A comparison of the energy diagrams of an RE and TM laser is given in Figure 2.1, showing the difference in crystal field splitting effect between the two types of laser ions [60].

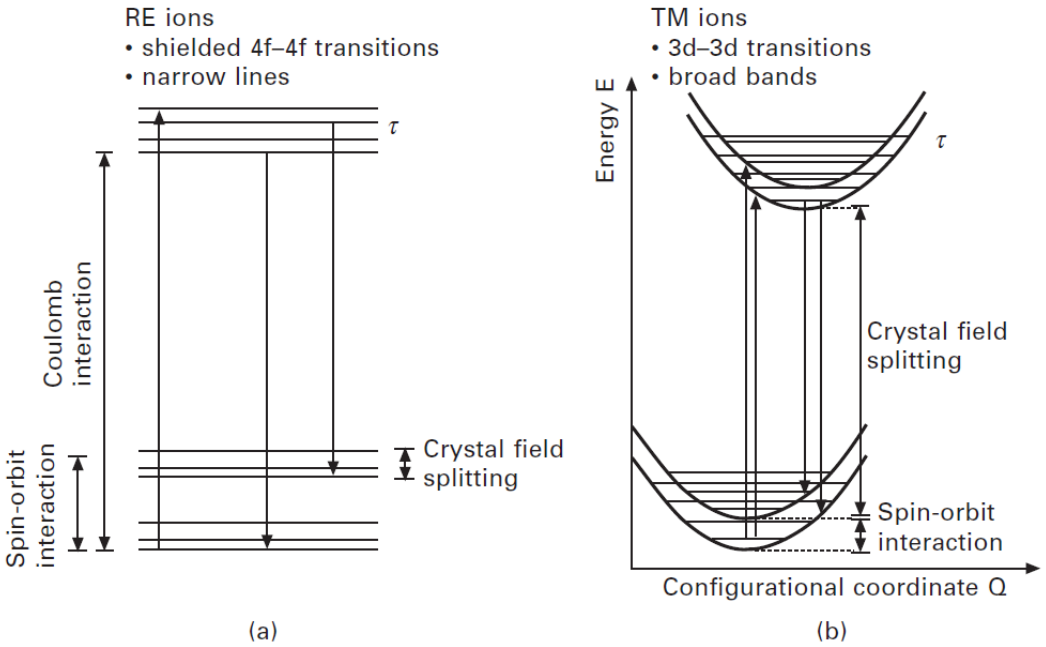

Figure 2.1. Energy level diagram showing weak and strong electron-phonon coupling in (a) RE and (b) TM ions respectively. This diagram has been reproduced from Petermann [60].

Transition metals located in a tetrahedral crystal field of a II-VI semiconductor have a ^5D ground state that is split into $^5T_2$ triplet and ^5E doublet levels from crystal-field splitting. For Cr^{2+} and Fe^{2+} all transitions to higher energy levels are spin-forbidden, thus there is no excited state absorption [61, 62]. The broad emission is not only because of vibronic broadening, there is also further energy level splitting from the Jahn-Teller effect [63]. This arises from the removal of the orbital electronic degeneracy by introducing a

distortion of the crystal, forming two separate energy levels. A schematic of this effect is shown in Figure 2.2 [64].

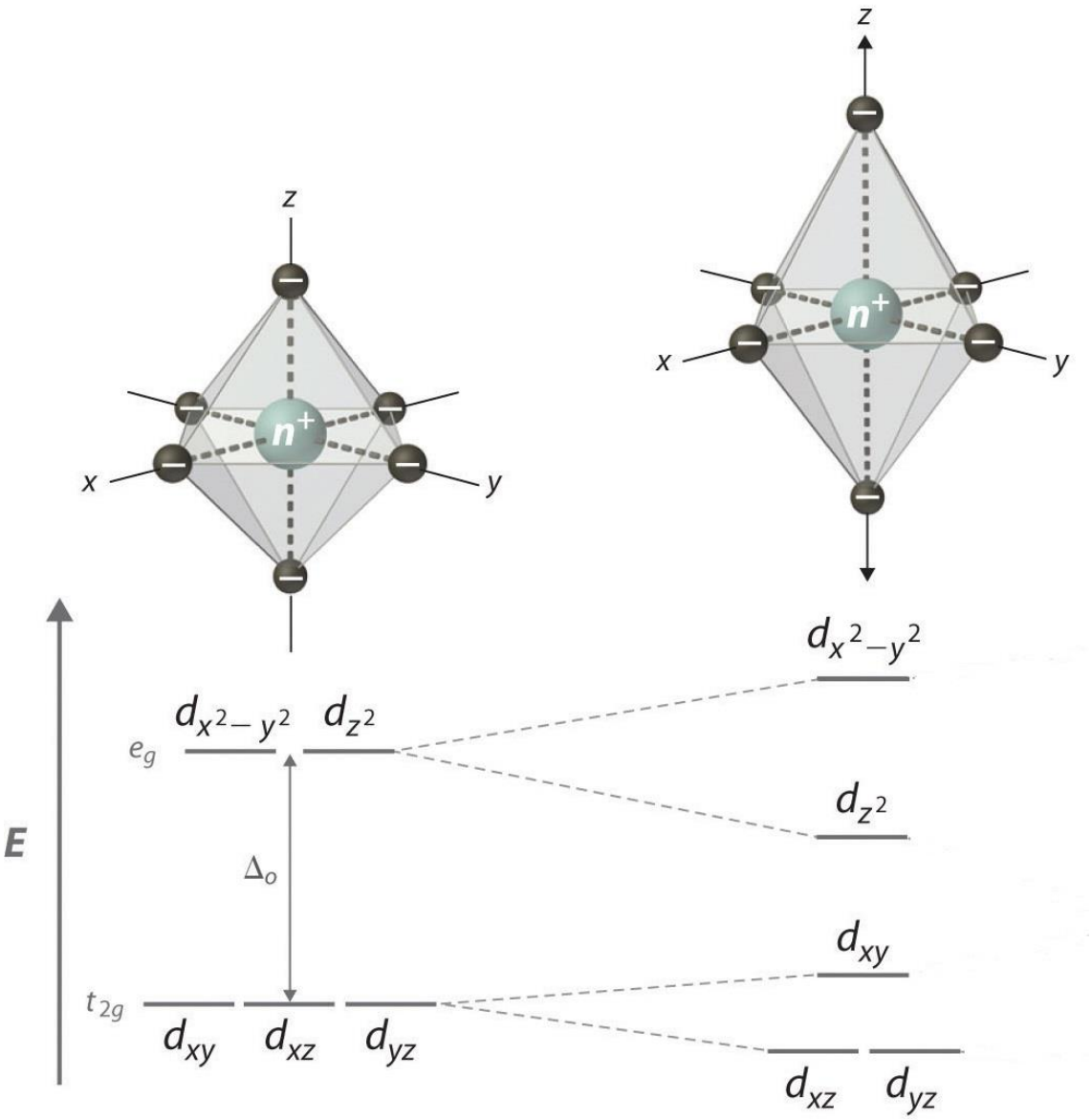

Figure 2.2. Schematic of the elongation of an octahedral crystal field arising from the Jahn-Teller effect, resulting in a splitting of the energy levels. This process is also present in a tetrahedral crystal field. This schematic has been reproduced from Lancashire [64].

The splitting is present in the valance and conduction band, but the amount of broadening is not equal. In Cr:ZnSe, the ground state level $^5T_2$ is split by 340 cm^{-1} and the excited state ^5E by 40 cm^{-1}[65]. The experimental implications of the Jahn-Teller effect have caused a great deal of confusion among many physicists and chemists over the years [66] and as such will not be discussed in further detail. More information on the Jahn-Teller

effect and its impact on TM:II-VI lasers can be found in [61, 65-67]. The spectroscopic absorption and emission bands of common TM:II-VI lasers are given in Figure 2.3:

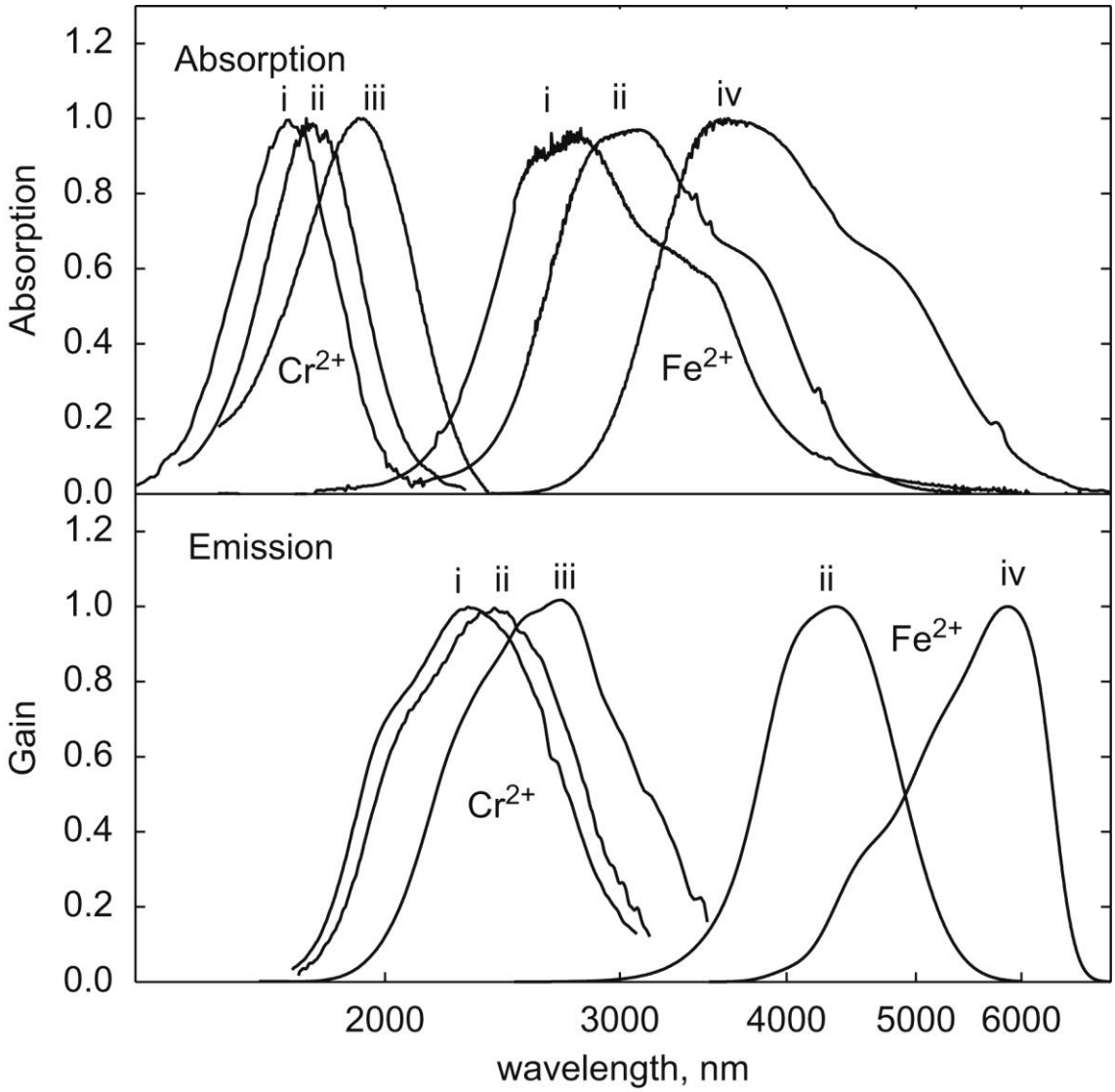

Figure 2.3. Normalised absorption and emission spectra of Cr^{2+} and Fe^{2+} doped into (i) ZnS, (ii) ZnSe, (iii) CdSe and (iv) CdMnTe. This graph has been reproduced from Mirov et al. [68].

When placed in a tetrahedral site, TM have larger transition cross-sections than those of octahedral configuration, but have shorter lifetimes. This makes the lasers suited to CW operation but limits the energy storage capability that is advantageous for Q-switched operation [61]. This limitation can be overcome by gain switching the TM laser with a Q-switched RE laser. In the case of Cr:ZnSe, a Ho:YAG Q-switched pump source is an effective option [69, 70].

2.2. Ultrafast Laser Inscription Absorption Processes

ULI results in laser-induced optical breakdown. This process leads to the deposition of optical energy in the material, resulting in the ionisation of a large number of electrons. These electrons transfer energy to the substrate lattice. This energy can generate a permanent change in refractive index or cause the formation of voids [31]. It is important to understand the absorption process for optimising waveguide parameters in glasses and crystals. When inscribing with a laser pulse width in the 10 fs to 10 ps regime, photons are initially absorbed by nonlinear ionisation processes. A diagram of the initial absorption process is detailed in Figure 2.4:

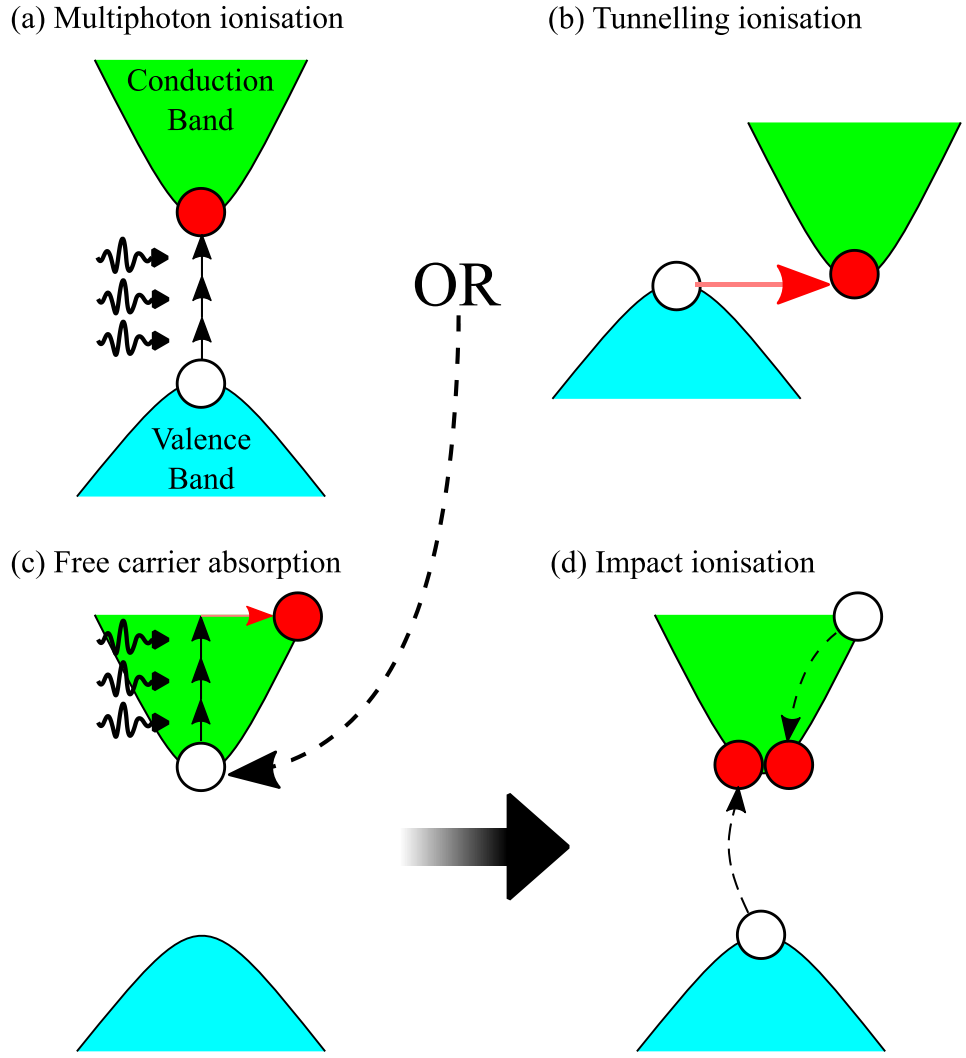

Figure 2.4. Diagram of ULI, initial absorption process is from (a) Multiphoton ionisation or (b) Tunnelling ionisation. These processes seed Avalanche ionisation which consists of (c) Free carrier absorption leading to (d) Impact ionisation.

These nonlinear ionisation processes can be multiphoton ionisation or tunnelling ionisation, depending on the bandgap and photon energy, outlined in 1964 by Keldysh [71]. Once an electron has been promoted to the conduction band, it is possible for it to absorb photons linearly through free carrier absorption. The excited electron can then promote further electrons from the valance band to the conduction band by impact ionisation, after it has gained more kinetic energy than that of the band gap. The combination of free carrier absorption and impact ionisation is called avalanche ionisation. This repeating process, if the illumination is sustained, will lead to an exponential increase in ionisation. Avalanche ionisation dominates the absorption process, hence the inscription parameters for substrates with different band gap energies are similar [31, 33]. Further details on the nonlinear modification processes involved in ULI have been discussed in greater detail by many authors, most notably by Oselame et al. [72], Gattass et al. [31] and Choudhury et al. [34].

2.3. Implementation of Ultrafast Laser Inscription

The nonlinear processes leading to a change in refractive index of transparent dielectric using ULI have been discussed. Implementation of ULI can be reduced to two components - an ultrafast laser and a xyz translation stage. Using these two components, waveguides can be formed in a number of different crystals and glasses.

The change in refractive index depends on the inscription laser pulse, of which the most important factors are the laser wavelength, laser repetition rate and pulse energy. However, a waveguide is not normally formed by focusing a femtosecond laser on to a single point in a substrate. To fabricate a waveguide, the sample must be translated through the focus of the beam using nanometre precision xyz translation stages. If a positive index is induced by the laser irradiances, a simple step index waveguide can be formed by translating the sample in one dimension. This method is not always sufficient for the guiding of light, particularly if a negative index change is induced, thus more complex inscription geometry must be implemented.

2.3.1. ULI Inscription Geometry

Inscription geometry is the direction in which the sample is translated, with an xyz stage, with respect to the laser beam. There are two main inscription geometries, defined as

longitudinal and transverse. For a longitudinal waveguide inscription, the sample is translated along the axis of the laser beam. In transverse geometry, the sample is translated at 90º to the laser beam. A schematic of these two inscription geometries is given in Figure 2.5:

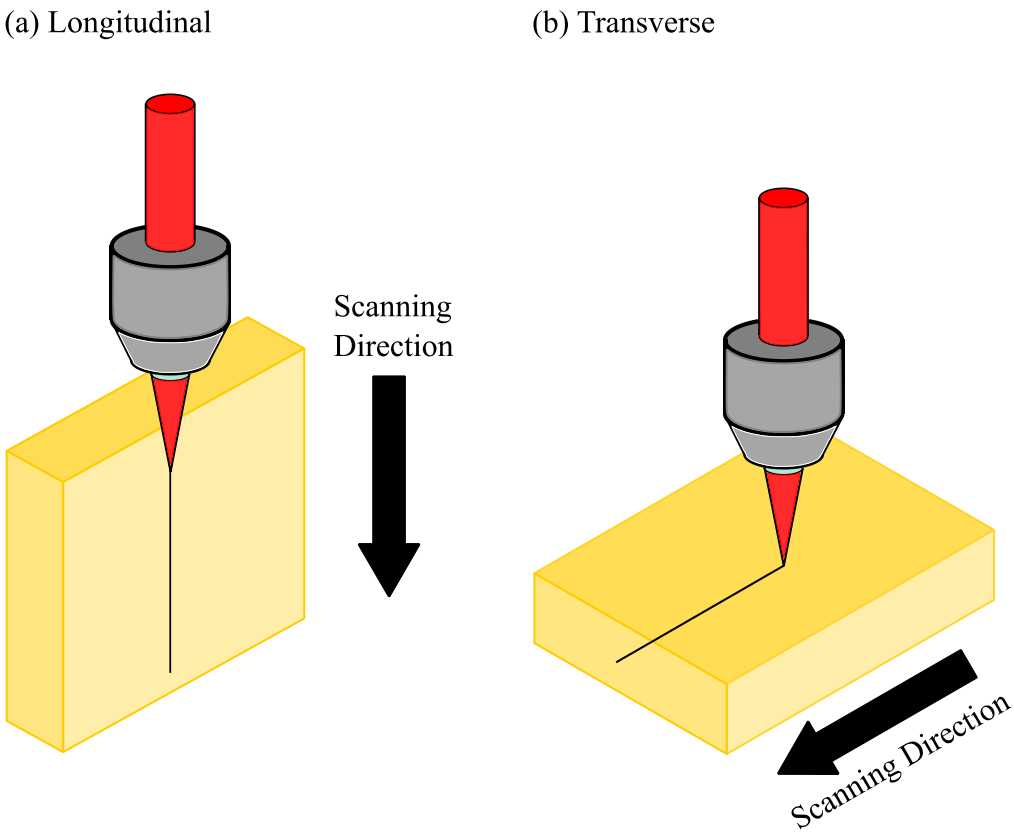

Figure 2.5. Schematic of (a) longitudinal and (b) transverse inscription geometry.

Longitudinal inscription has the advantage of symmetric modification. This arises from the radial uniformity of the Gaussian beam. Longitudinal geometry is, however, limited by the working distance of the inscription lens. The working distance of a typical 0.4 NA lens is only a few millimetres. This limitation can be relaxed by utilising lower NA lenses. However low NA lens have larger focal volumes at the focus of the lens; thus higher peak powers are needed to generate sufficient intensity to seed the modification process. This increase in peak power can mean nonlinear effects as such Kerr lensing become an issue. The effect of Kerr lensing on ULI has been shown to cause the formation of long filaments of refractive index change [52]. In many cases, this effect is seen as a negative factor which must be mitigated. However, Caulier et al. [73] use this to form long waveguides, overcoming the working distance limitations of the lens. The long inscription times of

this method are limiting compared with other transverse methods which are discussed later. The inscription time for a single filament, between 120-200 μm in length, with a 0.1 NA lens was 10 minutes in silica glass [74]. In comparison, common transverse inscription methods can typically inscribe the same waveguide length in a few tenths of a second [75]. Thus the working distance limitations can be overcome, but writing speed is drastically reduced. A different method is to move away from a common Gaussian beam and implement a Bessel beam. This mitigates the working distances limitation and has been used to fabricate waveguides in fused silica [76]. However, this method is not widely used due to the modification having a depth dependent component making consistent modifications along the waveguide challenging [34].

In transverse inscription geometries, the waveguide length is only limited by the translation range of the xyz stages. Lapointe et al. [77] recently demonstrated a 1 m long waveguide inscribed at a translation speed of up to 300 mm/s using a transverse inscription geometry. The possible inscription depth to which a waveguide can be inscribed is limited by the working distance of the lens. However, this is not normally a limitation, because samples are often only a few millimetres thick. A single element's modification cross-section is asymmetrical. This arises from the difference between the beam waist diameter and confocal parameter at the focus of the lens given in Equation 1 and 2 respectively [78].

$$\text{Beam waist diameter} = 2w_0 = \frac{2f\lambda}{\pi w(f)} \approx \frac{2\lambda}{NA\pi}$$

Equation 1

$$\text{Confocal parameter} = 2R = \frac{2\pi n\omega_0^2}{\lambda}$$

Equation 2

where n is the refractive index of the irradiated substrate. From these equations, it can be seen that only when the beam waist radius (w_0) is close to $\lambda/n\pi$ will the modified area be symmetrical. It is possible with a high NA lens, but will result in waveguide diameters too small to support effective wave guiding with the 10^{-3} refractive index change normally induced by ULI. For that reason, waveguides fabricated by a single element with a standard single lens setup in transverse inscription mode will be asymmetrical when not inscribing in the thermal regime [56, 78].

2.3.2. Multi Element Waveguide Schemes

Forming a single waveguide with multiple passes of the sample through the focus of the laser is a flexible way of forming symmetrical waveguides. It is possible to overcome the asymmetrical issue with single pass transverse laser inscription by using the slit beam shaping technique [79] or implementing a deformable mirror [80], but this makes the inscriptions system significantly more complex. A simpler method, in terms of the inscription system, is to construct a waveguide with multiple elements. ULI can induce a positive or negative change in refractive index, depending on the material and inscription parameters [34]. Type I modification is the term used to describe a waveguide formed for a positive change in refractive index. Type I asymmetric modification elements can form a symmetric square core by translating the sample through the focus of the laser beam multiple times with a slight offset in the x axis on each pass, as shown Figure 2.6. This method is termed the multiscan technique and has been successfully used to fabricate symmetrical output mode NIR waveguide lasers and passive devices [35, 81].

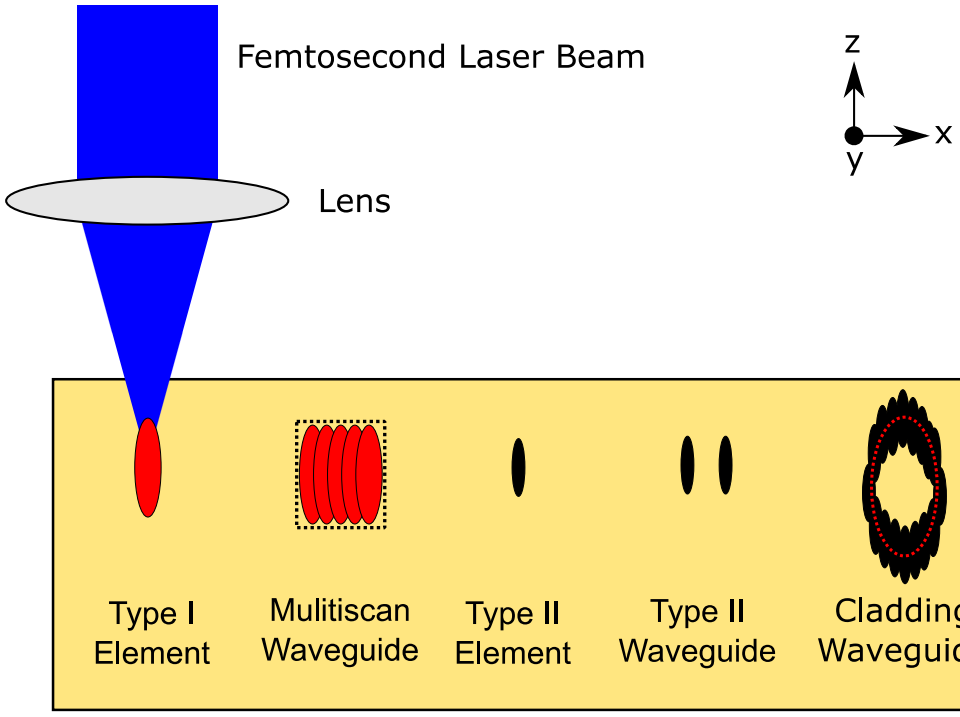

Figure 2.6. Schematic of waveguides fabricated with a femtosecond laser viewed from the end facet of the waveguide. Red represents a localised increase in refractive index. Black modification represents a reduction in refractive index.

A negative refractive index change can be formed around a modified element by the strain-optic effect. In this case, two parallel modification lines are needed to form a track like waveguide, known as Type II. The guiding region between the two tracks is formed from the modification elements overlapping strain fields. Type II modification is often induced by a damage line which appears black on a visible microscope [82]. One benefit of Type II waveguides is that the guiding region is unmodified, which can be favourable in active applications [83]. However, it should be noted that Type I waveguide lasers have been demonstrated with near quantum limit efficiency [56].

Depressed cladding waveguides consist of an array of Type II modification elements arranged in an annular pattern, as shown in Figure 2.6. This type of waveguide was first demonstrated in 2005 by Okhrimchuk et al. [84] in Nd:YAG. This particular Nd:YAG waveguide had a rectangular cross-section to match the diode pump laser's asymmetric output. Depressed cladding waveguides have been an effective method for demonstrating lasers in doped crystal substrates such a YAG, ZnSe and ZnS [53, 58, 85]. This method is not limited to crystals Tm:ZBLAN glass depressed cladding waveguide lasers have been demonstrated with a slope efficiency of up to 50% [86]. Depressed cladding waveguides are a powerful tool for fabricating Mid-IR waveguides because they can be scaled in size, from 10 μm to 300 μm, without issues of the sample cracking from excess strain [51, 87]. Each individual modification element is spaced apart from the others and this spacing can be maintained when increasing the waveguide diameter, which is needed to reduce the cut off frequency for Mid-IR guiding. Additionally, the waveguides can be increased in diameter without the need to increase the pulse energy of the inscription laser. This is often required with Type II track waveguides [88]. Hence a maximum element height is enforced from the ablation threshold of the irradiated substrate.

The guiding mechanism for depressed cladding waveguides is different from that of the common step index guide. It is not strictly true that the depressed cladding waveguide supports a guided mode. For a step-index profile, as shown in Figure 2.7 (a), the supported guided modes are lossless in the absence of material absorption and scattering loss. This is not the case for a depressed cladding waveguide, which can be modelled as a W-type slab waveguide, as shown in Figure 2.7 (b). The mode supported is called a 'leaky mode' [89]. Leaky modes can be conceptually understood by thinking about the effect of changing parameter *b*, in Figure 2.7 (b), on a normal guided mode. For the case of b tending to infinity, the guided mode is conserved since this is identical to a step-index

profile as shown in Figure 2.7 (a). In the case of *b* tending to *a*, there will be no index contrast and so no guided mode is supported. The W-Type index profile is rather a superposition of both in the sense that light is guided from one end of the waveguide to the other, but there is always a loss element conceptually similar to a quantum tunnelling effect. Further explanation of leaky modes in waveguides can be found in an article by Hu and Menuk [89]. However, this fundamental loss has not prevented depressed cladding waveguides from demonstrating laser operation in a large number of substrates [51, 53, 58, 84, 86, 87, 90].

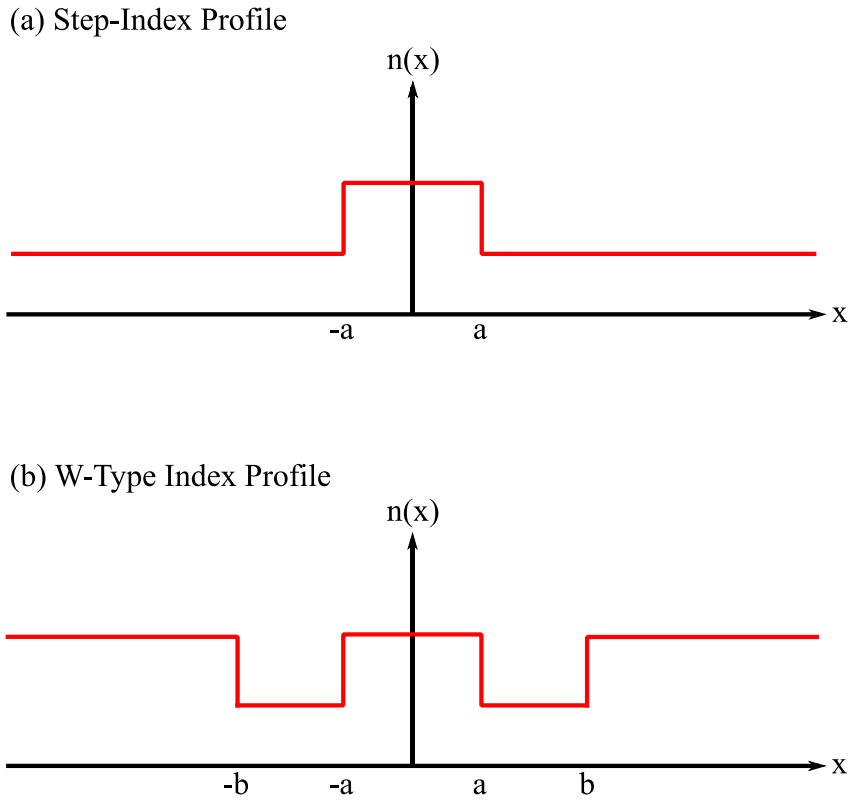

Figure 2.7. Refractive index profile of (a) step-index waveguide and (b) W-type waveguide. This diagram has been reproduced from Hu and Menuk [89].

2.4. Ultrafast Laser Inscription in ZnSe Substrates

ULI has been an effective tool in demonstrating waveguides in glasses and crystals [34]. Of the materials investigated, fused silica and YAG have been the most widely investigated due to their transparency in the visible range. These materials have the addition benefit of wide commercial availability, this reduces the cost of devises.

However, their long wavelength transmission in the Mid-IR range is limited. For Mid-IR transmission, Arsenic-based Chalcogenides are an effective option, such as AsSe. However, in AsSe there is no visible transmission band and there are additional safety procedures that must be implemented when working with As [91]. ZnSe is an excellent substrate for Mid-IR applications since its transmission range spans from 500 nm to 22000 nm, as seen in Figure 2.8. The advantage of having visible transmission for a substrate intended for Mid-IR applications is the ability for visual inspection with Si-based cameras during the fabrication stage. To implement a ULI waveguide, the substrate must be transparent at the inscription wavelength, commonly 1064 nm, resulting in nonlinear absorption being the dominant process. This rules out some of the Mid-IR substrates for ULI fabricated waveguides, including high quality Si substrates originally developed for the semiconductor industry. Furthermore, ZnSe can be doped with transition metals to produce broadband lasers with demonstrated laser emission spanning the 2 – 5 μm range. In addition, there is a potential to extend the laser emission to a longer wavelengths with tertiary substrates [70]. The excellent passive and active properties of ZnSe with ULI waveguide technology will allow for compact, cost effective Mid-IR photonic devices.

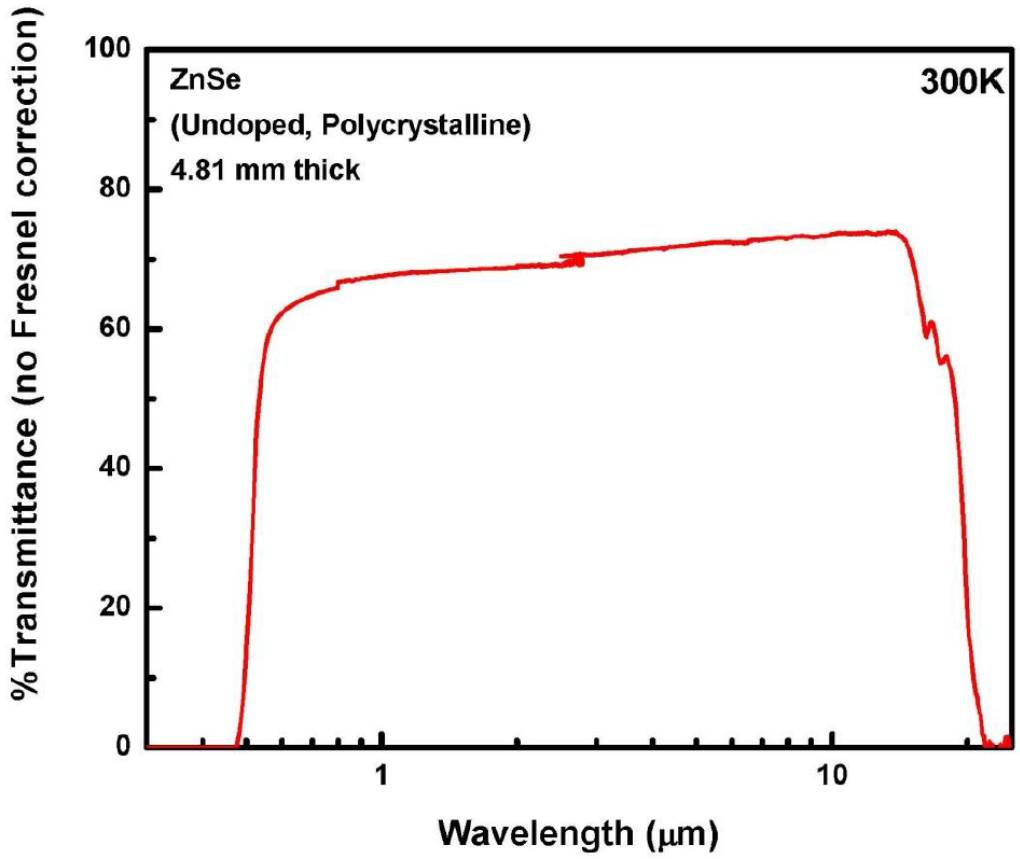

Figure 2.8. Transmission of 4.81 mm thick polycrystalline ZnSe sample. Transmittance has not been Fresnel corrected. This graph has been reproduced from Berry et al. [92].

ULI waveguide fabrication in ZnSe was found to be very challenging [23, 52, 54]. An initial investigation into ultrafast laser modification of ZnSe by Okhrimchuk et al. [54] was not successful in producing any modification, even with pulse energies greater than 10 μJ. This investigation uses a 1 kHz amplified modelocked Ti:Sapphire laser centred at 800 nm with a pulse width of 115 fs and an 0.55 NA lens. Using the same inscription system YAG, BK7 and fused silica were modified with pulse energies of 61 nJ, 44 nJ and 55 nJ respectively [54]. This led to the thought that the refractive index of ZnSe could not be modified with a femtosecond laser system. However, a later investigation by MacDonald et al. [23] demonstrated permanent refractive index modification and successful fabrication of a NIR waveguide in ZnSe using ULI. Successful modification was demonstrated by reducing the impact of optical nonlinearities on the propagating inscription beam. The inscription laser used in MacDonald's work was an amplified modelocked Yb:fibre system centred at 1047 nm with pulse width of ≥ 500 fs, a 0.67 NA lens and pulse energy of 190 pJ. The use of longer pulse widths and moving to a

wavelength with lower n_2 value in ZnSe are the main contributing factors that led to the first successful demonstration of a ULI fabricated waveguide in ZnSe [23].

2.4.1. Mitigating Nonlinear Effects for ULI in ZnSe

There are a number of nonlinear effects that can reduce the intensity of the inscription laser pulse at the focus of the lens inside the target substrate. If their effects are large, such as those found in ZnSe, it can reduce the intensity to below that required to generate the plasma needed to start the ULI process. The nonlinear effects can be split into two types; spatial and temporal. Ultrafast laser modification requires extremely high intensities at the focus of order 10^{13} Wm^{-2} [31] . At such high irradiances, the Kerr effect is present for materials with a non-zero nonlinear refractive index, n_2. For such materials, the total refractive index experienced by the beam with a varying intensity *I* is given as a function of electric field in the standard form shown in Equation 3 [93]:

$$n = n_0 + \bar{n}_2\langle\tilde{E}^2\rangle$$

Equation 3

From this equation, it is clear that for a collimated Gaussian beam propagating through a material with positive n_2, such as ZnSe, it will experience a greater refractive index at the centre of the beam. This results in a positive lens being formed, thus creating a self-focusing effect as shown in Figure 2.9. This effect is termed a Kerr lens, with an effective focal length z_{sf} given by Equation 4 [94].

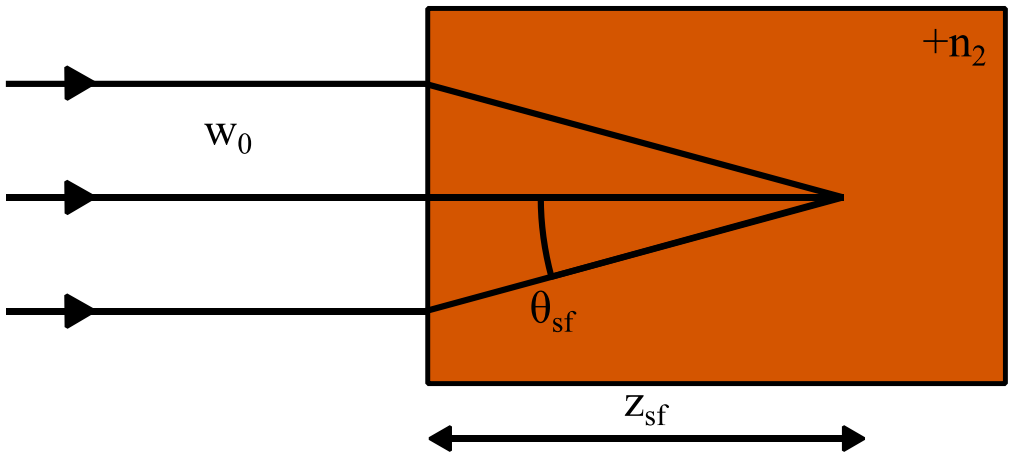

Figure 2.9. Schematic of self-focusing of a collimated Gaussian laser beam showing the Kerr effect as predicted by Fermat's principle. Reproduced from Boyd [94]

$$z_{sf} = \frac{2n_0 w_0^2}{\lambda_0} \frac{1}{\sqrt{\frac{P}{P_{cr}} - 1}}$$

Equation 4

where P is the peak power and P_{cr} is the critical power given by Equation 5 [94].

$$P_{cr} = \frac{\pi(0.61)^2 \lambda_0^2}{8 n_0 n_2}$$

Equation 5

When the power, or peak power if using a pulsed source, is equal to the critical power, the self-focusing effect is balanced by diffraction effects which forms a self-trapping effect of a focused laser beam, as shown in Figure 2.10.

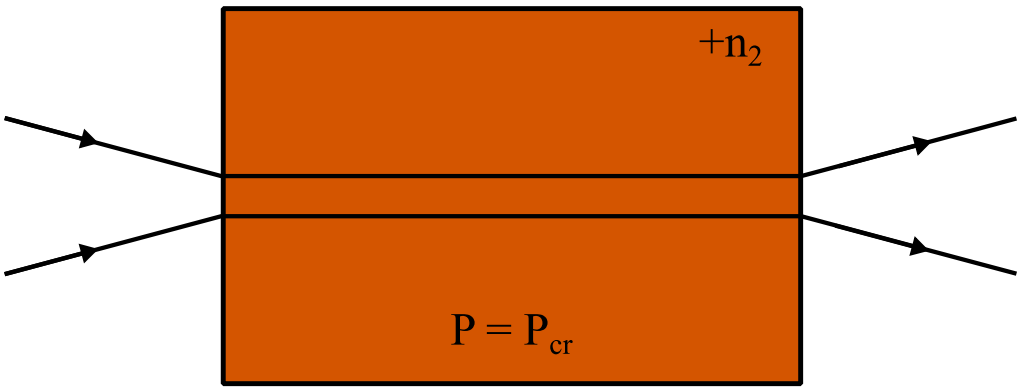

Figure 2.10. Schematic of self-trapping of light when P = P_{cr}. Reproduced from Boyd [94].

For peak powers much greater than the critical power, filamentation occurs, as shown in Figure 2.11 (a). Filamentation of the beam results in it being broken up into many filaments, each having approximately the power P_{cr} [94]. ZnSe n_2 is at a local maxima at 800 nm, as shown in Figure 2.12, so operating away from this wavelength increases the threshold for filamentation [95]. MacDonald et al. [23] observed filamentation in ZnSe after irradiation with a 1047 nm femtosecond beam when using shorter pulses. In this case, 500 fs as shown in Figure 2.11 (b). ZnSe could be modified with 500 fs pulses, but this is not useful for the uniform refractive index change needed for waveguide fabrication. However, with picosecond pulse widths MacDonald et al. [23] demonstrated

successful uniform modification of ZnSe without filamentation. This is due to the reduction in Kerr lensing for longer pulses.

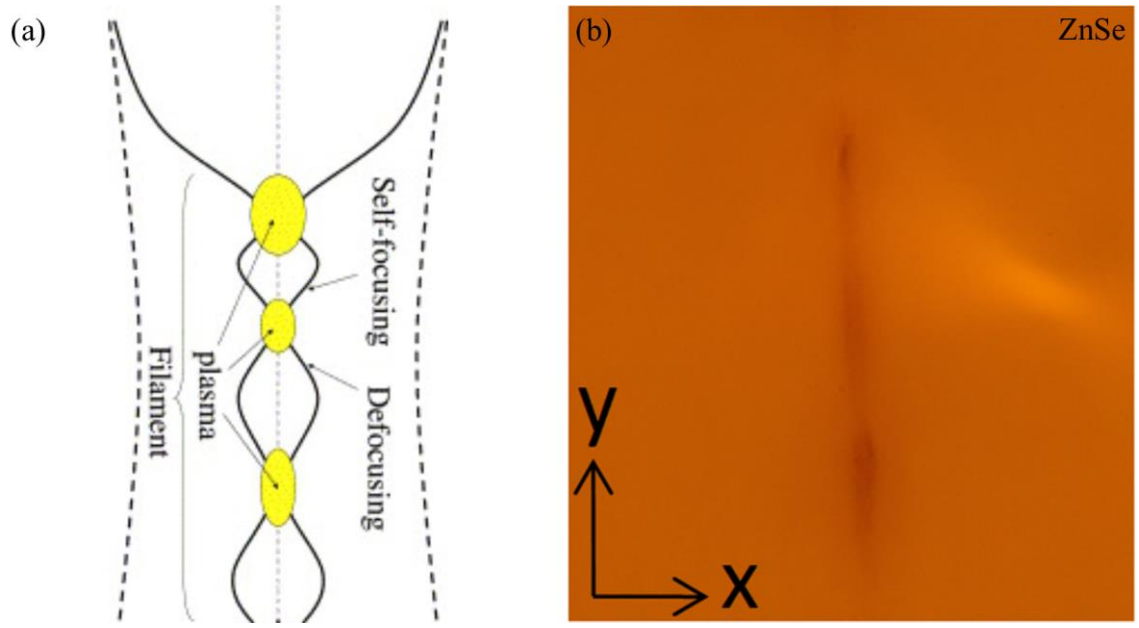

Figure 2.11. (a) Schematic of self-focusing followed by filamentation leading to defocusing and then repeating. This has been reproduced from Couairon and Mysyrowicz [96]. (b) Transmission microscope image of ZnSe end facet shows a filamentation structure formed after ULI. The field of view of the image is 90 μm by 100 μm. The inscription laser had a pulse width of 500 fs at 1047 nm. This image has been reproduced from MacDonald et al. [23].

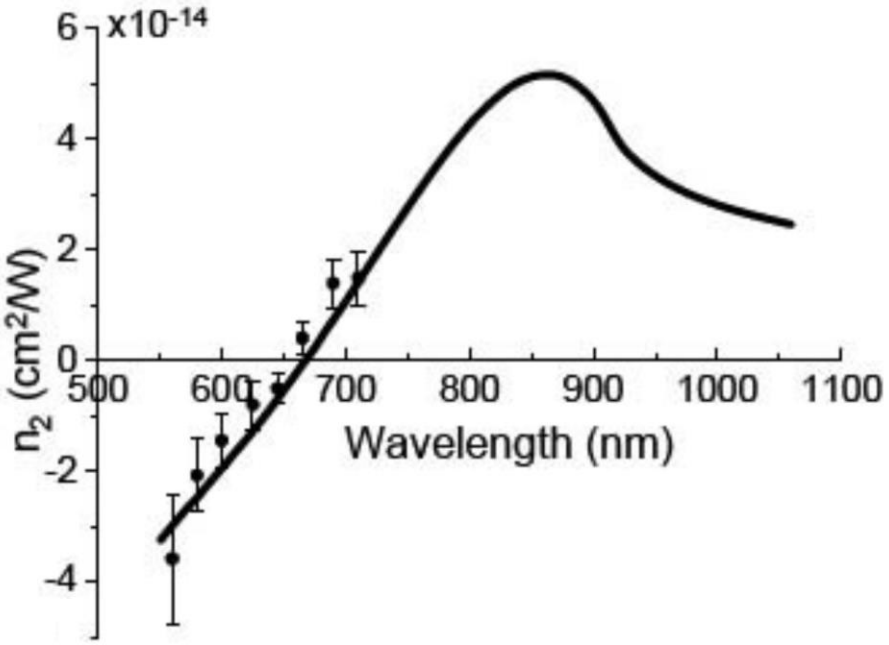

Figure 2.12. Nonlinear refractive index of ZnSe in the visible to NIR. Figure reproduced from M. Balu et al. [95].

Temporal stretching of the pulses is another factor that must be considered. Chromatic dispersion arises when the phase velocity and group velocity of light propagating through a dielectric depends on the wavelength of the light. This means that for a fully compressed modelocked laser pulse, the blue end of the pulse will propagate at a different velocity to the red end, thus the pulse width will be elongated over time. This is called a chirped pulse. A material at a given wavelength is classified as having normal dispersion or anomalous dispersion. In normal dispersion materials, such as ZnSe, group velocity decreases with increasing optical frequency. This means blue light will travel slower than red light. The opposite is the case for anomalous dispersion materials.

To evaluate the effect of chromatic dispersion on an inscription pulse we must calculate the group velocity dispersion (GVD). To do this, we first take the Taylor expansions of k as a function of angular frequency ω centred around a frequency ω_o, given in Equation 6:

$$k(\omega) = k_0 + \frac{\partial k}{\partial \omega}(\omega - \omega_0) + \frac{1}{2}\frac{\partial^2 k}{\partial \omega^2}(\omega - \omega_0)^2 + \frac{1}{6}\frac{\partial^3 \omega}{\partial \omega^3}(\omega - \omega_0)^3 + \cdots$$

Equation 6

The GVD arises from the second order term as shown in Equation 7:

$$GVD = \frac{\partial^2 k}{\partial \omega^2}$$

Equation 7

GVD can be written in the form of a refractive index as a function of wavelength given in Equation 8. The derivation of this equation is given in a letter by Rosete-Aguilar et al. [97]

$$GVD = \frac{\lambda_0^3}{4\pi c^2}\frac{d^2 n}{d\lambda_0^2}$$

Equation 8

where λ_0 is the central wavelength of the laser pulse and c is the speed of light in a vacuum.

Expressing GVD in the form of refractive index means the material dependant information can be taken from the Sellmeier dispersion formula given in Equation 9 [98]. The Sellmeier equation is an empirical relationship linking refractive index and wavelength in a transparent dielectric medium. Each optical material has different experimentally determined constants (B_1, B_2, B_3, C_1, C_2 and C_3) to match their different refractive index as a function of wavelength. The Sellmeier coefficients of ZnSe, BK7 and fused silica are given in Table 1.

$$n^2(\lambda_0) - 1 = \frac{B_1\lambda_0^2}{\lambda_0^2 - C_1^2} + \frac{B_2\lambda_0^2}{\lambda_0^2 - C_2^2} + \frac{B_3\lambda_0^2}{\lambda_0^2 - C_3^2}$$

Equation 9

Material	BK7 [99]	Fused Silica [100]	ZnSe [101]
B_1	1.03961212	0.6961663	4.45813734
B_2	0.231792344	0.4079426	0.467216334
B_3	1.01046945	0.8974794	2.89566290
C_1 (μm)	0.00600069867	0.0684043	0.200859853
C_2 (μm)	0.0200179144	0.1162414	0.391371166
C_3 (μm)	103.560653	9.896161	47.1362108
Valid range	0.31 – 2.33 μm	0.21 – 3.71 μm	0.54 – 18.2 μm

Table 1. Table of Sellmeier coefficients for calculation of refractive index of BK7, Fused Silica and ZnSe

From Equation 8, it is clear that differentiating Equation 9 twice will yield an expression for GVD. This expression for GVD as a function of refractive index can be found in Equation 25 of Rosete–Aguilar et al. [97]. GVD is plotted in Figure 2.13 for ZnSe for a range of wavelengths using the Sellmeier coefficients given in Table 1. From this, we can see that the GVD of ZnSe at 800 nm is 1075 fs^2/mm, almost double that of the value at 1064 nm. For context, the GVD of fused silica at 800 nm is 36 fs^2/mm [100]. The large normal dispersion of ZnSe at the inscription wavelength is the reason MacDonald et al. [23] gave for using a negatively chirped inscription pulse.

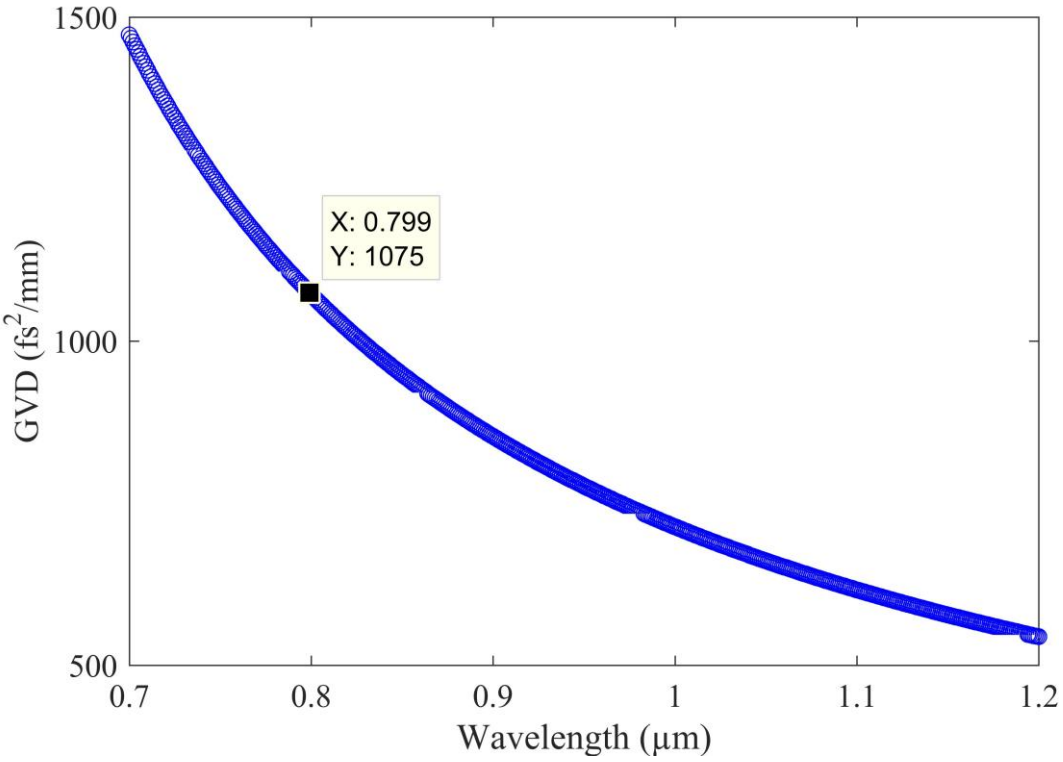

Figure 2.13. Group velocity dispersion (GVD) of ZnSe for 0.7–1.2 μm. Values calculated for Sellmeier coefficients of ZnSe given in [101] using equations detailed in [97].

The duration of a Gaussian profile pulse width τ after propagating through a length of material *L* is given in Equation 10 [102]:

$$\tau(L) = \tau_0 \sqrt{1 + \left(\frac{4 \cdot GVD \cdot L \cdot ln(2)}{\tau_0^2}\right)}$$

Equation 10

where τ_0 is the initial pulse width. Using Equation 10 and the method stated for calculating GVD, the pulse stretching for 10, 100 and 1000 fs long pulses after travelling though 300 μm, typical waveguide inscription depth of ZnSe is plotted for a range of wavelengths in Figure 2.14, Figure 2.15 and Figure 2.16. From this figure, we observe greater pulse stretching at shorter wavelengths as expected from the GVD graph. For a 10 fs pulse travelling through 300 μm of ZnSe, it will exit at 90 fs and 60 fs for 800 nm and 1064 nm respectively. Thus in the 10 fs regime mitigation methods are worth investigating. However, for longer pulses at 100 and 1000 fs the pulse stretching through 300 μm of ZnSe is significantly less, hence no mitigation methods are required. Therefore we can deduce that MacDonald et al.'s [23] successes in inscription of ZnSe with longer wavelength and pulse width were not due to the pulse chirping compensation effect.

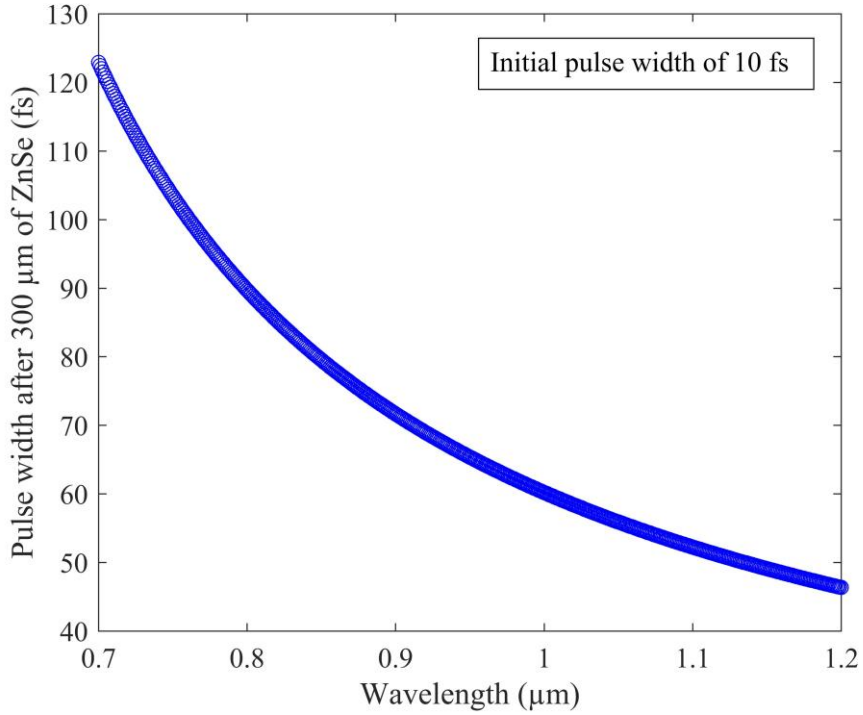

Figure 2.14. Modelling of Gaussian pulse width after propagating through 300 µm of ZnSe. The initial pulse width was 10 fs. Calculations were based on Sellmeier coefficients for ZnSe given in Table 1.

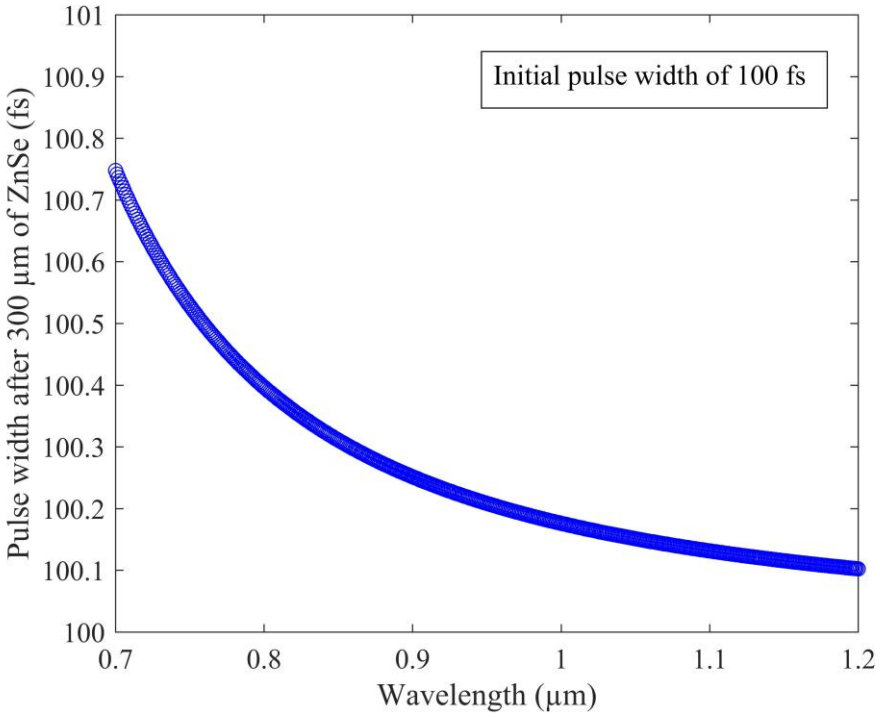

Figure 2.15. Modelling of Gaussian pulse width after propagating through 300 µm of ZnSe. The initial pulse width was 100 fs. Calculations were based on Sellmeier coefficients for ZnSe given in Table 1.

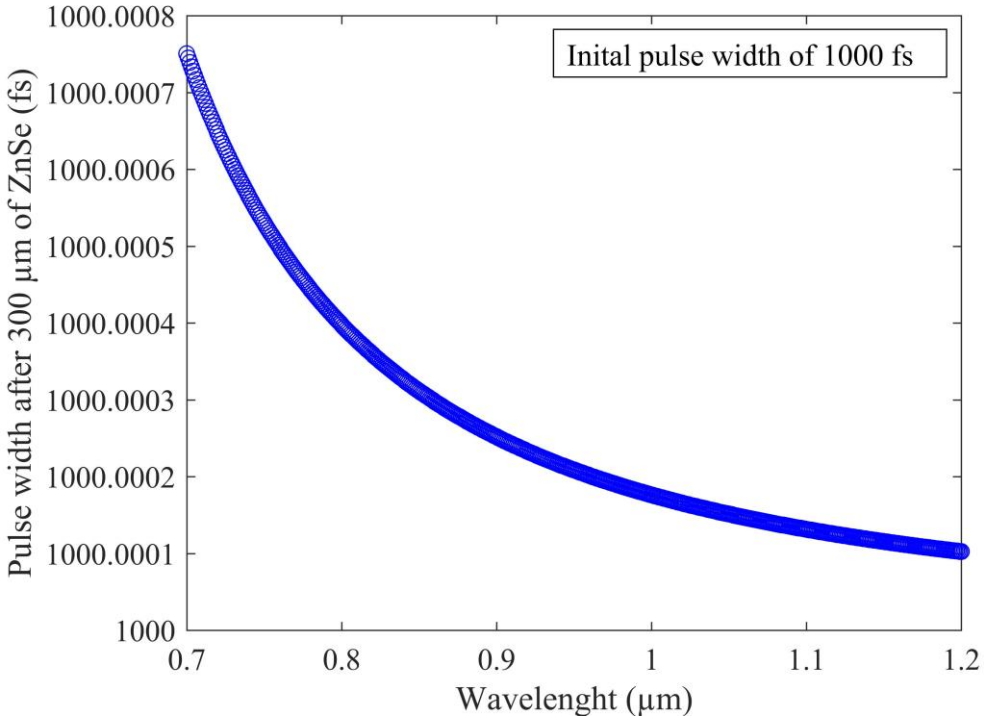

Figure 2.16. Modelling of Gaussian pulse width after propagating through 300 µm of ZnSe. The initial pulse width was 1000 fs. Calculations were based on Sellmeier coefficients for ZnSe given in Table 1.

The nonlinear effects that make femtosecond refractive index modification of ZnSe challenging have been discussed. From this it is clear that spatial distortion by the high n_2 of ZnSe is dominant over temporal effects. Thus to modify ZnSe, careful consideration of inscription wavelength and pulse widths are the main factors to consider adjusting for waveguide fabrication using ULI.

2.4.2. NIR Waveguides in ZnSe

The first demonstration of a ULI fabricated waveguide in ZnSe was a multiscan waveguide. The propagation loss of the waveguide was measured at 1550 nm to be 1.07 ± 0.03 dB·cm^{-1}, which is comparable to that of multiscan waveguide in other materials [23, 33]. A microscope image of the end facet of a ZnSe multiscan waveguide and a guided mode at 1550 nm are shown in Figure 2.17:

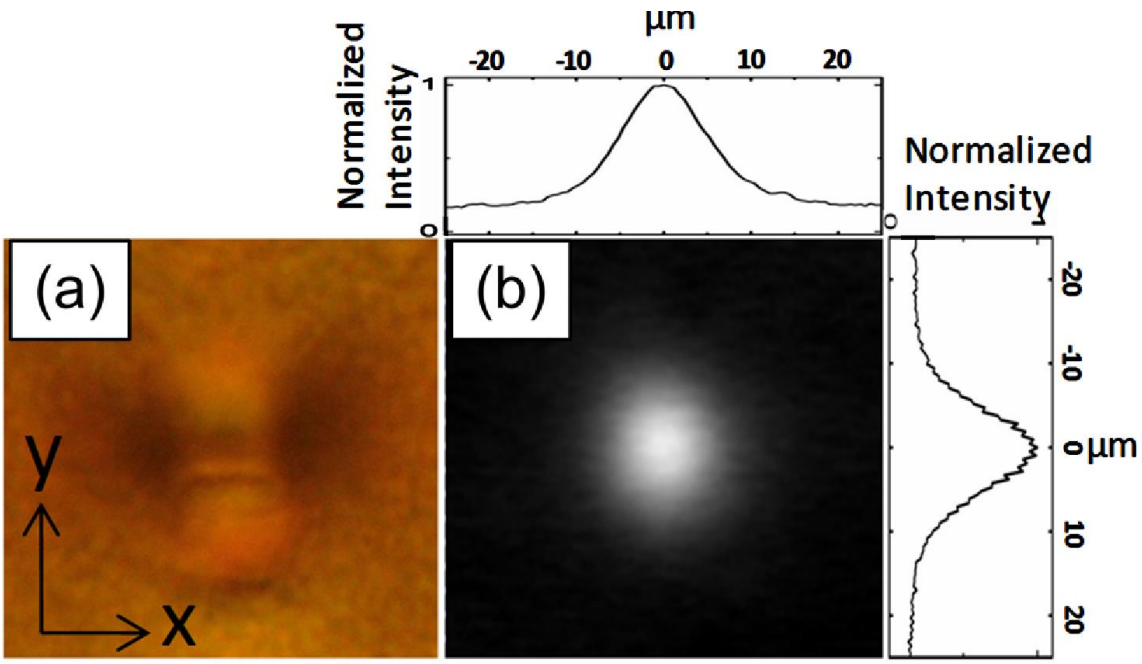

Figure 2.17. (a) is a transmission microscope image of a ZnSe multiscan waveguide end facet.The waveguide structure was inscribed with a 1.5 ps laser pulse width. (b) Near-field mode image of the waveguide output at 1550 nm. The field of view of (a) and (b) is 50 µm x 50 µm. This figure has been reproduced from MacDonald et al. [23].

The waveguide shown in Figure 2.17 (a) did not guide light at 1.9 µm [52], a key wavelength for pumping a Cr:ZnSe laser. The reason for this was that the waveguide's cut-off frequency was less than 1.9 µm. There are two ways to increase the cut-off frequency. The first is to increase the size of the waveguide, but this will increase the MFD and thus reduce the intensity in the waveguide, which is not desirable for laser and nonlinear devices. The second is to increase the refractive index change between the core and the cladding, which ULI can generally do by increasing the pulse energy of the inscription laser. MacDonald could not investigate this because of the limitations of the inscription laser when operating at pulse repetition frequencies between 2-3 MHz needed for Type I modification [52].

2.4.3. Mid-IR Waveguides in ZnSe

Mid-IR waveguides in ZnSe have been fabricated using a reduction in refractive index and thus the cladding region of the waveguide is inscribed. The waveguides were inscribed at a lower repetition rate (100 kHz) than previous work [23, 57]. The reason for this was that the laser used in the experiments produced higher pulse energies when operating at lower repetition rates. It was found that inscribing at 100 kHz induced a

negative change in refractive index. Negative index change is common in crystals such as YAG when using larger pulse energies [103].

There have been two successful geometries used to implement reduction in refractive index modification for fabricating ZnSe waveguides. One is based on arranging multiple multiscan sections to create a box like cladding region with an unmodified section for the core as shown in Figure 2.18. The other is the circular cladding waveguide. It has been found that the circular cladding is superior because it supports a more symmetrical mode and has lower propagation losses [52, 58, 87].

The inscription parameters used to fabricate cladding waveguides in ZnSe appear black on a visible microscope, indicating a considerable amount of scattering or absorption. This is because a higher pulse energy is need to get sufficient negative index change in ZnSe, damaging the host. However, most of the guided mode will propagate in the core region and as such will not interact with the laser modified cladding. Thus propagation losses of a depressed cladding waveguide are sufficiently low despite the large amount of optical damage induced in the waveguide fabrication step.

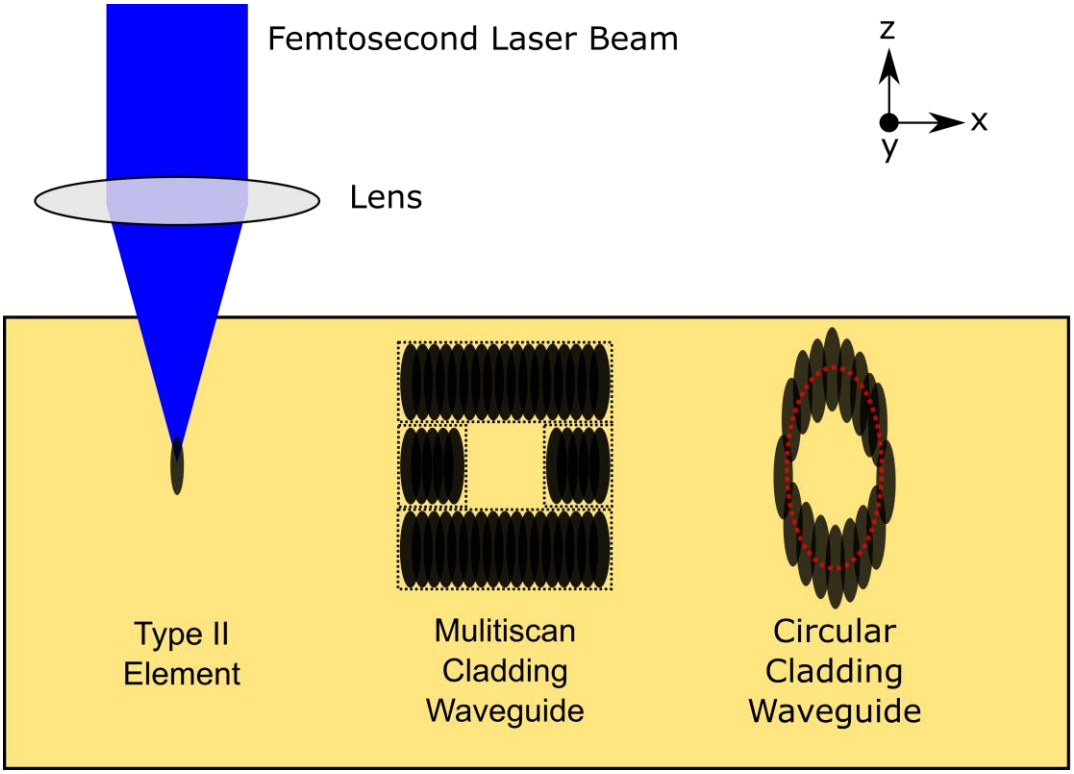

Figure 2.18. Schematic of cladding waveguide structures in ZnSe viewed from the end facet. Left is a negative index change element. Centre is a box section multiscan cladding waveguide. Right is a circular depressed cladding waveguide.

2.4.4. Ultrafast Laser Inscription in Cr:ZnSe

Doping ZnSe with Cr^{2+} was found to significantly change the modification parameters for inscription [87]. This effect can be clearly seen in Figure 2.19, where a section of multiscan has been inscribed in ZnSe and Cr:ZnSe with identical laser inscription parameters. The Cr:ZnSe sample did not experience as much refractive index change as the ZnSe. The single multiscan cladding waveguide design did not form an effective waveguide in Cr:ZnSe [52] .

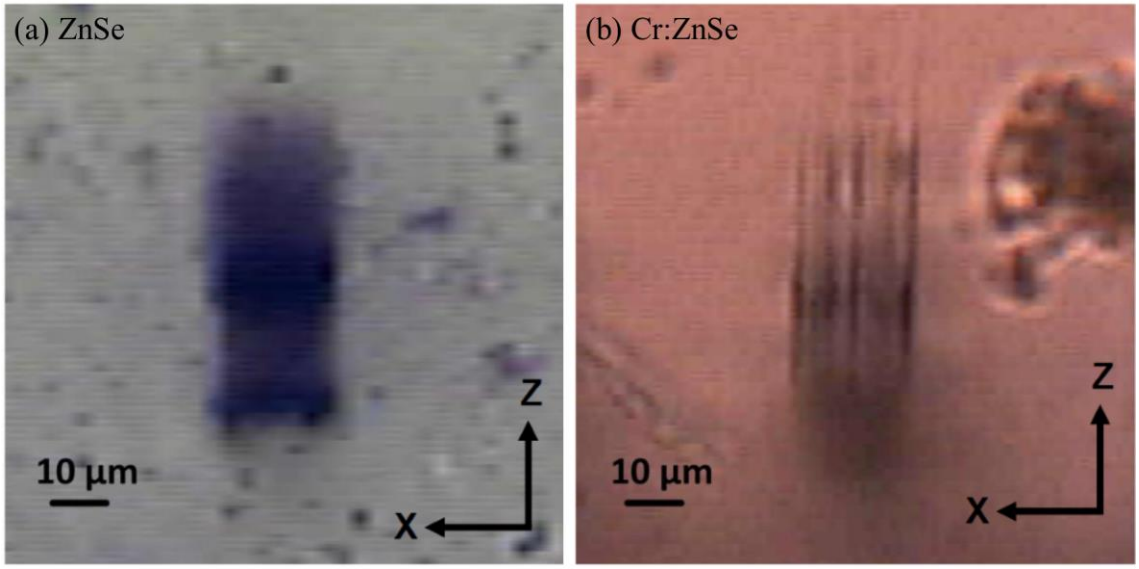

Figure 2.19. Multiscan structure inscribed in (a) ZnSe and (b) Cr:ZnSe with identical inscription parameters. Reproduced from MacDonald [52].

Increasing the inscription pulse energy creates stronger index contrast, but was also found to increase the scattering losses of the waveguide. This issue was mitigated by having an inner cladding inscribed with a lower pulse energy, < 0.5 µJ, and an outer cladding inscribed with a higher pulse energy of 1 µJ. The multiscan double cladding waveguide geometry was found to overcome this issue and produce an effective Mid-IR waveguide in Cr:ZnSe [57]. A schematic of the waveguide design is given in Figure 2.20:

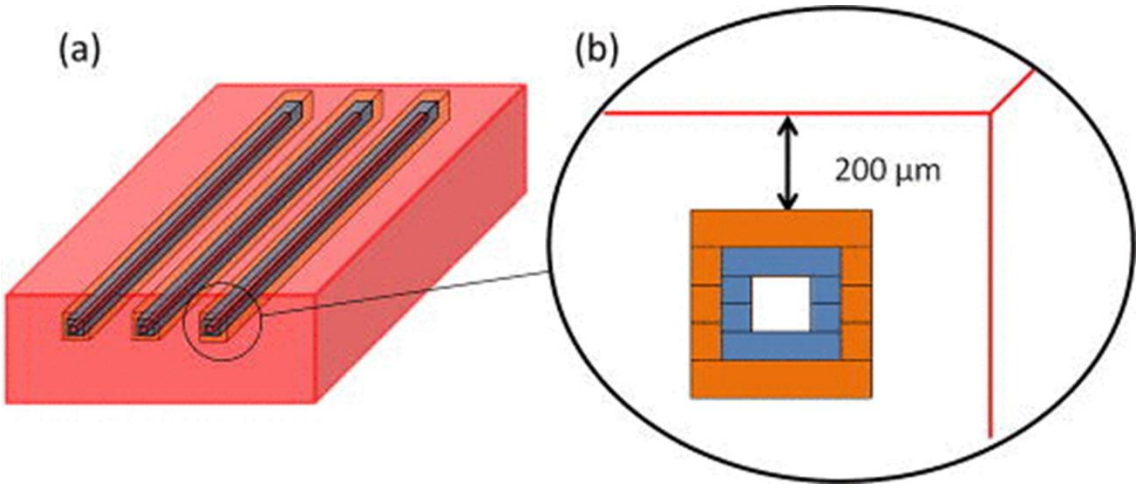

Figure 2.20. Schematic of double cladding waveguide in Cr:ZnSe. Diagram (a) shows the entire waveguide sample, (b) is a zoomed in image of the end facet. The blue inner cladding is inscribed with less than 500 nJ pulse energy. The orange outer cladding was inscribed with 1 µJ pulse energy. Reproduced from MacDonald et al. [53].

The multiscan double cladding waveguides were found to guide light from 1928 nm to 3392 nm [57]. These are important wavelengths since they represent the pump wavelength and the end of the emission band of Cr:ZnSe [70]. The multiscan double cladding waveguide was built into a laser cavity which was found to lase at 2573 nm with an output power of 18.5 mW for 1.2 W of pump power. The slope efficiency was only 5% because of the high waveguide propagation losses of 3.5 $dB \cdot cm^{-1}$ [53]. The high propagation losses are attributed to micro-cracking formed along the propagation direction of the waveguide. These micro cracks were formed from the stress induced by the modification elements on the Cr:ZnSe substrate. This same problem was also found in multiscan single cladding waveguides in ZnSe [52]. The cracking was mostly from the side walls of the multiscan cladding waveguides.

Circular depressed cladding waveguides were not found to have the issue of micro-cracking. This is because there are fewer modification elements, particularly in the sides of the waveguide, when compared with the multiscan type which reduces the stress on the substrate. When built into a laser cavity, these waveguides demonstrated 285 mW of output power at 2486 nm with a pump power of 1.11 W [58]. These waveguides had a notable propagation loss of only 0.7 $dB \cdot cm,^{1}$ which is comparable with waveguides in other doped crystals [104]. The output of the waveguide laser was slightly asymmetrical, with an M^2 of 1.80 and 1.05 in the x-axis and y-axis respectively. This is attributed to the asymmetrical index modification which arises from the modification elements being taller than they are wide. For reference, the inscription parameters used by MacDonald et al. [58] for inscribing the optimum single mode circular depressed cladding waveguides are given in Table 2. The low loss depressed cladding waveguide parameters developed primarily by MacDonald during his PhD [52] have formed the basis for the waveguide lasers presented in this thesis.

ULI parameters of Cr:ZnSe		
Laser parameters	Laser repetition rate	100 kHz
	Laser pulse energy	2.5 μJ
	Polarisation	Horizontal
	Pulse width	750 fs
	NA of inscription lens	0.65 NA*
Geometric parameters	Waveguide diameter	80 μm
	Number of elements	60
	Number of overwrites of each element	50
	Sample translation speed	9 mm·s^{-1}

*Table 2. Optimum inscription parameters for polycrystalline Cr:ZnSe with dopant concentration of 8.5 × 10^{18} cm^{-3}. * The lens is stated as 0.6 NA in publications, but it was found during this PhD that the lens had been mislabelled and was actually a 0.65 NA lens [24, 58, 105].*

2.5. Conclusion

Transition metal II-VI lasers as a group can output laser light from 2 – 6 μm, making them an excellent set for tuneable and modelocked lasers sources in the Mid-IR. The spectroscopic properties that led to their ultra-broad bandwidth have been detailed in this chapter. It is important to note there is additional broadening from the Jahn-Teller effect as well as the vibronic broadening. This section gives the spectroscopic background to the Cr:ZnSe, Cr:ZnS and Fe:ZnSe laser experiment discussed in subsequent chapters.

This chapter has introduced the 3D waveguide fabrication method ULI. ULI is a disruptive technology that allows fabrication of waveguides in a vast number of glasses and crystals. It also has the benefit of not requiring a clean room environment, is easily computer automated and is a maskless process. The combination of these traits make it an excellent waveguide prototyping method.

The challenges of applying ULI waveguide fabrication to ZnSe first noted by Okhrimchuk et al. [54] were examined. The main challenge was to mitigate geometric distortions of the focal volume. These arise from the large positive n_2 of ZnSe, but can be reduced by inscribing at a longer wavelength and the use of picosecond pulses demonstrated by MacDonald [55]. Details of circular depressed cladding waveguides in

Cr:ZnSe are then outlined. These waveguides have demonstrated relatively low loss for a ULI inscribed waveguide, and are capable of guiding Mid-IR light. For this reason, the waveguide laser investigation detailed in later chapters of this thesis all used this waveguide geometry.

3. Cr:ZnSe tuneable waveguide laser

3.1. Introduction

The low loss waveguides inscribed in Cr:ZnSe by Macdonald et al. [58] are used in this chapter to demonstrate widely tuneable waveguide lasers. In bulk, Cr:ZnSe lasers have been demonstrated to be continuously tuneable from 1973-3339 nm with a minimum output power of 10 mW across the entire range [106]. This is possible because of the large, homogenously broadened gain bandwidth of Cr:ZnSe. Laser diodes and QCLs are transitioning into the market in the 2 – 3 μm range but their bandwidth will only cover a small range of wavelengths per emitter. It can be seen from Figure 3.1 that a laser with broad emission bandwidth is needed to detect more than a single substance. For remote sensing applications a small portable laser system is preferable. This is difficult to achieve with bulk laser systems with typical cavity lengths of 1 m. A waveguide laser does not require many of the required free space optics and thus present a compact tuneable laser system. This chapter investigates CW wavelength tuneable operation of Cr:ZnSe circular depressed cladding waveguide lasers.

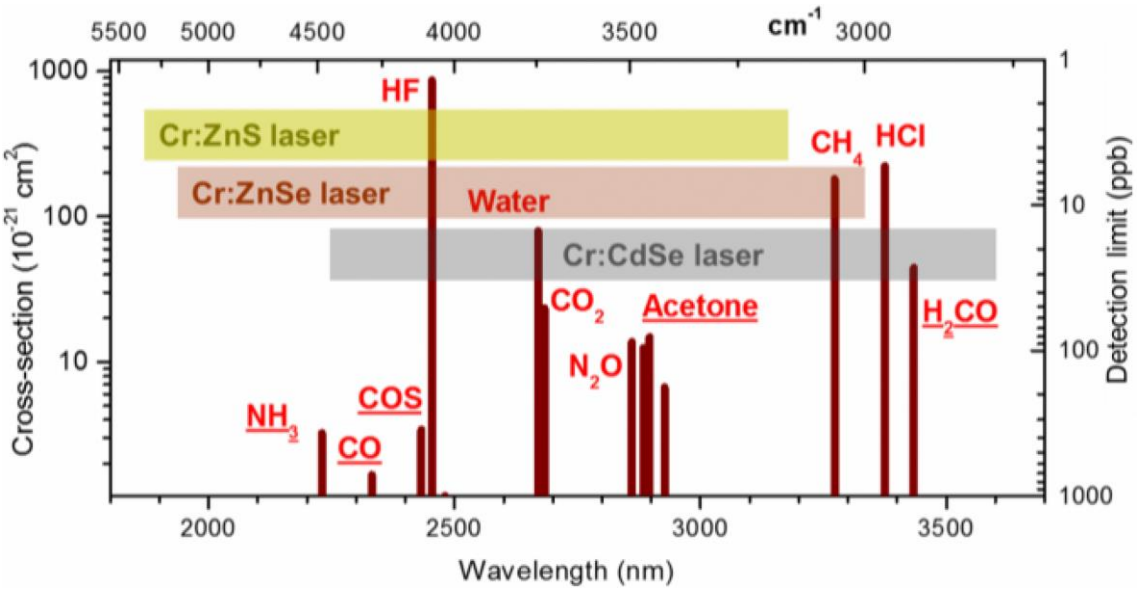

Figure 3.1. Spectral tuneability range of Cr^{2+} lasers and spectral positions of trace gas absorption lines with minimum detectible concentrations. This graph has been reproduced from Sorokina and Sorokin [106].

Wavelength tuning of a solid-state laser works on the fact that a laser will lase at the wavelength of highest gain and lowest cavity loss. Thus, there are two ways to tune a laser. We can either change the wavelength dependent loss or the wavelength dependent gain characteristics of the lasers crystal. For tuneability over a wide range, loss tuning must be used. Gain control methods, such as temperature tuning, will not work over a wide range. Common methods used for wavelength tuning via loss mechanisms in the laser cavity include: gratings, prisms, birefringent filters and Fabry-Perot [61].

3.2.1. Blazed gratings tuning

We know a monochromatic beam of light incident on a diffraction grating will be reflected by angle θ_m for the order m given in Equation 11 [107]. The diffraction angle is wavelength dependent thus we have a selective way of spatially separating a laser's gain bandwidth. Wavelength selective laser operation can be achieved by selectively coupling back a small portion of the bandwidth into the laser cavity:

$$a(\sin(\theta_i) + \sin(\theta_m)) = m\lambda$$

Equation 11

where a is the groove spacing known as pitch, θ_i is incident angle and θ_m is diffracted angle of the m^{th} order. For improved efficiency, blazed gratings are used. These are designed to produce optimal diffraction efficiency at a given wavelength for a given order, in most cases the first order. There are two common cavity configurations for gratings in tuneable lasers: Littrow and Littman-Metcalf, as shown in Figure 3.2:

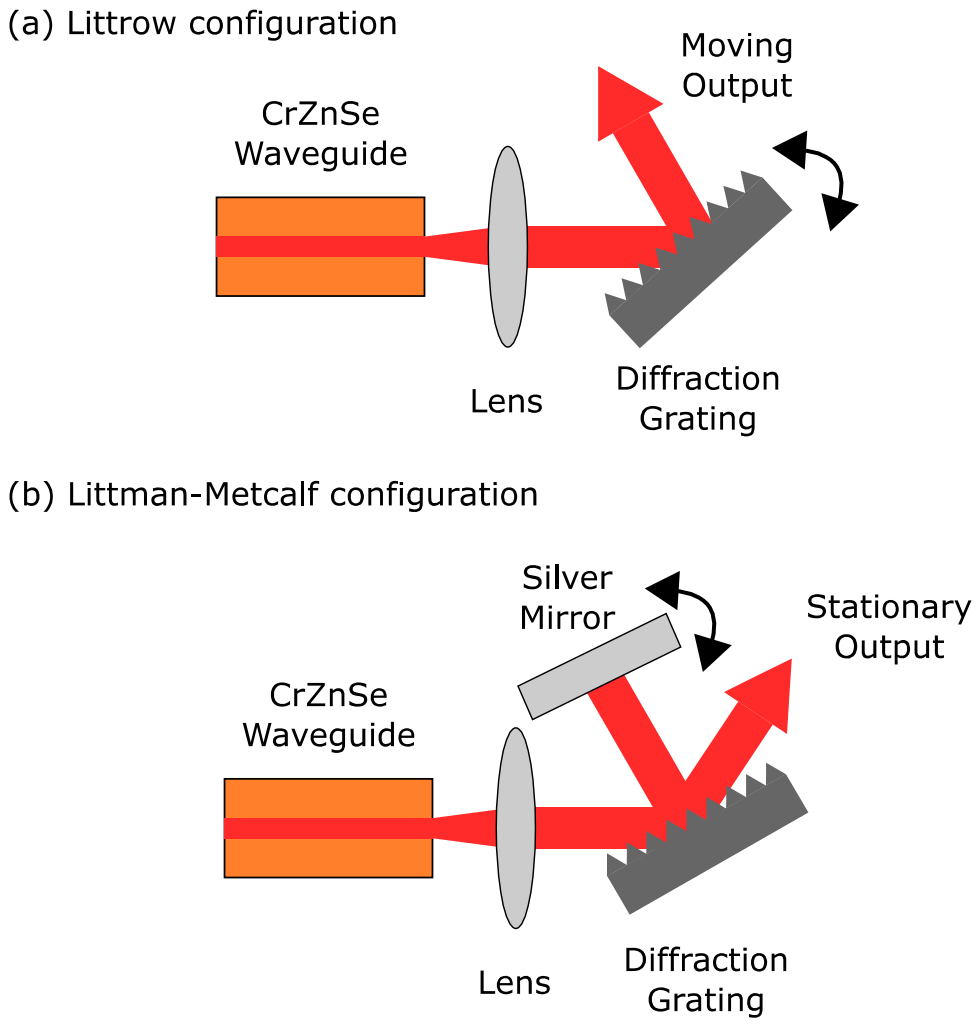

Figure 3.2. Schematic of extended cavity wavelength tuning designs using a blazed grating (a) is the Littrow configuration and (b) is the Littman-Metcalf configuration

The Littrow configuration is the simplest of the two as the only optical components are a collimating lens and a grating [108]. In this configuration, the 1st order is reflected back to the laser cavity and the 0^{th} order is the output coupler as shown in Figure 3.2.(b). Thus for Equation 11, $\theta_i = \theta_m = 1$. The disadvantage of this method is that tuning the laser wavelength requires a rotation of the grating, which changes the angle of the output beam. The wavelength resolution of a Littrow grating setup is given by Equation 12 [107], where ω is the FWHM beam waist of a Gaussian laser beam.

$$\Delta\lambda_{FWHM(Littrow)} = \frac{\lambda^2}{2\pi\omega tan(\theta_i)}$$

Equation 12

In the Littman-Metcalf configuration, as shown in Figure 3.2. (b), the output from the waveguide is collimated and incident on the diffraction grating at a grazing angle. The 1st order reflection is sent to the mirror then reflected back on to the diffraction grating and then into the laser by a rotating mirror. This double pass of the grating improves the resolution by a factor of 2, as shown in Equation 13:

$$\Delta\lambda_{FWHM(Littman-Metcalf)} = \frac{\lambda^2}{4\pi\omega\tan(\theta_i)}$$

Equation 13

This configuration has a stationary output which can be advantageous in field applications where a skilled operator will not be present. However, the cavity loss contribution from the grating is doubled. The size of the grating must also be increased for the same tuning range, which could be a limiting factor for very compact systems [107].

In both of these configurations, a blazed grating is often used which is optimised for a specific wavelength. There is an efficiency drop-off with this central wavelength region with blazed gratings. This is not an issue for lasers with small tuning ranges, but with TM:II-VI lasers having typical emission bandwidths spanning 1 μm it could be a limiting factor. Another method of wavelength tuning for broad ranges is to use a prism. The tuning range is then only limited by the transmission bandwidth of the prism's substrate, which, depending on the material can be very large. For example, ZnSe has a transparency range of 0.6 to 21.0 μm [109].

3.2.2. Prism tuning

The angle of propagation for any laser beam though a prism will be deflected. The magnitude of this deflection depends on the refractive index. Chromatic dispersion results in angular separation of the wavelengths making up the laser beam spectra. Wavelength selectivity is achieved by only a small portion of the light being sufficiently aligned to form a laser resonator on the reflection back through the prism. The additional parasitic cavity losses induced by a Brewster cut prism can by minimised by aligning the incident polarised beam at a Brewster angle to the prism's face. A cavity configuration for a single prism is given in Figure 3.3:

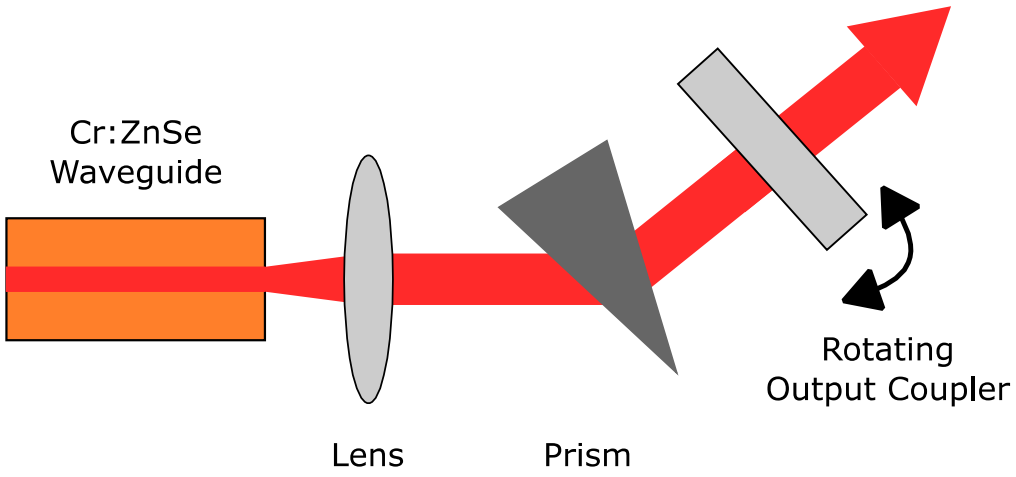

Figure 3.3. Schematic of extended cavity wavelength tuneable waveguide laser cavity using a single stationary prisms and rotating output coupler

The output direction of the cavity setup shown in Figure 3.3 will deviate with the rotation of the output coupler. The deviation is much less than that of the diffraction grating in the Littrow configuration, as shown in Figure 3.2 (a). The spectral bandwidth of a single mode Gaussian beam of radius ω_0 passing through a prism configuration is given in Equation 14.

$$\Delta\lambda_{FWHM(Prim)} = \frac{\lambda}{2\omega_0}\left(\frac{dn}{d\lambda}\right)^{-1}$$

Equation 14

3.2.3. Theoretical comparison of grating and prisms tuning extended cavities

To make an informed decision on what tuneable elements to integrate into an extended-cavity Cr:ZnSe waveguide laser, the bandwidth and laser efficiency of gratings and prisms are compared. For the modelling of the Littrow and Littman-Metcalf grating configurations, the number of grooves per mm is set to 600. Equation 12 and Equation 13 were used to calculate the cavity acceptance bandwidth for each case. In these calculations, the angle of incidence on the grating θ_i was set by the tuning condition $sin(\theta_i) = \lambda/2d$ where d is the distance between grating lines. From the equations, it is clear that at a given wavelength the Littman-Metcalf configuration has an acceptance bandwidth of half of that of the Littrow configuration. The acceptance bandwidth is over the 2-3 μm

range of both grating configurations are plotted in Figure 3.4. For this set of conditions, the Littman-Metcalf grating has an acceptance bandwidth of 0.45 nm at 2500 nm.

The acceptance bandwidth of a single prism in the Littrow configuration with a substrate of ZnSe, CaF_2 and Si were calculated using Equation 14. The radius of the beam ω incident on the prism was set to 2 mm for this calculation. Differentiation of refractive index with respect to wavelength for each material was calculated by numerically differentiating the appropriate Sellmeier equation. The form of the Sellmeier equation and its constants for ZnSe are given in Equation 9 and Table 1. The form of the Sellmeier equation and its constants for the CaF_2 and Si prisms are detailed in Table 3. As can be deduced from Figure 3.4, Si has the narrowest acceptance bandwidth of the three with a 5 nm bandwidth at 2500 nm.

Material	CaF_2 [110]	Si [111]
Transmission range	0.13 to 10 μm	1.2 to 15 μm
Sellmeier equation	$n^2(\lambda_0) - 1 = A + \frac{B_1\lambda_0^2}{\lambda_0^2 - C_1^2} + \frac{B_2\lambda_0^2}{\lambda_0^2 - C_2^2} + \frac{B_3\lambda_0^2}{\lambda_0^2 - C_3^2}$	$n^2(\lambda_0) - 1 = A + \frac{1}{\lambda_0^2} + \frac{B_1}{\lambda_0^2 - C_1^2}$
A	0.33973	10.67316
B_1	0.69913	0.004482633
B_2	0.11994	1.108205
B_3	4.35181	-
C_1	0.09374	-
C_2	21.18	-
C_3	38.46	-

Table 3. Table of Sellmeier coefficients for calculating refractive index of CaF_2 and Si

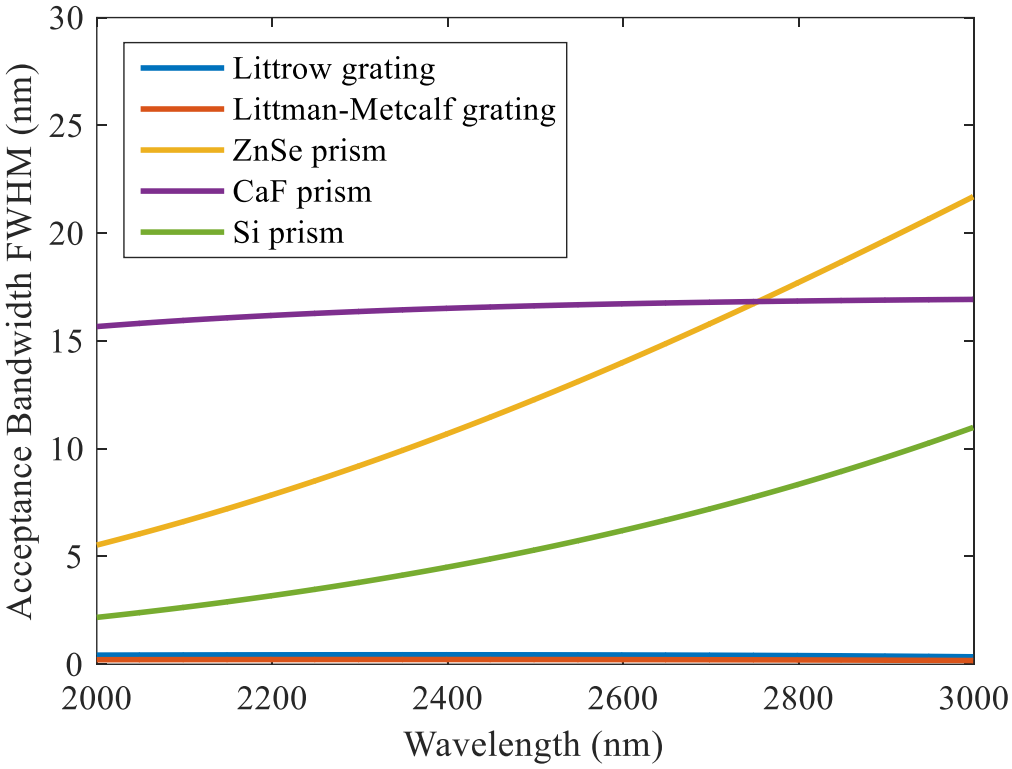

Figure 3.4. Acceptance bandwidth of grating and tuneable elements. The grating used for the Littrow (blue) and Littman-Metcalf (red) has 600 grooves per mm. The angle of incidence on the gratings is set to sin(θ) = λ/2d. For this calculation the prisms are arranged in the Littrow configuration. The prism materials examined are ZnSe (yellow), CaF_2 (purple) and Si (green).

As shown in Figure 3.4, it is clear the section of a Littman-Metcalf grating tuning element will give the narrowest wavelength emission from a Cr:ZnSe waveguide laser. The other factor that must be included is the losses induced by the laser tuning elements. For the prism configuration, the input beam angle with respect to a Brewster cut prism surface can be set at a Brewster angle which removes the Fresnel losses. The material loss for well developed optical martials such as ZnSe, CaF_2 and Si at 2.5 μm is negligible. Therefore, a Brewster cut prism will induce negligible cavity losses for an enforced linearly polarised laser cavity [107].

To examine the grating cavity loss, two typical and commercially available gratings are compared. They are the Thorlabs GR25-0616 and Thorlabs GR1325-45031. These gratings are optimised by the manufacturer for 1.6 μm and 3.1 μm respectively. The efficiency curves for a Littrow configuration of GR25-0616 are given in Figure 3.5. Figure 3.6 presents the results for GR1325-45031. From this data, it is clear that in the 2–3 μm range, GR25-0616 has the lowest losses, of around 10% at 2.5 μm for light polarised

perpendicular to the grating. As can be seen from Figure 3.5 and Figure 3.6, the granting set-ups have highest losses for light polarised parallel to the gratings which will be detrimental when used in an non polarisation enforced laser cavity.

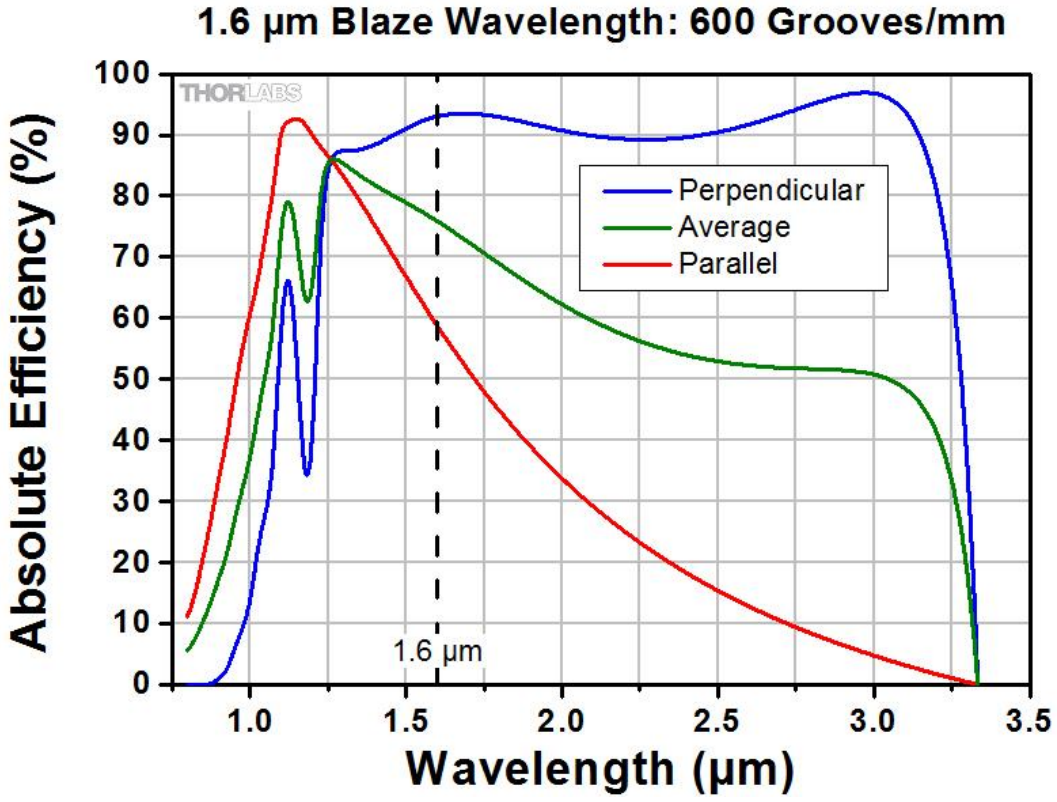

Figure 3.5. Efficiency curve for Littrow configuration of Thorlabs GR25-0616 grating. The incident laser light polarised perpendicular (blue) and parallel (red) to the lines of the grating are shown. The graph has been reproduced from the Thorlabs specification sheet.

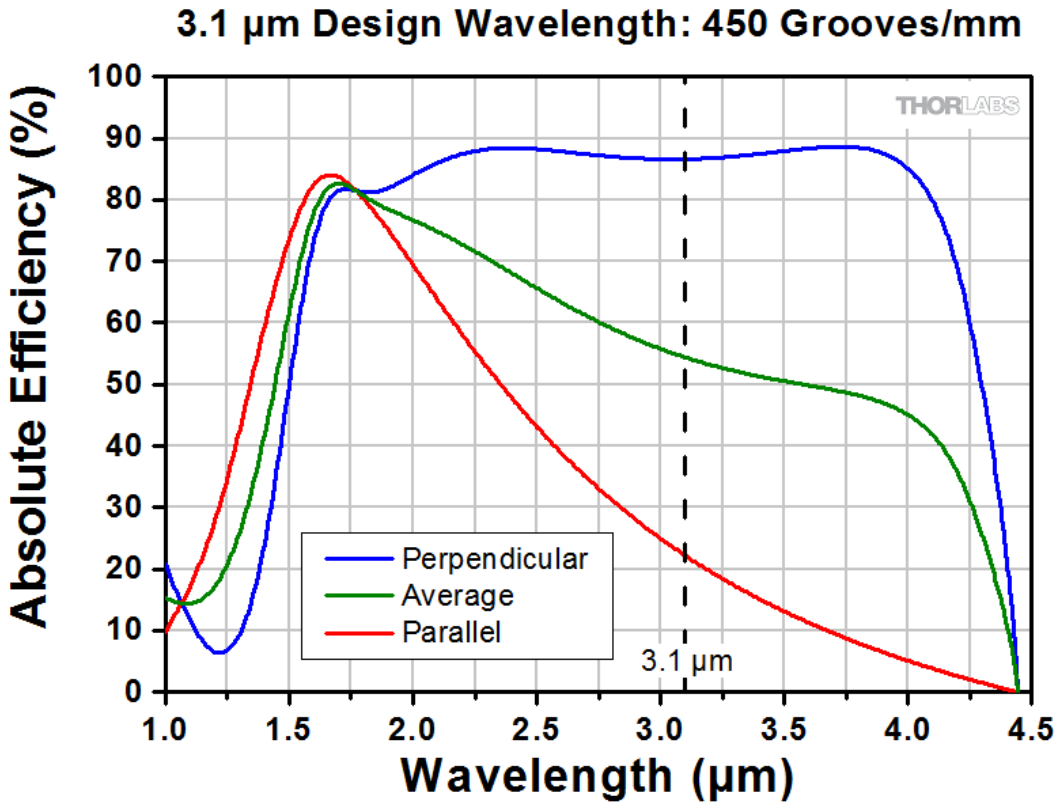

Figure 3.6. Efficiency curve for Littrow configuration of Thorlabs 1325-45031 grating. The incident laser light polarised perpendicular (blue) and parallel (red) to the lines of the grating are shown. The graph has been reproduced from Thorlabs' specification sheet.

It is evident that a grating configuration will give the narrowest laser linewidth, but a prism will result in a more efficient laser. Thus the best choice of cavity design is application dependent. There is therefore merit in experimentally investigating both configurations, and this is discussed further in following sections of this chapter.

3.3. Cr:ZnSe wavelength tuning with blazed grating

The investigation into tuneable continuous wave operation used an extended cavity design in order to incorporate a tuning element into the cavity. A blazed grating was assembled in the well known Littman-Metcalf configuration as displayed Figure 3.2 (b). The Littman-Metcalf configuration benefit over the Littrow configuration is the fixed output beam direction. In a Littrow configuration, the output beam angle varies with the rotating grating element used for wavelength tuning. This is a particular problem when tuning across a broad wavelength range since the output angle would vary considerably. In addition to overcoming this problem, the Littman-Metcalf configuration provides greater wavelength selectivity, due to the signal performing a double pass of the

diffraction grating. This increased wavelength selectivity should lead to a narrowerlinewidth. The disadvantage of the Littman-Metcalf is the loss of the zero-order reflection upon the second pass of the grating. This increases cavity loss thus also laser threshold, which potentially could limit the wavelength tuneable range of the laser. However, the main aim of this laser is to demonstrate a narrow linewidth CW wavelength tuneable lasers source, thus the Littman-Metacalf grating configuration is the most appropriate choice.

An important consideration for any laser is the pump source. Cr:ZnSe has a broad absorption banned centred at 1.8 μm and spanning 350 nm [70]. The absorption cross-section of CrZnSe is shown in Figure 3.7:

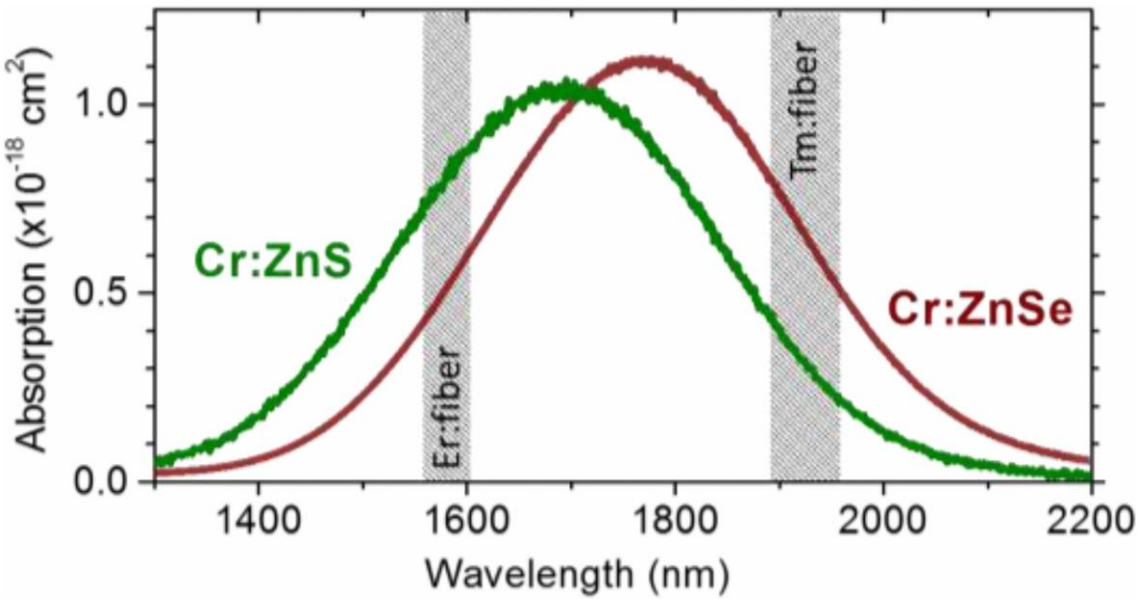

Figure 3.7. Absorption cross-section of Cr:ZnS (green) and Cr:ZnSe (red). The emission wavelength of Er and Tm doped fibre lasers have been superimposed on top of the graph to show their overlap with Cr:II-VI materials absorption. This graph has been reproduced from Sorokina et al. [106].

As marked in the figure, Cr:ZnSe can be pumped with Er or Tm doped fibre lasers. The advantage of these sources is singe mode output average powers of over 100 W [112]. Direct diode pumping of Cr:ZnSe bulk lasers has been demonstrated, but has not been used in this investigation of Cr:ZnSe waveguide lasers because of the lower brightness when compared with fibre sources [113]. A Tm:Fibre pump laser was chosen over an Er:fibre laser because there is a smaller quantum defect between pump and signal. Thus the Tm:Fibre pump will deposit less heating into the laser's crystal. Considerations of

thermal management are an important step of the design process with Cr:ZnSe lasers because of their large dn/dT which limits power scaling [15].

For this experiment, a 1.4 W randomly polarised Tm:fibre laser manufactured by AdValue Photonics with emission centred at 1920 nm was used as the pump source. The product number of the source is AP-Tm-0028. The laser has a spectral linewidth of < 0.1 nm. The delivery fibre is SMF-28, resulting in M^2 <1.1 single mode output. The output of the SMF-28 fibre was collimated using a 12 mm focal length AR coated ZnSe aspheric lens. The pump light was coupled into the waveguide by a 50 mm D coated CaF_2 plano-covex lens.

The laser crystal used was a polycrystalline Cr:ZnSe sample with dimensions of 8.5 × 6.5 × 2.1 mm. The Chromium ions were diffusion doped into polycrystalline ZnSe by IPG Photonics. The Cr^{2+} concentration of the sample investigated was 8.5×10^{18} per cm. This level of doping concentration is suitable for a CW pump of Cr:ZnSe $^5T_2 \rightarrow {}^5E$ transition at room temperature [70].

The waveguides inscribed in the sample were circular depressed cladding waveguides fabricated using ULI. The inscription parameters are given in Table 2 (page 36). After the inscription, the end facets were polished back and then AR coated from 2 – 3 μm. AR coating mitigates the cavity losses induced by Fresnel reflections. For an uncoated ZnSe sample with a refractive index of 2.4, the Fresnel loss is around 18 % reflection per surface at normal incidents. Hence the need to add the AR coating step even though this increases cost and time to the waveguide optimisation process. A transmission microscope image of the end facet of the waveguide is given in Figure 3.8:

Figure 3.8. Transmission microscope image of the Cr:ZnSe waveguide end facet used in the wavelength tuneable experiments. A x20 microscope lens was used to image the end facet. Horizontal diameter of waveguide is 80 µm.

A tuneable laser cavity was formed by placing a pump mirror at the input facet of the waveguide and an extended Littman-Metacalf grating configuration at the output, as shown in Figure 3.9:

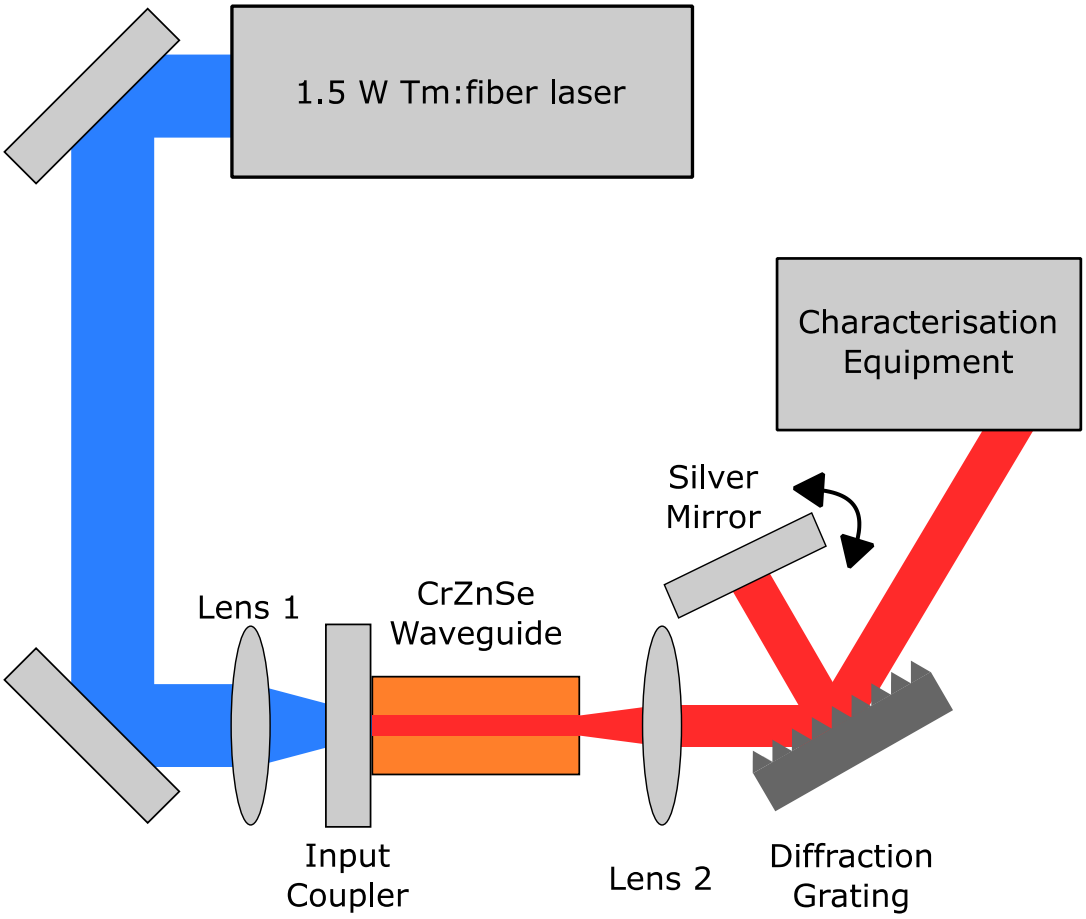

Figure 3.9. Schematic of extended cavity Littman-Metacalf grating configuration wavelength tuneable Cr:ZnSe waveguide lasers. Lenses 1 and 2 are D coated 50 mm focal length plano-convex CaF_2 lens. Wavelength tuning of the cavity is achieved by rotating the silver mirror as shown above.

The pump power and output power of the laser were characterised with a thermal power meter (Spectra-Physics 407). Unabsorbed pump light was dumped before the power meter with two 2000 nm longpass filters. The output power versus wavelength is plotted in Figure 3.10 for a constant pump power 1.4 W. A maximum output power of 120 mW was demonstrated at 2446 nm which correspond well with the peak emission cross-section of the laser. The wavelength of the laser was measured with a Monochromator (Zolix Omni-λ 300) with a resolution of 0.4 nm. The laser was found to be continuously tuneable from 2077 - 2770 nm with an output power of greater than 15 mW at all wavelengths.

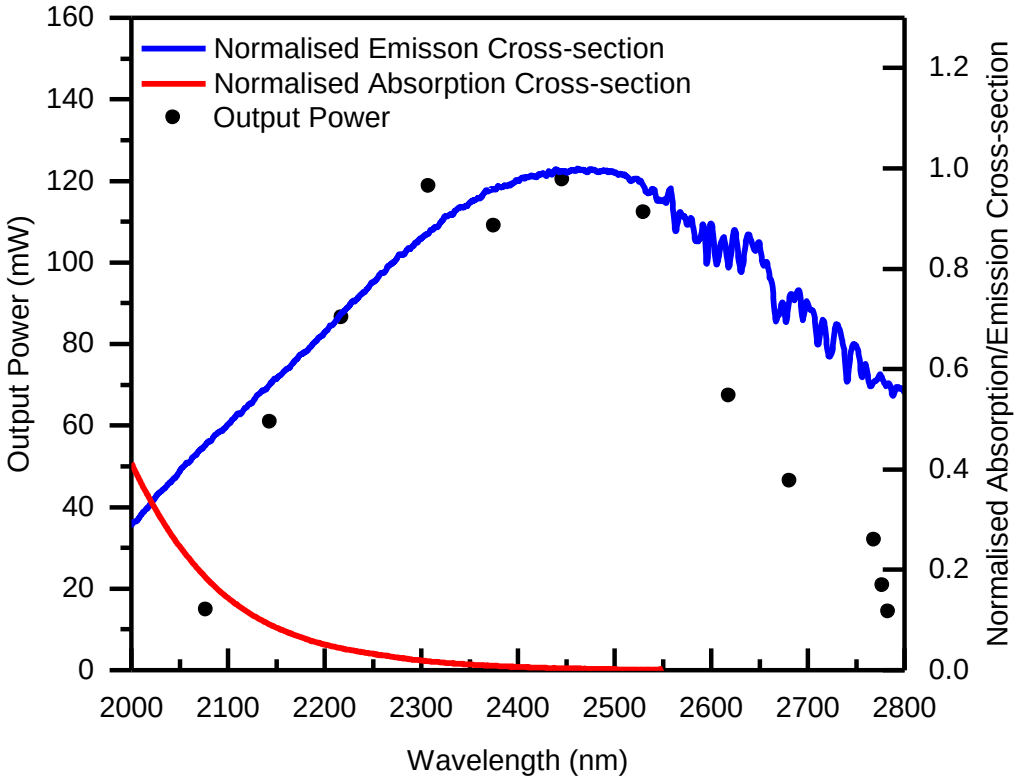

Figure 3.10. Littman-Metcalf tuneable grating Cr:ZnSe waveguide laser performance. The wavelength was tuned by rotating the tuning mirror. The pump power for these measurements was set to 1.4 W. Black dots show the measured output power of the laser for a corresponding wavelength. The red and blue lines show the normalised absorption and emission cross-section of Cr:ZnSe.

The FWHM linewidths of all the wavelength spectra were found to be around 0.4 nm, the limit of the monochromator's resolution. This suggests that the measurement's linewidth was limited by the monochromator and the true linewidth may be narrower. This was investigated using an optical spectrum analyser (OSA) manufactured by Yokogawa (model number AQ6375). The linewidth of the laser was investigated up to the wavelength limit of the OSA, 2.4 μm. The resolution of the Yokogawa AQ6375 OSA was 0.05 nm. The linewidth measurements for the sub 2.4 μm section of the laser's tuning range are given in Figure 3.11.

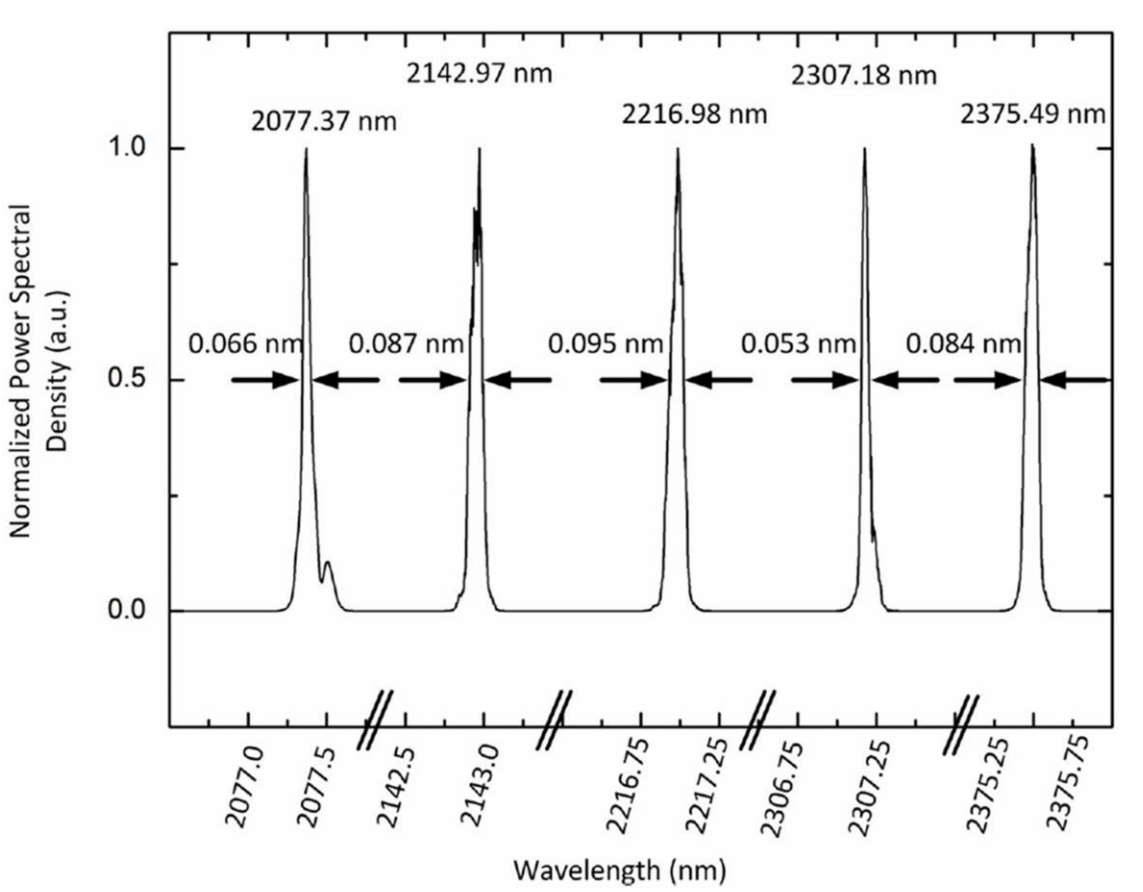

Figure 3.11. Wavelength spectra of grating tuned extended cavity Cr:ZnSe waveguide laser. Measurements were taken with Yokogawa AQ6375 with a resolution of 0.05 nm.

The minimum linewidth measured was 0.053 nm, centred at 2307.18 nm. All other measurements had a linewidth of sub 0.1 nm. Wavelengths longer than 2.4 μm could not be taken due to equipment limitations, but this is something that could be investigated in the future with an extended range of Mid IR OSA.

The continually tuneable wavelength range of 2077 - 2770 nm is notable for a waveguide laser, but wider tuning ranges in bulk Cr:ZnSe cavity have been demonstrated [17] previously. This discrepancy is attributed to additional wavelength dependent loss in the waveguide cavity. There are many different cavity configurations that could be investigated to improve the performance of the waveguide laser. This was numerically investigated with the aim to extend the tuning range of the laser.

3.4. Modelling of diffraction grating

John R. MacDonald, the Research Associate also working on this project at the time of this experiment, modelled the wavelength tuneable Cr:ZnSe waveguide laser as published

in [105]. This model is based on the bulk Cr:ZnSe MOPA modelling by Berry [15]. MacDonald's numerical model makes use of the plane wave approximation. The model starts by making assumptions about the irradiance of the pump and signal based on the experimentally measured MFD of the waveguide. These are then co-propagated through the gain region in a stepped process. The number of steps was set to 10^4. The output after a single pass of the gain region was then attenuated by the cavity loss. Loss from the intra cavity lens, grating and silver tuning mirror were included in the attenuation calculation. The pump and signal were then counter propagated through the gain region. The propagating and counter propagating irradiances were combined at each site of the model. Once the counter propagating beam reached the start of the waveguide, it was attenuated by the input coupler's transmission and was then sent back through the gain media. These steps were then repeated until a steady state was reached. For this numerical mode, several parameters were set to fit the experimental data, as shown in Table 4. The absorption and emission cross-section value use for Cr:ZnSe in the model were experimentally measured by S. Hedge at the University of Dayton Research Institute, and are given in the appendix of this paper by MacDonald et al. [105].

Parameters	Value
Cr^{2+} ion concentration	8.5×10^{18} cm^{-3}
Upper-state lifetime of Cr:ZnSe	4 μs [114]
Waveguide length	6.0 mm
MFD of pump and signal	40 μm
Waveguide propagation losses	0.7 dB/cm [58]

Table 4. Fitting parameters used in numerical modelling of Littman-Metcalf tuneable grating Cr:ZnSe waveguide laser.

The experimental results for output power across the tuning range have been superimposed with the results for the numerical model in Figure 3.12. No free parameters were used in the fitting. Overall, the model fits reasonably well with the results obtained. There is a noticeable divergence between the model and the experimental results after 2.6 μm. This can in part be attributed to intra cavity water absorption. There is a large amount of atmospheric water absorption at wavelengths beyond 2.6 μm which the model does not account for [115]. In addition, at longer wavelengths the assumption that the signal and pump share the same MFD is not as valid as it is when the two wavelengths are similar. This will lead to reduced pump signal overlap and hence reduced performance,

which is observed in the experiment. This part of the model could further be improved by characterising the waveguide loss and MFD across the full wavelength range of the laser.

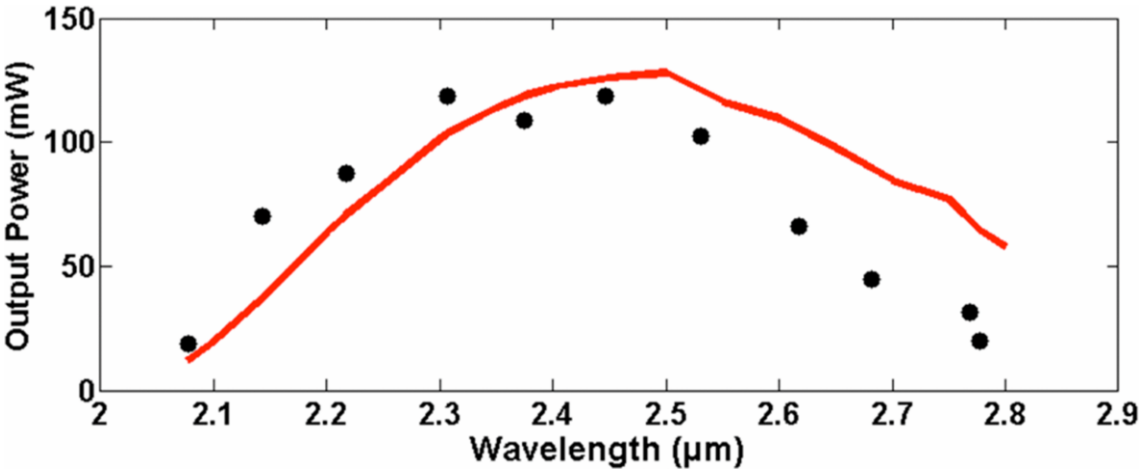

Figure 3.12. Cr:ZnSe tuneable waveguide laser experimental results and numerical model overlaid. The black dots represent the experimental data. The red line is the numeric model.

Limitations of the model aside, it is useful when comparing different tuneable cavity configurations for tuneable bandwidth and output power. The model found that the Littrow configuration would extended the tuning range to 900 nm. The loss of the Thorlabs GR25-0616 grating, shown in Figure 3.5, is over 85 % for wavelengths greater that 2.5 μm polarised perpendicular to the grating lines. Since the cladding waveguides are not polarisation maintaining, there will be a large loss which will limit the tuning range. Use of a blazed grating with a central designed wavelength of 2.5 μm would partially solve this issue. As can be seen from GR25-0616, the loss of the parallel polarisation is reduced to 40%. However, implementing an optimised grating would not remove the losses induced by the zeroth order and the loss of the silver mirror. The modelling found these elements were limiting the wavelength tuning range. Thus, a prism tuned cavity was investigated to extend the tuning range of the laser.

3.5. Cr:ZnSe Wavelength Tuning with Silicon Prism

The finite element analysis showed that the grating was reducing the tuneability range at longer wavelengths. This arises from the loss of the grating's zeroth order and the poor grating efficiency at longer wavelengths. A Si Brewster cut prism was proposed to expand the tuneability range and increase overall laser performance. The prism has the advantage

of not having an efficiency drop off at 3 µm. The Fresnel losses from the air substrate interface can be mitigated by placing the Brewster prism at a Brewster angle The extended prism cavity, shown in Figure 3.13, was built into a similar cavity arrangement as that of the Littrow grating.

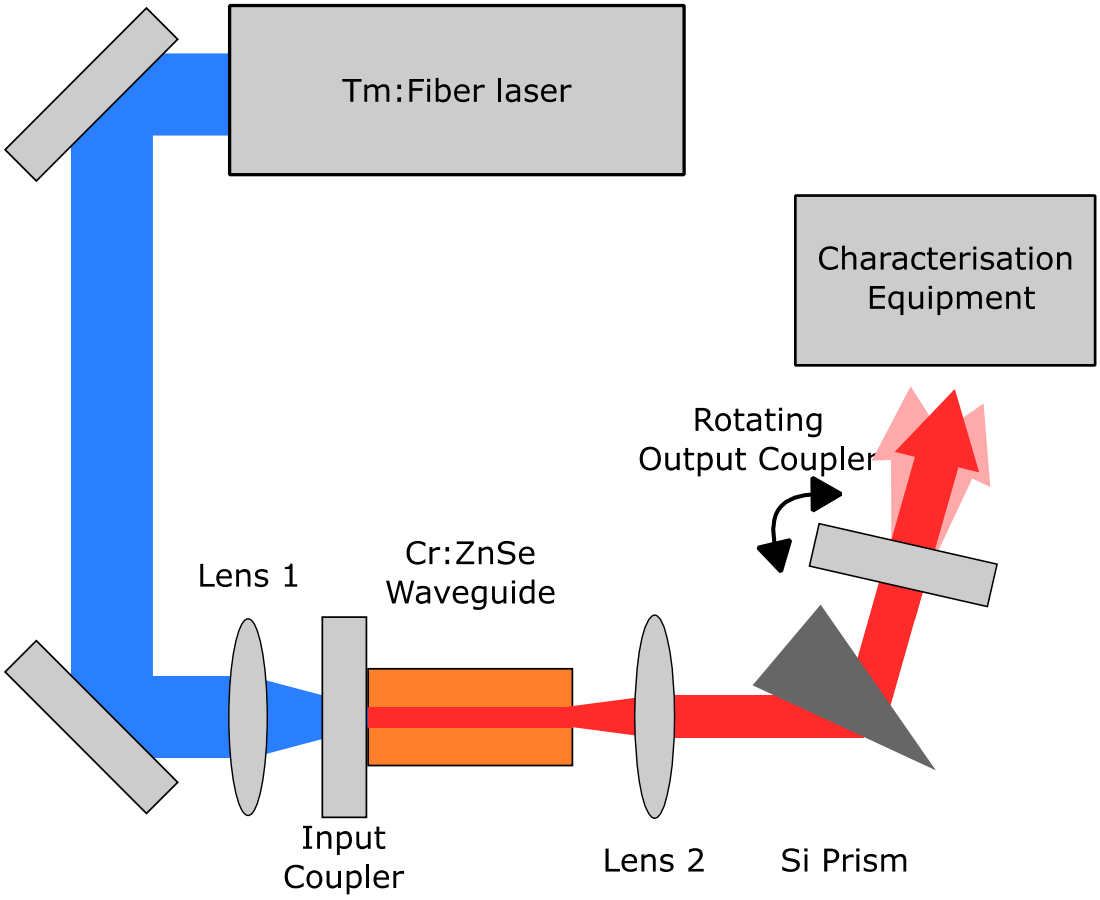

Figure 3.13. Experimental arrangement of the wavelength tuneable Cr:ZnSe external cavity waveguide laser using a Si prism. The output coupler is rotated to tune the lasing wavelength. Lens 1 and 2 are 50 mm and 20 mm focal length lenses respectively, which are D coated CaF_2 plano-convex lenses.

A Si prism was chosen based on the theoretical analysis of acceptance bandwidth as outlined in Section 3.2.3. From these calculations, the FWHM of the spectral emission using a Si prism is more than half that of the same tuneable laser cavity with a CaF_2 or ZnSe prisms.

A Thulium fibre laser was used as the pump source with a maximum power of 1.4 W. The pump was focused through the dichroic mirror on to the facet of the waveguide using a 50 mm D coated CaF_2 lens. The large gain bandwidth of Cr:ZnSe, spanning

approximately 1950 to 3350 nm [61], is much larger than the flat reflection response of the dielectric mirrors commercially available. Therefore, the mirror set needed to be changed as the laser output wavelength was tuned. A list of the mirrors used and operational wavelength ranges are given in Table 5:

Mirror Type	Reflectance (%)	Range (nm)	Set
Input Coupler	> 99.9	2000-2500	Short wavelength
Input Coupler	> 99.6	2500-3000	Long wavelength
Output Coupler	80 ± 5	1700-2700	Short wavelength
Output Coupler	89 ± 1	2800-3070	Long wavelength

Table 5. List of mirrors used in Si prism tuneable Cr:ZnSe external cavity waveguide laser investigation

An intra cavity D coated CaF_2 lens was used to collimate the output of the waveguide. The Si prism was aligned at Brewsters angle with respect to the collimated beam. The output coupler was rotated to tune the output wavelength of the cavity. This rotation deflected the output beam slightly, meaning the alignment of the characterisation equipment had to be optimised for each measurement at a different wavelength. The tuneable laser output power plotted against wavelength is shown in Figure 3.14. The pump power for these output power measurements was kept constant at 1.4 W.

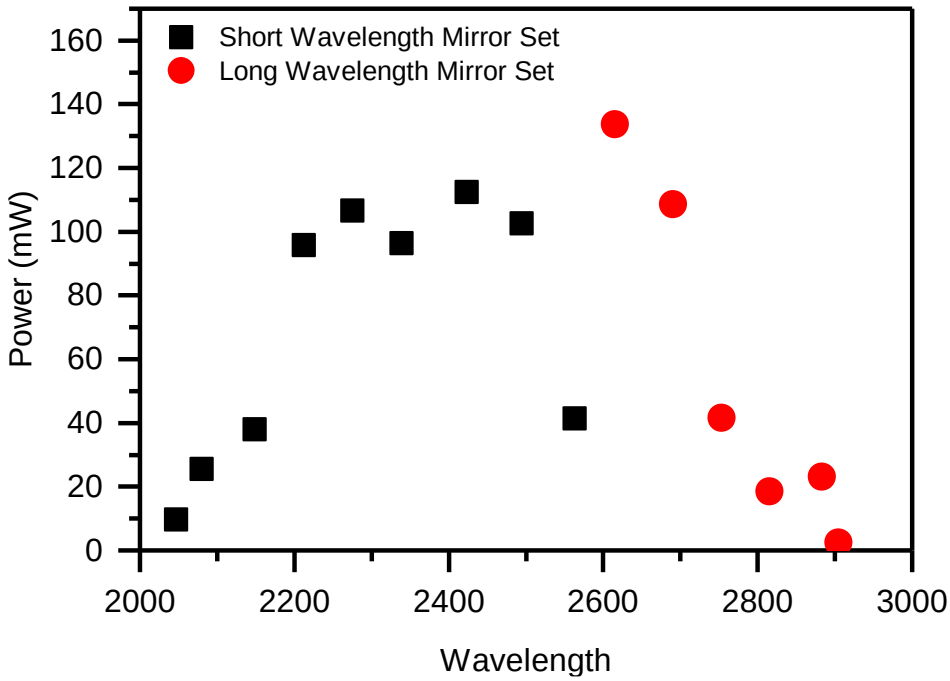

Figure 3.14. Wavelength tuneable Cr:ZnSe laser performance using a Si prism. The short wavelength mirror set (black squares) used a pump mirror with reflectance > 99.9 % for a range of 2000-2500 nm and an output coupler with reflectance 80 ± 5 % for a range of 1700-2700 nm. The long wavelength mirror set (red dots) used a pump mirror with reflectance > 99.6 % for a range of 2500-3000 nm and an output coupler with reflectance 89 ± 1 % for a range of 2800-3070 nm.

The extended cavity demonstrated continuous lasing over 2080-2883 nm with an output power greater than 15 mW over the whole wavelength range. The maximum output power 134 mW was measured at a wavelength of 2615 nm. An improvement in tuning range performance was observed using the Si prism tuning element which achieved an additional 101 nm of tuneability over the results obtained using the blazed grating. The output power was slightly higher ≈ 10 %. This was much lower than initially expected. This arises from the prism only being low loss if the laser is linearly polarised. The output of the waveguide was found to be randomly polarised. Thus the loss at the prism will be 50%, which is larger than it will be for a single pass for the grating. When taking into account the double pass of the grating and a silver mirror, the overall loss of the prism system is lower at longer wavelengths hence, the extended tuning range.

The wavelength spectra of the laser at different tuning angles was characterised with the Zolix Omni-λ 300 monochromator. Figure 3.15 shows different spectra taken across the full tuning range. A typical spectrum for the short wavelength mirror set is shown in

Figure 3.16. A Gaussian function was used to fit the data. This was used to determine the central wavelength of the spectra and the FWHM of the emission. Figure 3.17 is a typical spectrum for the long wavelength mirror set. Spectra taken across the tuning range were fitted with a Gaussian function. The centre wavelength and FWHM are summarised in Table 6.

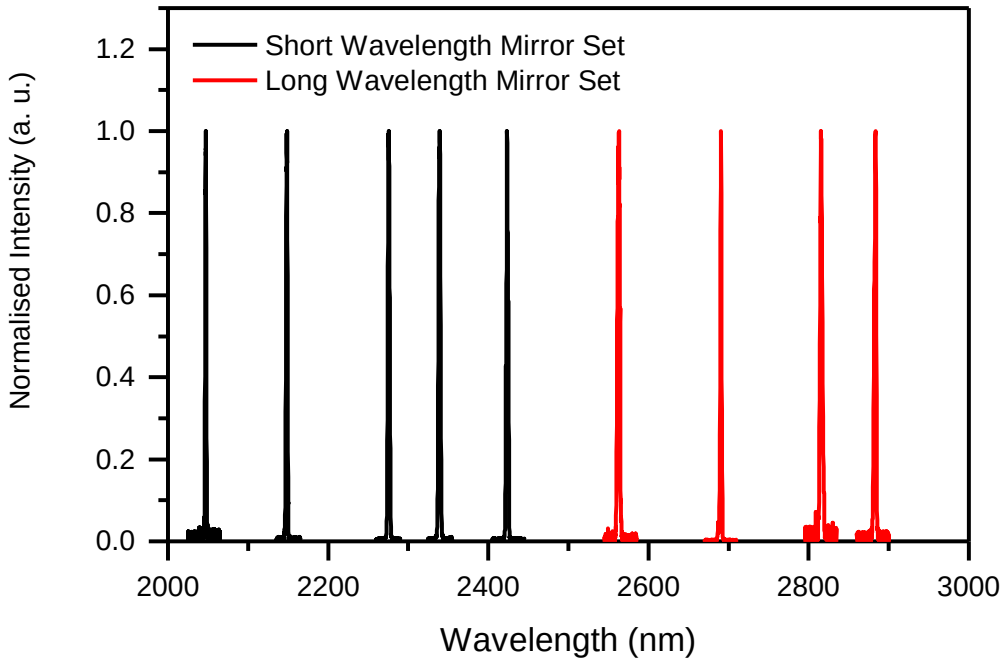

Figure 3.15. Normalised intensity spectrum of Si prism wavelength tuned Cr:ZnSe waveguide. Measurements taken with Zolix Omni-λ 300 monochromator. Spectra taken with a short mirror set are black. Spectra taken with a long mirror set are red.

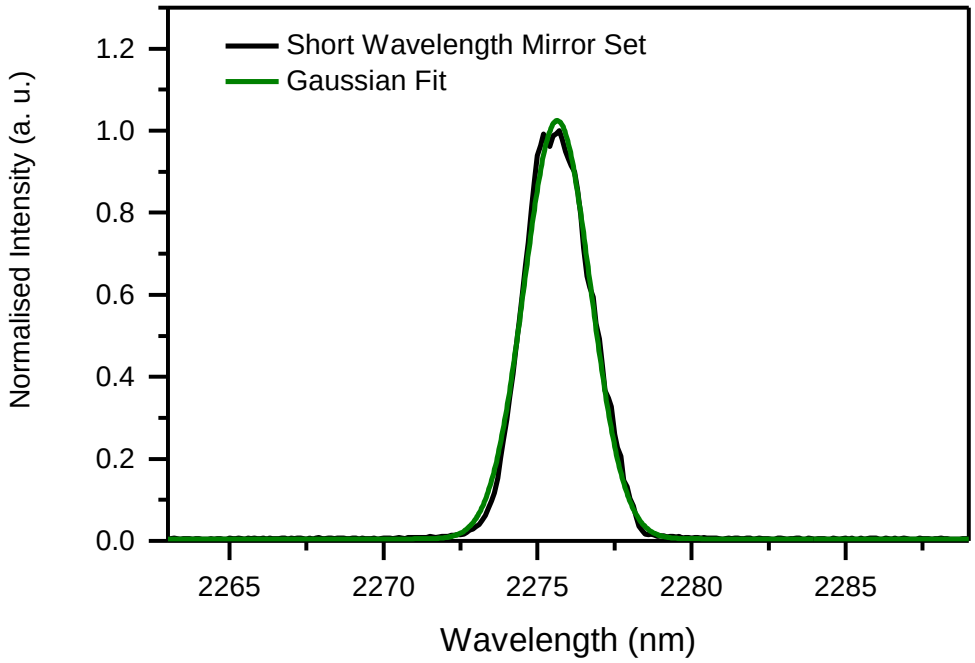

Figure 3.16. Typical spectra of Si prism tuned Cr:ZnSe waveguide laser with short wavelength mirror set. Green line is a Gaussian fit to the data. From the fit the peak was found to be centred at 2275.7 nm with a FWHM of 2.6 nm.

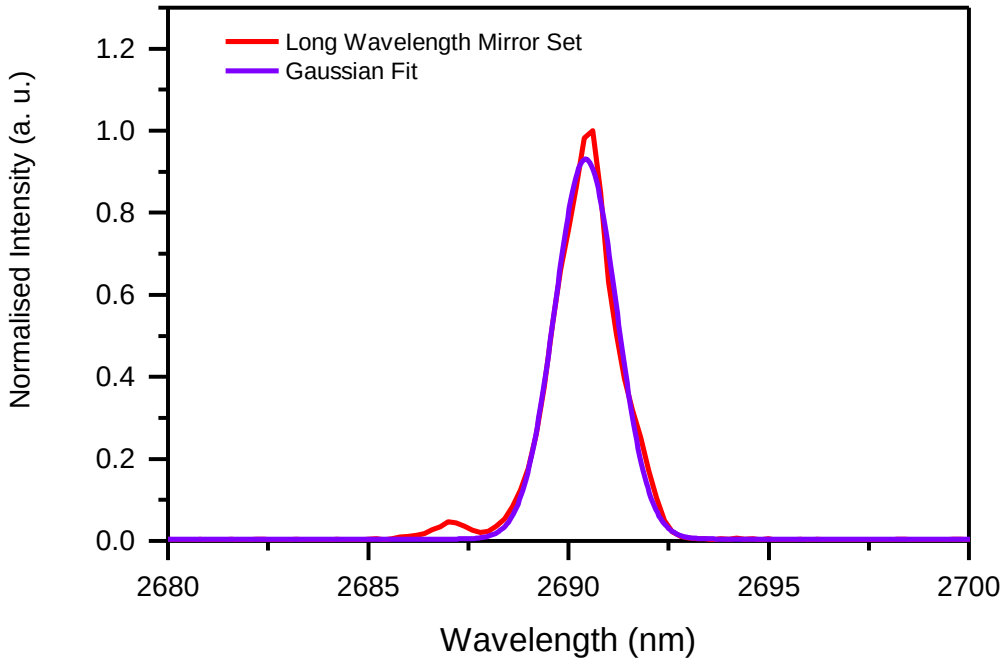

Figure 3.17. Typical spectra of Si prism tuned Cr:ZnSe waveguide laser with long wavelength mirror set. Purple line is a Gaussian fit to the data. From the fit the peak was found to be centred at 2690.6 nm with a FWHM of 1.7 nm.

Central Wavelength (nm)	Full width half maxima (nm)	Mirror set
2047.1	1.7	Short wavelength
2080.3	2.5	
2148.7	2.2	
2212.8	2.3	
2275.7	2.6	
2339.2	2.8	
2423.3	2.8	
2494.3	2.5	
2615.4	1.2	Long wavelength
2690.6	1.7	
2753.2	0.9	
2815.2	3.0	
2883.4	3.2	
2905.0	1.5	

Table 6. Summary of spectra and full width half maximum for prism tuned Cr:ZnSe waveguide laser. Measurements take with Zolix Omni-λ 300 monochromator. Spectra fitted with Gaussian profile.

The minimum linewidth measured was 0.9 nm at 2753.2 nm. This measurement was taken with the monochromator that has a resolution of 0.4 nm. The resolution of the monochromator is sufficient if there is no underling structure in the spectra. An OSA would be more suitable for this work, but we did not have access to one at the time of this investigation. Comparing the linewidth of the prism with the grating, there is a 20 fold increase in linewidth. This linewidth broadening for the prism tuning element was expected from the modelling discussed earlier in Section 3.2.3. However, the modelling also expected the linewidth to increase with wavelength, which is not found in this experiment. The modelling of the acceptance band width of a Si prism tuning element is plotted over the experimentally measured FWHM in Figure 3.18. Details of this model can be found in Section 3.2. The beam radius incident on the prism was set to 2 mm to match that of the experiment. The experimental linewidth at the short wavelength end of the tuning is closest to the model. However at longer wavelengths this is not the case. At this point, it should be remembered that the acceptance bandwidth is the low loss wavelength range of the cavity and not the expected bandwidth of the lasers. For example, a free running homogeniously broadened laser can have an exceptionably narrow bandwidth, without the need for any additional wavelength control. Free running polycrystalline Cr:ZnSe bulk lasers have demonstrated bandwidths of around 50 nm consisting of numerous narrow spikes [15]. Hence the narrower than expected linewidth is attributed to selecting a single narrow spike.

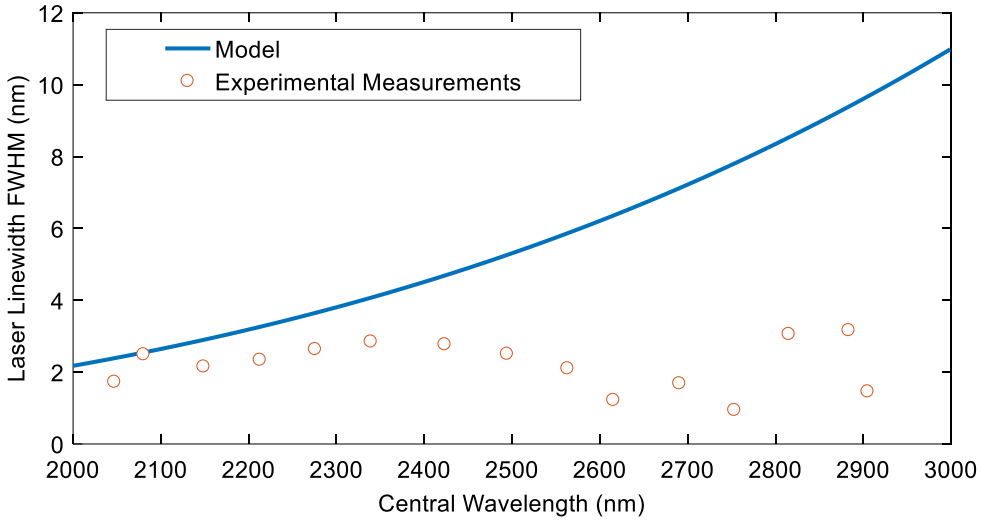

Figure 3.18. Red dots are experimental measurements of FWHM linewidth of Si prism tuned Cr:ZnSe waveguide laser. Blue line is the acceptance bandwidth of a Si prism tuned cavity expected form the model. The beam radius was to 2 μm for the model. Sellmeier coefficients used for calculating dn/dλ are detailed in Table 3.

Taking a step back from the extended cavity tuning experiments and examining free running lasers in Cr^{2+} polycrystalline ZnSe, there is a discrepancy between the bulk and waveguide laser linewidth. The free running depressed cladding waveguide demonstrated by MacDonald et al. [58] had a linewidth of 1.6 nm compared with 50 nm linewidth measured in a bulk free running Cr:ZnSe laser by Berry et al. [15]. From this it is clear the waveguide itself has an impact on the linewidth of the lasers. At the time of this work, the reason for the linewidth discrepancy between bulk and waveguide was not known. A recent paper by Stites et al. [116] has found hot isostatic pressing (HIP) of the Cr:ZnSe results in free running laser operation with narrow linewidth. In this paper, hot isostatic pressing (HIP) of transition metal ions into ZnSe and ZnS host is demonstrated. This a different process from the post growth diffusion methods that have been commercialised and hence most widely studied [15-17], including all work covered in this thesis. It was found that the forced diffusion of ions at high temperature and pressured by HIP treatment reduced the spectral bandwidth of free running Cr:ZnSe laser by orders of magnitude [116]. The reason for line narrowing in the HIP treated samples is attributed to the fact that the process increases the grain size of ZnSe [117] and removes crystal defects [118]. From the narrowed linewidth observed in single mode Cr:ZnSe waveguide lasers, it is thought a similar effect is happening to the host from the ULI process. This involves similar pressures and temperature to those of HIP treatment, thus we believe this remove defects in the host Cr:ZnSe during the inscription process [119].

Extending the cavity of the waveguide laser means there is a 32 cm section of the laser cavity that is free space propagation through atmosphere. Thus atmospheric absorption from water vapour must be considered when operating in the water absorption spectral region 2400-2900 μm. Sorkin at al. [17] measured the atmosphere absorption for a round trip bulk resonator length of 120 cm. The atmospheric transmission and bulk Cr:ZnSe output power vs. wavelength measured by Sorkin is given in Figure 3.19. From this figure, it is clear that there are very large intra cavity losses at the narrow water absorption lines. Sorkin found that the laser would only operate in between absorption lines, and that some of the spectra would have a double peak under strong pumping. From this, it is possible the linewidth of the waveguide laser is being narrowed by adjacent water absorption lines. The solution to this problem would be to encapsulate the laser in a box and purge with dry air, but this adds complexity to the system and hence was not investigated.

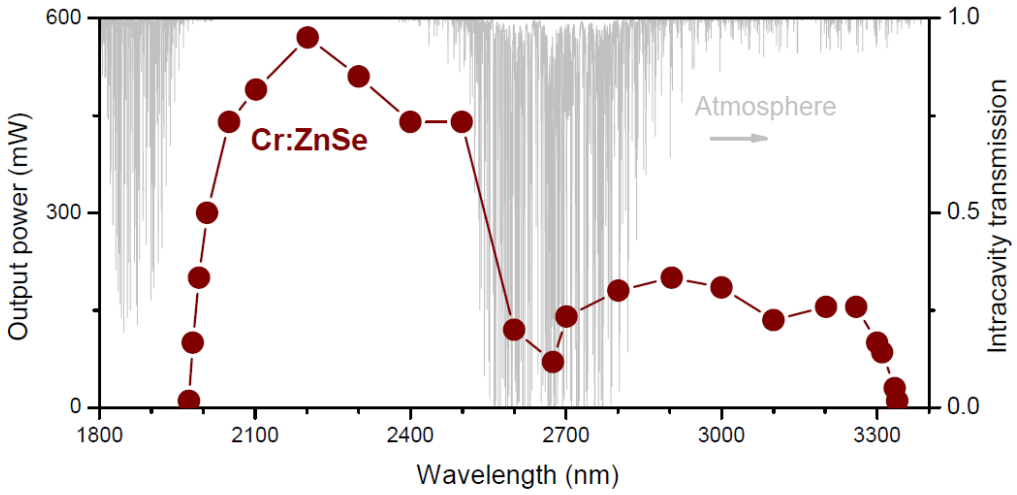

Figure 3.19. Bulk Cr:ZnSe lasers tuned with CaF_2 prism. Red dots are output powers at a given wavelength for 5 W of pump incident on the sample. Grey line represents the intra cavity transmission of a resonator with a round trip length of 120 cm with the room at 40 % r.h.. The absorption is from water vapour. This graph has been reproduced from Sorkin et al. [17].

The narrower than expected linewidth of the Si prism tuning arises form a combination of the acceptance bandwidth of the prisms, the free running bandwidth of a polycrystalline Cr:ZnSe depressed cladding waveguide and water absorption lines. This makes modelling of the linewidth of the laser challenging. The prisms tuning has facilitated an extra 100 nm of lasing bandwidth compared with an identical system using a grating. The efficiency of

the lasers and tuning range could be further improved by developing polarisation maintaining waveguides to minimise the loss at the Brewster cut prism. This could be implemented by inscribing large damage lines to the left and right of the waveguide, which would create a waveguide similar to polarisation maintaining fibre designs. Furthermore, passive characterisation of the waveguide losses at longer wavelengths should be investigated. This would require a tuneable laser source in the 2-3 μm range.

3.6. Conclusion

Depressed cladding waveguides inscribed in Cr:ZnSe by ULI were investigated for broadband tuneable lasers. Wavelength tuning of the waveguide laser was achieved with extended cavities. For narrow linewidth, a blazed grating was added to the cavity in the Littman-Metcalf configuration. This resulted in a continually tuneable bandwidth of 700 nm, 36.4 THz, from 2077-2770 nm with greater than 15 mW of output power over the range. This result is the widest tuning range demonstrated by any waveguide laser in the Mid-IR, ULI fabricated or by any other method, to the best of the authors' knowledge. The linewidth of the laser was measured to be as low as 53 pm, limited by the detection equipment. This marks a step forward for probing of molecular transitions in the Mid-IR transmission window in non-lab environments. This work was published as a letter in the IEEE Journal of selected topics in Quantum Electronics [105].

Seven hundred nanometres of wavelength tuning is an impressive result for any laser but bulk Cr:ZnSe lasers have been shown to lase from 1973 - 3349 nm [17]. Numerical modelling was investigated to find out what is limiting the waveguide lasers tuning range. The model found that the tuning range was being limited at the long wavelength end of the emission from grating loss. From this it was proposed to investigate a prism for wavelength tuning as there is not a strong wavelength dependent loss with this tuning element.

The application of a Brewster cut prism resulted in a tuneable bandwidth of 803 nm over the range of 2080 - 2883 nm with more than 15 mW of output power. As expected from the modelling, the linewidth is broader than the grating extended cavity. A minimum linewidth of 0.9 nm was centred at 2753.2 nm. The maximum average power of the laser was 134 mW at 2615 nm. Further tuning of the laser at longer wavelengths is limited by: waveguide loss at increasing wavelengths, polarisation induced loss at the prism and atmospheric absorption.

4. Modelocking of Cr:ZnSe waveguide laser

4.1. Introduction

Ultrashort pulsed laser sources in the Mid-IR (2 – 5 μm) are of interest for their many applications such as LIDAR, supercontinuum generation and material processing. For pulsed sources in this range, modelocked solid state lasers combined with OPOs are commonly used to generate Mid-IR pulses with very wide wavelength tuning ranges. However, these systems are complex because of their relatively large size and numerous free space optics, resulting in issues making the laser sources vibrationally insensitive [120]. Electrically excited QCLs have the advantage of being optically the most simplistic Mid-IR laser sources, but are not suitable for modelocking [120, 121].

Transition metal doped II-VI semiconductor lasers, first demonstrated by DeLoach et al. [12], offer direct generation of widely tuneable light in the Mid-IR due to their vibrational broadened gain media. Of these materials, Cr:ZnSe has the useful properties of a non-overlapping absorption and emission cross-sections with a CW room temperature operation. Bulk Cr:ZnSe laser has been demonstrated to be continuously tuneable from 1973 nm to 3339 nm. If all of this bandwidth is used to produce a modelocked pulse a $sech^2$ pulse width of 6 fs would be formed. To date, Cr:ZnSe modelocked lasers have not demonstrated pulses that lock the full bandwidth, however, an impressive 80 fs was demonstrated with a semiconductor saturable absorber mirror (SESAM) [122]. Cr:ZnSe has been modelocked with a wide variety of passive and active methods, detailed in Table 7, making it a well-developed modelocked laser. However, these are all bulk lasers, there has be no demonstration of modelocking in a Cr:ZnSe waveguide.

Modelocked Bulk Cr:ZnSe Lasers			
Modelocking mechanism	Pulse width	Pulse repetition frequency	References
AOM	4.4 ps	81 MHz	[123]
Graphene saturable absorber	116 fs	99 MHz	[124]
Kerr lens modelocking	92 fs	95 MHz	[125]

SESAM	80 fs	180 MHz	[122]

Table 7. Modelocked Cr:ZnSe bulk lasers with different modelocking configurations

Cr:ZnSe waveguide sources have facilitated the development of compact, environmentally robust Mid-IR lasers. Single crystal fibre has been fabricated in ZnSe, but there has not yet been any laser demonstration of a doped sample. Slab waveguides have been fabricated using PLD, but the output powers have been limited to sub mW [126]. One method of achieving a monolithic laser system while still retaining the advantage of bulk Cr:ZnSe is to fabricate a waveguide in the material using ULI.

Fabrication of waveguides using ULI in polycrystalline Cr:ZnSe was first demonstrated by Macdonald et al. [57]. Later work using ULI resulted in depressed cladding waveguides with a slope efficiency of 45% [58]. The tuning range with the addition of a Si prism was found to be 2080 - 2883 nm, as discussed in the previous chapter. If this full bandwidth can be modelocked, there is potential for demonstrating a compressed pulse of 9 fs. The depressed cladding waveguides in ZnSe have been shown to have low propagation losses of <1 dB/cm in the Mid-IR and have also been shown to propagate light out to 4122 nm [51]. From these demonstrations, it is clear that Cr:ZnSe depressed cladding waveguides have suitably low losses over the large range needed to take full advantage of the Cr:ZnSe emission bandwidth while providing the advantage of a monolithic laser cavity.

It is challenging to fabricate a conventional bulk modelocked laser with a pulse repetition frequency (PRF) greater than 1 GHz because the PRF is inversely linked to the cavity length [59]. The cavity length of a waveguide laser can effortlessly be reduced to that of the gain medium by having two plane mirrors butt coupled to the end facets of the waveguides. Examples of modelocked waveguide laser with PRF > 1 GHz are Nd:YAG [85], Yb:Glass [127] and Tm:YAG [128] with PRF of 11 GHz, 15 GHz and 7.8 GHz respectively.

This chapter details the theory of modelocked lasers and the measurement of ultrashort femtosecond pulses. The first demonstration of a modelocked Cr:ZnSe waveguide laser will be presented. Furthermore, the power scaling and increases of the PRF to over 1 GHz are investigated.

4.2. Background Theory of Modelocked Lasers

Modelocking is a powerful technique to produce pulses of femtosecond to picosecond with timescales. Modelocked lasers are split into two categories: active and passive. Both work by the same principle of having a loss mechanism in the cavity that can vary with time. A diagram of a modelocked laser resonator is given in Figure 4.1. The key difference between a modelocked laser's cavity and a CW laser is that the loss element is not constant in the modelocked laser, as shown in Figure 4.1:

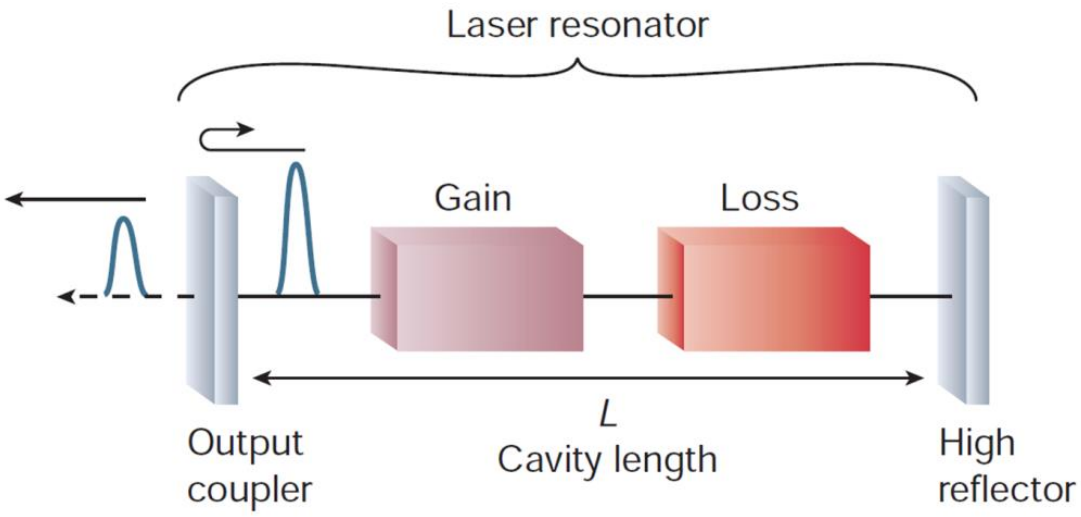

Figure 4.1. Model cavity design showing the optical elements needed for a modelocked laser cavity. This has been reproduced from Keller [59].

Active modelocking uses an external signal to modulate the loss of the cavity; this can be achieved with an acoustic optic modulator (AOM). The loss of the cavity is modulated as a sinusoidal function in time and the cavity is set up in a way that the saturated gain is only larger than the signal loss for a small section of the sine waves at its minima, as shown in Figure 4.2:

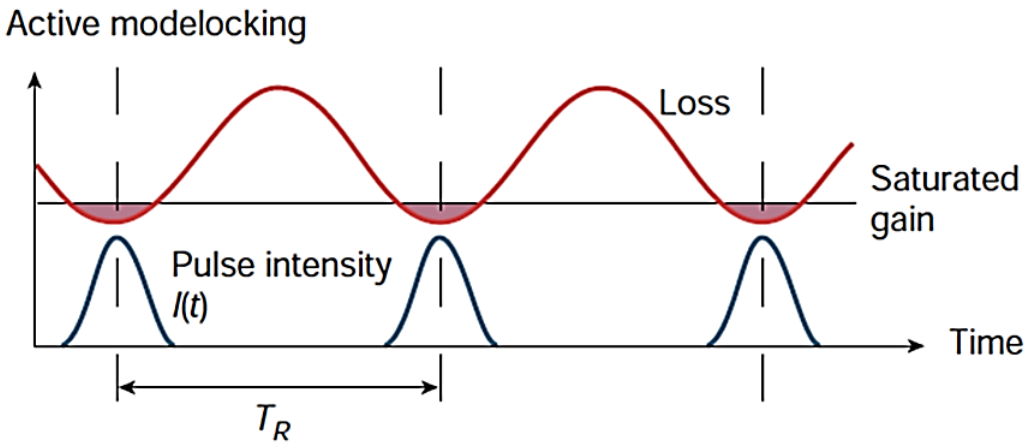

Figure 4.2. Schematic of loss modulation in an active modelocked laser. This has been reproduced from Keller [59].

By implanting this loss modulation, the lasers can only reach threshold when the AOM is low loss. This causes the laser to lase in a pulsed manner. If the AOM is operated at the same frequency as the cavity frequency, a laser can be formed with a continuous train of modelocked pulses at a stable repetition rate. The cavity round trip time (T_R), and thus laser repetition rate, for a single pulse circulating the cavity is linked to the cavity length (L), given by Equation 15:

$$T_R = \frac{2L}{v_g}$$

Equation 15

where v_g is the group velocity. Typical modelocked lasers have a cavity length of around 1.5 m, resulting in a repetition rate of 100 MHz. One key advantage of active modelocking over passive methods is the electronic signal controlling the modulator can be used as a trigger for characterisation equipment. However, the pulse width of active modelocked lasers are often limited to the picosecond region [59].

Passive modelocking does not use an external control signal. This allows for a simplification of the laser system and the ability to work at higher repetition rates, faster than most electronics. For passive modelocking, a saturable absorber (SA) is placed in the cavity. This is used to create a self-modulating amplitude of the light in the cavity. This introduces loss to the cavity which is large for small signals but relatively small at high irradiance. This creates a situation in which the low intensity wings of a pulse are supressed, while the peak of the pulse propagates with low loss. The peak of the pulse

experiences more gain than loss for each round trip; while the SA supresses small signals. This system starts from a small noise fluctuation in the CW laser output. A small single noise spike is all that is needed to saturate the SA and thus start mode-locked operation. The spike will grow with each round trip, saturating the SA by a larger extent each time until the laser reaches steady state operation, as shown in Figure 4.3:

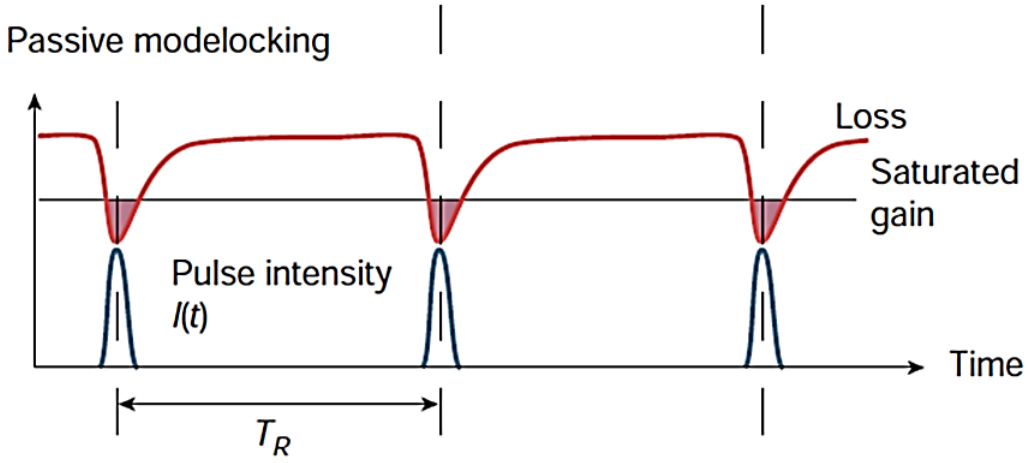

Figure 4.3. Schematic of passive modelocking showing the interaction of the loss induced by an SA and a circulating laser pulse. This has been reproduced from Keller [59].

Once the laser has reached a steady state, the pulses leaving the laser will be separated in time by a constant value with the same amplitude creating a comb like structure. Typically, shorter pulses can be achieved with a passive system because the recovery time of the SESAM based SA is much faster than the current method of actively modulating the loss mechanism. However, by careful consideration of the cavities group delay dispersion and self-phase modulation, soliton modelocking can be implemented, resulting in the potential for demonstrating pulse widths shorter than the loss modulation [129].

In frequency space, we have a phase locked frequency comb as shown in Figure 4.4. Modelocking is a well-known and developed method of producing ultrashort laser pulses. A detailed mathematical description of active and passive modelocking can be found by Haus et al. [130].

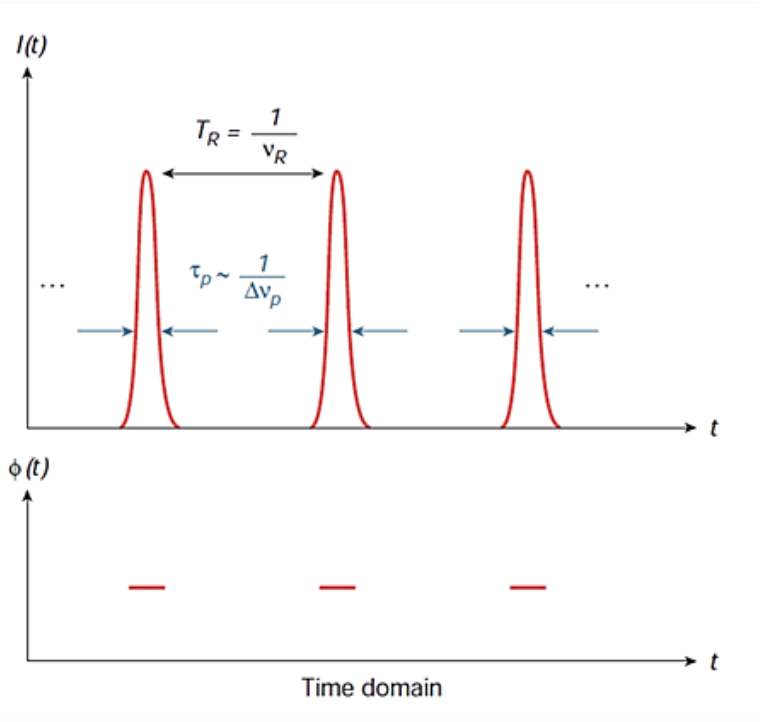

Figure 4.4. Schematic of modelocked laser in the time domain, where I is the intensity of the laser pulse and φ is the phase. This has been reproduced from Keller et al. [59].

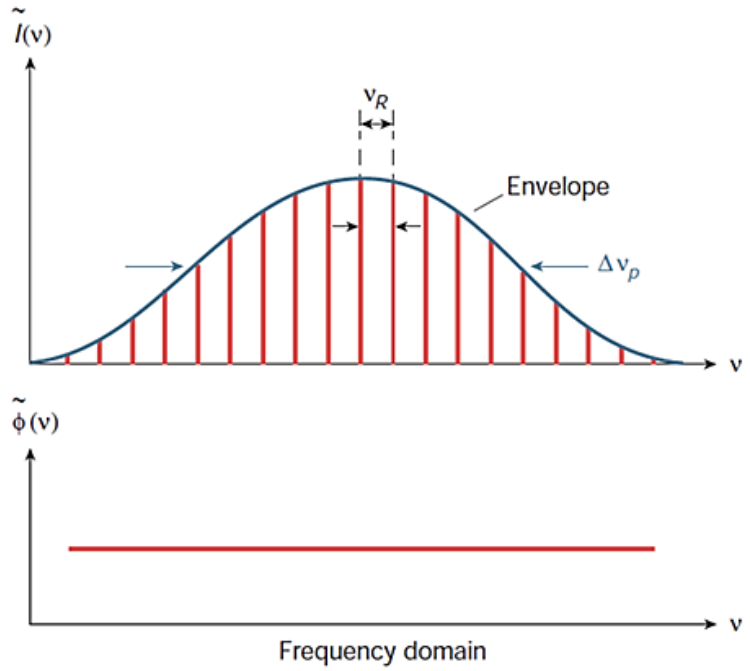

Figure 4.5 Schematic of modelocked laser operation in frequency space, note the constant phase. This has been reproduced from Keller et al. [59].

The fundamentals of modelocking are well understood, however, implementation into a working laser system presents a number of challenges. The initial report of modelocked laser by DeMaria et al. [131] did not show the constant intensity pulse train in time that

was discussed above. Indeed, the intensity of the pulses modulated over time with a repetition rate much slower than the repetition rate of the laser, and this is known as Q-switched modelocking (QML). QML is a dynamic instability resting from an undamped relaxation oscillations. In QML, the pulse circulating the cavity builds up in intensity then depletes in a repeating cycle. The threshold for stable modelocked pulse trains is given by the criteria in Equation 16:

$$E_P^2 > E_{sat,g} E_{sat,a} \Delta R$$

Equation 16

where ΔR is the is the modulation depth of the SA and E_P is the intra cavity pulse energy given by Equation 17:

$$E_P = \frac{P_{out}}{f_{rep} \times T_{OC}}$$

Equation 17

P_{out} is the output power of the laser, f_{rep} repetition frequency of the laser and T_{oc} is the transmission of the output coupler at the signal wavelength.

The saturation energy of the gain medium $E_{sat,g}$ is given by Equation 18:

$$E_{sat,g} = F_{sat,g} \times A$$

Equation 18

where A is the cross-sectional area of the signal in the gain medium, in the case of a waveguide. this is calculated from the mode field diameter (MFD) at the signal wavelength. The saturation fluence of the gain media $F_{sat,g}$ can be calculated using Equation 19:

$$F_{sat,g} = \frac{E_{photon}}{N(\sigma_e + \sigma_a)}$$

Equation 19

where E_{photon} is the energy of a single photon at the signal wavelength. N is the number of passes through the gain media per round trip of the cavity, normally $N=2$. The emission cross-section and absorption cross-section at the signal wavelength are given by σ_e and σ_a respectively.

The saturation energy of the saturable absorber $E_{sat,a}$ in Equation 16 can be calculated using Equation 20:

$$E_{sat,a} = F_{sat,a} \times A$$

Equation 20

where $F_{sat,a}$ is the saturation fluence of the SA. This is a fixed design parameter of the SA. However, the surface area of the beam waist incident on the SA, A_{sa}, can easily be varied by changing the focusing onto the SA. ΔR is the modulation depth of the SA.

Mitigation of QML instabilities are a challenge with GHz repetition rate lasers due to their lower pulse energy. For these lasers careful consideration of the SA parameters is needed [90, 132].

The SESAM [59] is one widely implemented SA. SESAMs have a low saturation fluence, hence they reduce the intra cavity pulse energy needed to supress QML instabilities. SESAMs have long been the industry standard for fast saturable absorbers, this is in part due to the use of pre-existing semiconductor fabrication techniques creating low defect material with control of the SAs properties [59, 133]. SESAMs have been used to demonstrate sub 100 fs pulses [134]. SESAMs have been designed to operate over a wide range of wavelengths covering the near-IR to IR spectral part of the EM spectrum, each with an operating bandwidth of ≈ 100 nm [59]. For a sub 100 fs pulse laser access to the full bandwidth of the laser is preferable, thus a bandwidth limitation from the SA is not desired. For materials with a strong nonlinearities, Kerr lens modelocking using the Kerr effect, discussed in Section 2.4, can induce an intensity dependent loss mechanism when a hard or soft aperture is placed in the cavity [135]. This has been an effective method for modelocking bulk Ti-Sapphire and Cr:ZnSe lasers, but has not been demonstrated in guided wave mode geometry [106].

One alternative SA to the SESAM is graphene which has been widely used for passive modelocking of lasers over a broad spectral range, ranging from the NIR to Mid-IR [133]. The key property of graphene is its wavelength independent features of absorption. These are possible because of graphene's zero band gap. It's also a highly adaptable material for modelocking different laser materials. In solid state bulk and waveguide lasers, graphene is predominantly used to coat resonator mirrors or output couplers resulting in a graphene saturable absorber mirror (GSAM). This is possible because of developments

in producing high quality few layer graphene using chemical vapour deposition [136]. There is currently a demand for environmentally robust fs pulsed lasers in the 2 – 2.5 μm Mid-IR range of the spectrum [106]. GSAMs are a compelling option for the 2 – 2.5 μm range because SESAMs availability at these wavelengths is limited [120]. However, issues with a low damage threshold at high reputation rates and high non-saturable losses limit GSAMs effectiveness in power scaling modelocked laser systems [137-139].

The background of active and passive modelocking has been discussed. For high repetition rate waveguide lasers, passive modelocking is necessary due to limitations in the electronic switching speed of active modelocked methods. Passive modelocking of Cr:ZnSe waveguide lasers will be investigated using a SESAM.

4.3. Measurement of Ultrafast Laser Pulses

Modelocking of lasers facilitates production of pulses to a timescale much short than can be achieved with electronics. However, it also means the pulses cannot be directly measured with electronic based detectors. For example, the fastest Mid-IR detectors commercially available, the Vigo Systems PC-10.6, has a rise time of 1 ns. Faster detectors are available in the visible to NIR but are still limited to the rise times of around 5 ps. Thus direct measurement of femtosecond pulses is not possible. There are many indirect methods that have been developed to overcome this limitation, such as autocorrelation and more complicated systems such as Frequency-Resolved Optical Gating (FROG) [140]. FROG records intensity and phase information which allows for calculation of pulse width without making assumptions of the original pulse shape. This makes the technique more robust than autocorrelation. However, the experiment apparatus requires is more complex and there is limited availability of linear arrays suitable for characterising Mid-IR pulses.

Autocorrelation is a convenient method for measuring the width of ultrashort laser pulses. This method uses the pulse to measure itself. An interferometric autocorrelator combines a Michaelson interferometer with a translation stage, nonlinear crystal and detector, as shown in Figure 4.6:

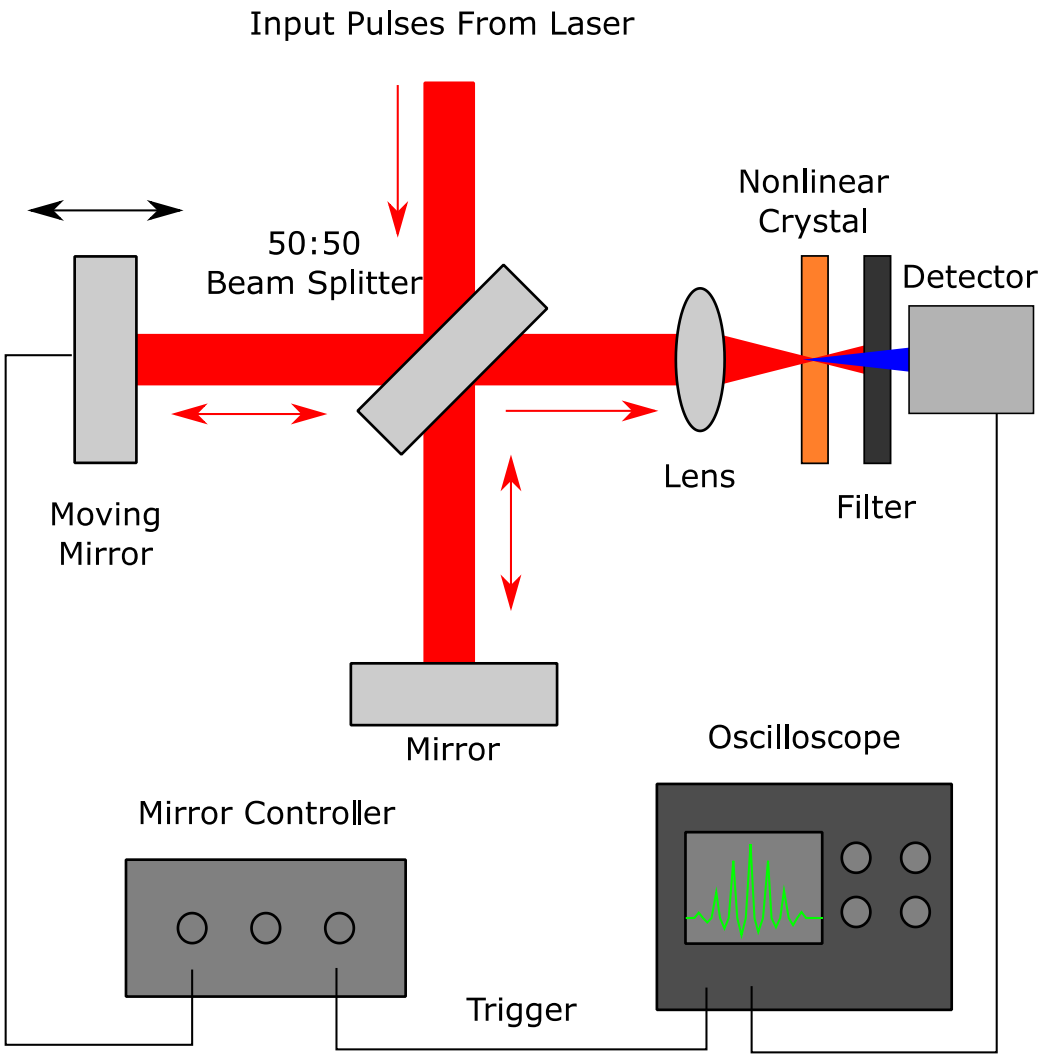

Figure 4.6. Schematic of interferometric autocorrelator experimental setup, with nonlinear crystal.

This system splits the incoming pulse in two at the beam splitter. The separate pulses then travel along the two arms of the interferometer. The pulses are recombined in space and time at the nonlinear crystal. A lens is used to focus the beam on to the nonlinear crystal which improves the two photon generation efficiency. The non-converted residue laser light is absorbed by a filter. The frequency doubled signal is incident on a slow large area detector. The pulse width is found by changing the path length of the two beam lines. This changes the pulse overlap in the nonlinear crystal. This is detected by a change in signal intensity at the detector. The signal change is linked to the mirror position by an oscilloscope which is triggered to the leading edge of the square wave used to modulate

the mirror position. An example of an interferometric autocorrelation of a modelocked Ti:Sapphire laser is given in Figure 4.7.

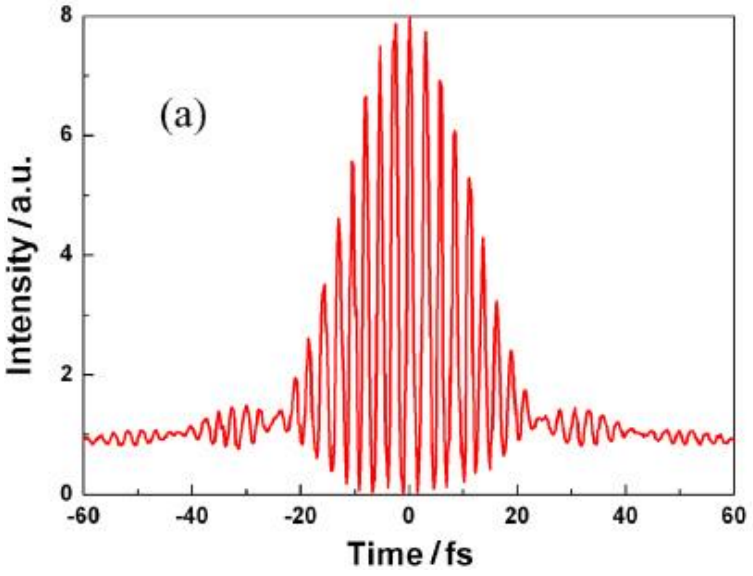

Figure 4.7. Interferometric autocorrelation of modelocked Ti- Sapphire laser. This graph has been reproduced from Yuqiang et al.[141].

Note from the figure there is an underlying fast oscillation inside the pulse envelope. The period of this oscillation is half that of the laser's central wavelength. This can be used to calibrate the movement of the mirror with the time base of the oscilloscope. The peak of this signal is formed when the two pulses overlap in time, thus causing constructive interference. This leads to a doubling of the amplitude at the peak of the signal compared with a single pulse, or four times the intensity. After the frequency doubling crystal, this results in a 8-fold increase in intensity compared with a single non overlapping pulse. From this an important check for a valid autocorrelation is that the base to peak of the signal at the oscilloscope must be a 1:8 ratio, as demonstrated in Figure 4.7.

The autocorrelation set-up shown in Figure 4.6 can be further simplified by using direct two photon absorption in the detector. This method was first demonstrated by Reid et al. [142]. It has the advantage of a reduced number of optical components and, in particular, removes the requirement for a nonlinear crystal.

4.4. Modelocking of Cr:ZnSe Waveguide Laser

Modelocking of polycrystalline Cr:ZnSe waveguide lasers was investigated. This laser was passively modelocked with a SESAM. For this initial demonstration of modelocking, an extended waveguide cavity was implemented. This reduces the PRF of the laser,

increasing the pulse energy for a given average power, thus making detection of the pulse more accessible.

The Cr:ZnSe sample used in the work had dimensions of 8.5 × 6.5 × 2.1 mm with a dopant concentration of 8.5×10^{18} cm^{-3}. The depressed cladding waveguide was fabricated using ULI. The single mode waveguide used in this investigation had a diameter of 80 µm and was inscribed with the parameters given in Table 2. The end facets of the waveguides were AR coated from 1.9 to 3 µm after inscription. The 80 µm waveguide was has been characterised in free running operation [58] and tuneable operation detailed in Chapter 3 of this thesis. The propagation losses were found to be 0.7 $dBcm^{-1}$ at the signal wavelength. These properties make the waveguide an ideal candidate for modelocked laser investigation because of the low propagation loss over a wide spectral band.

The pump source used for the laser experiments was a randomly polarised 1.3 W CW single mode Tm:fibre laser (AdValue Photonics) operating at 1920 nm. For modelocked operation the Cr:ZnSe, waveguides were inserted into an extended laser cavity as shown in Figure 4.8:

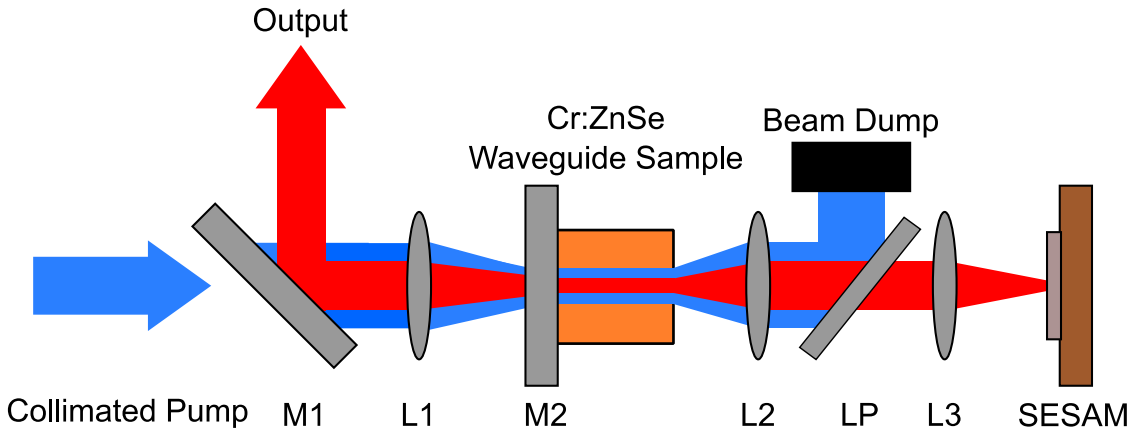

Figure 4.8. Schematic of modelocked Cr:ZnSe waveguide laser. M1 is a 45º AR coated at 1.9 µm and HR coated at 2.3 - 3 µm dichroic mirror. M2 is a dichroic mirror with AR at 1.9 µm and 98 % reflecting at 2 - 3µm coatings. L1, L2 and L3 are 50 mm plano-convex lenses AR coated from 1.65 to 3.0 µm. LP is a 2000 nm longpass filter.

An AR coated 50 mm CaF_2 lens was used to focus the pump light into the waveguide and collimate the signal output of the waveguide. A 98% reflective (2 - 3 µm) output coupler was butt coupled to the end facet of the Cr:ZnSe waveguide. The resonator length of the laser cavity was extended to 50 cm by two intra-cavity AR coated 50 mm CaF_2 lenses. The lens L2 was used to collimate the output of the waveguide and lens L3 was used to

focus onto the SESAM. The SESAM is used to passively modelocked the Cr:ZnSe waveguide laser and is also the end cavity mirror. The specification of the SESAM given by the manufacturer (Del Mar Photonics SAM-2400-1-25) is a saturation fluence, relaxation time constant and modulation depth of 90 μJ/cm^2, 500 fs and 0.6% respectively. The SESAM was mounted on a passively cooled copper block of diameter 25.4 mm and thickness 5 mm. A 45° highly reflective dichroic mirror at the signal wavelength was used to separate the output of the laser from the pump beam. A 2000 nm longpass filter was inserted in between lenses L2 and L3 to remove unabsorbed pump light. This removed issues with the pump interacting with the SA properties of the SESAM. In addition, it prevented optical damage to the surface of the SESAM by the pump source.

The initial investigation used a two mirror butt coupled laser cavity, length 6.5 cm. However, no modulation was observed, and the laser was found to operate in pure CW mode. The cavity of the laser was then extended to a length of 34.5 cm, with the cavity configuration shown in Figure 4.8. The laser was found to be modelocked with a PRF of 580 MHz, but there was also an overlapping Q-switched envelope with a frequency of 2.5 MHz at 1.3 W of pump power. The cavity of the laser was extended to 50 cm to increase the pulse energy. The increase in pulse energy supresses the Q-switched instability as expected from Equation 16. In this configuration, the laser was found to reach laser threshold with 300 mW of incident pump power at the waveguide end facet. Modelocked operation was self-starting for pump powers greater than 800 mW. Stable self-starting CW modelocking was observed from 800 mW to the limit of the available pump power 1300 mW. CW modelocking was confirmed using a CMT detector (VIGO system PVM−10.6) with a 1 ns time constant and a 13.2 GHz RF spectrum analyser (Agilent E4405B). From laser threshold to 800 mW, pure CW operation was observed with no transition into Q-switched modelocked operation observed. The RF spectrum of the laser operating under 1.3 W of pump power is shown over a long and short frequency band in Figure 4.9 and Figure 4.10 respectively.

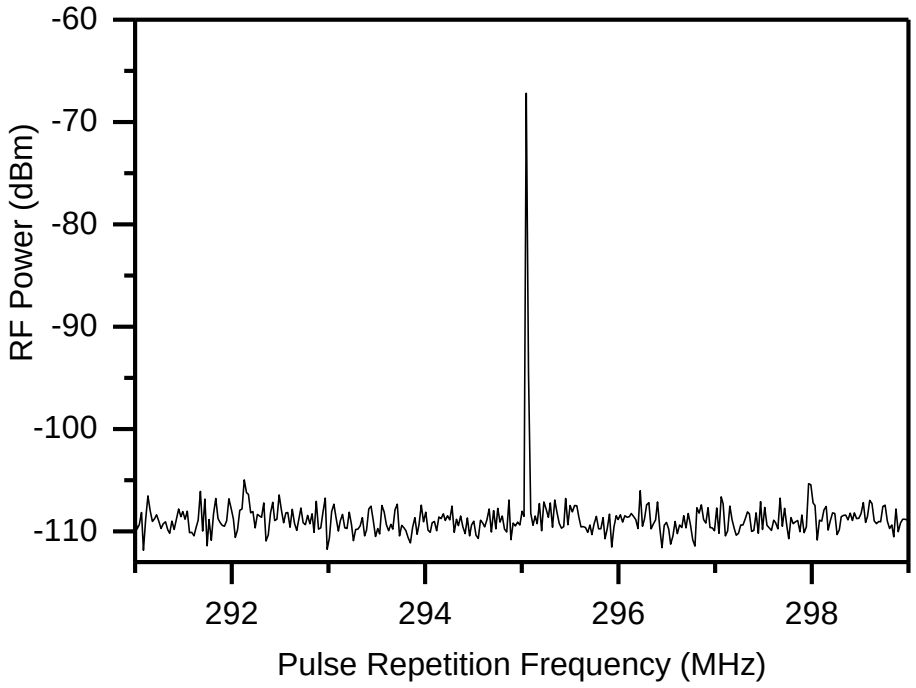

Figure 4.9. RF spectrum of CW modelocked Cr:ZnSe waveguide laser operating with 1.3 W of pump power. The graph has a span of 9 MHz and the measurement was taken with a resolution bandwidth of 1 kHz.

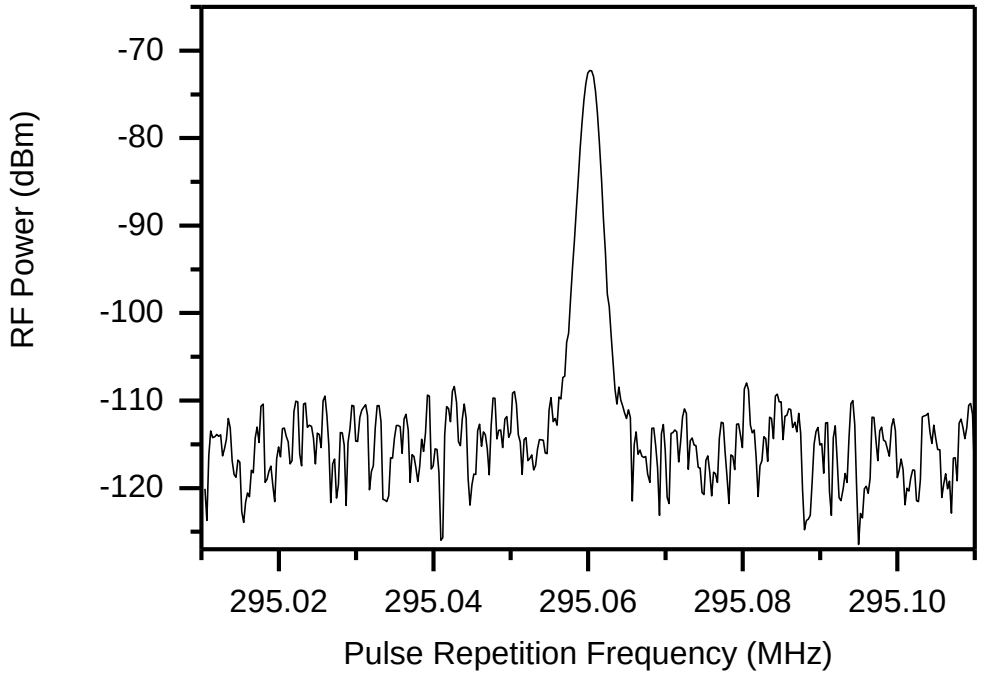

Figure 4.10. RF spectrum of CW modelocked Cr:ZnSe waveguide laser operating with 1.3 W of pump power. The graph has a span of 100 kHz and the measurement was taken with a resolution bandwidth of 1 kHz.

The maximum average power of the laser was measured to be 5 mW with a pump power of 1.3 W. The slope efficiency of the laser in the CW modelocked regime was calculated from the linear fit to be 0.63 %. The laser's output power was measured for a range of pump powers shown in Figure 4.11.

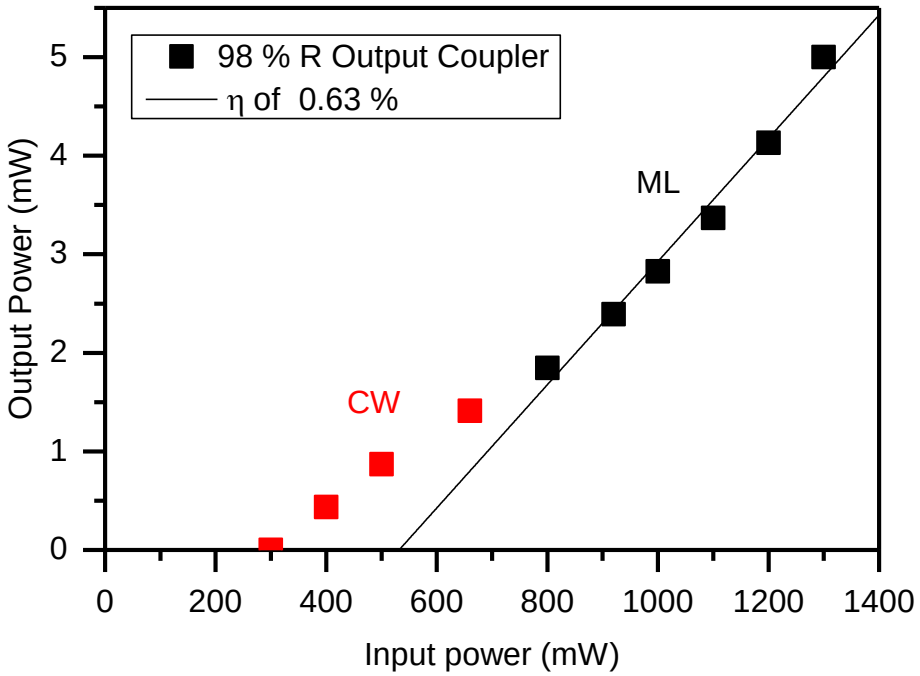

Figure 4.11. Power performances of modelocked Cr:ZnSe waveguide lasers with PRF of 295 MHz. Slope efficiency of laser was calculated from a linear fit of the black data points where the laser was found to be modelocked from the RF spectrum. The red data points are when the laser is operating in pure CW operation.

From Figure 4.11, we observe that the onset of modelocking, in addition to a RF peak, at 800 mW of pump power from the slope efficiency increasing. This is from the reduction in cavity loss when the SESAM is saturated. The slope efficiency of the modelocked laser is an order of magnitude less than demonstrated in the Cr:ZnSe waveguide laser [24]. This was because the output coupler reflectively was chosen to match the saturable absorption of the SESAM. However, this is over coupled compared with the coupling needed for optimum laser performance in a Cr:ZnSe waveguide [24].

The MFD of the waveguide laser was imaged using a 500 mm uncoated CaF_2 lens and a Mid-IR camera (FLIR SC7000), as shown in Figure 4.12:

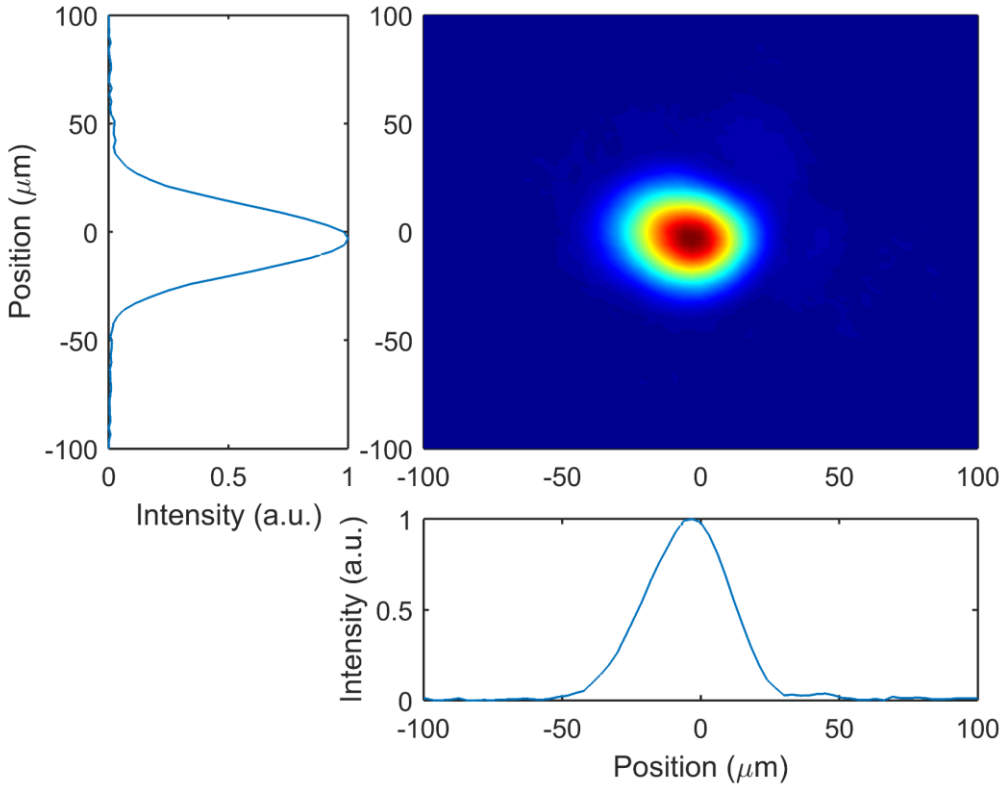

Figure 4.12. MFD of Cr:ZnSe modelocked laser. Imaged with a 500 mm lens with the laser pumped with 1.3 W of pump power.

The MFD of the waveguide laser was found to be single mode with FWHMs of 60.0 µm and 57.7 µm in the x-axis and y-axis respectively. This is in good agreement with previous work with this waveguide.

The wavelength spectrum of the laser was investigated using an OSA (Thorlabs OSA205). This OSA has an operating range of 1 - 5.6 µm, a noise floor of -40 dBm per nm and a resolution of 150 pm at 2.5 µm. The spectra of the Cr:ZnSe laser in CW modelocked operation with 1300 mW of incident pump power is shown in Figure 4.13.

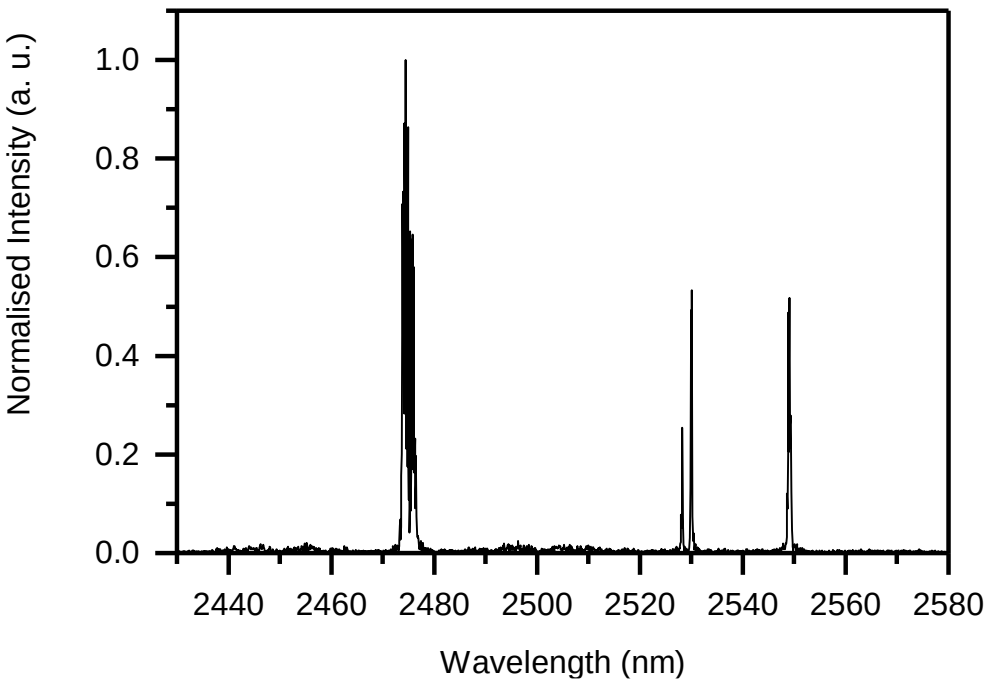

Figure 4.13. Full wavelength spectra of modelocked Cr:ZnSe waveguide laser

As can be seen from Figure 4.13, the laser has the majority of its spectral emission centred at 2475 nm with two other smaller emission peaks centred at 2530 nm and 2550 nm. This multi peak spectra is a common feature of free running bulk polycrystalline Cr:ZnSe lasers [15]. Figure 4.14 shows an expanded view of the spectrum centred at 2475 nm with clearly visible fringes.

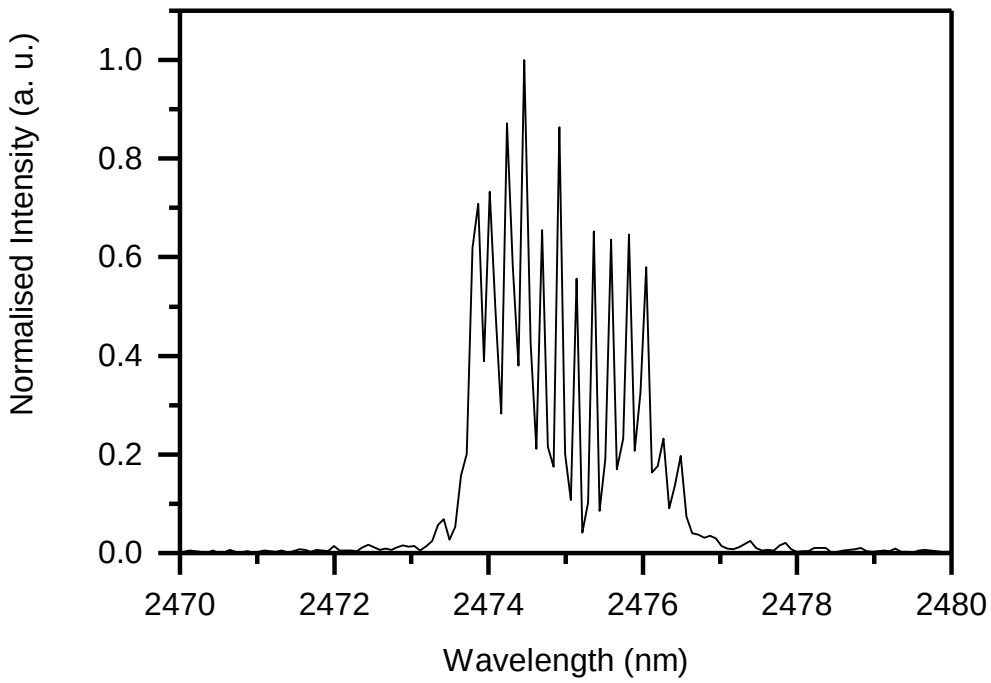

Figure 4.14. Expanded view of main spectral emission peak of modelocked Cr:ZnSe waveguide laser.

This source of the fringes where investigated. The effect was confirmed not to be from the modelocking of the laser because the same result was observed when the SESAM was replaced with a 100% reflecting dichroic mirror, in this case the laser is operated in CW mode. The possibility of the fringes being formed by a Fabry-Perot etalon was investigated. The main etalon for consideration was the end facets of the Cr:ZnSe waveguide sample. This was investigated, but the length of the sample did not match the frequency of the fringes. In addition, the Cr:ZnSe sample is AR coated, which will suppress any effects from the etalon. In addition, the spacing of the intra-cavity etalons did not match the measurement. The laser appears to be operating as an inhomogeneous broadened laser, which was found to be an issue in non-HIP treated polycrystalline Cr:ZnSe lasers [116, 119]. These multiple peaks can be suppressed by HIP treatment in a free running CW Cr:ZnSe bulk laser resonator to linewidths of less than 200 pm [116].

Characterisation of the pulse width of the laser was investigated using two autocorrelators. The first was a commercially available system that used a frequency doubling crystal (APE Pulse Check). The second was an interferometric autocorrelation that replaced the need for a doubling crystal with two photon absorption in an InGaS detector. A lower bound for the pulse width can be inferred from the wavelength spectra.

This gives a transform limited $sech^2$ pulse of 2.8 ps from the available spectra bandwidth. From this assuming the pulse width of the laser is 2.8 ps the peak power can be calculated. From this a maximum in the peak power of the laser is calculated to be 5.34 W. This is not sufficient for frequency doubling in a crystal, or two photon absorption in an InGaS detector. This explains why an autocorrelation trace could not be obtained with either of the two autocorrelators. The small pulse energy is attributed to a combination of low average power, relatively high repetition rate and long pulse width of the laser.

In conclusion, we have demonstrated a CW modelocked Cr:ZnSe waveguide laser. The cavity length was extended beyond that of the laser sample length in order to demonstrate CW modelocked operation with the available SESAM and laser pump power. The main spectral emission peak of the modelocked laser was centred at 2475 nm with a FWHM of 2.3 nm when operated with the maximum available pump power of 1.3 W. From this, a lower bound on the pulse width of the laser is calculated to be 2.8 ps. The laser demonstrated an output of 17 pJ per pulse at a fundamental pulse repetition rate of 295 MHz. Implementation of dispersion control will result in the modelocking of a larger bandwidth resulting in the demonstration of shorter pulse widths. This is the first demonstration of a guide mode modelocked Cr:ZnSe laser.

4.5. Power Scaling of Modelocked Cr:ZnSe Waveguide Laser

The initial investigation of a modelocked Cr:ZnSe laser was limited by the available pump power. This limitation manifested in two parts of the investigation, the most important being modelocking, which could not be confirmed with an autocorrelator due to insufficient pulse irradiance. The second was that the cavity had to be extended to increase the pulse energy to be sufficiently large to suppress Q-switched instabilities, as shown in Equation 16. For this work, a new pump laser with of 20 W CW power was used. This had more than 10 times the available power than that of the pump source used in previous work.

4.5.1. Pump Laser Characterisation

The high power pump laser is from IPG Photonics, model number TLR-20-1908-LP. This laser is a CW Tm:Fibre laser that emits a maximum power of 20 W at 1908 nm. The laser is also linearly polarised. With this laser, a change in the far field MFD was observed with a Mid-IR camera (FLIR SC7000) when moving the delivery fibre. This was investigated because a laser with poor beam quality will reduce the coupling efficiency

into a single mode waveguide, and hence reduce the laser performance. The output beam quality characteristics of the laser were characterised using the M^2 method.

The beam quality factor more commonly known as the M^2 of the laser was measured with the laser operating at different power levels spanning its operational range. A diffraction limited Gaussian beam has an M^2 of 1. Values of less than 1 are not possible. A laser with good beam quality will have a value close to 1. The measurement of a laser's M^2 is defined by the ISO Standard 1146 [143]. This states that the half-angle beam divergence of the laser is Equation 21:

$$\theta = M^2 \frac{\lambda}{\pi \omega_0}$$

Equation 21

where θ is the half-angle beam divergence and ω_0 is the beam waist at the focus of the beam. Hence to find the M^2 of a laser, we need to measure both these quantities. A convenient way to do this is to collimate the output of the laser and then focus it with a lens. The dimeter of the beam is then measured at different points along the z-axis using the scanning knife-edge method. With this method, we pass a knife-edge through the beam perpendicular to its propagation direction. The power of the laser light that is not blocked by the knife was measured with a thermal power meter. With this method, the beam waist *w(z)* at point *z* can be calculated for the perpendicular positon of the blade at the 90% and 10% transmission points using Equation 22:

$$w(z) \cong 0.780(x_{10\%} - x_{90\%})$$

Equation 22

For an accurate value of M^2 and ω_0 to be calculated for a set of knife-edge measurements, a numerical fit must be made to Equation 23:

$$\big(w(z)\big)^2 = [\theta^2]z + [-2\theta^2 z_0]z + [w_0^2 + \theta^2 z_0^2]$$

Equation 23

Using this method, the M^2 of the pump laser was investigated. The pump laser collimated output beam was focused with a 50 mm lens. The beam waist was measured at different locations along the propagation axis using the knife-edge method. The beam waist measurement for the laser when set to 40% diode current is plotted in Figure 4.15:

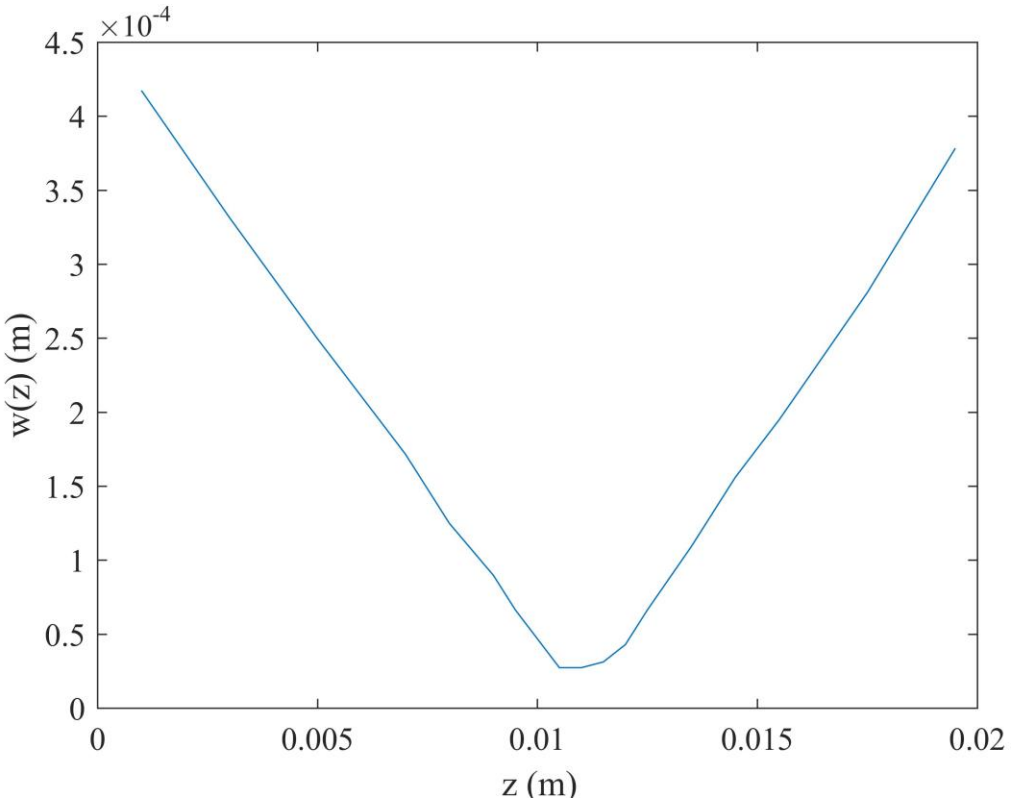

Figure 4.15. Plot of IPG laser beam waist along the z axis for M^2 measurement. The collimated output of the IPG laser was focused with a 50 mm lens. The IPG laser was set to 40% diode power for this measurement.

To form a robust fitting of the raw data, the beam waist was squared and replotted, as shown in Figure 4.16. This removes issues of fitting imaginary numbers by removing the square root in the equation. To perform the graphing and fitting of the data, a MatLab script was written. The fitting function calculated a M^2 of 1.4 when the laser is operated at a 40% diode current.

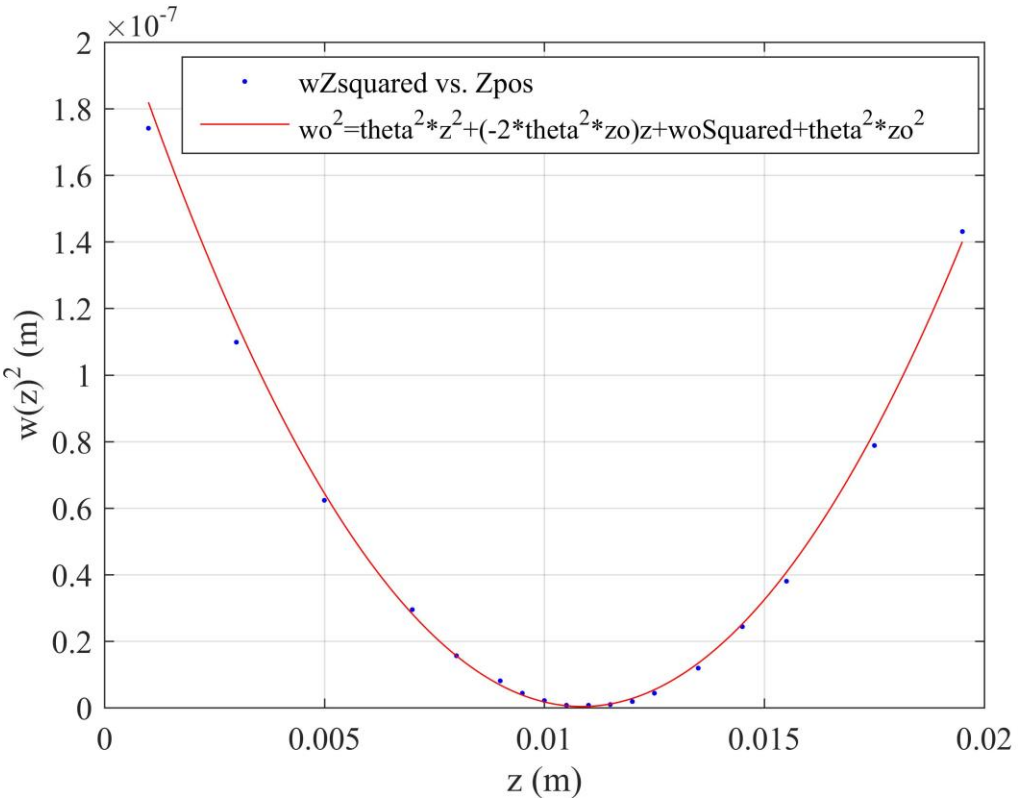

Figure 4.16. Plot of beam waist squared against propagation in the z axis. The IPG laser was operated at 40% diode power. This plot was fitted with Equation 23 using Matlab's lense squared curve fitting tool. This fit found the free parameters to be w_o= 19.11 µm, z_0 = 10.86 mm, θ = 0.0432 rad and M^2 of 1.361.

The output characteristics of the laser were investigated for a number of different diode currents, the results of which are given in Table 8:

IPG Photonics TLR-20-1908-LP Characterisation			
Diode power (%)	M^2	w_o (µm)	θ (rad)
20	2.2	30.4	0.046
40	1.4	19	0.043
60	1.5	22	0.044
80	2.4	35	0.044

Table 8. Summary of beam characterisation of Tm pump lasers using 50 mm lens

As can be seen in the table, the beam quality is optimum at 40% diode power. This corresponds to an output power of waist after the fibre beam collimator. This has sufficient pump power for the modelocked investigation Cr:ZnSe waveguide laser because it is half that of the damage threshold of the AR coating [144].

Operating the pump laser at a constant diode current will provide a stable beam profile but an external method of power control is needed. The low power pump laser used a rotating metal coated ND disk for power control. However, the pump laser was found to damage the ND disk at powers above 2 W. Hence a different approach was needed. The IPG pump laser was linearly polarised, hence a combination of wave plates and polarising beam splitters can be used as a non-absorbing power control method. A diagram of the power control setup is given in Figure 4.17:

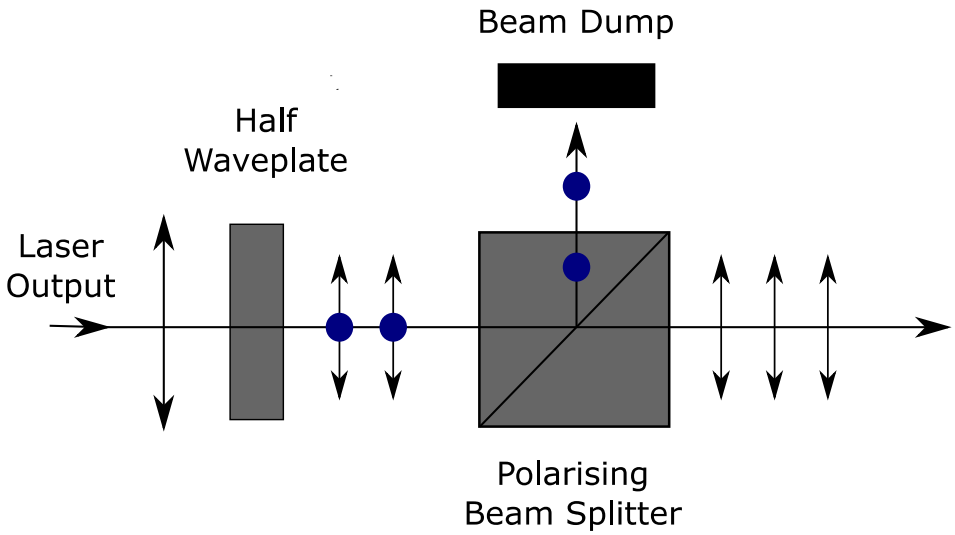

Figure 4.17. Power control system for IPG pump laser

4.5.2. Waveguides and Cavity Setup

With the pump laser characterised and its power control systems implemented, the experiment was ready to progress to the modelocking of the Cr:ZnSe waveguide laser. The Cr:ZnSe waveguides were inserted into a laser cavity as shown in Figure 4.18 for high power modelocked laser operation:

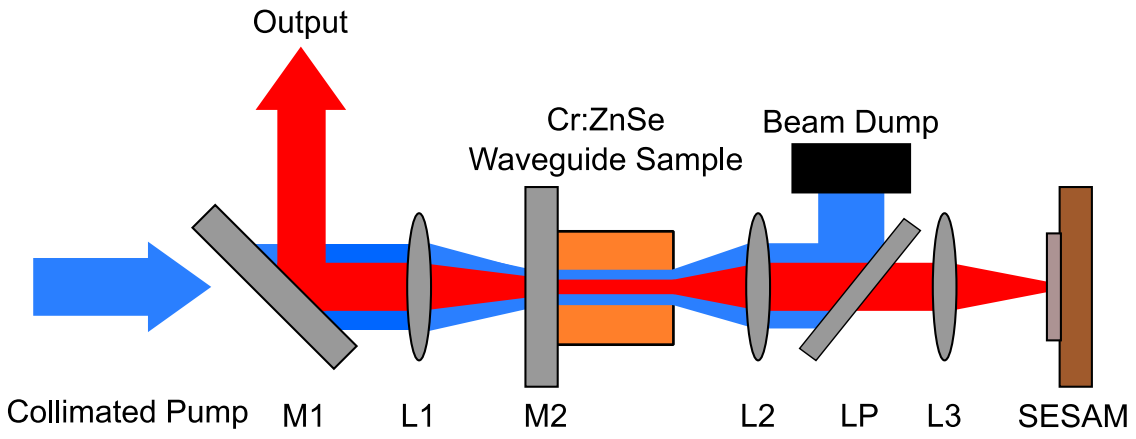

Figure 4.18. Schematic of modelocked Cr:ZnSe waveguide laser. M1 is a 45° AR 1.9 µm and HR 2.3 - 3 µm dichroic mirror. M2 is a dichroic mirror that is AR at 1.9 µm and 98%, reflecting at 2 - 3 µm. L1, L2 and L3 are 50 mm CaF_2 plano-convex lenses AR coated from 1.65 - 3.0 µm.

The pump source used for the laser experiments was a 20 W linearly polarised single-mode Tm:fibre laser (IPG Photonics TLR-20-1908-LP) operating at 1908 nm. An AR-coated 50 mm CaF_2 lens was used to focus the pump light into the waveguide end facet. Due to this laser input and output being located at the same end of the cavity, L1 also collimated the signal output of the waveguide. A 98% reflective (2 - 3 µm) output coupler was butt coupled to the end facet of the Cr:ZnSe waveguide. The resonator length of the laser cavity was extended to 48 cm by two intra cavity AR coated 50 mm CaF_2 lenses. Referring to Figure 4.18, the lens L2 was used to collimate the output of the waveguide and lens L3 was used to focus onto the SESAM. The specification of the SESAM (Del Mar Photonics SAM-2400-1-25) is a saturation fluence, relaxation time constant and modulation depth of 90 µJ/cm^2, 500 fs and 0.6% at 2400 µm respectively. The SESAM was mounted to a passively-cooled copper block of diameter 25.4 mm and thickness 5 mm. A 2 µm longpass filter LP was placed in the cavity to prevent any pump interactions with the SESAM. A 45° highly reflective dichroic mirror at the signal wavelength was used to separate the counter-propagating output and pump beams.

4.5.3. Modelocked Laser Results of 300 MHz Cavity

The laser was characterised using 5 W of incident pump power. At this pump power the laser was found to operate in stable self-starting CW modelocked regime. The PRF of the laser was measured with a CMT detector (VIGO system PVM−10.6) which had a 1 ns time constant. This detector was connected to a 3 GHz RF spectrum analyser (Rigol

DSA1030A). CW modelocking was confirmed from a single peak at 308.1 MHz on the RF spectrum, as shown in Figure 4.19. For the RF spectrum measurement, the bandwidth of the analyser was set to 300 Hz.

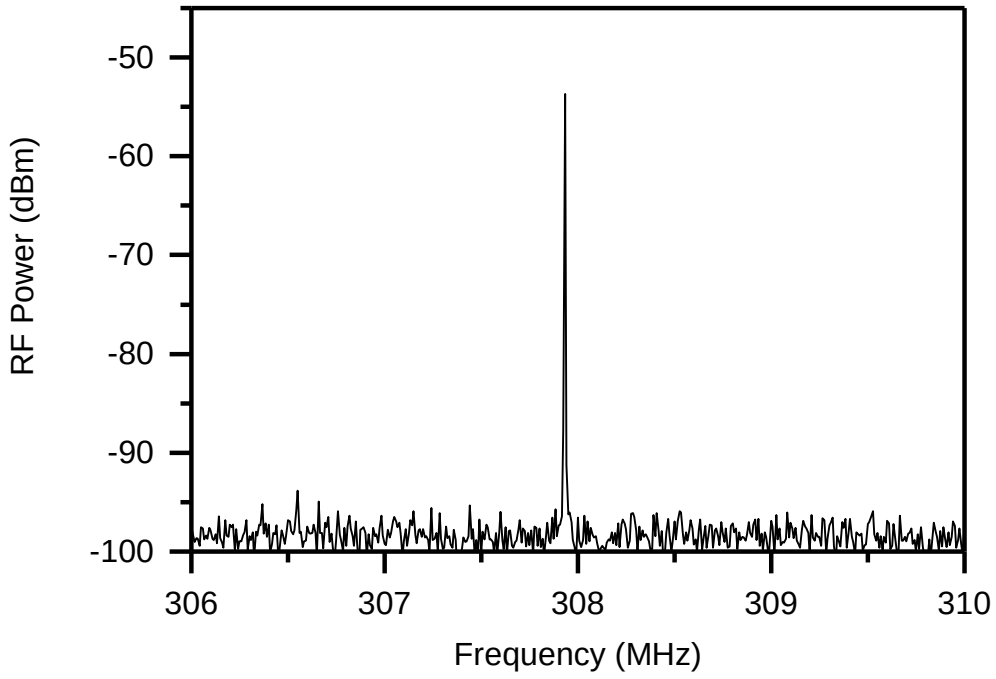

Figure 4.19. RF spectrum of CW modelocked Cr:ZnSe waveguide laser operating with 5 W of pump power. The graph has a span of 4 MHz and the measurement was taken with a resolution bandwidth of 300 Hz.

The wavelength of the laser was measured using a OSA (Thorlabs OSA205), which has an operating range of 1 - 5.6 μm, noise floor of -40 dBm/nm and a resolution of 150 pm at 2.5 μm. The spectral output of the modelocked laser with a PRF of 308 MHz with 5 W of incident pump power is given in Figure 4.20:

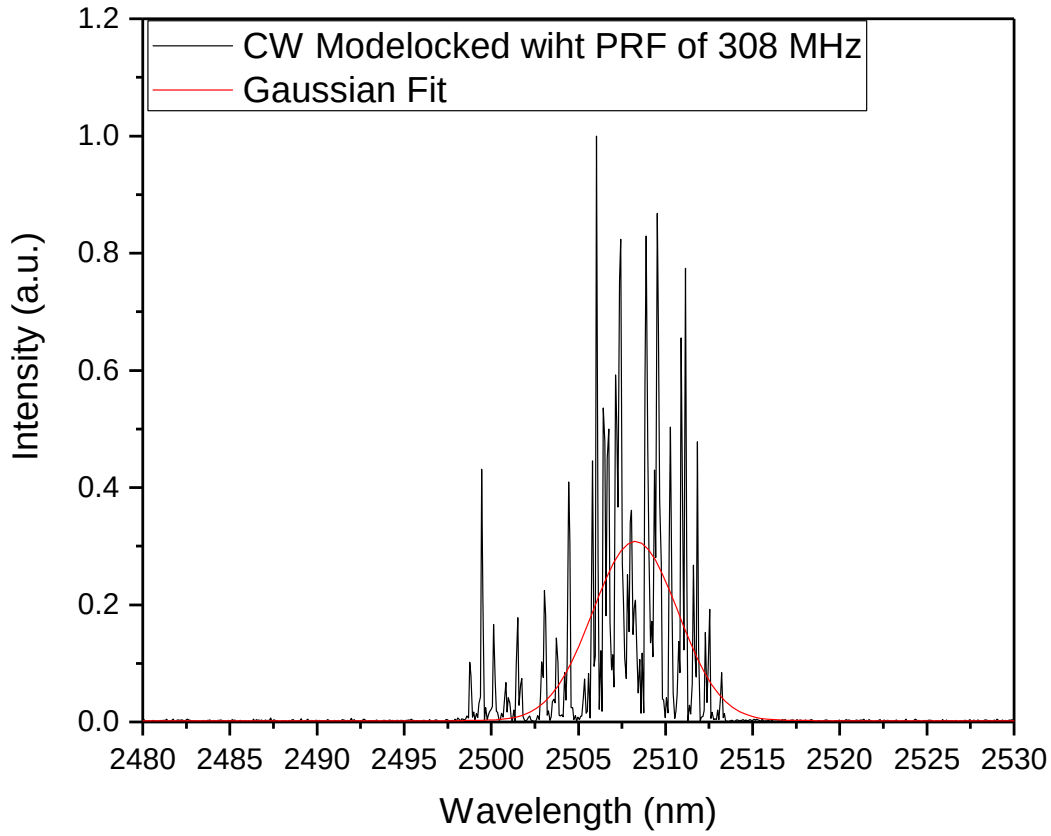

Figure 4.20. Wavelength spectrum of modelocked Cr:ZnSe waveguide laser. A Gaussian fit was applied to the data. From the fit, the central wavelength was found to be 2508 nm with a FWHM of 6 nm. The laser was operated with PRF of 308 MHz at a pump power of 5W.

The laser was found to have a single group of sharp spikes centred at 2508 nm with a FWHM of 6 nm. A spectra with this type of shape has been previously observed with bulk TM:II-VI lasers [116].

The pulse of the laser was characterised in time using an interferometric autocorrelator using two photon absorption in the Ge detector (New Focus 2033). A diagram of the system is given in Figure 4.21:

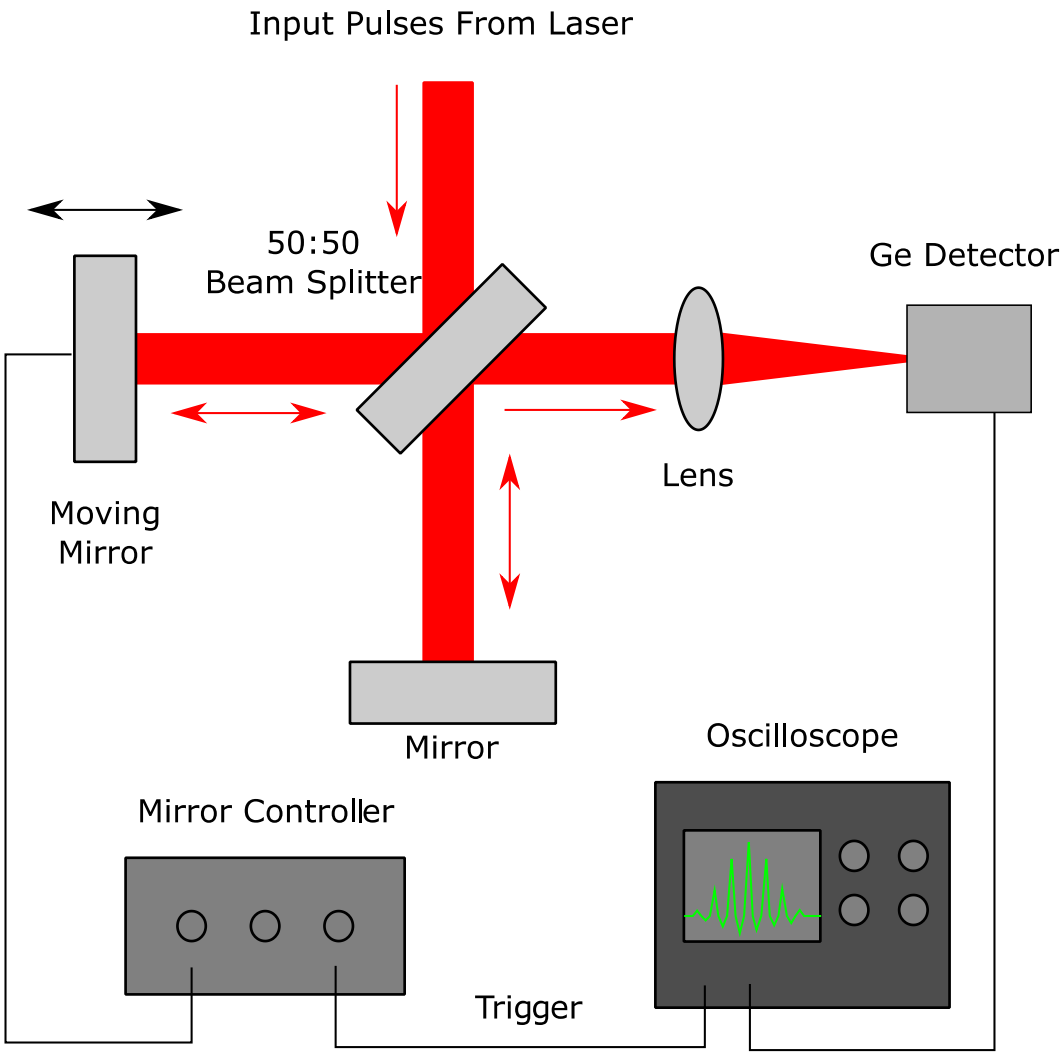

Figure 4.21. Schematic of 2-photon interferometric autocorrelator

It was found that three long-pass filters were needed to sufficiently suppress any signal from the pump source for this measurement. The trace on the oscilloscope and the movement of the mirror were calibrated by the fringes in the autocorrelation trace. The autocorrelation trace of the laser with a PRF of 308 MHz under 5 W of pump power is given in Figure 4.22.

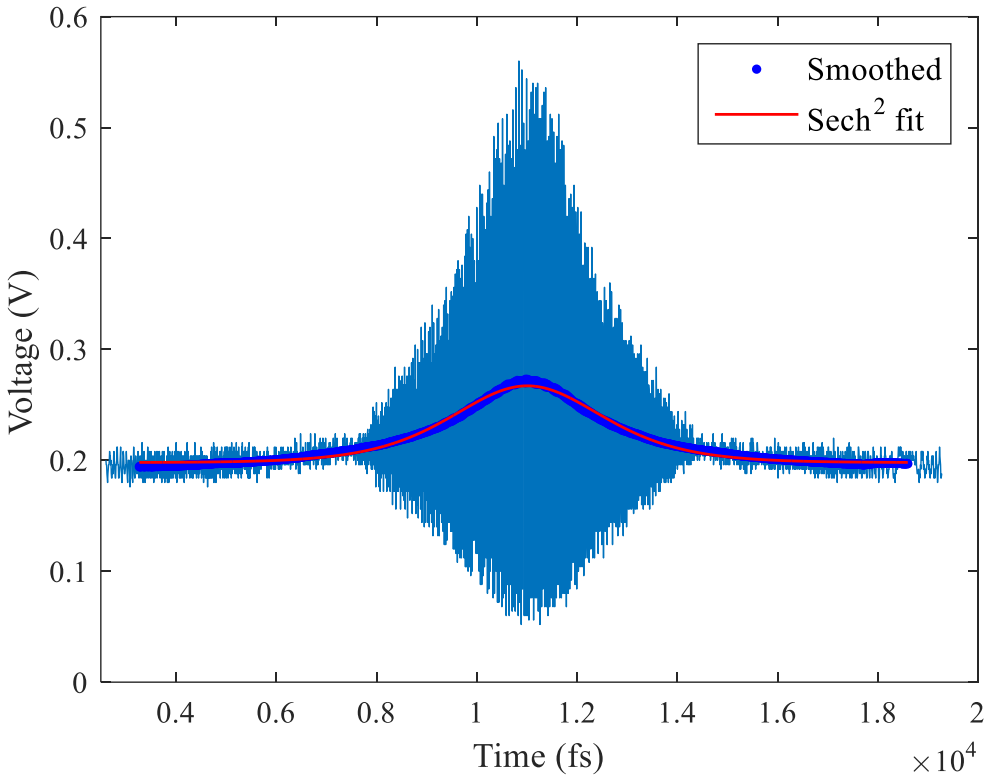

Figure 4.22. Autocorrelation of Cr:ZnSe waveguide laser with PRF of 308 MHz with pump power of 5 W. Light blue line is the autocorrelation trace. Dark blue dots are smoothed data setup using the nearest neighbour method. Red line is a sech^2 fit of the autocorrelation trace. From the fit, the pulse width was calculated to be 638 fs.

A nearest neighbour smoothing was applied to the autocorrelation trace before fitting a Sech^2 function to the data. The FWHM of this function was 982 fs, which gives a calculated pulse width of 638 fs, assuming a sech^2 pulse. Under 5 W of pump power the laser emitted 85 mW of average power. Thus the laser is emitting a pulse energy of 275 pJ at a PRF of 308 MHz. This represents a seventeen fold increase in average power compared with the initial work in modelocking Cr:ZnSe waveguide lasers with the low power pump source.

Since there is not a 1:8 ratio in Figure 4.2 the is the potential for this signal to be from a noise spike. This is also the case for the following autocorrelations.

4.5.4. Modelocked Laser Results of Gigahertz Cavity

The next stage of the investigation takes advantage of reduced cavity lengths possible with waveguide geometry to demonstrate a PRF of greater than 1 GHz. To reduce the cavity size, L2 originally a 50 mm lens, from Figure 4.18, was changed to a 20 mm focal length lens. For this work there are limitations on the ability to fully characterise the

laser. This is from the lack of availability of detectors faster than 1 GHz in the Mid-IR. To overcome this, the distance between the two intra cavity lenses was reduced to give an optical cavity length of 15.6 cm, resulting in a PRF of 961 MHz as shown in Figure 4.23:

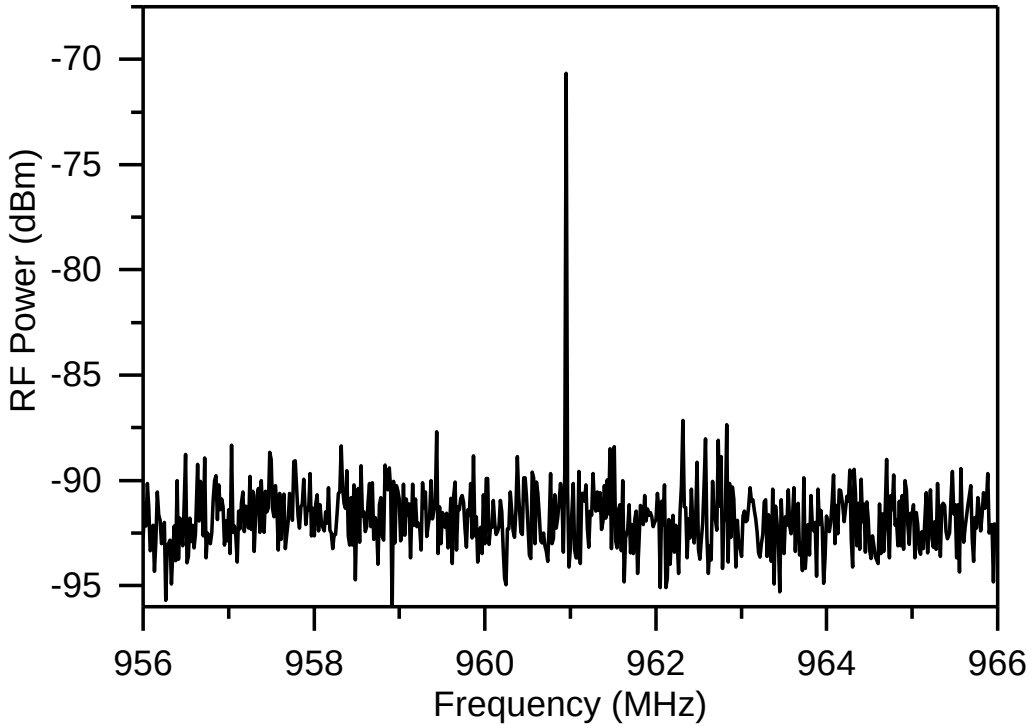

Figure 4.23. RF spectrum of CW modelocked Cr:ZnSe waveguide laser operating with a PRF of 961 MHz. The laser was pumped with 5 W. The graph has a span of 10 MHz and the measurement was taken with a resolution bandwidth of 300 Hz.

With 5 W of pump power the laser was found to operate in the CW modelocked regime from the RF trace at a PRF of 961 MHz. The output power was measured to be 74 mW after losses from the pump filters were removed. The spectrum of the laser was measured with the Thorlabs OSA 205, given in Figure 4.24:

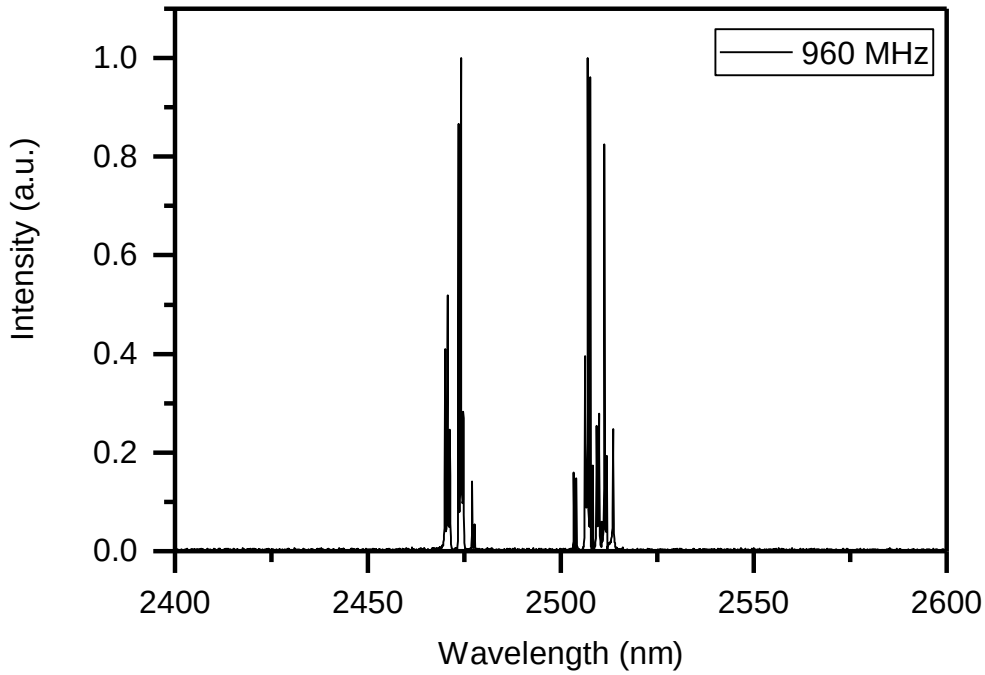

Figure 4.24. Wavelength spectra of modelocked Cr:ZnSe waveguide laser. The laser was operated at 961 MHz with a pump power of 5 W.

As can be seen from the wavelength spectra, the laser is operating in two separate spectral bands. This is similar to what has been observed with the initial lower pump power work. The laser was autocorrelated with the two photon autocorrelator, the trace is shown in Figure 4.25:

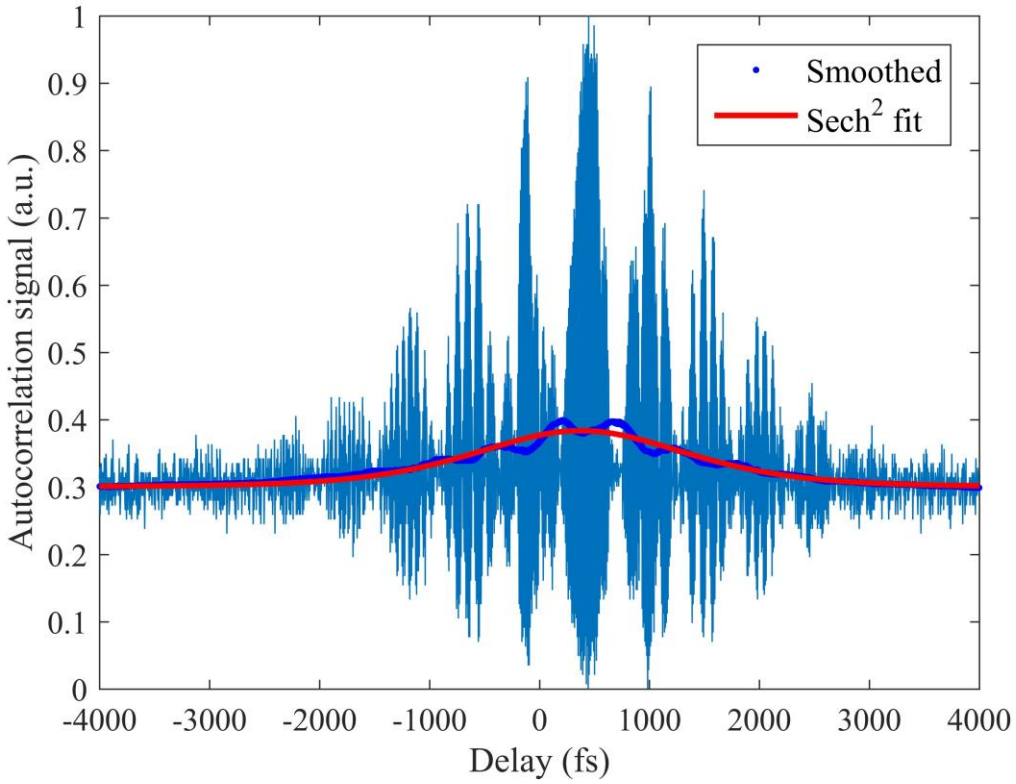

Figure 4.25. Autocorrelation of Cr:ZnSe waveguide laser with PRF of 961 MHz with pump power of 5 W. Light blue line is the autocorrelation trace. Dark blue dots are the nearest neighbour smoothing of the autocorrelation trace. Red line is a sech^2 fit of the autocorrelation trace. From the fit, the pulse width was calculated to be 1477 fs.

The autocorrelation was found have an overlapping beat. This is thought to be from the interference of the two different bands in the wavelength spectrum, as shown in Figure 4.26. It is possible to decouple the two wavelength components with a filter; however, such a specialised filter was not available at the time of the experiment. A sech^2 fit was applied to the trace to give an indication of the pulse width. For this the FWHM was calculated to be 2272 fs, resulting in a pulse width of 1477 fs assuming a sech^2 pulse.

The beat wave can be generated by the laser operating in two different regimes. The first is a single pulse travelling around the resonator with the double wavelength spectra peaks formed from a material property of polycrystalline Cr:ZnSe. The second is that there are two pulses circulating the resonator which are independent of each other but are still in phase. The pulses have to be in phase because if this was not the case we would observe more than one spike on the RF spectrum. Further investigation of the pulse is needed with more sophisticated methods of measuring the pulse, such as a FROG [140].

The cavity length of the laser was further reduced to a modelocked laser with a PRF faster than the symbolic target of greater than 1 GHz. For this experiment, there is a limitation created from the detector which cannot detect signals faster than 1 GHz, hence there is no RF trace for this cavity. The distance between the two lenses, L2 and L3, was reduced by a further 1 cm for the 961 MHz, resulting in a calculated PRF of 1.03 GHz. This distance was measured with a vernier caliper in order to have an accurate PRF measurement. The autocorrelation and wavelength spectra of the laser operating at 1.03 GHz under 5 W of pump power is given in Figure 4.26 and Figure 4.27 respectively.

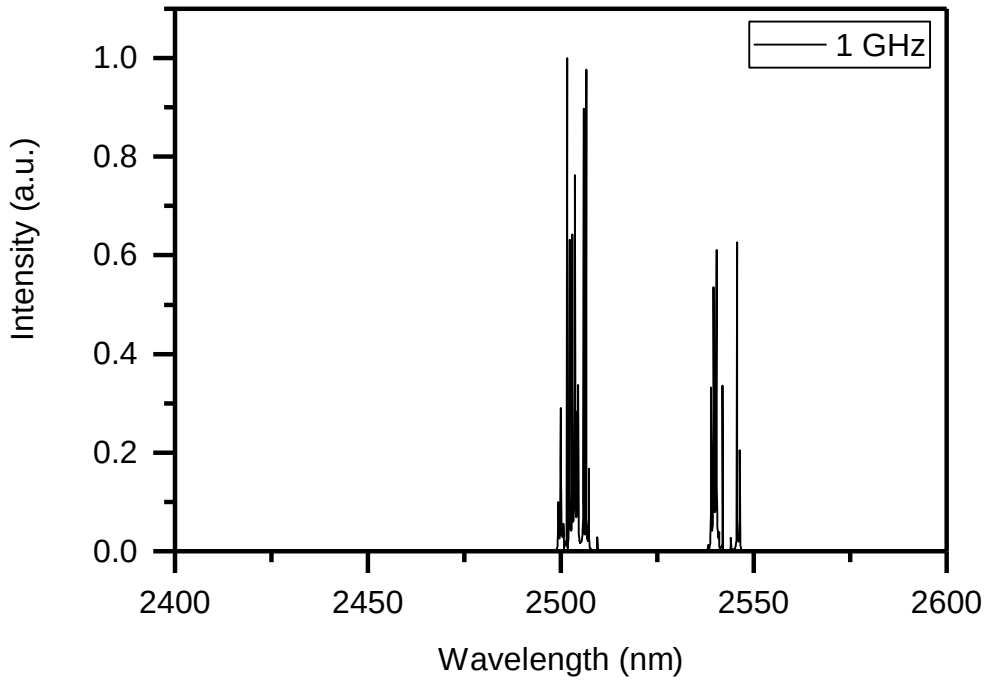

Figure 4.26. Wavelength spectra of modelocked Cr:ZnSe waveguide laser. The laser was operated at 1.03 GHz with a pump power of 5 W.

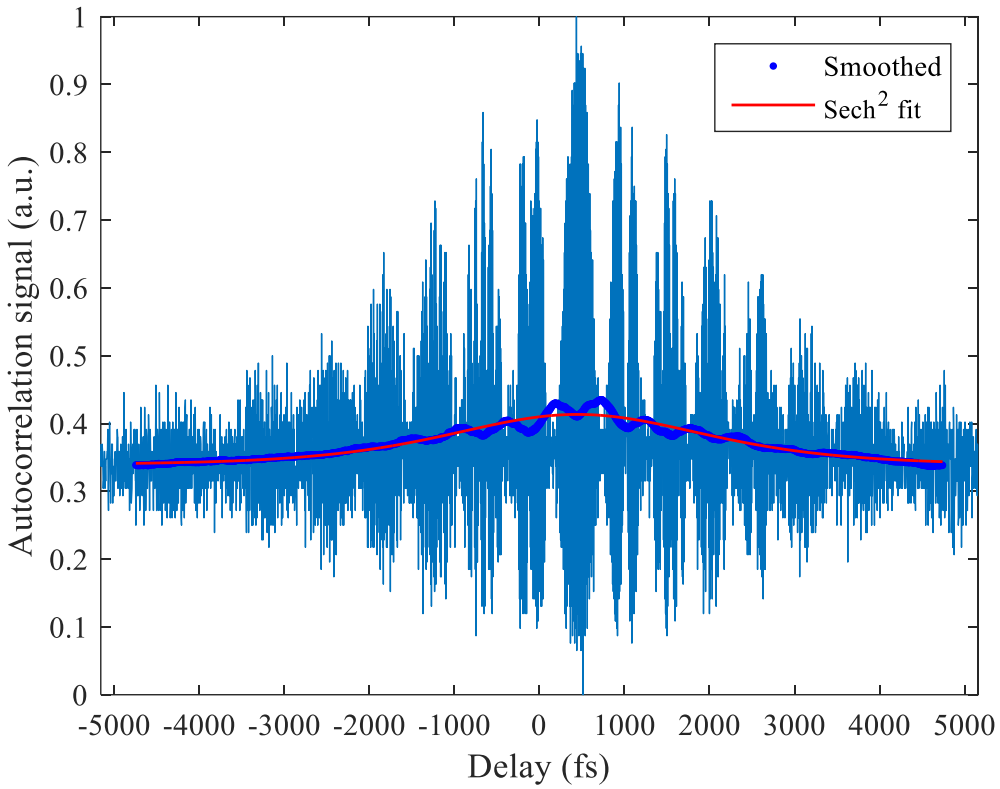

Figure 4.27. Autocorrelation of Cr:ZnSe waveguide laser with PRF of 1.03 GHz, operated with a pump power of 5 W. Light blue line is the autocorrelation trace. Dark blue dots are the nearest neighbour smoothing of the autocorrelation trace. Red line is a sech^2 fit of the autocorrelation trace. From the fit, the pulse width was calculated to be 2024 fs.

At this calculated PRF of 1.03 GHz, the output power was 80 mW when pumping with 5 W. From the autocorrelation, given in Figure 4.27, the FWHM was found to be 3562 fs, resulting in a pulse width of 2024 fs, assuming a sech^2 pulse. From this the pulse energy is thought to be 78 pJ assuming a single pulse circulating the resonator.

Further characterisation of the twin spectral peaks found in the shortened laser resonator configuration is need to fully investigated. However, shortly after completing the 1 GHz measurements, the end facet of the last single mode waveguide was damaged by the pump laser. This limited further investigation in this work. This work could be continued with a new Cr:ZnSe sample. An HIP treated sample would be of great interest for future investigations.

4.5.5. Conclusion of Modelocked Power Scaling

We have demonstrated a CW modelocked Cr:ZnSe waveguide laser with 17 times more average power than our initial demonstration. To achieve this, the original 1.3 W pump

source was replaced with a 20 W Tm:fibre laser. The length of the cavity was extended to 50 cm to increase peak power of the modelocked laser pulses. In this configuration, the laser operated in pure CW modelocked regime with a PRF of 308.1 MHz and average power of 85 mW when pumped with 5 W at 1908 nm. The pulse width was found to be 638 fs, assuming a $sech^2$ pulse shape, thus resulting in a pulse energy of 275 pJ. This is the largest pulse energy demonstrated by a modelocked Cr:ZnSe waveguide laser. The spectral emission peak of the modelocked laser was centred at 2506 nm. To facilitate faster PRF operation, the cavity length was reduced, resulting in the demonstration modelocked laser with a PRF of 1.03 GHz. Modelocking was confirmed with an autocorrelation trace of the pulse.

4.6. Conclusion

Depressed cladding waveguides inscribed in Cr:ZnSe by ULI were investigated for the creation of a compact modelocked laser. This work built on the broad wavelength tuning demonstrated in these waveguides as discussed in Chapter 3. In this investigation, an extended waveguide cavity design was implemented, this meant the RF characteristics of the laser were within the characterisation equipment operation range. The laser was passively modelocked with a SESAM.

The initial investigation used a 1.3 W pump source. This laser demonstrated CW modelocked operation, confirmed from a single peck in the RF spectrum. The main spectra emission peak of the modelocked laser was centred at 2475 nm with a FWHM of 2.3 nm when operated at the maximum available pump power of 1.3 W. From this wavelength spectrum a lower bound on the pulse width of the laser was calculated to be 2.8 ps. The laser demonstrated an output pulse energy of 17 pJ at a fundamental pulse repetition rate of 295 MHz. However, there was not sufficient peak irradiance available to produce a successful autocorrelation.

The pump source of the laser was increased in output power to an available power of 20 W. However, only 5 W was used to avoid thermal load issues and ablation of the waveguide end facets. CW modelocking was demonstrated with a PRF of 308 MHz with an average power of 85 mW. The peak power was sufficient for an autocorrelation, a pulse width of 638 fs was measured, assuming a $sech^2$ pulse shape.

The next step of the investigation looked at increasing the PRF to over 1 GHz. The issue of detectors being limited to detecting signals below 1 GHz was overcome by demonstrating a CW modelocked RF spectrum at 961 MHz and then shortening the cavity. From this the laser is inferred to be CW modelocked at 1.03 GHz from the cavity length. Modelocking was confirmed at 1.03 GHz by autocorrelation of the pulse. Further work is needed to investigate the beat wave found on the shortened cavity autocorrelation. However, this was not investigated because the waveguide was damaged during this investigation.

The work on modelocked Cr:ZnSe laser with the incorporation of a waveguide geometry will allow future work into the development of fully monolithic master oscillator power amplifier systems. In particular, integration of dispersion compensation into the laser cavity may be an effective method for reducing the pulse width of the laser. Using the ULI inscribed waveguides in Cr:ZnSe will provide a simple method for reducing cavity length and thus make a greater than 1 GHz fundamental repetition rate modelocked laser in the Mid-IR possible.

5. Cr:ZnS Waveguide Laser

5.1. Introduction

Cr:ZnSe has been the focus of development of the Cr doped chalcogenide lasers. This has resulted in the demonstration of CW output powers of 57 W [18], widely tuneable output from 1973-3339 nm [17] and single longitudinal mode output [145]. Furthermore, modelocked operation which uses this large bandwidth for femtosecond pulses has been demonstrated with SESAM, Graphene and Kerr lens [106, 146, 147]. Cr:ZnSe lasers have matured to the point where CW and modelocked systems are now commercially available from IPG Photonics. However, further scaling of average power is limited in ZnSe lasers by thermal lensing effects from its relatively large dn/dT [148, 149], five times larger than that of YAG [68, 150]. Indeed, the notable 57 W average power demonstrated by Mirov et al. [18] was only achieved with a double pass of a spinning disk gain element. This cavity configuration was effective in power scaling the laser, but the addition of moving parts increased the laser's footprint and reduced reliability. Thus an alternative is needed to further power scale TM:II-VI lasers without increasing cavity complexity. One potential solution is using Cr^{2+} doped Zinc Sulphide (Cr:ZnS) as the gain media.

Cr:ZnS has a number of material properties that reduce the impact of a thermal lens on cavity instability compared with Cr:ZnSe. The dn/dT of Cr:ZnS is 46×10^{-6} K^{-1} compared with the 70×10^{-6} K^{-1} of Cr:ZnSe [149]. Cr:ZnS also benefits from having a thermal conductivity of 0.27 W/cm·K compared with the 0.18 W/cm·K of Cr:ZnSe [68]. The higher thermal conductivity of Cr:ZnS improves the power scaling limit of the laser by more effective distribution of heat away from the laser field that forms the thermal lens inside the resonator. Cr:ZnS is further suited to power scaling because of its higher damage threshold of 1.5 J/cm compared with the 0.5 J/cm of Cr:ZnSe [151]. A summary of the material properties of ZnS, ZnSe and YAG is given in Table 9.

	ZnS	ZnSe	YAG
Transparency range (μm)	0.4 - 14	0.5 - 20	0.2 – 5.5
Refractive index at 2.5 μm	2.26 [152]	2.44 [101]	1.79 [153]
Thermal conductivity (W/cm·K)	0.27 [68]	0.18 [68]	0.14 [154]
dn/dT (K^{-1})	46×10^{-6} [149]	70×10^{-6} [149]	7.3×10^{-6} [154]
Damage threshold (J/cm)	1.5 [151]	0.5 [151]	1400 [155]

Table 9. Mechanical properties of ZnS, ZnSe and YAG

Initial power scaling of Cr:ZnS single crystal lasers were limited to the mW level due to high optical losses [156]. Post-thermal diffusion of Cr into separately grown high quality polycrystalline ZnS has been developed with reduced passive losses compared with single crystal ZnS [109]. This has led to the demonstration of a Brewster cut polycrystalline Cr:ZnS in a Z-cavity laser emitting 10 W of CW output power at 2380 nm [157].

Cr:ZnS retains the spectroscopic properties of Cr:ZnSe but with a 100 nm blue shift in both the absorption and emission cross-section as shown in Figure 5.1:

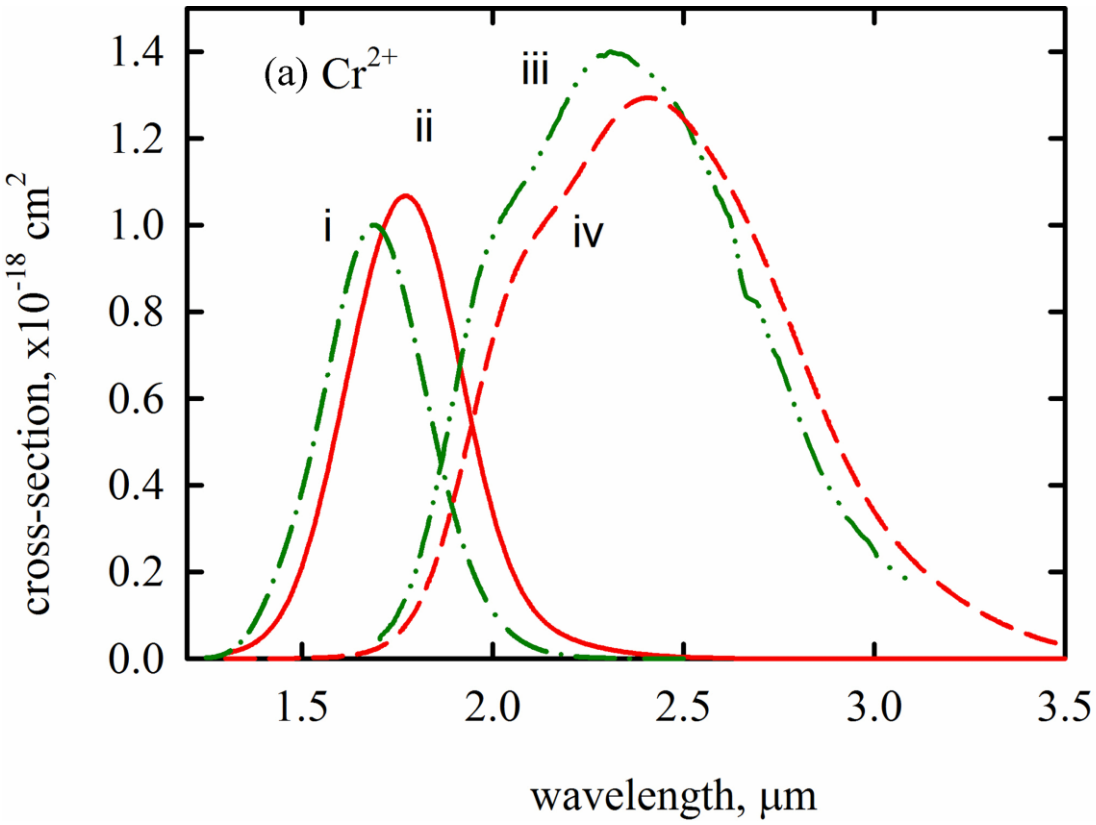

Figure 5.1. Absorption cross-section of (i) Cr:ZnS and (ii) Cr:ZnSe. Emission cross-section of (iii) Cr:ZnS and (iv) Cr:ZnSe. Figure reproduced form Mirov et al. [70].

This shift results in Er doped lasers being a more effective pump source for Cr:ZnS because their absorption peak is centred at 1.69 μm compared with the 1.77 μm of Cr:ZnSe [70]. This shift also allowed the pumping of Cr:ZnS with InGaAsP-InP diode strips emitting at 1.6 μm [156]. Diode pumping brings the advantage of a reduction in both system size and cost. In addition, by removing the need for a fibre laser pump the total system efficiency can be improved because this laser is also diode pumped. This could be a key factor in future applications , leading to Cr:ZnS being the preferred choice of TM:II-VI gain media.

The blue shift of the emission cross-section can either be a positive or negative feature depending on the application. The blue shift of Cr:ZnSe emission cross-section has improved overlap with the 2 – 2.4 μm atmospheric transmission region [106]. This is a key benefit for modelocking because it will allow for shorter pulses to be generated in a non-water vapour purged cavity. A Kerr-lens modelocked Cr:ZnS laser has produced pulses of 69 fs with an average power of 550 mW [106]. This is significantly improved over the 126 fs pulses emitted for the Kerr-lens modelocked Cr:ZnSe lasers with an average power of 20 mW [106, 158]. For modelocked applications, Cr:ZnS also benefits from its lower chromatic dispersion at its signal wavelength which is half that of Cr:ZnSe [106]. This is particularly beneficial for waveguide lasers with long gain regions.

One challenge with Cr:ZnS laser cavity design is its temperature-dependent upper state lifetime, shown in comparison with that of Cr:ZnSe and Ti:Sapphire in Figure 5.2:

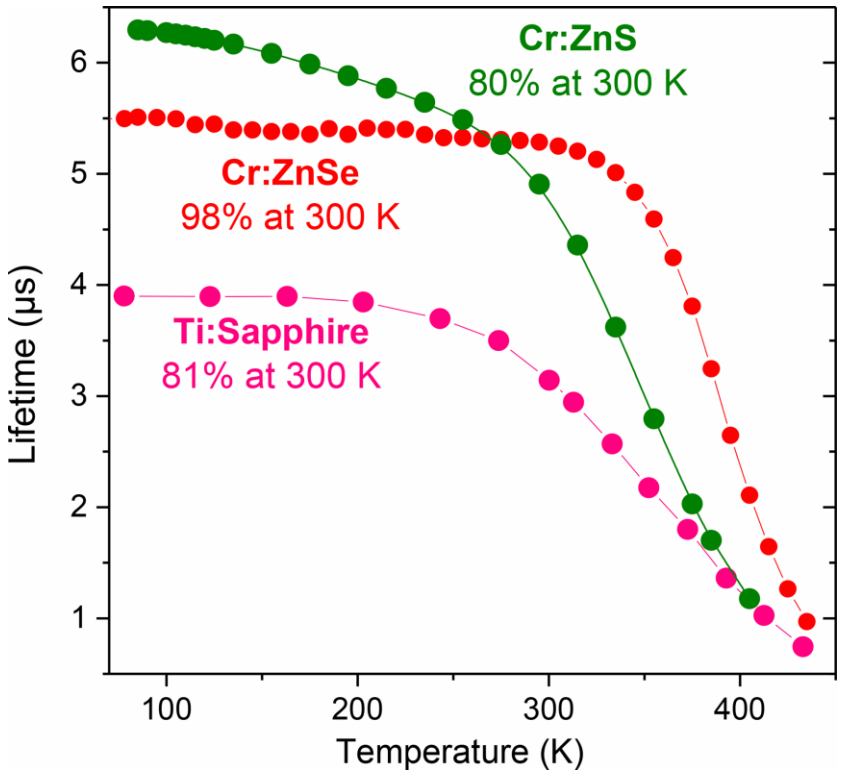

Figure 5.2. Temperature dependent upper state lifetime of vibronically-broadened gain media. Green dots are Cr:ZnS, red dots are Cr:ZnSe and pink dots are Ti:Sapphire. This graph has been reproduced from Sorokina et al. [106].

The upper state lifetime of Cr:ZnS is 4.7 µs compared with the 5.4 µs of Cr:ZnSe at room temperature. The 20% reduction in Cr:ZnS upper state lifetime at room temperature is not an issue for laser operation, the challenge arises for the fast drop off after 300 K. However, the lifetime of Ti:Sapphire, as shown in Figure 5.2, follows a similar trend and this has not stopped it from becoming one of the most widely used lasers sources in scientific research [59]. However, with common thermal management solutions such as water cooling and gain-switched operation, it is possible to mitigate issues from high thermal loads[69]. Additionally, pumping closer to the emission wavelength with Tm lasers will reduce the quantum defect and hence thermal load.

Another effective thermal management method is to implement a waveguide geometry [24]. Waveguide geometry improves thermal management through a number of factors. The longer interaction lengths possible with waveguide implementation permits a reduced doping concentration to be implemented. The reduced doping spreads the heat deposition over a larger volume, due to the lower absorption per unit length, and thus improves the thermal transfer between the heat sink and gain media. One of the most notable implementations of power scaling using a waveguide geometry is Yb-doped fibres, which

have demonstrated CW laser oscillators with single mode outputs and average powers of over 10 kW available from IPG Photonics. In materials with large dn/dT, such as ZnS and ZnSe, waveguide geometry is an effective method of mitigating the thermal lens induced [19, 58]. It also brings the benefit of minimising free space optics which reduces the lasers size and improves environmental robustness [87].

Waveguides have been developed in Cr:ZnSe using PLD technique and ULI but no waveguides have been demonstrated in Cr:ZnS. Of the two technologies used for waveguide fabrication, ULI has shown vastly superior output power and slope efficiencies [22, 58]. Of the ULI waveguide types demonstrated in ZnSe and Cr:ZnSe, annular depressed cladding waveguides were found to have the lowest propagation losses of 0.7 dB/cm [160]. With Cr:ZnS and Cr:ZnSe having many similarities it was decided to take the depressed cladding waveguide developed in Cr:ZnSe and transfer the technology to Cr:ZnS.

In this chapter, I will discuss the development of a Cr:ZnS waveguide laser. This work used a Cr:ZnS sample given to Heriot-Watt University by Sergey B. Mirov at the University of Alabama in Birmingham, USA and IPG Photonics.

5.2. Waveguide Fabrication in Cr:ZnS

For this investigation, polycrystalline Cr:ZnS fabricated by IPG Photonics was used. This sample was doped by post-growth thermal diffusion. Work by Mirov et al. [109, 161] has improved the quality of the diffusion process to have a uniform doping concentration and low passive optical loss of 1-3% per pass of the sample [53]. Details of the doping process can be found in the US patent filled on the 1st of December 2011 by Mirov and Fedorov [161]. The Cr:ZnS sample used in this investigation had a Cr^{2+} doping concentration of 8.3×10^{18} cm^{-3} with dimensions $6 \times 5 \times 2$ mm.

The waveguide design used a reduction in refractive index from the ULI inscription. This allowed us to create the waveguide's cladding, allowing for greater control of the waveguide diameter. The waveguide is an annular cross-section depressed cladding structure, fabricated from an arrangement of negative refractive index modification elements, drawn out longitudinally. This design was similar to that used in Nd:YAG [84] and the same as Cr:ZnSe [58]. A diagram of the waveguide geometry implemented is given in Figure 5.3:

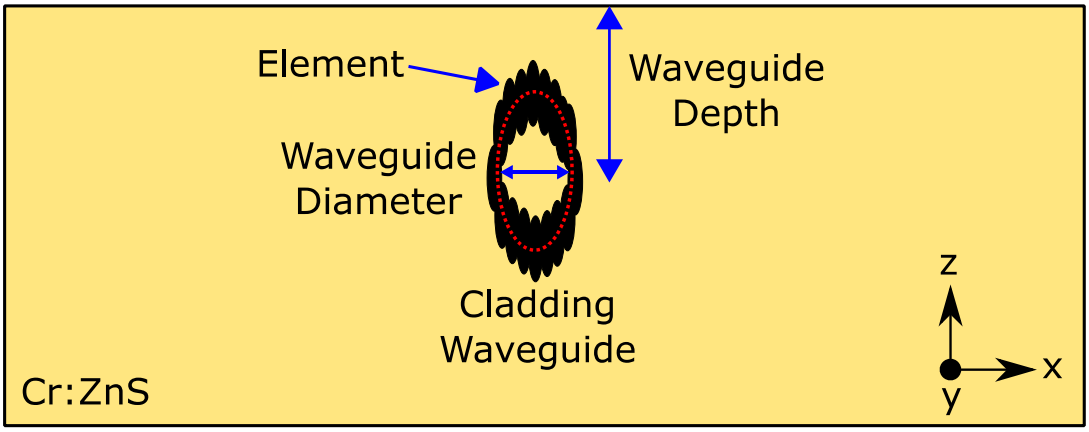

Figure 5.3. Diagram viewing from the end facet of a depressed cladding waveguide inscribed in Cr:ZnS. Conventions used for waveguide depth, diameter and element are given.

The inscription laser used for this work was an IMRA μJewel D400. The laser supplied 400 fs pulses at a repetition rate of 100 kHz, and pulse energies of 0.3 - 1.5 μJ were investigated for optimum waveguide parameters. A slightly overfilled 0.6 NA lens was used to focus the beam beneath the sample surface. The inscription beam was polarised perpendicular to the waveguide propagation axis. The sample transverse translation inscription velocity was investigated for the range of 9 – 20 mms^{-1}. Waveguides with diameters over the range of 30 – 80 μm were inscribed with 40 and 80 elements. The waveguides were inscribed so the light propagates through the longest length of the sample (6 mm, y axis as shown in Figure 5.3). The sample's end facets were then polished after inscription to remove any surface damage and waveguide non-uniformity. A transmission microscope image of a waveguide fabricated in Cr:ZnS viewed from the end facet is shown Figure 5.4 (b).

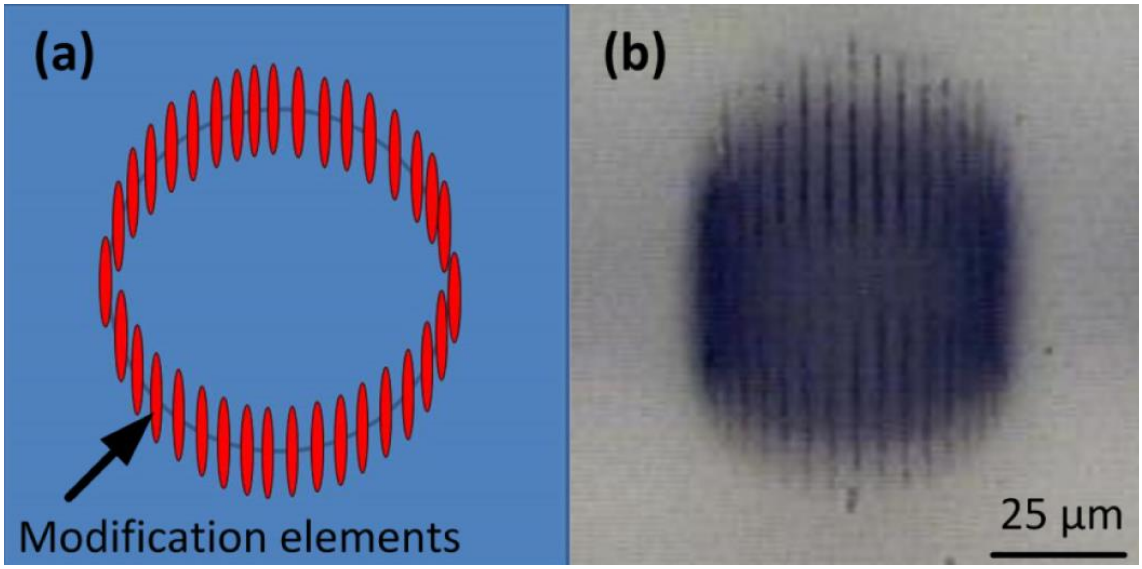

Figure 5.4.(a) Schematic of depressed cladding waveguide, red elements represent the irradiated area of the Cr:ZnS. (b) transmission microscope image of waveguide viewed from the end facet. This waveguide had a diameter of 60 µm and was made up of 40 elements.

It was found that an optimum modification single element was inscribed with 0.3 µJ of pulse energy. There were a large number of waveguides fabricated in the Cr:ZnS sample with this pulse energy. In order to optimise the single mode waveguide parameters, 1.9 µm pump light was coupled into the waveguides with a 50 mm CaF_2 lens. The outputs of the waveguides were then imaged on to a Mid-IR camera with a 50 mm CaF_2 lens. A pump filter was placed before the camera so it imaged the fluorescence of the sample. All the waveguides were checked for single mode guiding and the peak intensity of the florescence was measured. It was found that the 40 µm waveguides did not guide light very well, and all the 80 µm waveguides were multimode. Of the 60 µm diameter waveguides, the one which consisted of 40 elements and inscribed at 20 mm/s was found to emit the highest peak fluorescence. It was this waveguide that was used for laser operation.

5.3. Cr:ZnS Waveguide Laser

A laser cavity was assembled around the 60 µm dimeter Cr:ZnS waveguide. A Tm:doped fibre laser was used as a pump source with a wavelength of 1918 nm. This is 228 nm red shifted from the peak of the absorption cross-section [70]. A longer pump wavelength was chosen to reduce the quantum defect of the laser system and thus reduce the amount of energy that gets transferred into heat. This should reduce the impact of Cr:ZnS high

dn/dT on the laser performance. This will allow further power scaling of the laser compared with conventional Er:Fibre pumping [157]. The disadvantage of reduced pump absorption can be mitigated from the longer single pump interaction length of a waveguide laser compared with a bulk laser. The pump laser used was a turnkey system manufactured by AdValue model number AP-Tm-0028 with 1.5 W of CW output power. The pump power was controlled with a variable reflective ND wheel. The reflected pump was sent to a beam dump. The pump light was coupled into the waveguide by an AR coated CaF_2 plano-convex lens with focal length 50 mm through the input coupler. The input coupler was AR coated for the pump wavelength and 99.6% reflective over the range 2050 – 2430 nm. The Cr:ZnS sample was mounted on a copper base that was passively air cooled. A range of output couplers reflectivity was investigated, ranging from 60% to 99% reflective at the signal wavelength. The laser output was collimated with an AR coated CaF_2 plano-convex lens with a focal length of 50 mm. A 2 μm longpass filter was placed after the output lens to filter out any non-absorbed pump light before the beam was incident on the characterisation equipment. Figure 5.5 shows a diagram of the laser setup:

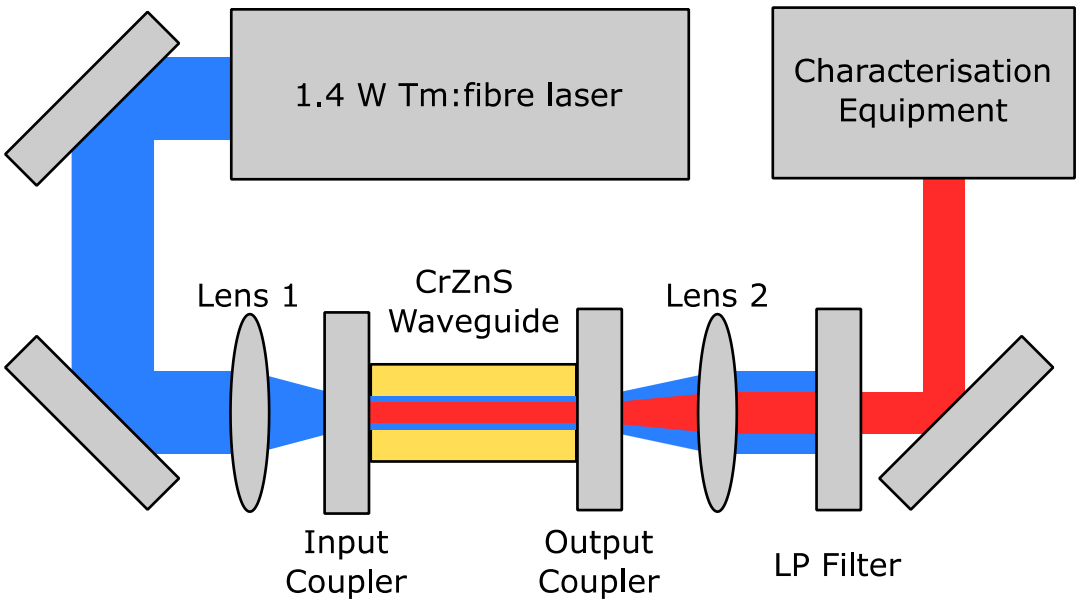

Figure 5.5. Schematic of Cr:ZnS waveguide laser used in the CW laser operation investigation. Lenses 1 and 2 are AR coated CaF_2 lenses with 50 mm focal length. LP is a 2000 nm longpass filter to remove any non-absorbed pump light.

The pump power and laser output power were measured with a thermal power meter (Spectra-Physics 407). The Cr:ZnS sample was not AR coated, thus there will be Fresnel reflections at each surface. The calculated Fresnel reflections of 15% at the input was subtracted from the value of the measured pump power before the input objective lens. This accounts for the maximum available pump power that can be coupled into the waveguide. A 2 μm longpass filter was placed after the output objective lens to filter any non-absorbed pump light before the beam was incident on the power meter. This filter has a transmission of 91.6% at the signal wavelength and hence the presented power values were adjusted to give the power that exited the laser. The pump power has been plotted against the output power for the four output couplers as shown in Figure 5.6:

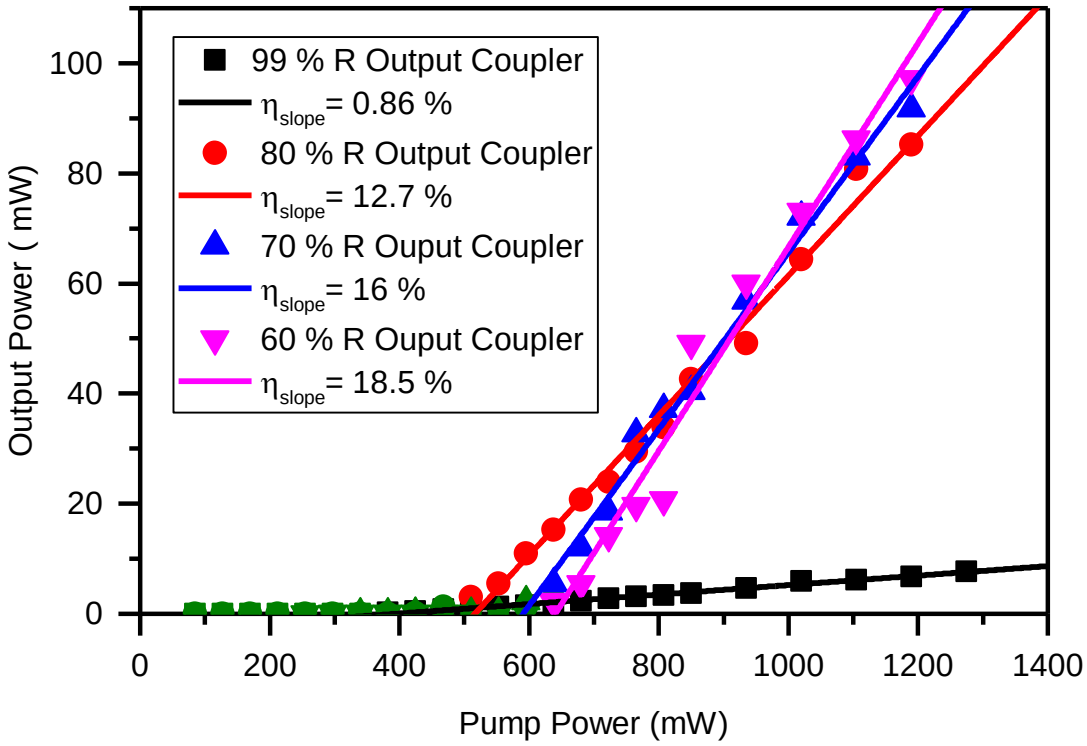

Figure 5.6. Characterisation of Cr:ZnS waveguide laser output power for different output coupler reflectance. The pump power has been compensated for a Fresnel reflection at the input of the air-Cr:ZnS surface. The output power of a 99% reflective (black squares), 80% reflective (red circles), 70% reflective (blue triangle) and 60% reflective (pink triangle) output couplers have been fitted with a linear fit. The green data points were near or at threshold and have been removed for the fitting.

The maximum output power was found to be 97 mW using a 60% reflectivity output coupler with a pump power of 1190 mW. The laser threshold was 641 mW and the slope efficiency was 18.5%. Threshold was 394 mW, 515 mW and 591 mW for the output

couplers of 99%, 80% and 70% reflectivity respectively. The maximum output power is only limited by the available incident pump power of 1190 mW. No thermal roll over was observed, which suggests that the laser can be further power scaled with a more powerful pump source [58].

The efficiency of the waveguide laser is lower than the 40% demonstrated in a bulk Cr:ZnS laser [162]. This is probably due to the cavity losses. Passive measurement of the Cr:ZnS waveguides would require a signal source at the laser wavelength, however this was not available. A different method is to use Findlay-Clay analysis, which is a method for calculating the total cavity loss [163]. This method uses the measurement of laser threshold for different output coupler reflectance. Using Equation 24 and extrapolating threshold power vs. -ln(1/Reflectivity) the cavity losses can be calculated [164].

$$-\ln(R) = 2g_0 l - \delta$$

Equation 24

where R is mirror reflectance at the signal wavelength, g_0 is the small signal gain, l is the cavity round trip length and δ is the total cavity loss. The Findlay-Clay analysis for the Cr:ZnS waveguide lasers is given in Figure 5.7.

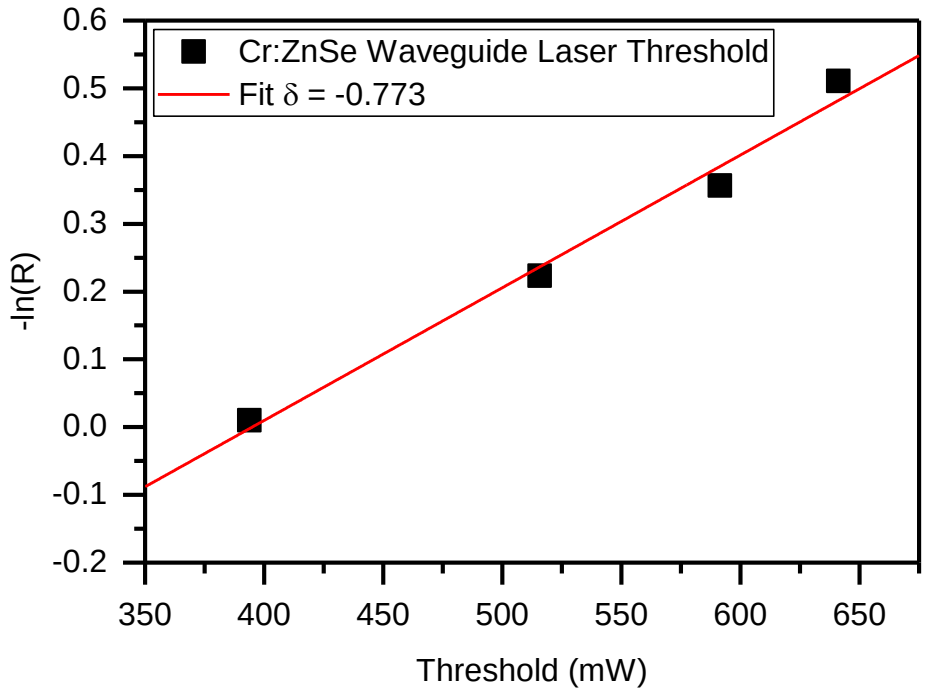

Figure 5.7. Findlay-Clay analysis of Cr:ZnS waveguide laser. From the linear fit the total cavity loss was is 6.4 dB.

From the graph, the total cavity losses were calculated to be of 6.4 dB. This is the total cavity round trip loss and hence accounts for more than the waveguide propagation loss. There are additional losses from Fresnel reflections, bulk material loss and coupling losses of the pump. The loss from the four Cr:ZnS-air Fresnel reflections per round trip is 2.8 dB. The bulk material single pass loss of diffusion doped Cr:ZnS is 0.4 dB/cm [157]. With these loss removed, an upper limit for the propagation loss of the Cr:ZnS waveguide is calculated to be 2.6 dB/cm. The waveguide propagation loss demonstrated in Cr:ZnS cladding waveguides is larger than that of Cr:ZnSe [58], which is expected from the reduced laser performance observed in Cr:ZnS.

The output mode of the laser was imaged using a Mid-IR camera (FLIR SC7000). For this measurement, a 30 mm focal length plano-convex lens was used to focus the output of the waveguide on to the focal plane of the camera. The focal plane of the camera was located 453 mm from the lens. The pixel pitch of the camera is 30 μm. From these three pieces of information, the magnification of the optical system was calculated using the thin lens approximation. The mode image, given in Figure 5.8, was taken with the 60% reflective output coupler and an incident pump of 1155 mW. The mode is near 2D Gaussian with a slight asymmetry. The raw data was fitted with a Gaussian function in the x and y axis. From the fit the mode was calculated to have a $1/e^2$ diameter of 35.8 μm and 31.3 μm in the x and y axis respectively.

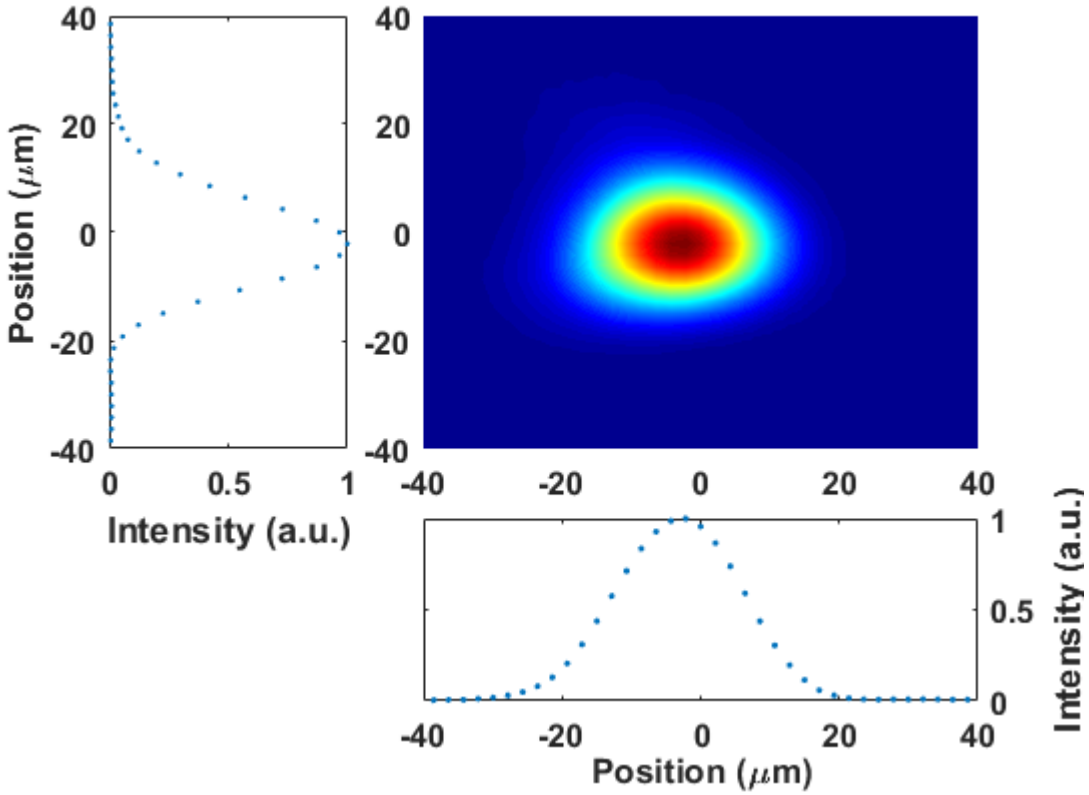

Figure 5.8. Output mode image of Cr:ZnS waveguide lasers. Image taken with 30 mm focal length lens and Mid-IR camera (FLIR SC7000).

The wavelength of the laser was measured with a monochromator (Zolix Omni-λ 300) with a resolution of 0.4 nm. The measurement was taken with the 60% reflective output coupler pumped with 1150 mW of pump power. The free running laser emission was centred at 2332.6 nm, corresponding to the peak of the emission cross-section [70], with a FWHM of 2.2 nm as shown in Figure 5.9:

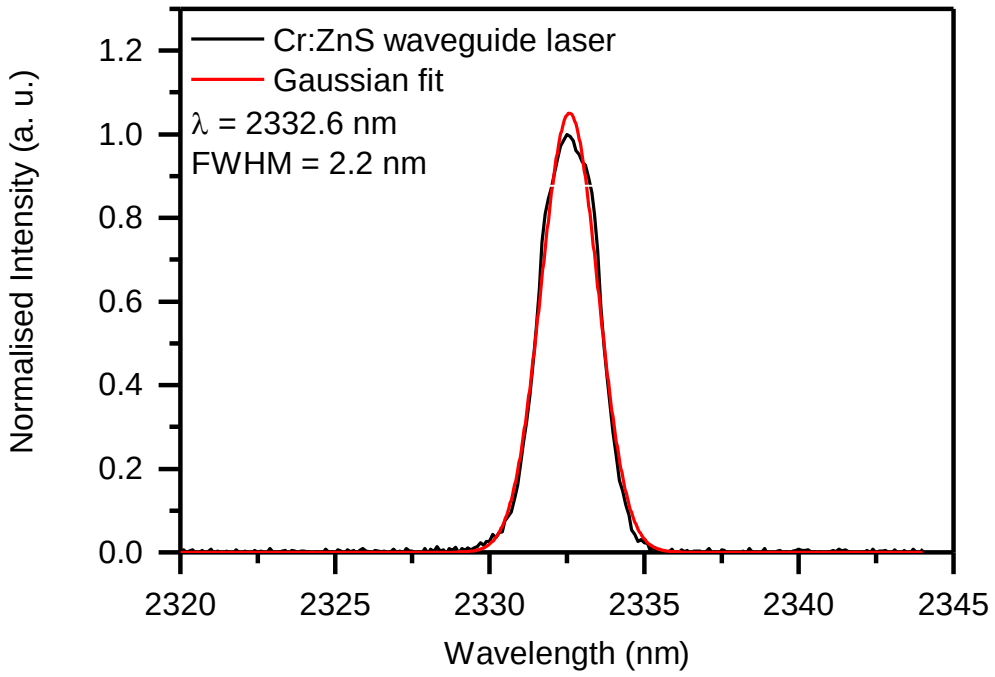

Figure 5.9. Normalised wavelength spectra of Cr:ZnS waveguide laser using Zolix Omni-λ 300 monochromator. The measurement was taken with a 60% reflective output coupler. From the Gaussian fit, the laser peak was calculated to be 2332.6 nm with a FWHM of 2.2 nm.

The measured linewidth of 2.2 nm from the waveguide laser is much narrower than that of the free running bulk lasers. A free running bulk microchip Cr:ZnS laser was found to have a 70 nm linewidth [165] and a >100 nm linewidth was measured in standard bulk cavity laser by Sorokin [17]. In my literature search, I noted that there are many papers on Cr:ZnS lasers that demonstrate free running lasers [149, 157, 166], but the linewidths of the free running lasers are omitted. From this gives further evidence that free running diffusion doped polycrystalline Cr:ZnS lasers have a tendency to emit a broad linewidth made up of many individual narrow spikes. Broad linewidth was not observed with the Cr:ZnS depressed cladding waveguides fabricated using ULI. Similar line narrowing in ULI fabricated waveguides in Cr:ZnSe and Fe:ZnSe have been observed [51, 57, 58].

5.4. Conclusion

For the first time, waveguides have been demonstrated in Cr:ZnS. The waveguides inscribed were the annular depressed cladding type. A waveguide laser was formed by butt coupling two mirrors to the waveguide end facets. This CW free running laser demonstrated a pump limited maximum output power of 97 mW with a 60% reflective

output coupler. The emission was centred at 2332.6 nm with a narrow linewidth of 2.1 nm. With this configuration, the laser had a threshold power of 641 mW. A low threshold power of 394 mW was demonstrated with a 99% reflective output coupler for lower power applications. The waveguide losses were found to be 2.6 dB/cm by Findlay-Clay analysis using the results for 99%, 80%, 70% and 60% reflective output couplers. The output mode of the waveguide laser was found to be near 2D Gaussian with a slight asymmetry. To improve laser performance, further optimisation of the waveguides to reduce propagation and coupling loss should be investigated. AR coating of the end facets of the substrate will reduce cavity loss and improve pump coupling.

Our implementation of guided wave geometry in Cr:ZnS has a lower slope efficiency than demonstrated in bulk Cr:ZnS lasers but this compromise can be accepted because of the compact size. This laser cavity had a total length of 18.7 mm, of which 12.7 mm is the dichroic mirrors. Direct coating of the waveguide end facet with the input and output coupler was not investigated in this work because of the flexibility offered by using different output couplers. Implementing this would reduce the cavity size to the length of the waveguides with no need for cavity alignment. The laser could then be pumped by butt coupling a fibre or pigtailed diode to the waveguide end facet and then bonding them in place. This would result in a compact laser system with no moving parts, making it resistant to vibrations. Implementing this design with diode pumping could reduce the total size of the system to something that will fit inside a laser pen platform, the cost reductions of which could facilitate Mid-IR lasers being implemented in consumer grade products. An example of this could be a replacement of Nd:YAG lasers for range finding, often used in golf to measure the distance to the hole. Cr:ZnS would be attractive for range finding because of its emission in the atmospheric transmission window and the added advantage of being at an eye safe wavelength.

This experiment was the first demonstration of a Cr:ZnS waveguide laser. This work has been published as a letter in the OSA journal Optics Express [53].

6. Fe:ZnSe Waveguide Laser

6.1. Introduction

Lasers operating in the atmospheric transmission windows of the Mid-IR (2-5 μm) spectral range are desirable for material processing of plastics, breath analysis, LIDAR and countermeasure applications [167, 168]. Cr^{2+} doped ZnSe and ZnS cover the 2 μm - 2.4 μm transmission window with high average power and narrow linewidth [70]. There is a second atmospheric transmission window in the Mid-IR from 3.5 μm to 4.2 μm, which is beyond the tuneable range of Cr doped II-VI lasers [17, 169]. However, changing the active ion to Iron (Fe) results in a broadly tuneable laser that covers this longer wavelength window. The shifting of the emission to longer wavelengths is from the d^6 electron configuration of Fe^{2+} ions experiencing a reduction in the strength of the field splitting in the ZnSe host when compared with the d^4 configuration of Cr^{2+} ions[61].

The first Fe:ZnSe laser was demonstrated in 1999 by Adams et al. [170]. This work built on the initial Cr:ZnSe laser research by Deloach et al. [12] and Page et al. [13]. It is worth noting that luminescence had also been demonstrated in Fe:ZnS as far back as 1967 at liquid helium temperatures by Slack and O'Meara [171]. Since then, Fe:ZnSe bulk lasers have demonstrated pure CW output powers of 1.5 W [70], gain switched output powers of 35 W [18] and wavelength tuneable output from 3700-5050 nm [70, 172]. One of the limitations of the Fe:ZnSe laser transition is the short upper state lifetime at room temperature due to multi-phonon quenching [170]. The variation of luminescence lifetime with temperature is plotted in Figure 6.1. The upper state life time of Fe:ZnSe at 77 K is 57 μs, which compares favourably with that of the Cr:ZnSe life time of 5.4 μs, but Fe:ZnSe lifetime drops to 0.38 μs at room temperature. The practical implication of this quenching is that Fe:ZnSe must be cryogenically cooled to achieve CW laser operation. However, room temperature operation has been demonstrated in gain switched operation with laser efficiencies of up to 34% [173].

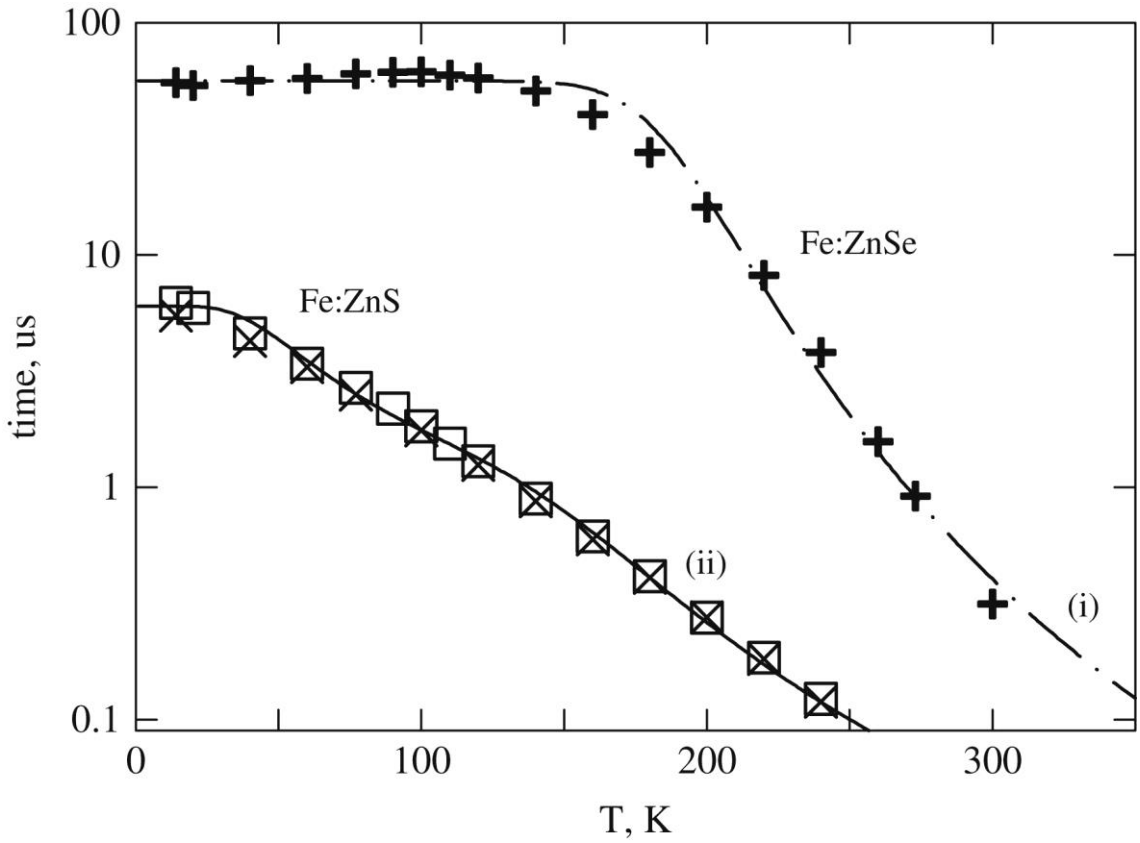

Figure 6.1. Luminescence lifetime of Fe doped ZnSe and ZnS. This graph has been reproduced from Myoung et al. [174].

Many of the potential applications for Mid-IR laser systems are in non-laboratory environments, such as countermeasure applications, hence it is desirable for the laser to be insensitive to vibrations and require minimal post-fabrication alignment. This criterion is not often met by bulk laser systems, which include many free space optics. A monolithic waveguide design geometry allows the removal of the need for free space optics in the laser system. ZnSe fibre is currently in development with propagation losses of < 1 dB/cm at 1550 nm, but there has not yet been any demonstration of transition metal doped ZnSe fibres lasing [21]. A solution is therefore needed to leverage the advantages of waveguide geometry in the commercially available bulk Fe:ZnSe polycrystalline samples [16]. Building on the initial work by MacDonald et al. [23] in developing ULI waveguides in ZnSe, it has been shown in subsequent papers and in this thesis to adapt well to new Cr:II-VI materials. Thus, the ULI of waveguides in Fe:ZnSe was investigated as a method to create the first fully monolithic 4 μm solid state laser system.

This investigation was performed at Heriot-Watt University in close collaboration with Dr Gary Cook from AFRL WPAFB. For this work, Dr Cook spent five weeks working

in the laboratory at Heriot-Watt with our research team developing the Fe:ZnSe waveguide laser.

6.2. Waveguide Fabrication and Passive Guiding Characterisation

Previous investigations into ULI fabricated waveguides in ZnSe and Cr:ZnSe have shown annular depressed cladding waveguides to be most suitable for Mid-IR guiding [58]. Hence inscription of annular depressed waveguides were investigated in Fe:ZnSe.

6.2.1. Waveguide Fabrication in Fe:ZnSe

As discussed in Chapter 2 the inscription laser is a key element in ULI waveguide fabrication. Many of the inscription laser's parameters such as repetition rate, maximum pulse energy and emission wavelength are fixed. This creates limitations on the waveguide fabrication because these properties have a strong effect on the induced refractive index change [34]. Recent waveguide fabrication in the NLO group at Heriot-Watt used one of two Yb:fibre laser systems [23, 53, 56, 160, 175, 176]. Initial work in the NLO group implemented amplified Ti-Sapphire lasers, but the low repetition rate of sub 10 kHz resulted in slow translation speeds and thus long waveguide fabrication times [177]. Ti-Sapphire lasers are also unsuitable for inscription in ZnSe because the emission peak of Ti:Sapphire laser is centred around 800 nm, which corresponds to the peak of ZnSe nonlinear refractive index [23]. Thus for Fe:ZnSe a Yb based inscription system will be used to investigate the potential for Mid-IR waveguides.

There were two chirp pulse amplified Yb:fibre lasers available for waveguide inscription in the NLO group - a Fianium and an IMRA system. The specifications of the lasers systems are given in Table 10:

Laser system	HE-1060-1uJ-fs	μJewel D400	Satsuma HP
Manufacture	Fianium	IMRA	Amplitude Systems
Laser type	Chip pulse amplified Yb:Fibre laser		
Maximum pulse energy	1 μJ	2.5 μJ	20 μJ
Pulse picker *before* amplifier section	No	Yes	Yes
Pulse picker *after* amplifier section	Yes	No	Yes

Repetition rate	Single shot to 2 MHz	100 kHz to 5 MHz	Single shot to 2 MHz
Adjustable pulse compressor	No	Yes, Manually controlled	Yes, Computer controlled
Pulse duration (manufacture specification)	<500 fs	<1 ps	<400 fs

Table 10. Chirp pulse amplified Yb:Fibre lasers considered for waveguide fabrication in Fe:ZnSe. Data taken from manufacturers' specification sheets shipped with the lasers.

The IMRA system has been used for all previous inscription work in ZnSe because of its higher maximum pulse energy and user adjustable pulse compressor. In Cr:ZnSe, it was found that inscription energies of 2.5 μJ and a stretched pulse of 750 fs or longer were needed [24, 58]. Therefore, of the two systems only the IMRA was suitable for ULI of waveguides fabrication in ZnSe.

Unfortunately, the IMRA laser failed the week before Dr Cook arrived at Heriot-Watt University with the Fe:ZnSe samples, so an alternative laser was needed. The IMRA laser system was removed from the optical table and shipped back to its manufacturer for repair. A Fianium laser was recommissioned from storage. The laser was aligned through the power control section, gantry and inscription lens of the automated waveguide fabrication rig detailed in [52, 78]. With the factory settings, the Fianium laser outputted 870 mW of average power at a repetition rate of 1 MHz, resulting in a pulse energy of 0.87 μJ. The pulse width of the laser was measured with an APE Pulse Check USB autocorrelator to have a FWHM of 4.8 ps, much longer than the <500 fs when new. From this, the laser had a sufficiently long pulse width for inscription in ZnSe, but not sufficient pulse energy.

The drive current of the diodes that pump the Fianium laser can be user adjusted with computer control up to a factory set maximum. The 870 mW was measured at the output of the laser head by using the factory set maximum. This current setting when the laser was new produced an output power of 1 W and pulse width of < 500 fs, but over time the efficiency of the diodes has reduced. The manufacturer was contacted to see if the factory set maximum current value could be increased. Fianium's user support team was very helpful and provided unlock codes to remove the current limit on the lasers. This allowed us to investigate the laser's output power and pulse width with different diode current

values. The current was increased from the factory default value of 700 a. u. to 860 a. u., which also increased the output power to 1.2 W. This resulted in a pulse energy of 1.2 μJ which is not sufficient to modify ZnSe. The pulse width for the increased diode current was reduced to 420 fs. The reason for this is that the non-user adjustable compressor was set in the factory for operating at around the 1 μJ energy level. The compressor was set to compensate for the linear and nonlinear dispersion of the optical fibre in the laser system at this energy level. The nonlinear dispersion varies with pulse energy in the fibre, thus the compressor must be adjusted to have an optimally compressed pulse at the output. When the diodes age and reduce in efficiency, the pulse energy reduces so less nonlinear dispersion is induced in the fibre. This resulted in the compressor overcompensating and chirping the exiting pulse.

The grating compressor of the Fianium laser is inside the laser head, access to which would require breaking the factory sealed box to adjust it. This would then void the manufacturer's warranty and so we did not investigate optimisation of the grating compressor. Further increasing of the diode current was also not investigated to avoid premature failure of the diodes. From these results, we found that the laser did not have a suitable pulse energy or pulse width for inscription in ZnSe. Equally, it was found to be a suitable system for the inscription of nanograting in fused silica. A combination of the nanograting inscription step and a post chemical etch step produced an imaging flow cytometry device. This was published by Jagannadh et al. [45] in IEEE Journal of Selected Topics in Quantum Electronics.

From this investigation it was clear there was no suitable laser inscription system at Heriot-Watt University for waveguide fabrication in Fe:ZnSe. Therefore, fabrication of the waveguides at an external site was the only viable option. The Fe:ZnSe sample with waveguide fabrication G-code was sent to Optoscribe for inscription. The polycrystalline Fe:ZnSe sample used in this work had dimensions of 1.82 mm × 4.76 mm × 6.94 mm and an Fe^{2+}-ion concentration of 8.88×10^{18} cm^{-3}.

The laser implemented in the inscription system at Optoscribe was Yb-fibre based and manufactured by Amplitude Systems. The laser has the ability to output pulses of 20 μJ and has a computer controllable pulse width from a few hundred femtoseconds to tens of picoseconds. Full specification of the laser is given in Table 10. An initial inscription test run at Optoscirbe was investigated using 2.1 μJ pulse energy. This was the pulse energy

found to give the optimum performance waveguides in Cr:ZnSe [58]. Using this pulse energy, the inscription laser was found to ablate the Fe:ZnSe at a depth of 81 μm. An image of the waveguides inscribe with are lower pulse energy is shown in Figure 6.2:

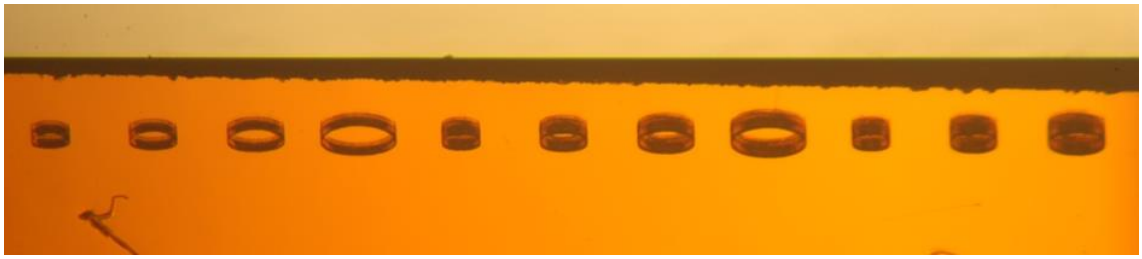

Figure 6.2. Transmission microscope image of waveguides fabricated in Fe:ZnSe. Inscription parameters are given in Table 11, waveguides are numbered from 1 to 11, left to right respectively. Field of view of image is 3.2 mm by 0.7 mm.

For successful waveguide fabrication, the pulse energy was reduced to 1.8 μJ. This was found to be sufficiently below the ablation threshold of the material. The full inscription parameters investigated for fabrication of the waveguides in Fe:ZnSe at Optoscribe are given in Table 11.

Inscription laser parameters												
Repetition rate	100 kHz											
Pulse width	1 ps											
Pulse energy	1.8 μJ											
Polarisation with respect to waveguide propagation direction	Horizontal											
Waveguide Geometry												
Waveguide #	1	2	3	4	5	6	7	8	9	10	11	12
Diameter (μm)	100	125	150	200	100	125	150	200	100	125	150	200
Number of elements	100	125	150	200	100	125	150	200	100	125	150	200
Number of overwrites	1	1	1	1	5	5	5	5	9	9	9	9
Translation speed (mm/s)	9	9	9	9	9	9	9	9	9	9	9	9

Table 11. ULI parameters for annular depressed cladding waveguides in polycrystalline Fe:ZnSe for laser applications.

For the first time, permanent modification by ULI in Fe:ZnSe has been demonstrated, as can be seen from the transmission microscope image in Figure 6.2. It was found that the modification pulse energy needed for Fe:ZnSe is less than that of Cr:ZnSe, but is similar to that of ZnSe. Further investigations at WPAFB by S. McDaniel and G. Cook found the larger pulse energy needed for modification in Cr:ZnSe arises from residual linear absorption of the Cr atoms at the inscription laser wavelength [24]. The difference in linear absorption at the inscription wavelength for Cr:ZnSe and Fe:ZnSe is given in Figure 6.3:

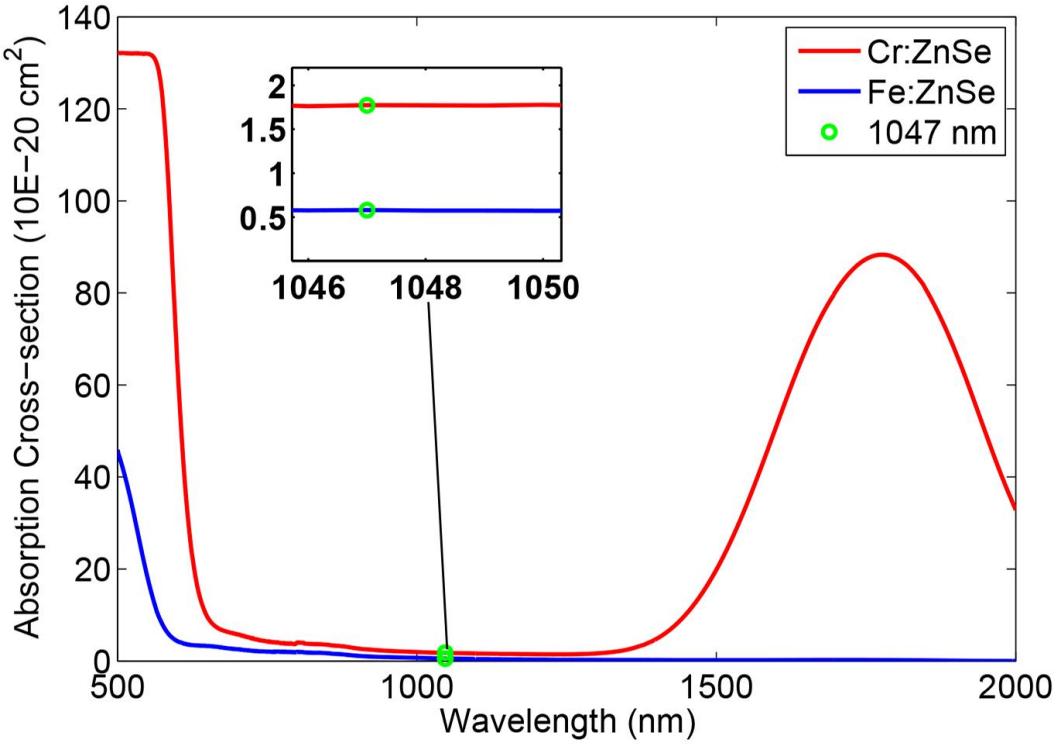

Figure 6.3. Absorption cross-section of Cr:ZnSe (red line) and Fe:ZnSe (blue line). Insert shows an expanded view of the absorption at the inscription laser wavelength 1047 nm. This graph has been reproduced from McDaniel et al. [24].

From visual inspection, it can be seen that the Fe:ZnSe waveguides are asymmetrical. This was caused by an error in the conversion of the code written for use at Heriot-Watt to the system at Optoscribe. The overall result was that the refractive index compensation was incorrect. However, a second inscription run at Optoscribe was not possible, so the waveguides were investigated for guiding and laser operation in the Mid-IR regardless.

6.2.2. Mid-IR Passive Characterisation of Fe:ZnSe Waveguides

The passive losses of the Fe:ZnSe waveguides in the Mid-IR were investigated. The laser used for the passive testing was a 1.5 W Er:thin disc laser operating at 2940 nm, corresponding to the peak of Fe:ZnSe absorption cross-section [68]. Due to high dn/dT of ZnSe, the waveguide mode size, coupling and propagation losses were expected to be temperature dependent. To investigate this passive characterisation was performed at 77 K, the temperature where the laser testing was to be performed and at room temperature.

Cooling of the sample below room temperature requires the sample to be inside a vacuum chamber to stop condensation forming which could freeze the sample and surrounding optics. The preparation steps used for mounting the sample inside the cryostat are as follows: the Fe:ZnSe sample was wrapped in indium foil to form an effective thermal contact with the cold finger. The cold finger is shown in Figure 6.4. The cold finger was mounted to the cryostat contact plate. A vacuum chamber was formed around the cold finger. The chamber was evacuated to 1×10^{-6} mbar with a turbo pump. This thermally isolates the sample and cold finger from the external uncoated CaF_2 windows, and hence stops condensation forming on the sample and windows.

Figure 6.4. Photograph of the copper cold finger. Note the image was taken with a wide angle lens (phone camera) hence has strong optical distortions. The diameter of the cold finger was 10 mm.

The free space passive characterisation set-up is shown in Figure 6.5. The set-up consisted of L1, an uncoated 100 mm focal length lens that is used to collimate the slightly divergent pump laser. The pump light was coupled into the Fe:ZnSe waveguides using an E coated 50 mm lens CaF_2 from Thorlabs model number LA5763-E. The Thorlabs E coating is designed to be antireflective from 2 – 5 μm. This lens was experimentally found to have a focal length of 35 mm at 2.94 μm. The output from the waveguides were imaged onto a Mid-IR camera (FLIR SC7000) with a second Thorlabs LA5763-E lens which was found to have a focal length of 45 mm.

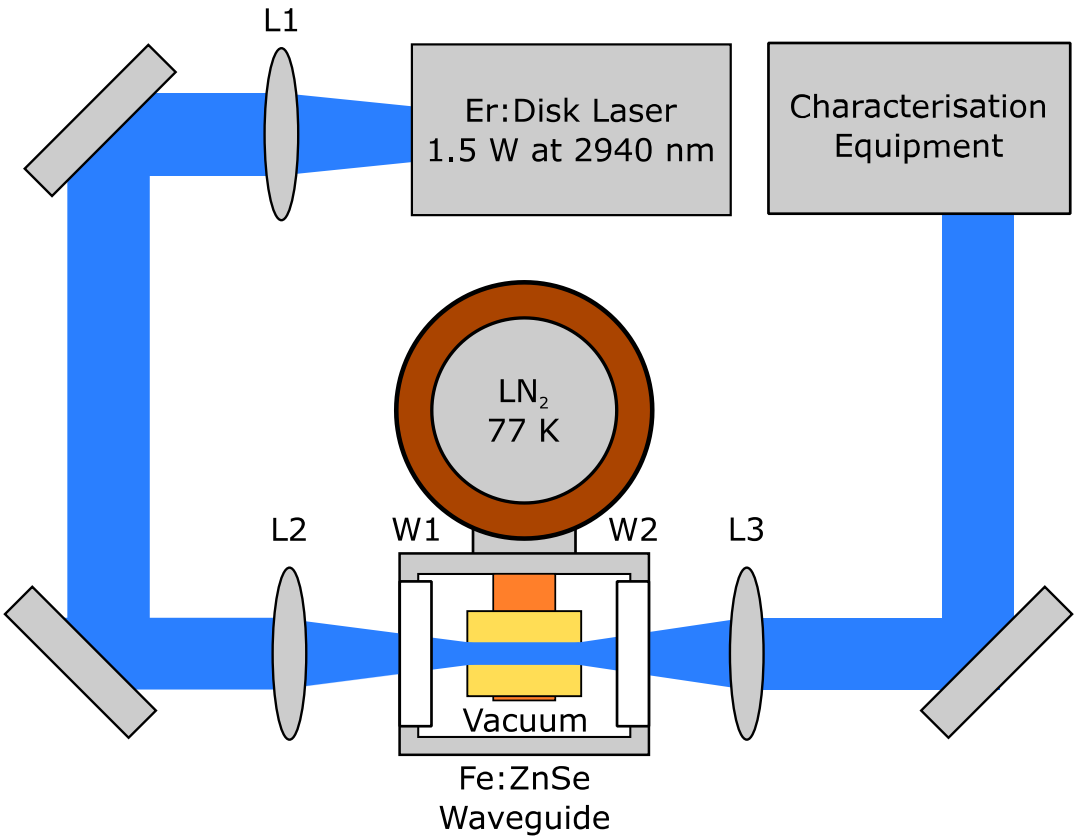

Figure 6.5. Passive waveguide test setup for Fe:ZnSe waveguides at 77 K. L1 is a non-AR coated 100 mm focal length CaF_2 lens. L2 and L3 are AR coated CaF_2 lenses with focal lengths of 50 mm. W1 and W2 are non-AR coated CaF_2 windows.

From the Mid-IR imaging, Waveguide 4 was found to be a promising single mode waveguide at 2940 nm. An estimate of waveguide propagation and coupling losses was taken by measuring the pump power before L2 and after L3. To remove the absorption from the Fe^{2+} ions, the sample was translated to a non-modified part of the sample and a power measurement at L2 and L3 were taken. The laser power before L2 was measured with a Spectra Physics power meter and after L3 was measured with a Laser Probe Rk-5720 Power radiometer which is more accurate at low powers. The measurements were taken at 77 K and room temperature. The loss from coupling and propagation of Waveguide 4 (see Table 11) were found to be 0.63 dB and 0.27 dB for 77 K and room temperature respectively. If all of this loss is attributed to propagation losses an upper limit value can be calculated to be 0.9 dB/cm and 0.4 dB/cm at 77 K and room temperature respectively. This is a promising result when compared with the 0.7 dB/cm losses demonstrated in Cr:ZnSe waveguides [58]. From this measurement, the waveguides were deemed viable for laser investigation.

Building on the demonstration of low loss Mid-IR waveguides in Fe:ZnSe, laser operation was investigated. For the first demonstration of a Fe:ZnSe waveguide laser, CW operation was investigated.

6.3.1. Optical Pumping of Fe:ZnSe and its Limitations

Compared with Cr:ZnSe where high power pump sources with average powers of over 100 W are readily available, the CW pump sources for Fe:ZnSe are limited [70]. Part of this can be attributed to the location of the Fe:ZnSe absorption band as shown in Figure 2.3, which is at a longer wavelength than can be supported by step index silica fibre. This means silica fibre lasers are not suitable for pumping Fe:ZnSe. Less common fibre based materials are available for low loss Mid-IR transmission such as ZEBLAN and Telluride based fibres, but they suffer from poor mechanical properties. Of the rare earth ions, Er^{3+} emitting on the $^4I_{11/2}$-$^4I_{13/2}$ line, 2.94 μm in a YAG host, is a suitable pump source for Fe:ZnSe [178]. However, CW operation and power scaling of this emission line are limited by the self-termination of the lower laser level $^4I_{13/2,}$ the 1550 nm emission line, this has limited the commercially available lasers to the few Watt range [179]. Two 1.5 W Er:YAG thin disk lasers were used in the Evans et al. demonstration of 804 mW of CW output power [180]. For high energy pulsed applications, pumping the Fe:ZnSe cavity with flash lamp pump Er:YAG lasers can be effective. Martyshkin et al. [181] demonstrated 0.35 J pulses from a Fe:ZnSe laser, with a total output average power of 35 W when pumped with four flash lamp pumped Er:YAG lasers. Mirov et al. [70] experimented with a higher temperature operation of Fe:ZnSe using the pulsed Er:YAG sources. With this, laser operation was demonstrated from 77 K to 250 K, opening up the option of using thermo-electric coolers [70]. Room temperature operation was not achieved because the typical pulse width of a flash lamp pumped Er:YAG laser is in the few hundreds of microseconds, much longer than the 300 ns upper state lifetime of Fe:ZnSe at room temperature [170, 181, 182]. A Q-switched Er:Cr:YSGG 2.8 μm source has been used to successfully pump a Fe:ZnSe laser at room temperature, but the pulse energy was limited to a few mJ [174]. The current power scaling record for room temperature operation has used a non-chain HF laser with a pulse width of 130 ns and maximum available pump pulse energy of over 1 J [173]. Using the HF laser as a pump, Fe:ZnSe demonstrated pulse energies of up to 192 mJ and slope efficiency of 34% at RT

[173]. The HF laser, however, is limited to its areas of applications because of safety concerns.

Cr:ZnSe lasers are being realised as a compelling pump sources for Fe:ZnSe lasers. This is because the output power of these lasers has been increasing rapidly, partially as a result of commercialisation by IPG Photonics [16]. A wavelength tuneable bulk Cr:ZnSe laser has demonstrated average powers greater than 5.5 W over the key 2.6-2.9 μm range[70]. This laser was used to pump a Fe:ZnSe laser. With this pump source, a Fe:ZnSe laser demonstrated an output power of 1.5 W with a slope efficiency of 30%. This represents the current power scaling record for a CW Fe:ZnSe laser [70]. Since this work was completed, a CW Cr:ZnSe laser producing 32 W at 2.94 μm has been developed [16]. This source has the potential to create a pure CW laser in the 10 W range at 4.1 μm. Additionally, tuneable waveguide lasers have been developed in Cr:ZnSe, as discussed early in this thesis. This work could be integrated with the Fe:ZnSe waveguides to create a fully monolithic laser system.

In this investigation, a compact CW Er:YAG thin disk laser was used because of its commercial availability from Sheaumann. For an initial laser demonstration, a 1.5 W thin disk laser was implemented as the pump source. The output of this pump laser was collimated with a CaF_2 lens of with focal length 100 mm. This pump laser has a small footprint, 6 cm by 10 cm, making it an ideal source for a compact Fe:ZnSe waveguide laser system.

6.3.2. Fe:ZnSe Waveguide Laser Operation

Laser operation of the low loss Fe:ZnSe waveguides were investigated. The laser was operated in pure CW, and so was cooled to 77 K with liquid nitrogen. A schematic of the Fe:ZnSe waveguide laser cavity is given in Figure 6.6. An extended cavity with intra cavity lenses was implemented to allow for change of the output coupler reflectance. The pump mirror was a flat mirror AR coated for 2.94 μm, the pump wavelength, and 99.9 % reflected at the signal wavelength. A 35 mm E coated lens was used to couple the pump light into the waveguides. The sample was mounted on a copper cold finger inside the cryostat using the method implemented in the passive waveguide characterisation section. The windows of the cryostat were CaF_2 disks, 25.4 mm in diameter and 4 mm thick. Liquid nitrogen was used as the coolant in the cryostat. The liquid nitrogen was topped up as and when required. The output of the waveguide was collimated with an E coated

CaF_2 50 mm lens. Flat 90% and 80% mirrors were used for the output coupler in this investigation. Laser operation was also investigated without an output coupling mirror. In this configuration, laser feedback was provided by the 17.5% Fresnel reflection for the ZnSe-vacuum interface. This configuration benefits from a reduced intra cavity loss, since W2 and L3 are outside the cavity. The unabsorbed pump light was blocked by a reflective longpass 3000 nm filter.

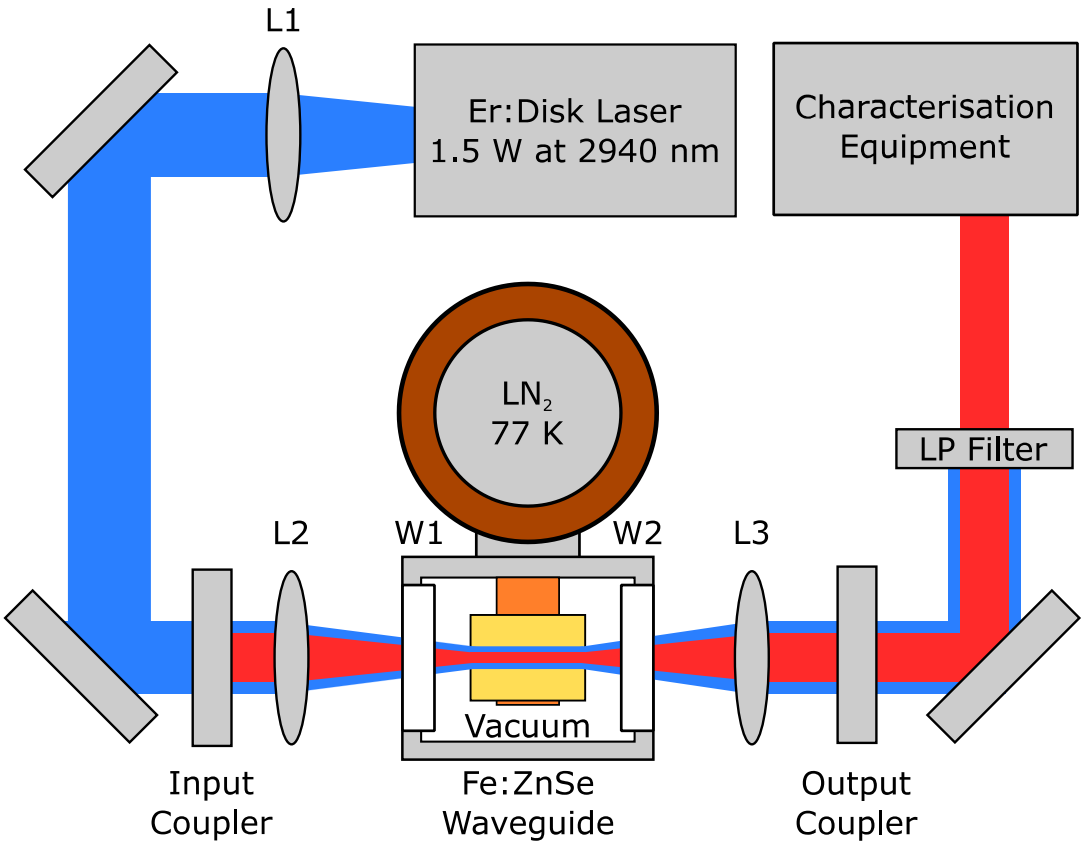

Figure 6.6. Schematic of Fe:ZnSe waveguide laser in a cryostat cooled by liquid nitrogen. L1 is a 100 mm focal length CaF_2 lens used to collimate the pump laser. L2 and L3 are AR coated intra cavity CaF_2 lenses with a focal length of 50 mm. W1 and W2 are CaF_2 windows. Longpass Filter is a 3000 nm longpass filter used to remove residual pump light.

Of the waveguides 3 and 4 (see Table 11) were found to lase with the available pump power. Both waveguides were characterised by the three different output coupling reflectance. The pump power and output power were measured with a thermal power meter. The pump power quoted is reduced by 17.5% because this would be reflected at the input facet and so will not be absorbed by the laser. The laser performances of waveguide Waveguides 3 and 4 are plotted in Figure 6.7 and Figure 6.8 respectively.

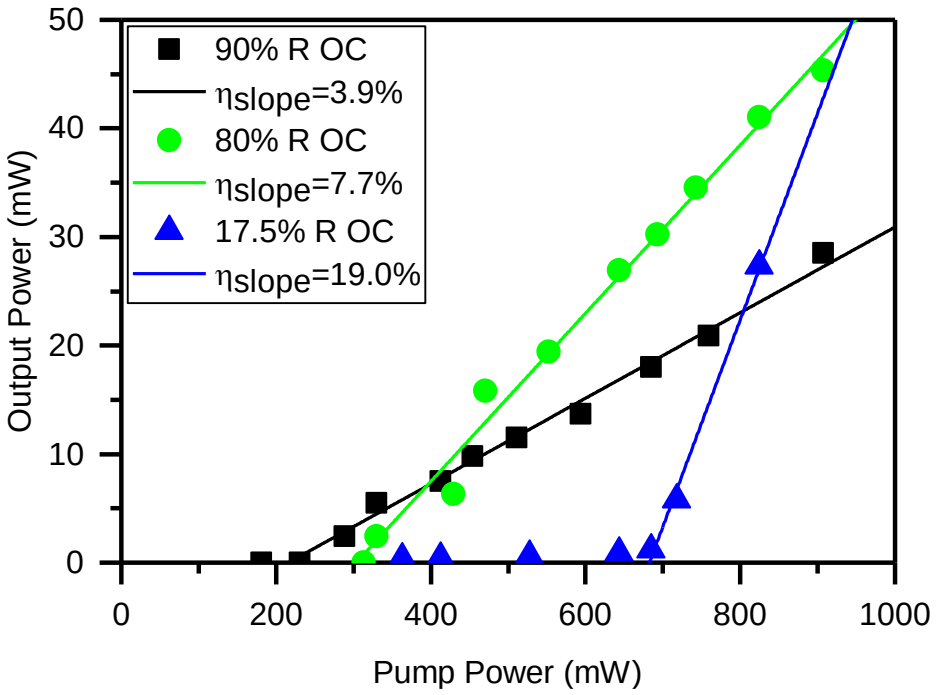

Figure 6.7. Waveguide 3: Input power vs. output power of Fe:ZnSe waveguide lasers. This waveguide had an inscription diameter of 150 μm.

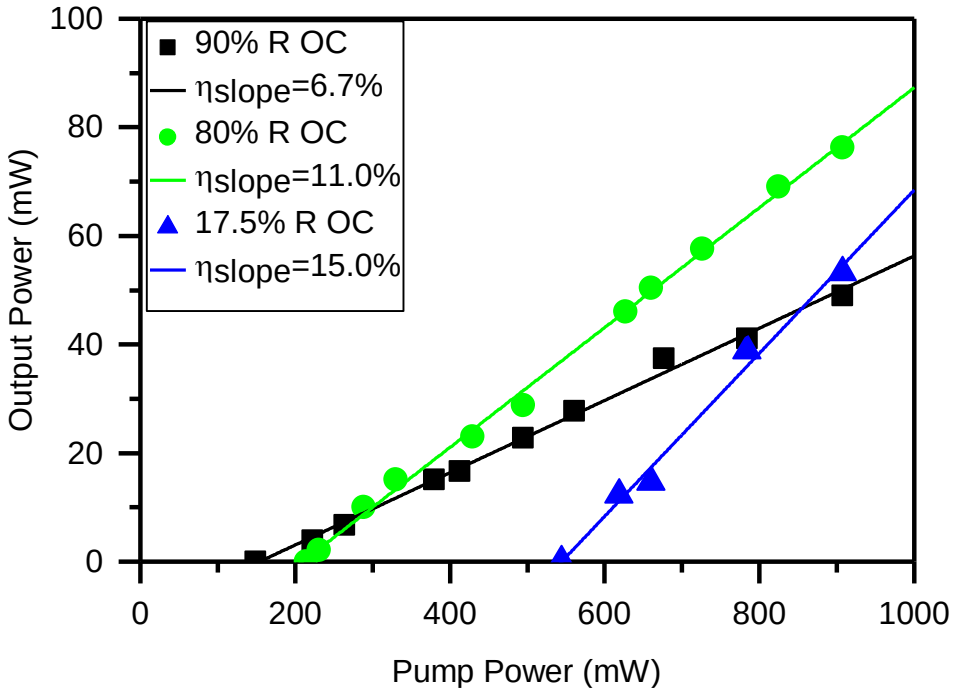

Figure 6.8. Waveguide 4: Input power vs. Output power of Fe:ZnSe waveguide lasers. This waveguide had an inscription diameter of 200 μm.

The slope efficiency and threshold power of both waveguides are summarised in Table 12:

Output coupler	Waveguide 3		Waveguide 4	
	Slope efficiency	Threshold	Slope efficiency	Threshold
90%	3.9%	216 mW	6.7%	154 mW
80%	7.7%	303 mW	11.0%	210 mW
17.5%	19.0%	683 mW	15.0%	544 mW

Table 12. Summary of slope efficiency and threshold power for ULI fabricated waveguides in Fe:ZnSe at 77 K. Values calculated from linear fit of input vs. output power measurements.

The inscription parameters of Waveguide 4 were found to be optimal for laser operation. This was expected from the passive investigations. Waveguide 4 demonstrated an output power of 76 mW with a slope efficiency of 11.0% using an output coupler with R = 80%. The threshold of laser action was found to be 210 mW. The lowest threshold of the waveguide laser was measured to be 153 mW with an output coupler with R = 90%. There was no observed rollover at the highest pump power of 908 mW, thus we can infer that that the laser performance was pump limited and further power scaling is possible [148]. In addition, for optimal laser performance, the end facets of the Fe:ZnSe sample should be AR coated.

The wavelength spectra of the laser were characterised. For this measurement, a monochromator (Zolix Omni-λ 300) with resolution of 0.4 nm was used. The monochromator found the main peak of the waveguide laser emission to be centered at 4122 nm with a FWHM of 6 nm. The spectra of Fe:ZnSe waveguide, number 4, laser under the full available pump power, 908 mW, is plotted in Figure 6.9.

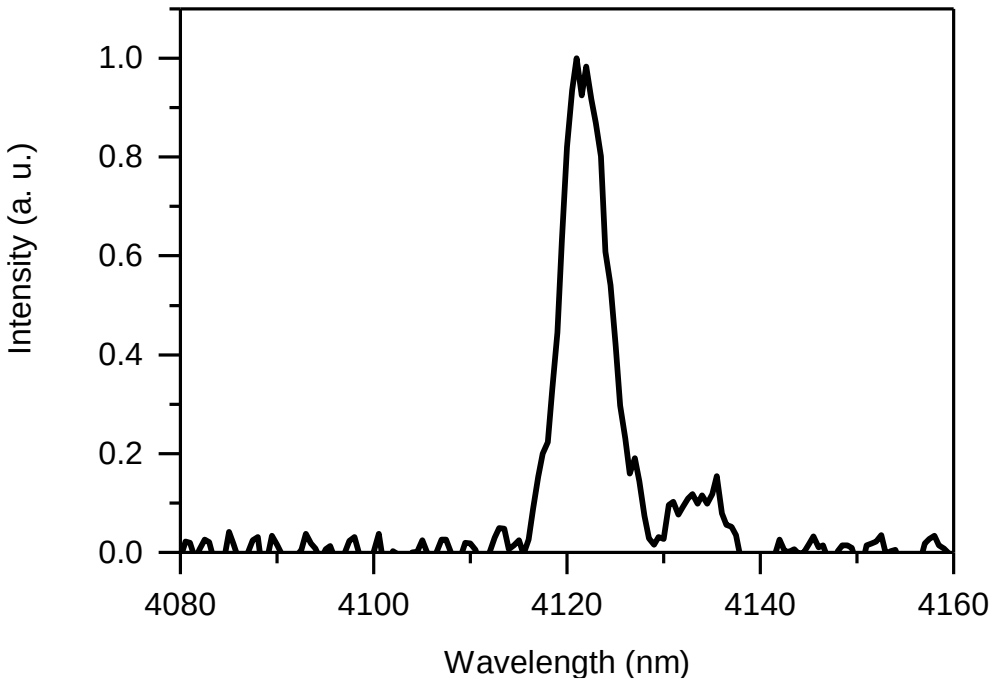

Figure 6.9. Normalised spectra of Fe:ZnSe waveguide laser under 908 mW of pump power. Waveguide 4: output coupler was 80% reflecting.

The mode quality of the waveguide laser was investigated by imaging the near field of the lasers guided mode with the Mid-IR camera. Both lasing Waveguides, 3 and 4, were imaged. The mode field images were taken with the waveguides lasing from the end facet Fresnel reflection. The magnification of the imaging system was calculated by measuring the distance from the back of the lens to the CCD plane of the camera and using the thin lens approximation. A diagram of the near field imaging setup is given in Figure 6.10.

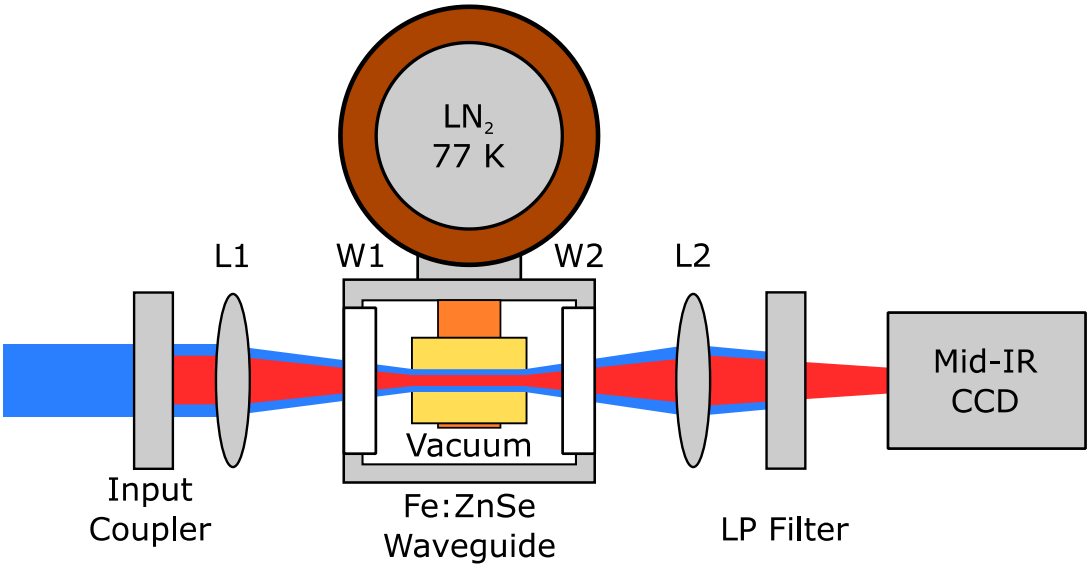

Figure 6.10. Near field mode imagining setup for Fe:ZnSe waveguides. L1 is a 35 mm AR coated CaF_2 lens. L2 is a 50 mm AR coated CaF_2 lens. LP filter is a 3000 nm longpass filter. The signal and pump guide modes where image with the setup. For pump guide mode imaging, the LP filter was removed.

The distance from L2 to the CCD plane was measured to be 1.1 m, resulting in an optical magnification of 21. The mode field images of the signal and pump with a transmission microscope image of the waveguide end facet is shown in Figures 6.11.

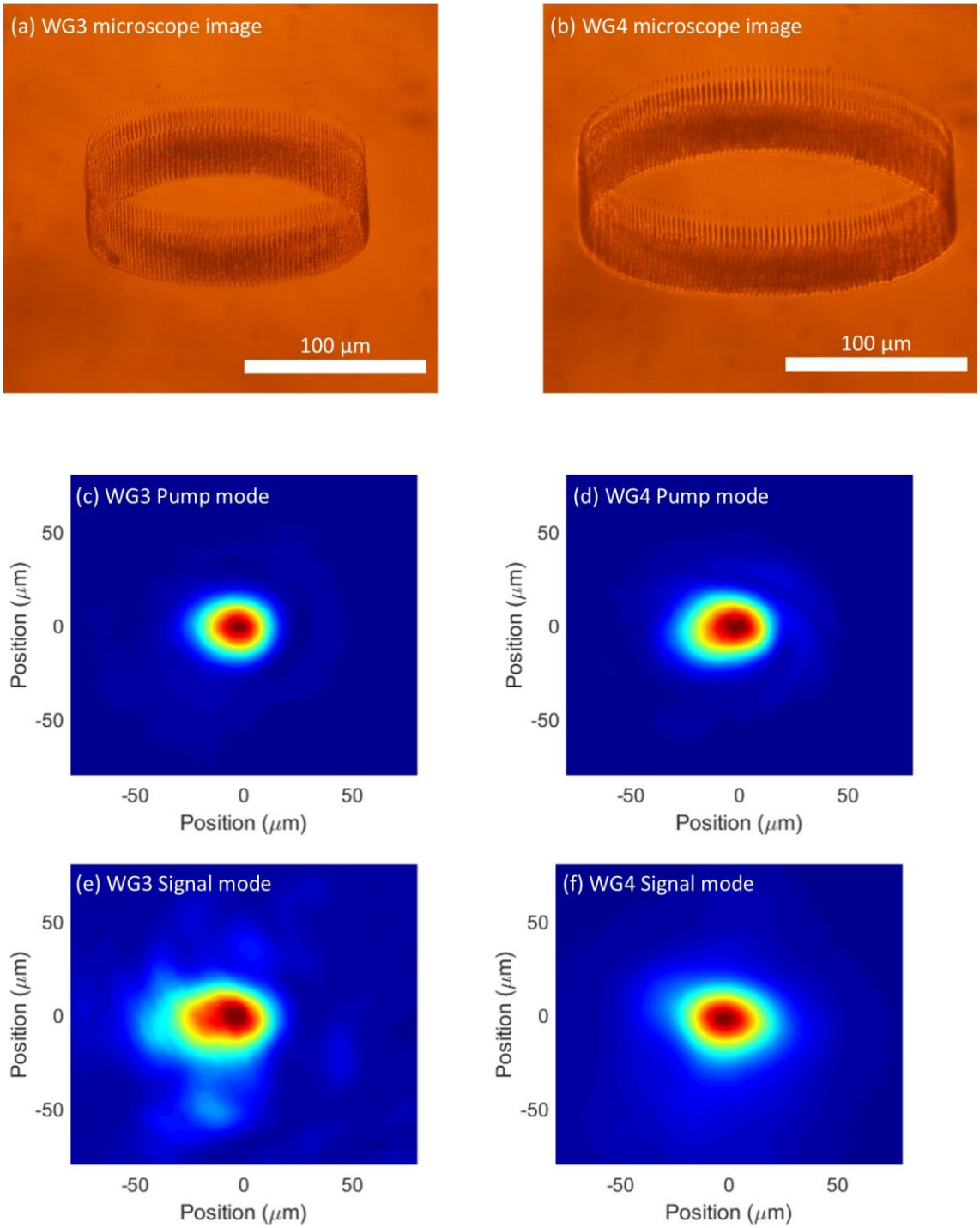

Figures 6.11(a) and (b)are transmisson microscope images of Waveguides 3 and 4 respectively. Images (c) and (b) are mode images of the pump mode from Waveguides 3 and 4 respectively. Images (e) and (f) are the mode images of the lasing signal mode of Waveguides 3 and 4 respectively.

The camera control software for the Mid-IR camera (FLIR SC7000) allows a single frame to be saved as a matrix of values in an Excel file. This file was imported into Matlab for

viewing and analysis. The mode field images were centred on the pixel with the highest intensity value. A slice in the x and y axes centred on this peak value was fitted with a Gaussian profile. The FWHM of the guided modes is summarised in Table 13:

Waveguide #	Type	FWHM in x-axis	FWHM in y-axis	Asymmetry ratio
3	Pump	27.1 μm	24.5 μm	1.1
3	Signal	42.9 μm	31.0 μm	1.4
4	Pump	33.0 μm	26.2 μm	1.3
4	Signal	37.2 μm	31.0 μm	1.2

Table 13. Summary of MFD measurements of Fe:ZnSe waveguides at 77 K

From the MFD measurements, Waveguide 4 showed a better overlap between the pump and signal mode. The smaller MFD of Waveguide 4 compared with its waveguide diameter mean that there is less interaction with the highly scattering modified cladding region, thus reducing the waveguide's losses. The effect of this is observed in the improved laser performance of Waveguide 4.

6.3.3. Fe:ZnSe Waveguide Laser Loss Analysis

Waveguide losses are often difficult to accurately measure without using destructive methods, for example the cutback method, because of the relatively short propagation length, in this case 7 mm. Three independent non-destructive loss measurement techniques were used to characterise the waveguide loss. These are direct measurements of transmission loss, Findlay-Clay analysis and imaging of the scattering loss.

Direct comparison with the transmitted 2.94 μm pump light under guiding and non-guiding conditions was investigated. These measurements alows the decoupling of loss contributions for the waveguide and sample absorption. This results in an estimate of the loss induced by the waveguide. Full details of this measurement were discussed in the passive characterisation section 6.2.2. An upper estimate of the optimum waveguide propagation losses at 77 K was calculated to be 0.9 dB/cm at the pump wavelength.

The propagation loss of the waveguide at the Fe:ZnSe laser's emission wavelength was investigated using Findlay-Clay analysis [163, 164]. Findlay-Clay analysis calculates the total cavity loss of a laser's resonator from the relation given in Equation 25:

$$-\ln(R) = 2g_0 l - \delta$$

Equation 25

where R is the reflectivity of the output coupler at the signal wavelength, g_0 is the small signal gain, l is the length of the gain medium in the cavity and δ is the total cavity loss. The total cavity loss is the y-axis intersect of a plot of $-ln(R)$ vs. laser threshold. Findlay-Clay analysis of the lasing waveguides is plotted in Figure 6.12:

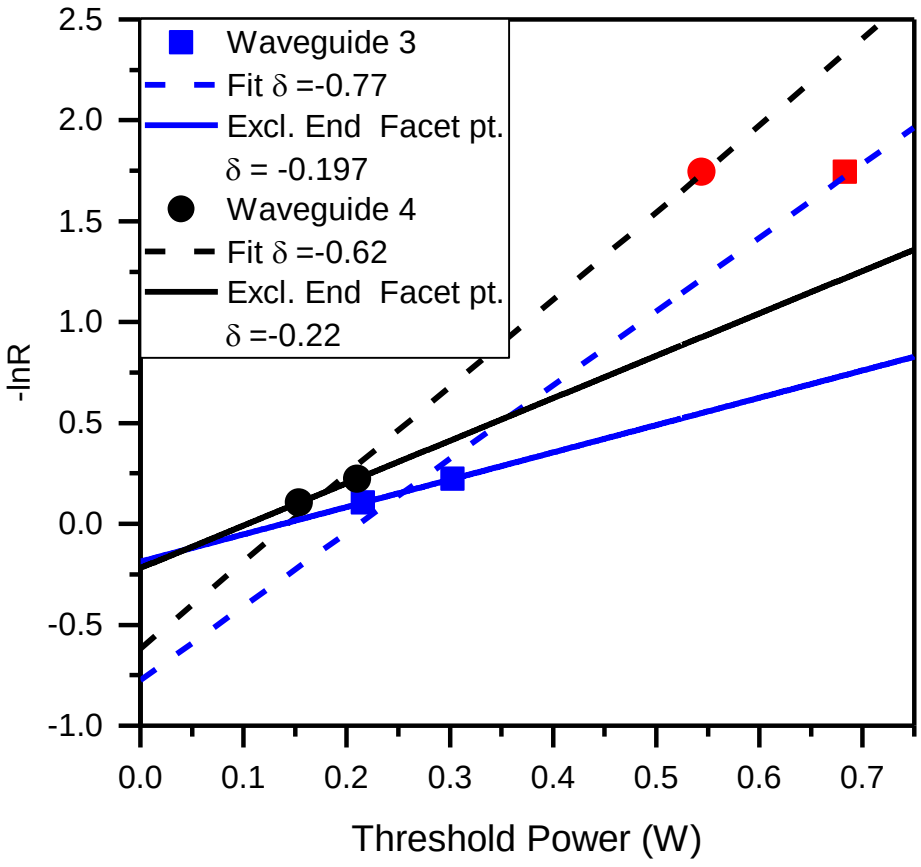

Figure 6.12. Findlay-Clay analysis of Fe:ZnSe waveguide laser. The blue lines are a linear fit for Waveguide 3 data points, as the black lines are for Waveguide 4. The dotted lines include all data points and the solid lines omit the lasing for the end facet data points.

Findlay-Clay is an effective method for calculating the waveguide losses of a waveguide laser cavity [53, 58, 84]. However, this method requires a different reflectivity output coupling mirror for each data point. Availability of mirrors suitable for laser operation of Fe:ZnSe at 4 μm is limited because of the small number of research groups working in this spectral band. For this experiment, we had access to an 80% and 90% reflective output coupler. In order to increase the number of data points used in the analysis, the lasers result from the Fresnel reflection as the feedback mechanism was included in the

data set. However, when lasing from the Fresnel reflection at the waveguide end facet, the total intra cavity losses are reduced when compared with the output coupler cavity. This is because the window and intra cavity lens were outside the cavity. This improved slope efficiency and reduced threshold power for the Fresnel lasing case. Hence, when adding this data point to the Findlay-Clay analysis in Figure 6.12, the linear fitting will calculate higher cavity loss. Conversely, not including this point results in a linear fit of two data points, which is not sufficient for a line of best fit due to a small error in the data points, creating very large deviations in the value of cavity loss extrapolated from the linear fit. The total cavity loss in dB for both data sets was calculated from Equation 26 and the results are tabulated in Table 14.

$$Total\ cavity\ loss\ in\ dB = 10 \cdot \log(1 - \delta)$$

Equation 26

To find the propagation loss of the waveguide from this, the other cavity losses must be removed. A diagram of the laser's cavity with the sources of intra cavity loss are shown in Figure 6.13:

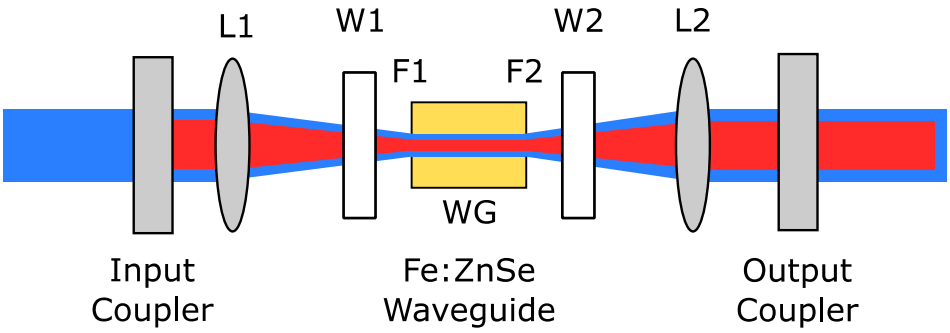

Figure 6.13. Schematic of intra cavity loss contributions in Fe:ZnSe waveguide laser. L1 and L2 represent the transmission loss the of the AR coated CaF_2 lens. W1 and W2 represent the transmission loss of the CaF_2 windows. F1 and F2 are the loss contributions from Fresnel reflections. WG is the propagation loss of the Fe:ZnSe waveguide.

As shown in the diagram, the extended cavity has four additional loss elements: the two windows and the two intra cavity lenses. The single pass transmission of the windows is 98.7% at the signal wavelength. There are two windows, therefore four instances of loss from the uncoated windows per round trip of the cavity. The total loss attributed to the windows in dB is 0.23 dB. The transmission loss of the two AR coated CaF_2 lens , L1 and L2, is 96.5% at the laser wavelength. From this, 0.62 dB of loss is attributed to the

lenses per round trip. These losses have been removed from the total cavity loss value calculated by the Findlay-Clay analysis to find the propagation loss of the waveguides given in Table 14:

Waveguide	Data points included	Total cavity loss (dB)	Loss of waveguide (dB)
3	90%, 80% and 17.5%	6.4	5.5
3	90% and 80%	1.0	0.1
4	90%, 80% and 17.5%	4.2	3.4
4	90% and 80%	1.1	0.2

Table 14. Fe:ZnSe waveguide laser cavity losses calculated by Findlay-Clay analysis

It is clear that the result of the Findlay-Clay analysis with the Fresnel reflection data included is invalid, due to the inconsistencies with previous passive measurements. The lowest loss waveguide calculated from Findlay-Clay analysis using only the two output coupling mirrors as data points was from Waveguide 3, with a total loss of 0.1 dB. This gives a waveguide propagation loss of 0.07 dB/cm, the lowest reported ULI waveguide loss in the Mid-IR by any material.

The propagation losses of the waveguides were measured using the scattering imaging technique, first demonstrated by Okamura et al. [183]. This method images the scattered photons along the direction of propagation of the waveguide. From the gradient of the scattered light reducing along the propagation axis, the waveguide losses can be calculated. Image analysis of the scattered light enables a non-destructive technique for estimating waveguide loss. This method also eliminates the need to carefully factor out entrance and exit coupling losses required for input/output measurements. This experiment was performed at room temperature because the side profile of the waveguide is not viewable in the cryostat. A diagram of the setup is given in Figure 6.14:

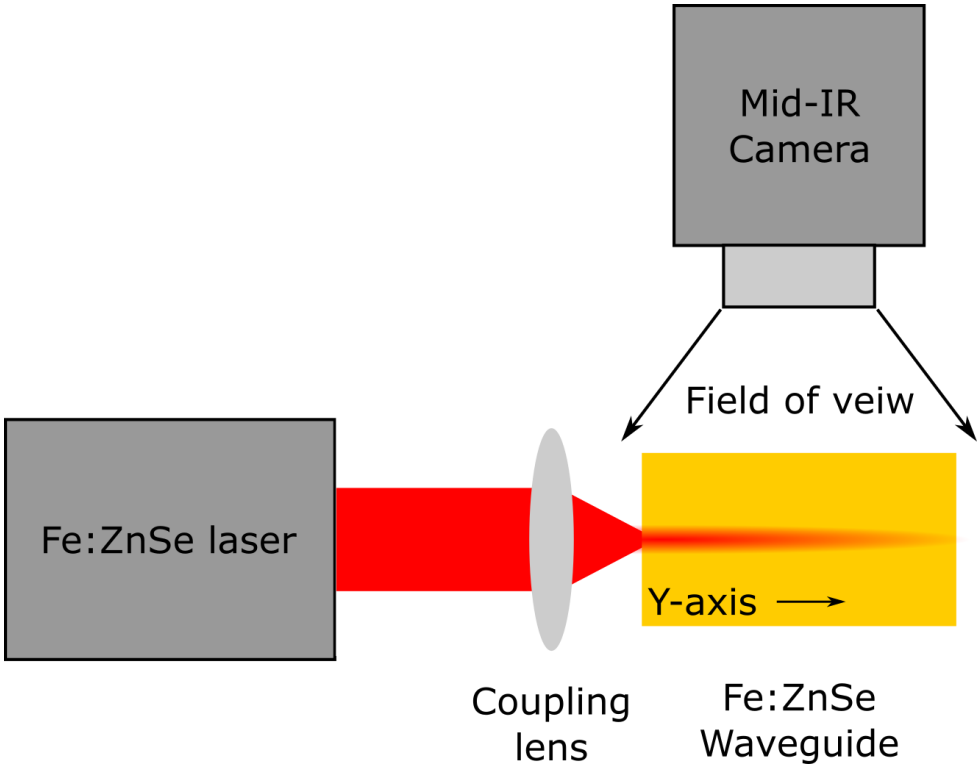

Figure 6.14. Schematic of experimental setup of scattering loss measurements using a Mid-IR imaging camera positioned transverse to the waveguide propagation direction

This experiment requires a signal source with the same emission wavelength as Fe:ZnSe lasers, which were not available at Heriot-Watt. A suitable Fe:ZnSe laser source was available at WPAFB. This experiment and data analysis was performed by S. McDaniel and J. Evens at WPAFB. The output of a free running bulk Fe:ZnSe laser operating at 4050 nm was coupled into the waveguide using a focusing lens. The scattering from the top of the waveguide was imaged using a Mid-IR camera (FLIR SC7000) with a wide field of view imaging objective.

Scattered intensity at any location along the waveguide propagation path in a sample is proportional to the beam intensity, *I*, at that point. The beam intensity at that point will be determined by the amount of light coupled into the waveguide reduced by all propagation losses, such as scattering and absorption, experienced by the guided mode up to that point. The intensity profile imaged by the camera will be proportional to the scattered and fluorescing light, if both are within the camera's wavelength detection range which is the case for this experiment. The change of intensity at position y along the y-axis is given by Equation 27. The reasonable assumption is that there is no nonlinear absorption.

$$\frac{dI(y)}{dy} = -(\alpha_S + \alpha_A)I(y)$$

Equation 27

where α_S is a scattering loss coefficient and α_A is the absorption coefficient. The absorption coefficient of Fe:ZnSe at the probe wavelength, 4050 nm, is negligible [170]. Thus α_A is set to zero and the solution to the first order differential equation is given by Equation 28.

$$I(y) = I_0 e^{-\alpha_s y}$$

Equation 28

where I_0 is the intensity at some starting point chosen by the researcher from the image. This point must not be the input facet of the waveguide due to the large amount of scattering from the end facet which is not linked to waveguide propagation loss.

S. McDaniel and J. Evens developed an image analysis process using MATLAB. This script converts an image to a plot of intensity vs. propagation distance, in this case pixel distance, as shown in Figure 6.15.

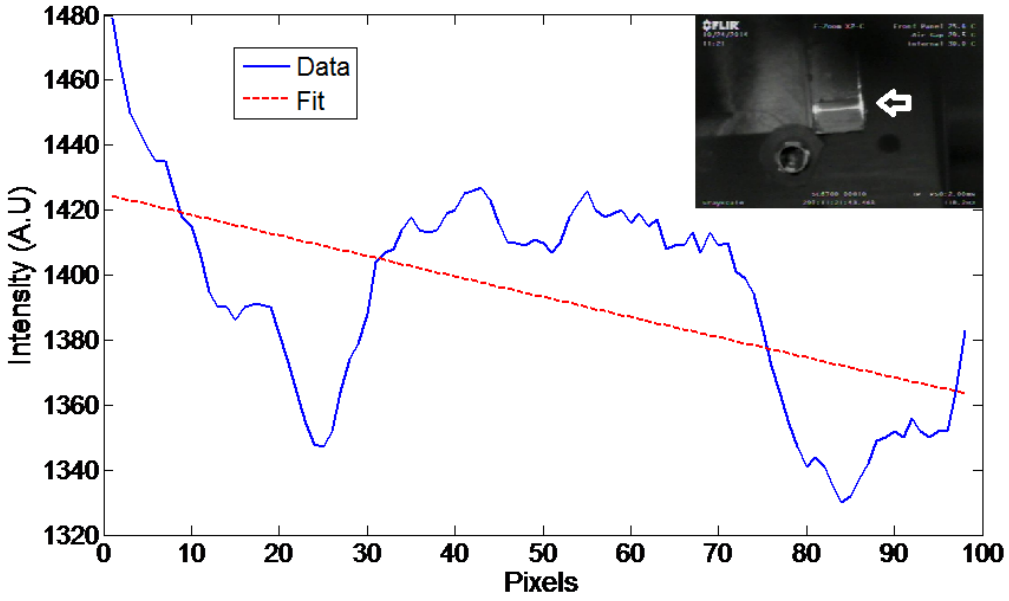

Figure 6.15. Scattering loss of Waveguide 4 measured by the scattering imaging method. The blue line is the measured data and the red dotted line is fit to that data. The inset shows the image captured by the Mid-IR camera. The arrow indicates the input facet.

The pixel data from the inset picture in Figure 6.15 was cropped to isolate the middle portion of the waveguide. This section was free from reflections at the crystal end facets.

The intensity was averaged in the transverse direction over the selected region to create a single dimensional vector of the field intensity along the propagation axis, the y-axis, as shown in Figure 6.14. The data in Figure 6.15 was fitted with an exponential of the form given in Equation 29:

$$I(t) = ae^{-\sigma y} + a_0$$

Equation 29

The fitting parameters were determined to be $a = 1425$, $\sigma = 4.5\times10^{-4}$, and $a_0 = 0.004$ by Matlabs least-squared fit tool. The waveguide losses can be calculated from the fitted values using Equation 30:

$$Waveguide\ propagation\ loss = -\frac{10}{L}\log_{10}(e^{-\sigma L})\ in\ untis\ of\ dB\ per\ cm$$

Equation 30

where σ is a fit parameter and L is the length corresponding to the selected section of the waveguide image used in the analysis in units of cm. This resulted in the propagation loss of Waveguide 4 at 4050 nm to be calculated as 0.46 dB/cm using the scattering imaging method. This shows that Waveguide 4 is low loss. The reliability of this technique deteriorates when the signal to noise ratio is small, which is the case when the scattering losses are low, as is the case with this experiment. Consequently, the values calculated here should be interpreted as an upper-bound of the propagation waveguide losses.

In summary, the value of the waveguide loss for the waveguide with the optimum inscription parameters for lasing was investigated using three methods. Direct measurement of the total waveguide loss at the pump wavelength gave a value of 0.4 dB/cm and 0.9 dB/cm at RT and 77K respectively. The Findlay-Clay method was used to calculate the in-situ total waveguide loss at the signal wavelength. This method found the total loss of the waveguide to be 0.14 dB/cm at 77 K. Imaging of the scattering loss at 4050 nm found the total waveguide loss to be 0.46 dB/cm at RT. From these results, waveguide loss at room temperature is in agreement from both the input/output measurement at the pump wavelength and the scattering loss measurement at close to the lasing wavelength to be around 0.4 dB/cm. At 77 K, the CW operating temperature of the laser, there is disagreement but the Findlay Clay analysis does not have a sufficient number of data points to be considered accurate. Thus a longer sample and application of the destructive cutback method is needed for a more accurate loss value. From the results

presented here, the losses are < 1 dB/cm. These losses are much higher than those of SM28 fibre, but the gain per unit length of Fr:ZnSe is typically greater than 20 dB/cm, making the waveguide loss sufficiently low for effective laser operation. Propagation losses of the Fe:ZnSe waveguides are comparable with previous demonstrations of ULI passive waveguide devices at 4 μm [184, 185].

6.4. Bulk Fe:ZnSe Laser

Bulk laser operation of Fe:ZnSe was investigated so that a direct comparison could be made with the work in ULI inscribed Fe:ZnSe waveguide lasers. Many examples of Fe:ZnSe bulk lasers have been demonstrated before, most notably the first one by Adams [170] and the current power scaling records for CW and pulsed operation [70]. However, the cavity configurations were not identical to those used in the waveguide experiments. A key difference is that the power scaling demonstrations mitigate loss from Fresnel reflections by implementing AR coatings on the end facets or implementing a Brewster cut crystal geometry. From this experiment, we wanted to get an in house measurement of the free running laser spectra since this has previously been commonly omitted [70, 173, 181, 182, 186]. Papers that have included a free running laser spectrum have found the emission to be made up a broadband of spikes spanning a range of around 50 – 100 nm [180, 187]. This broad spectral emission was not observed in the Fe:ZnSe waveguide laser demonstration. An example of this is given in Figure 6.16:

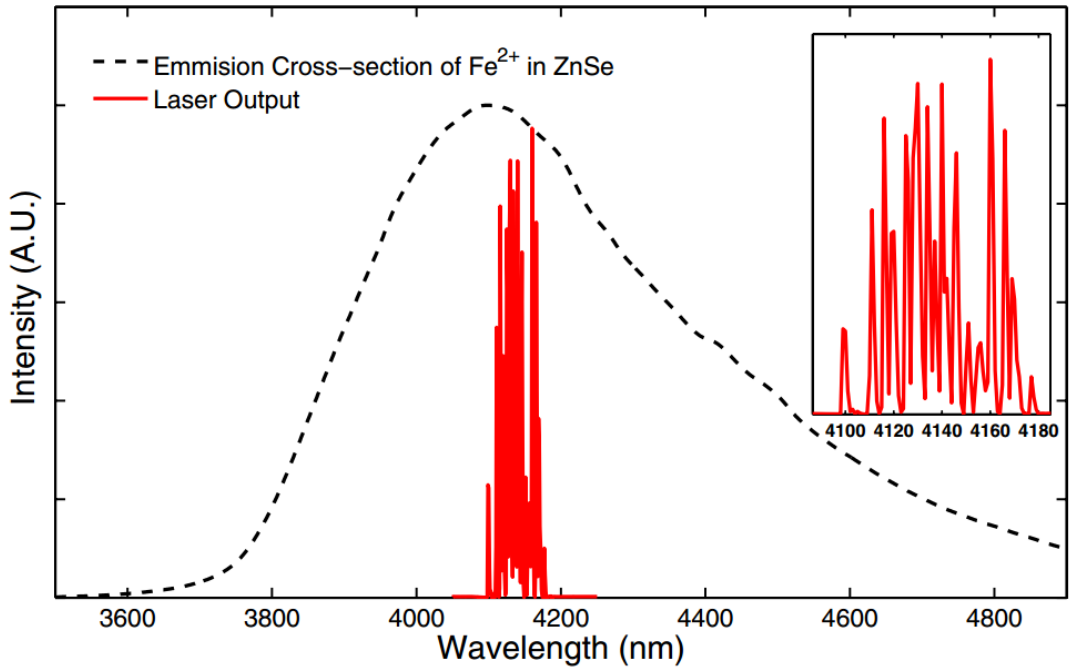

Figure 6.16. Emission spectrum of diffusion doped polycrystalline Fe:ZnSe bulk laser, red line. Insert shows an expanded view of the laser emission. Emission cross-section is shown by the black dotted line. This graph has been reproduced from Evans et al. [180].

The experimental setup for the bulk laser used the same optical components as those of the waveguide laser operation demonstrated in section 6.3.2 for consistency of results. A diagram of the bulk laser cavity is given in Figure 6.17. An extended cavity with intra cavity lenses was implemented. The pump mirror was a flat mirror AR coated for 2.94 µm, the pump wavelength, and 99.9 % reflected at the signal wavelength. A 35 mm E coated lens was used to couple the pump light into the waveguides. The sample was mounted in the cryostat using the method implemented in the passive waveguide characterisation section. The windows of the cryostat were CaF_2 disks, 25.4 mm in diameter and 4 mm thick. Once the vacuum in the cryostat had been formed, the liquid nitrogen was poured into the top of the cryostat. The liquid nitrogen was toped up as and when required. The output of the waveguide was collimated with an E coated CaF_2 50 mm lens. For the output coupler, a flat 90% mirror was used for the investigation. The unabsorbed pump light was blocked by a reflective longpass 3000 nm filter. To convert the waveguide cavity, as discussed in the previous section, into a bulk laser, the two intra cavity lenses were translated so that their focus moved from the end facets to the centre of the Fe:ZnSe sample. The Fe:ZnSe sample was translated horizontally, so that the pump and signal pass through to an unmodified section of the sample. The sample was not

translated in depth because there was a gradient in the dopant concentration. Lasing at the same depth below the top of the sample in the bulk and waveguide case ,maintained a uniform doping concentration between the two experiments. Uneven doping concentrations can be an issue with diffusion doping of ions into a host [116].

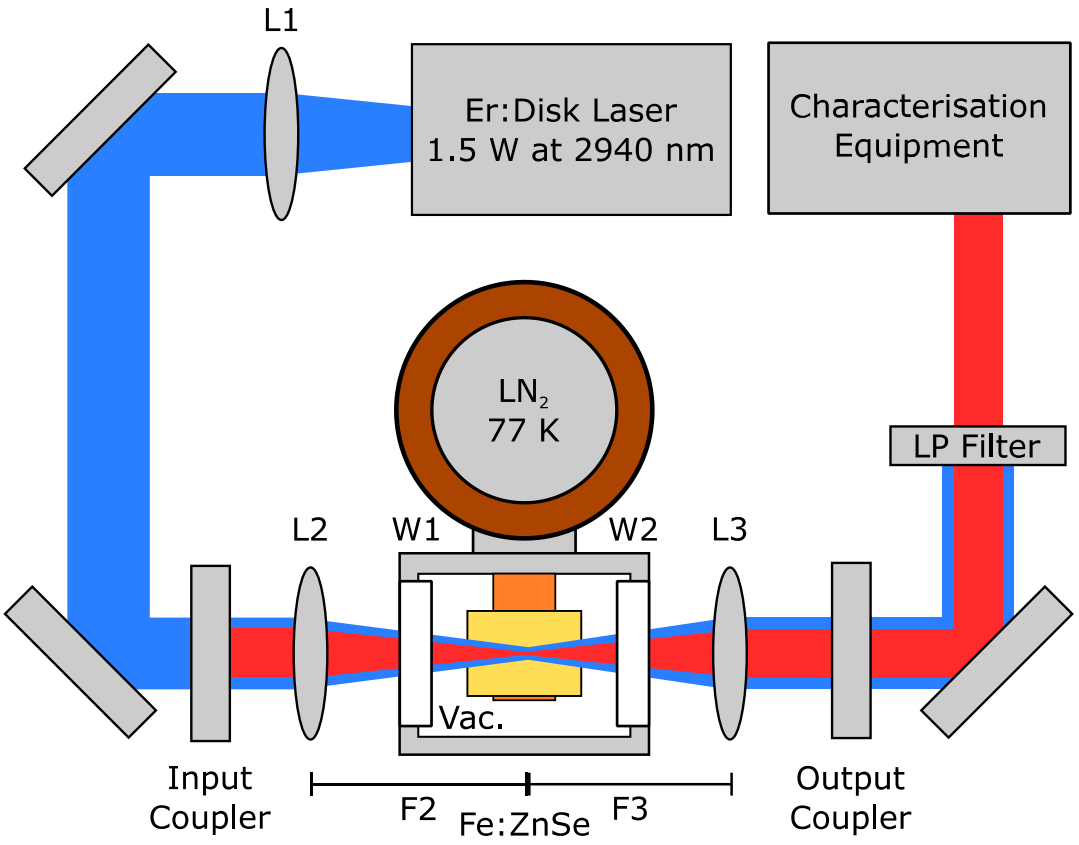

Figure 6.17. Fe:ZnSe bulk laser cavity for CW operation. L1 is a non AR coated CaF_2 lens used for collimation of the pump laser. L2 is a 35 mm focal length AR coated CaF_2 lens. W1 and W2 are non-coated CaF_2 flat windows. L3 is a 45 mm focal length AR coated CaF_2 lens. F2 and F3 size is the same as the focal lengths of lens L2 and L3 respectively.

For CW laser operation, the Fe:ZnSe sample was cooled to 77 K using liquid nitrogen. Bulk laser operation was investigated with a 90% reflective output coupler at the signal wavelength. The input vs. output characterisation of the bulk laser is given in Figure 6.18. The laser results for the best Fe:ZnSe waveguide with the 90% output coupler are included in the figure for comparison, full details of which are given in Section 6.3.2. The bulk laser was found to emit a maximum output power of 49 mW when pumped with 908 mW at 2940 nm. The output power is believed to be pump limited because there is no

observed thermal rollover [58]. The bulk laser reached laser threshold at 340 mW of pump power and had a slope efficiency of 8.1%.

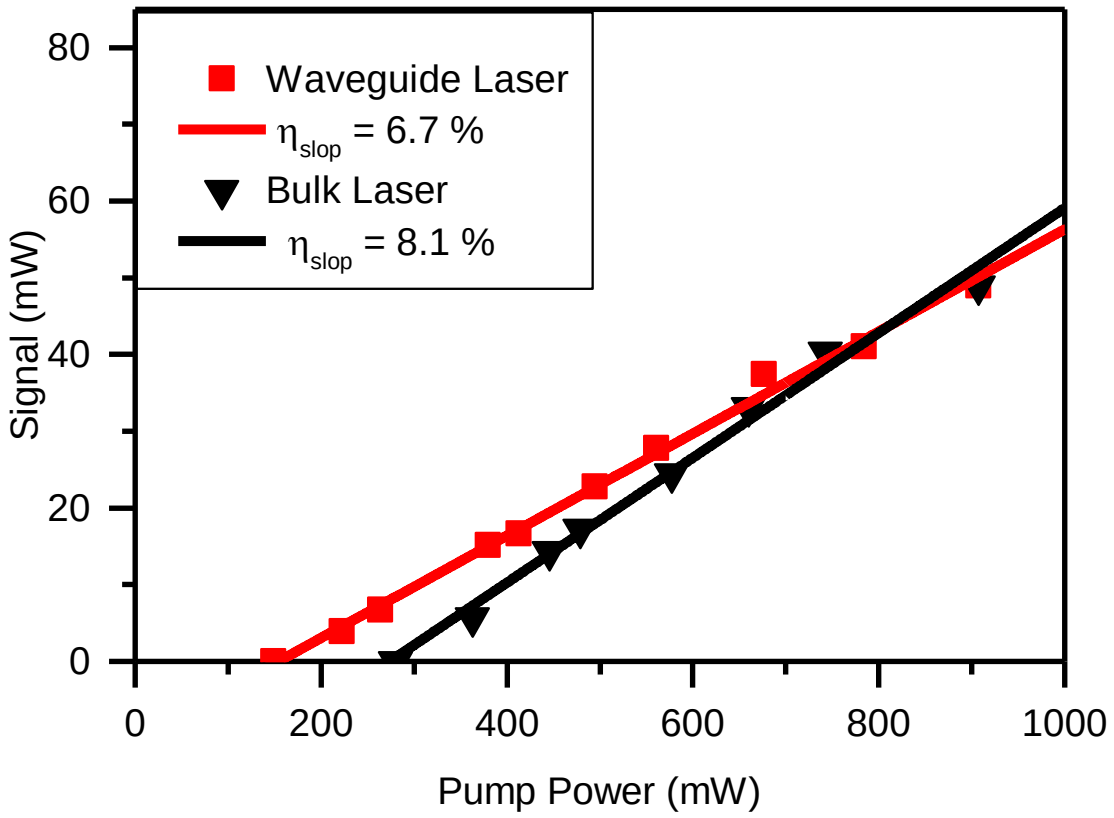

Figure 6.18. Output power of Fe:ZnSe bulk laser black triangles and waveguide laser red squares. For both cases the laser had a 90% reflective output coupler at the signal wavelength. The pump power has been reduced by the first Fresnel reflection on the input facet.

Comparing the output power performance of the waveguide and bulk Fe:ZnSe lasers can help improve the knowledge of both systems by examining their differences. In terms of power performance there are two key differences between the laser types. The first is the slope efficiency of the bulk laser is higher than that of the waveguide laser, 8.1% compared with 6.7% respectively. This is expected because the waveguide will induce some coupling loss and since it is a leaky mode will fundamentally have some propagation loss in addition to any scattering loss from the ULI fabrication process [58, 89]. However, by implementating waveguide geometry the pump power required to reach laser threshold is reduced, in this case to 45% of that needed for the bulk cavity. This result makes the waveguide lasers more suitable for compact low power applications.

The mode field diameter of the Fe:ZnSe laser was imaged with a Mid-IR camera (FLIR SC7000) to compare the mode quality of both cavity configurations. This measurement was performed with both lasers lasing from the 17.6% Fresnel reflection of the end facet when pumped with 908 mW. The MFD was imaged on to a Mid-IR camera using a 50 mm AR coated CaF_2 lens. The MFD of the bulk and waveguide laser are given in Figure 6.19. The MFD of the Bulk laser signal mode was found to have a FWHM of 45.65 µm and 53.7 µm in the x-axis and z-axis. This is 25% and 74% greater than the MFD of the waveguide laser in the z and x axis respectively. From this result, the lower threshold of the waveguide laser is attributed to the tighter confinement facilitated by the waveguide implementation.

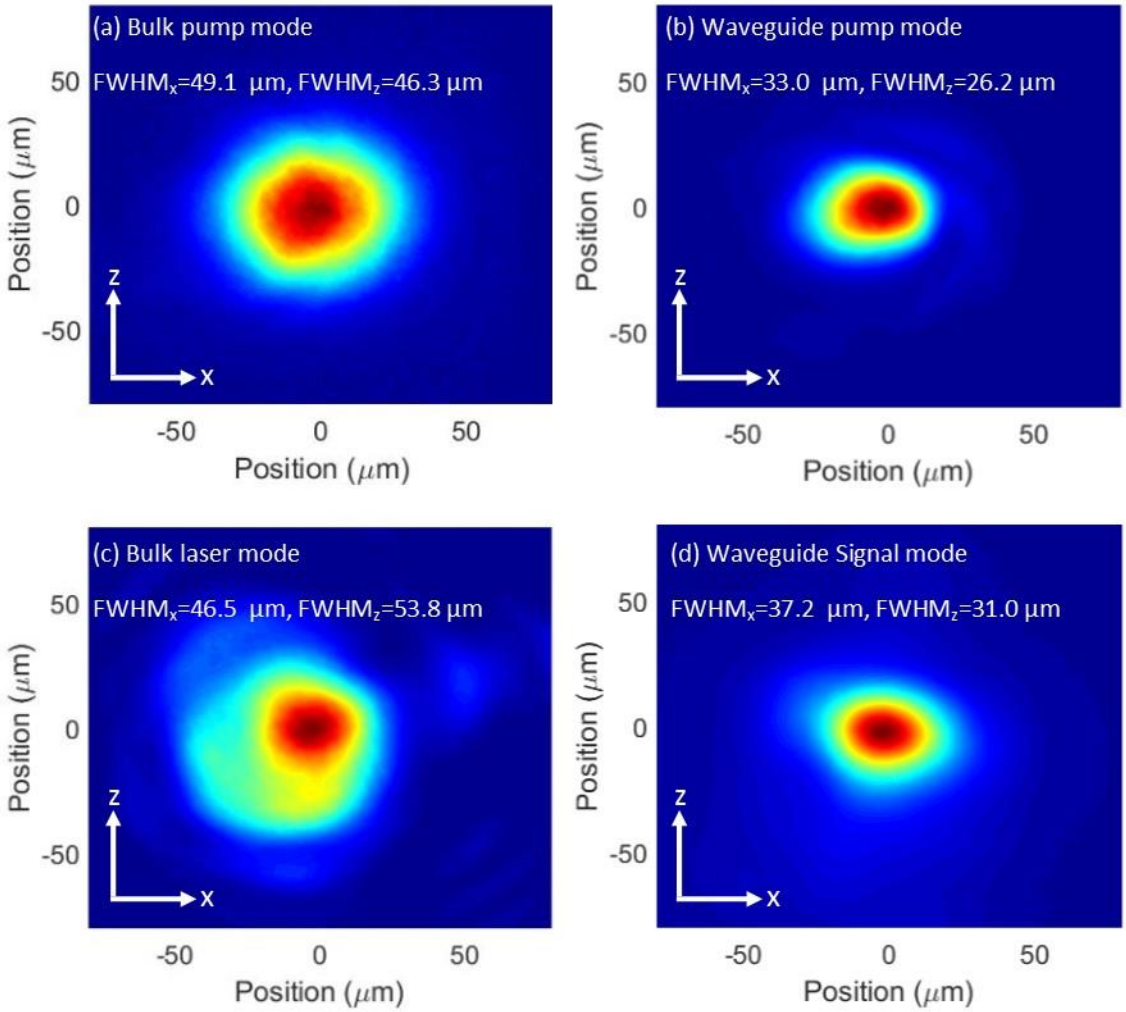

Figure 6.19.(a) Pump mode of bulk laser cavity. (b) Pump mode image of waveguide laser. (c) Waveguide laser mode image at 4122 nm imaged at end facet when lasing from Fresnel reflection at output facet. (d) Bulk laser output mode centered at 4123 nm lasing from Fresnel reflection at output facet.

The spectral emissions of the bulk laser were also investigated for comparison with the waveguide laser. The wavelength spectra of the waveguide and bulk laser were measured with a monochromator (Zolix Omni-λ 300), and this device has a resolution of 0.4 nm. For this measurement, the maximum available pump power 908 mW was used. The normalised spectra of the bulk and waveguide laser are given in Figure 6.20:

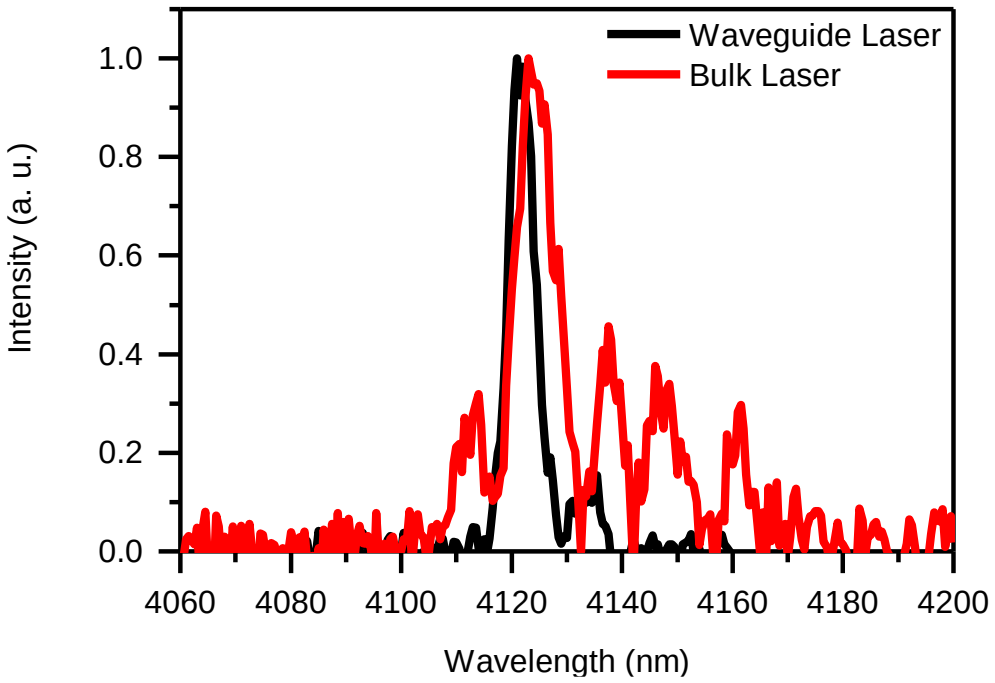

Figure 6.20. Normalised wavelength spectra of Fe:ZnSe lasers. The resolution of the spectra are 0.4 nm. Red dotted line is a bulk cavity configuration. Black solid line is a waveguide cavity configuration.

The bulk emission consisted of multiple peaks spanning 50 nm, the largest centred at 4123 nm. This result is in agreement with the work previously carried out in a bulk Fe:ZnSe laser by Evans et al. [180]. The waveguide laser was found to emit at a central wavelength of 4122 nm with a FWHM of 6 nm, which is considerably narrower than that demonstrated in bulk. It has been found experimentally that the spectral linewidth of the Cr and Fe doped ULI depressed cladding waveguide lasers are considerably narrower than their typically bulk counterparts [15, 58].

A recent paper by Stites et al. [116] has demonstrated free running TM:II-VI lasers with a single emission line of sub 140 pm linewidth. The laser crystals are treated with a hot isostatic pressing (HIP) process. The process heats the sample to 1050 ° C at a pressure of 300000 PSI. This method differs from the low pressures used in post growth diffusion

doping of polycrystalline ZnSe which has been used in previous laser reports[15-17]. The HIP process can be applied to post growth diffusion samples and also used to dope polycrystalline ZnSe. Both processes resulted in narrow linewidth free running laser sources. The line narrowing of treated samples is attributed to the increase in grain size of ZnSe [117] and removing crystal defects [118]. From the narrowed linewidth observed in single mode Cr:ZnSe, Cr:ZnS and Fe:ZnSe waveguide lasers, it is has been proposed that a similar effect to HIP is being induced in the irradiated area by the ULI process. ULI involves creating a plasma at the focus of the inscription beam, which is believed to remove defects in the host Cr/Fe:ZnSe/ZnS [119].

The performance of the waveguide laser was compared with that of a bulk laser using a 90% reflective output coupler. The bulk laser design was found to be more efficient. This is due to the loss induced by the waveguide from scattering losses, as discussed in Section 6.3.3. However, the waveguide cavity was found to reduce the lasing threshold of the laser by 44% compared with the bulk system using the same intra cavity optics. This is because of the tighter confinement, increased overlap and interaction length between the pump and signal in the waveguide. This result is important for future low power applications, and could open the possibility of direct diode pumping.

6.5. Conclusion

The first demonstration of an Fe:ZnSe waveguide laser has been presented. The waveguide structure was an annular depressed cladding structure fabricated by ULI. The inscribed waveguides were found to have low propagation losses of <1 dB/cm at the lasing wavelength. The waveguide laser emitted a maximum output power of 76 mW, which was limited by the available pump power of 906 mW at wavelength of 2940 nm. The tighter confinement of the pump and laser signal beams by the waveguide resulted in a low laser threshold of 154 mW, which is a 44% reduction compared with an otherwise identical bulk system with a laser threshold of 274 mW. A narrow spectral linewidth of 6 nm was demonstrated by the waveguide laser. To the best of the author's knowledge, this is the narrowest linewidth demonstrated in any free running Fe:ZnSe laser. Demonstration of an Fe:ZnSe laser in a guided wave configuration will enable the creation of a compact, all solid state laser system for LIDAR and use in defence applications.

This work is a result of close collaboration between HWU and WPAFB, funded by EOARD, and resulted in a conference paper at CLEO15 [188] and a journal paper in Applied Physics [51].

7. Conclusions and Future Work

7.1. Conclusions

The work presented in this thesis is focused on the development of guided wave laser technology in TM:II-VI semiconductors. Chapters 3 and 4 focused on the development of Cr:ZnSe waveguide lasers to produce widely tuneable and modelocked laser sources. In Chapter 5, ULI waveguide fabrication in Cr:ZnS is investigated. This was successful and lead to the first waveguide laser in Cr:ZnS. The aim of this work was to enable further power scaling of lasers in the 2 - 3 μm spectral band. Chapter 6 investigates the suitability of Fe:ZnSe for ULI waveguide fabrication and lasers demonstrating with the aim of producing a high brightness laser sources in the 3.7 - 5 μm spectral band. The following paragraphs provide a summary of each chapter.

Chapter 3 examines the integration of Cr:ZnSe waveguides with wavelength tuning elements to produce a widely tuneable Cr:ZnSe waveguide laser. Tuning with a diffraction grating in a Littman-Metcalf configured cavity demonstrated a narrow linewidth of 53 pm. The tuning range of this laser was 2077 - 2777 nm with output powers of more than 15 mW available across the full range. Computer modelling of the laser showed the optical loss of the grating, particularly at longer wavelengths, was limiting the tuning range. The grating was replaced with a Si prism. This resulted in a CW tuning range increasing to 2080 - 2883 nm. This resulted in a tuneable bandwidth of 39 THz which is the widest range demonstrated by a Mid-IR waveguide laser.

Chapter 4 advances the number of future applications available to compact TM:II-VI lasers by demonstrating modelocked waveguide lasers in Cr:ZnSe. The laser was passively modelocked using a SESAM. Initial investigations demonstrated the suitability of the depressed cladding waveguide and SESAM to produce a CW modelocked laser. However, this was only detected on a RF spectrum analyser, an autocorrelation trace required pulses with larger pulse energy. Thus the system was power scaled with a 20 W pump source. CW modelocking was demonstrated with a PRF of 308 MHz and an average power of 85 mW when pumped with 5 W. This laser was autocorrelated, demonstrated a pulse width of 982 fs, assuming a sech^2 pulse shape. The next step of the investigation was increasing the PRF to over 1 GHz. The laser was shortened to have a calculated PRF of 1.03 GHz from the cavity length. Modelocking was confirmed at 1.03

GHz by measuring an autocorrelation of the pulse. This resulted in the fastest PRF laser demonstrated in the modelocked Cr:ZnSe laser family.

Chapter 5 investigates a potential alternative to a ZnSe laser host, ZnS. This material has improved thermal characteristics over ZnSe and as such presents a path for further power scaling. Fabrication of depressed cladding waveguides in Cr:ZnS was demonstrated with prorogation losses of 2.6 dB/cm. These waveguides were assembled into a monolithic laser cavity by butt coupling an input and output coupler to the end facets. Free running CW laser operation was demonstrated with pump limited output powers of 97 mW at 2333 nm.

Chapter 6 transfers the knowledge of waveguide fabrication discovered in Cr:ZnSe and Cr:ZnS to the 3.7 - 5 μm wavelength band with a Fe:ZnSe waveguide laser. Firstly, low-loss laser waveguide parameters were investigated in Fe:ZnSe. The passive characterisation found the waveguide propagation losses to be as low as 0.4 dB/cm, this is much lower than those demonstrated in other ULI cladding waveguides in Cr:ZnSe and Cr:ZnS [53, 58]. The low loss waveguides were inserted inside a cryostat for CW laser operation. Free running CW laser operation with a Fe:ZnSe waveguide laser was demonstrated. An output power of 76 mW was produced at 4122 nm with a pump power of 908 mW. This work highlights the operational wavelength versatility of ULI fabricated depressed cladding waveguides.

7.2. Future Work

7.2.1. Monolithic Wavelength Tuned Waveguide Laser

The ZnSe waveguide lasers demonstrated in this thesis used extended cavity designs. Future work should investigate replacing these with monolithic designs. This will reduce the total cavity size and improve cavity robustness.

In Chapter 3, free space methods of wavelength tuning Cr:ZnSe waveguide lasers were demonstrated. Incorporating a fully monolithic tuning method is the next stage of this work. Bragg gratings in guided wave form are an effective method of wavelength selection. Bragg gratings have been demonstrated in ULI single line and multiscan waveguides operating at telecoms wavelengths [189, 190]. However, once fabricated, the Bragg wavelength is fixed. There is the possibility to temperature tune the Bragg peak, but this is limited to small tuning ranges. One technique of extending the tuning range

would be to inscribe a Bragg grating in an electro-optic material such as Lithium Niobate or Strontium Barium Niobate. Applying an electric field across the waveguide with the addition of a Bragg grating will change the peak of the Bragg reflection. Thus, placing this inside a Cr:ZnSe laser resonator as a feedback mechanism will create a monolithic tuning element. A diagram of the proposed device is given in Figure 7.1:

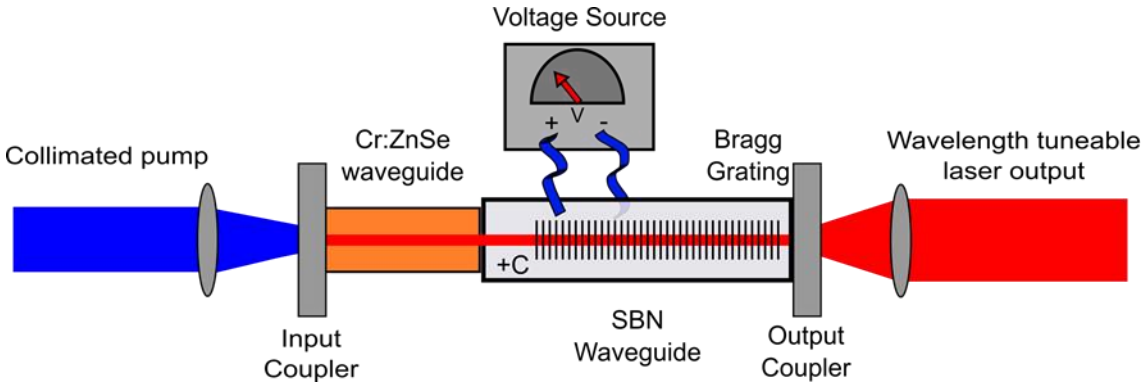

Figure 7.1. Schematic of electro-optic tuned Bragg grating for monolithic wavelength tuning of Cr:ZnSe waveguide lasers.

The electro-optic substrate recommended for this application is Strontium Barium Niobate (SBN). SBN is chosen over the more commonly implemented Lithium Niobate as it has larger electro-optic coefficients which will allow for greater tuning ranges. The r_{33} coefficient of SBN:75 is 844 pm/V [191] compared with the 31 pm/V in Lithium Niobate [192]. Initial work in ULI fabrication, characterisation of waveguides in SBN at Mid-IR wavelengths and the effect of an electric-field are detailed in Appendix Section 1.

An alternative method of implementing tuneable Bragg grating is to use a photorefractive material. The materials are used for other applications such as data storage because of the relatively long timescales involved in the process [193]. We propose forming a Bragg grating in a prefabricated ULI waveguide by using two interfering laser beams. This will allow the creation of a tuneable Bragg grating because the grating period is proportional to the angle between the interfering green laser beams. This has been implemented at 1550 nm in a thin film waveguide as shown in Figure 7.2. Doping of SBN with Cerium (Ce) forms an effective photorefractive material. ULI waveguides compatible with a Cr:ZnSe waveguide resonator have been fabricated in Ce:SBN:61, as detailed in Appendix Section 1. Laser tuning is still to be investigated.

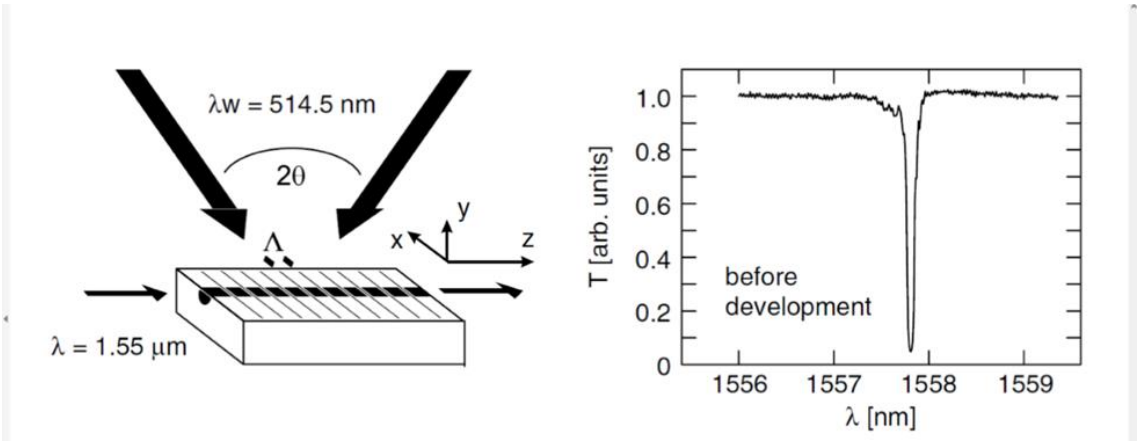

Figure 7.2. Holographically recorded reflection filters in $LiNbO_3$:Ti:Cu channel waveguides. (a)Geometry for recording and read-out of the grating, and (b)typical transmission spectrum T(λ) of a 15 mm-long filter. The c-axis referred to in the report is the z-axis in this schematic. These figures have be reproduced from Gunter and Huignard [193].

7.2.2. Monolithic Dispersion Compensated Modelocked Waveguide Laser

In Chapter 4, modelocked Cr:ZnSe waveguide lasers were investigated. However, dispersion compensation was not implemented. To generate ultrashort pulses, it is paramount that the cavity round trip time of all the modelocked pulses frequency components are the same. Thus there is no phase change of each frequency component with respect to each other after one round trip of the cavity. If there is a phase change of some of the frequency components, they will not constructively interfere with the other components. This will limit the bandwidth of the system and lead to pulse width broadening. In most bulk laser cavities, this problem can be resolved by the simple addition of a Brewster cut prism pair. This system allows positive and negative group velocity dispersion (GVD) compensation by changing the distance between the prism pair. Tolstik et al. [194] used a YAG prism pair to demonstrate a CW modelocked Cr:ZnS laser with a pulse width of 41 fs and a pulse repetition frequency (PRF) of 108 MHz. A schematic of the laser cavity used by Tolstik is given in Figure 7.3. The disadvantage of GVD compensation from prism pairs is the requirement for free space beam propagation which is not compatible with compact monoclinic laser cavities.

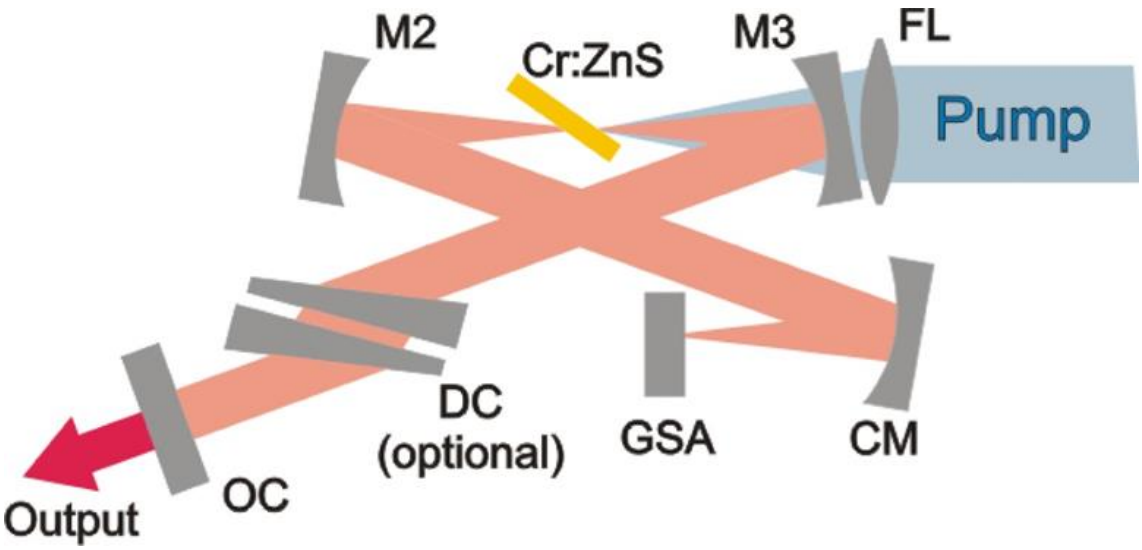

Figure 7.3. Schematic of CW modelocked Cr:ZnS bulk laser operating with a pulse width of 41 fs at a PRF for 108 MHz. FL is the pump focusing lens (f= 40 mm), M2 and M3 are HR dielectric mirrors, CM is a concave chirped mirror, GSA is a graphene-based saturable absorber mirror, DC is the YAG prism pair and OC is the output coupler. This diagram has been reproduced from Tolstik et al. [194].

Chirped or dispersive cavity mirrors are one alternative method of GVD compensating which is compatible with a monolithic laser cavity. These mirrors use Bragg stacks to phase shift some frequency more than others, thus allowing for GVD compensation. These mirrors are limited in the bandwidth of frequencies in which they can be used. Many high quality, low loss and large bandwidth GVD mirrors have been developed for Ti:Sapphire lasers, but they are not as well developed for the 1.9 - 3.4 μm range needed to use the full bandwidth of Cr:ZnSe. The GVD compensation of the mirrors is also set at fabrication and does not allow for any optimisation once fabricated.

A small gap between an uncoated waveguide end facet and a plain mirror can create negative GVD by forming a Gires-Tournois interferometer [195]. Lagatsky et al. [127] demonstrated the effectiveness of the method with a 15 GHz fundamentally CW mode-locked Ytterbium doped glass waveguide laser. Lagatsky showed that tuneable GVD control can be achieved in a quasi-monolithic flat mirror butt coupled waveguide laser by adjusting the gap between one of the mirrors and the waveguide end facet. Figure 7.4 shows a diagram of a modelocked Ytterbium doped bismuthate glass waveguide laser that has been demonstrated by Lancaster et al. [196] using the Lagatsky dispersion control method.

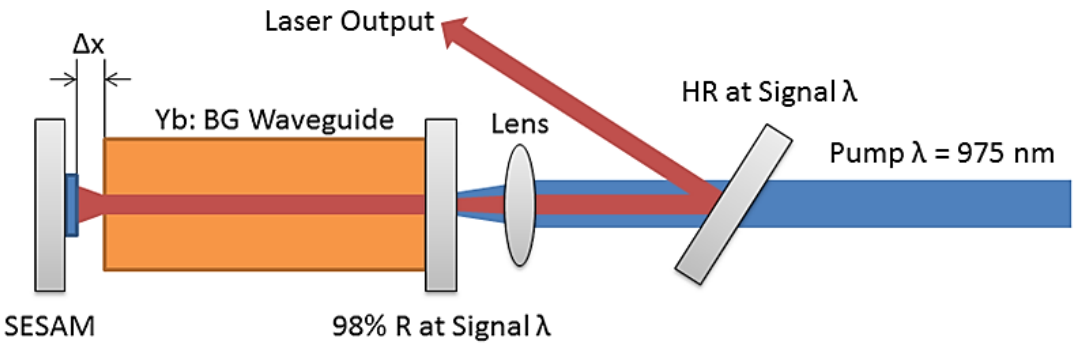

Figure 7.4. Diagram of CW modelocked Ytterbium doped bismuthate glass waveguide laser with GVD compensation from adjusting the gap Δx.

This method has been found to be very effective in the demonstration of compact CW modelocked lasers. One issue, however, is the gap must be controlled to a precision of a few microns and, because of this gap, the laser is no longer a truly monolithic system. This means that it is not an "assemble and forget" system, thus the main advantage of using a monolithic waveguide laser cavity is lost.

A different approach to GVD compensation in Cr:ZnSe/ZnS modelocked lasers is using CaF_2 waveguides. At the peak of Cr:ZnSe emission cross-section, 2.45 μm, CaF_2 is an anomalously dispersive material and ZnSe is a normally dispersive media. Thus, by inserting a sufficient length of CaF_2 inside the cavity, we can compensate for GVD induced by the Cr:ZnSe/ZnS waveguide. In order to do this and still have a fully monolithic laser system, the waveguides must be fabricated in CaF_2 with mode field diameters (MFD) that are similar to those of the current ultrafast waveguides in Cr:ZnSe/ZnS which have an MFD of around 50 μm [53, 58]. This may be achievable by developing depressed cladding waveguides in CaF_2 fabricated by ultrafast laser inscription. The advantage of using ULI over the more common lithographic methods is the ability to fabricate fully 3D structures and the low index contrasts of negative index change. Using this method will facilitate larger single mode MFDs needed for efficient butt-coupling into the Cr:ZnSe waveguides. Once low loss single mode waveguide ULI fabrication parameters are developed, the CaF_2 waveguide will be placed inside the Cr:ZnSe/ZnS waveguide laser as shown in Figure 7.5:

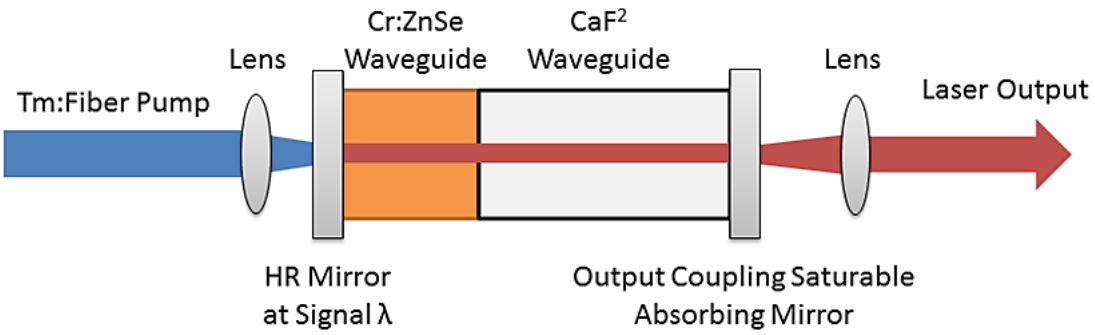

Figure 7.5. Schematic of cavity design for a monolithic passively modelocked Cr:ZnSe waveguide laser. GVD control is managed with a ULI inscribed waveguide in CaF_2. Passive modelocking is achieved using a SESAM or multilayer layer graphene saturable absorber.

Assuming the modelocked Cr:ZnSe (217.8 fs^2/mm) laser operates at the peak of the emission cross-section (2.45 µm) the CaF_2 (-51.7 fs^2/mm) waveguide would need to be 4.2 times longer than the Cr:ZnSe waveguide. This would lead to a CaF_2 waveguide of 25 mm if we use a 6 mm Cr:ZnSe waveguide consistent with the modelocking work discussed in Chapter 4. It can be beneficial to operate a modelocked laser in the soliton modelocked regime. This is achieved by a slightly anomalous GVD cavity, by increasing the length of the CaF_2. Using the proposed Cr:ZnSe and CaF_2 waveguides will lead to a modelocked laser with a fundamental PRF of 3 GHz. Post waveguide fabrication adjustment of the negative GVD of the CaF_2 waveguide can be accurately adjusted by polishing the end facet of the sample. This makes the CaF_2 an attractive and cost effective alternative to the use of chirped mirrors in monolithic modelocked waveguide laser systems. An initial demonstration of Mid-IR depressed cladding waveguides fabricated in CaF_2 by ULI is given in Appendix, Section 2.

7.2.3. Monolithic Optical pumping of TM:II-VI Waveguide Laser

The TM:II-VI waveguide lasers demonstrated in this thesis were pumped by collimated fibre lasers. Future work should investigate replacing these with monolithic designs. This will reduce the total cavity size and improve cavity robustness.

For optical pumping of Cr:ZnSe Tm:fibre lasers an attractive source due to the high power CW sources that are commercially available [24]. If the MFD of the fibre is matched to that of the waveguide the fibre can be directly but coupled to the end facet of the waveguide. Further reduction in cavity component can be implemented by directly

coating the waveguide endfacets with the input and output coupler refelctivities. A diagram of the proposed fully monothic laser design is given in Figure 7.6:

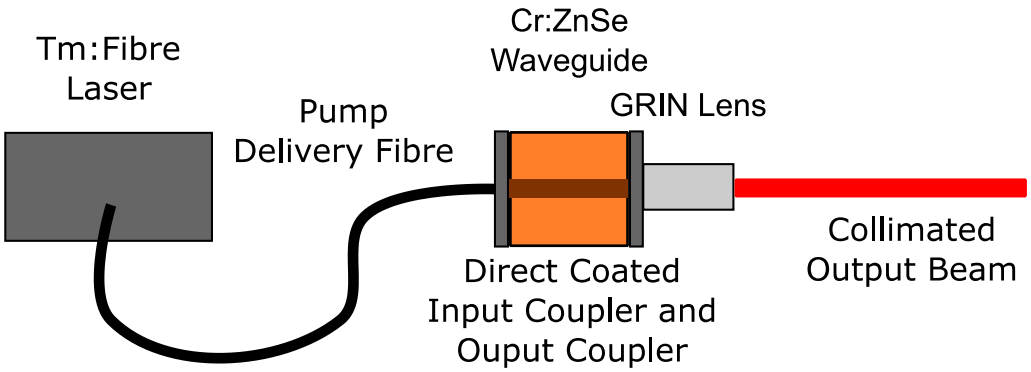

Figure 7.6. Proposed design of fully monolithic Cr:ZnSe waveguide laser system.

A gradient-index (GRIN) lens is butt coupled to the end facet of the waveguide output to produce a collimated laser output. This example couple be added to the delivery head of current Tm:Fibre lasers and would only add a few centimetres is length. Thus facilitating an compact 2 – 3 μm laser system capable of outputting watt level CW powers.

This fully monolithic laser design could also be implemented as a pump source for Fe:ZnSe waveguide lasers. A diagram of the proposed setup is given in Figure 7.7:

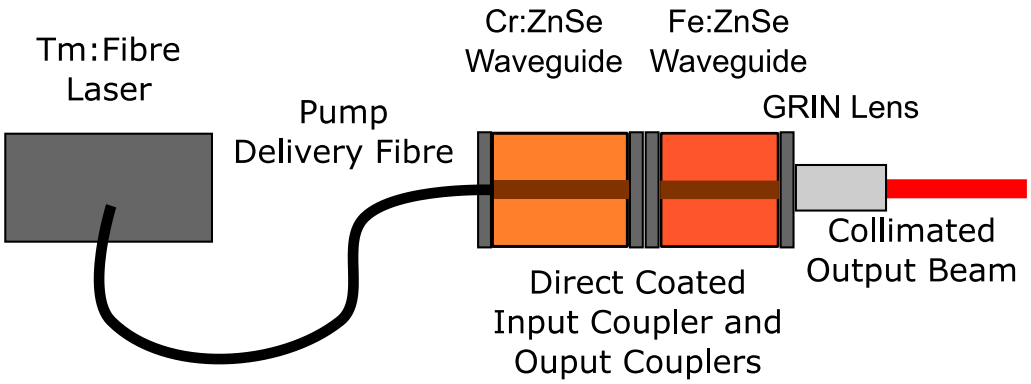

Figure 7.7. Proposed design of fully monolithic Fe:ZnSe waveguide lasers system.

There is an added complication in this laser's system because of Fe:ZnSe's short upperstate life time of 0.57 μm at room temperature [70]. For CW operation a cooling system would also need to be incorporated, however room temperature would be possible with pulsed pumping [182].

References

1. T. H. Maiman, "Stimulated Optical Radiation in Ruby," Nature **187**, 493-494 (1960).
2. W. Koechner, "Introduction," in *Solid-State Laser Engineering*

   Six ed. (Springer, 2006).
3. J. E. Geusic, H. M. Marcos, and L. G. Van Uitert, "Laser Oscillations in Nd-Doped Yttrium Aluminum Gallium and Gadolinium garnets," Appl. Phys. Lett. **4**, 182-184 (1964).
4. J. N. Walpole, A. R. Calawa, T. C. Harman, and S. H. Groves, "Double-heterostructure PbSnTe lasers grown by molecular-beam epitaxy with cw operation up to 114 K," Appl. Phys. Lett. **28**, 552-554 (1976).
5. J. Faist, F. Capasso, D. L. Sivco, C. Sirtori, A. L. Hutchinson, and A. Y. Cho, "Quantum Cascade Laser," Science **264**, 553-556 (1994).
6. Y. Yao, A. J. Hoffman, and C. F. Gmachl, "Mid-infrared quantum cascade lasers," Nat Photon **6**, 432-439 (2012).
7. Y. Bai, S. Slivken, S. Kuboya, S. R. Darvish, and M. Razeghi, "Quantum cascade lasers that emit more light than heat," Nat Photon **4**, 99-102 (2010).
8. Y. Bai, N. Bandyopadhyay, S. Tsao, S. Slivken, and M. Razeghi, "Room temperature quantum cascade lasers with 27% wall plug efficiency," Appl. Phys. Lett. **98**, - (2011).
9. R. M. Matthew, B. Yury, W. Gerard, L. Rafal, and K. T. Frank, "Recent advances of laser-spectroscopy-based techniques for applications in breath analysis," Journal of Breath Research **1**, 014001 (2007).
10. Q. Ren, V. Venugopalan, K. Schomacker, T. F. Deutsch, T. J. Flotte, C. A. Puliafito, and R. Birngruber, "Mid-Infrared laser ablation of the cornea: A comparative study," Lasers in Surgery and Medicine **12**, 274-281 (1992).
11. I. T. Sorokina and K. L. Vodopyanov, *Solid-State Mid-Infrared Laser Sources* (Springer, 2003).
12. L. D. DeLoach, R. H. Page, G. D. Wilke, S. A. Payne, and W. F. Krupke, "Transition metal-doped zinc chalcogenides: spectroscopy and laser

demonstration of a new class of gain media," IEEE J. Quant. Electron. **32**, 885-895 (1996).

13. R. H. Page, K. I. Schaffers, L. D. DeLoach, G. D. Wilke, F. D. Patel, J. B. Tassano, Jr., S. A. Payne, W. F. Krupke, K. T. Chen, and A. Burger, "Cr^{2+}-doped zinc chalcogenides as efficient, widely tunable mid-infrared lasers," IEEE J. Quant. Electron. **33**, 609-619 (1997).
14. E. Sorokin and I. T. Sorokina, "Tunable diode-pumped continuous-wave Cr^{2+}:ZnSe laser," Appl. Phys. Lett. **80**, 3289-3291 (2002).
15. P. A. Berry and K. L. Schepler, "High-power, widely-tunable Cr^{2+}:ZnSe master oscillator power amplifier systems," Opt. Express **18**, 15062-15072 (2010).
16. S. B. Mirov, I. Moskalev, M. S. Mirov, S. Vasilyev, V. Fedorov, D. Martyshkin, V. O. Smolski, and V. Gapontsev, "Transitioning Cr2+ and Fe2+ doped Zn chalcogenide laser technology to commercial products - lessons learned," in *Conference on Lasers and Electro-Optics*, OSA Technical Digest (online) (Optical Society of America, 2016), JF1K.4.
17. E. Sorokin, I. T. Sorokina, M. S. Mirov, V. V. Fedorov, I. S. Moskalev, and S. B. Mirov, "Ultrabroad continuous-wave tuning of ceramic Cr:ZnSe and Cr:ZnS lasers," in *Advanced Solid-State Photonics*, (Optical Society of America, 2010), AMC2.
18. S. B. Mirov, V. Fedorov, D. Martyshkin, I. Moskalev, M. Mirov, and S. Vasilyev, "High Average Power Fe:ZnSe and Cr:ZnSe Mid-IR Solid State Lasers," in *Advanced Solid State Lasers*, OSA Technical Digest (online) (Optical Society of America, 2015), AW4A.1.
19. J. Nilsson and D. N. Payne, "High-power fiber lasers," Science **332**, 921-922 (2011).
20. H. Baker, J. Lee, and D. Hall, "Self-imaging and high-beam-quality operation in multi-mode planar waveguide optical amplifiers," Opt. Express **10**, 297-302 (2002).
21. J. R. Sparks, R. He, N. Healy, M. Krishnamurthi, A. C. Peacock, P. J. A. Sazio, V. Gopalan, and J. V. Badding, "Zinc Selenide Optical Fibers," Advanced Materials **23**, 1647-1651 (2011).
22. J. Williams, J. Goldstein, D. Martyshkin, V. Fedorov, I. Moskalev, R. Camata, and S. Mirov, "Mid-IR Laser Oscillation In Cr:ZnSe Planar Waveguide Structures

And In Cr:ZnSe/As_2S_3:As_2Se_3 Composite Materials," in OSA Technical Digest (CD) (Optical Society of America, 2010), FThL3.

23. J. R. Macdonald, R. R. Thomson, S. J. Beecher, N. D. Psaila, H. T. Bookey, and A. K. Kar, "Ultrafast laser inscription of near-infrared waveguides in polycrystalline ZnSe," Opt. Lett. **35**, 4036-4038 (2010).
24. S. A. McDaniel, A. Lancaster, J. W. Evans, A. K. Kar, and G. Cook, "Power scaling of ultrafast laser inscribed waveguide lasers in chromium and iron doped zinc selenide," Opt. Express **24**, 3502-3512 (2016).
25. K. C. Kao and G. A. Hockham, "Dielectric-fibre surface waveguides for optical frequencies," Electrical Engineers, Proceedings of the Institution of **113**, 1151-1158 (1966).
26. Corning, "Corning Celebrates 45 Years on the Cutting Edge with Optical Fiber" (Corning, 2016), retrieved 21/07/2016, http://www.corning.com/worldwide/en/innovation/culture-of-innovation/corning-celebrates-45-years-on-cutting-edge-with-optical-fiber.html.
27. R. J. Mears, L. Reekie, I. M. Jauncey, and D. N. Payne, "Low-noise erbium-doped fibre amplifier operating at 1.54 μm," Electronics Letters **23**, 1026-1028 (1987).
28. M. J. R. Heck, J. F. Bauters, M. L. Davenport, D. T. Spencer, and J. E. Bowers, "Ultra-low loss waveguide platform and its integration with silicon photonics," Laser & Photonics Reviews **8**, 667-686 (2014).
29. A. Erik, K. Magnus, A. R. Chraplyvy, J. R. David, M. K. Peter, W. Peter, R. Kim, F. Johannes Karl, J. S. Seb, J. E. Benjamin, S. Marco, R. K. Frank, L. Andrew, P. Josep, T. Ioannis, E. B. John, S. Sudha, B.-P. Maïté, and G. Nicolas, "Roadmap of optical communications," Journal of Optics **18**, 063002 (2016).
30. R. G. Hunsperger, "Ch 4, Waveguide Fabrication Techniques," in *Integrated Optics: Theory and Technology* (Springer, New York, 2009).
31. R. R. Gattass and E. Mazur, "Femtosecond laser micromachining in transparent materials," Nat. Photon. **2**, 219-225 (2008).
32. K. M. Davis, K. Miura, N. Sugimoto, and K. Hirao, "Writing waveguides in glass with a femtosecond laser," Opt. Lett. **21**, 1729-1731 (1996).
33. D. Choudhury, J. R. Macdonald, and A. K. Kar, "Ultrafast laser inscription: perspectives on future integrated applications," Laser & Photonics Reviews, n/a-n/a (2014).

34. D. Choudhury, J. R. Macdonald, and A. K. Kar, "Ultrafast laser inscription: perspectives on future integrated applications," Laser & Photonics Reviews **8**, 827-846 (2014).
35. R. Mary, D. Choudhury, and A. K. Kar, "Applications of Fiber Lasers for the Development of Compact Photonic Devices," IEEE J. Sel. Top. Quant. Electon. **PP**, 1-1 (2014).
36. J. Zhang, A. Čerkauskaitė, R. Drevinskas, A. Patel, M. Beresna, and P. G. Kazansky, "Eternal 5D data storage by ultrafast laser writing in glass," Proc. SPIE 9736. (2016).
37. R. R. Thomson, H. T. Bookey, N. D. Psaila, A. Fender, S. Campbell, W. N. MacPherson, J. S. Barton, D. T. Reid, and A. K. Kar, "Ultrafast-laser inscription of a three dimensional fan-out device for multicore fiber coupling applications," Opt. Express **15**, 11691-11697 (2007).
38. R. G. H. van Uden, R. A. Correa, E. A. Lopez, F. M. Huijskens, XiaC, LiG, Schülzgen A, H. de Waardt, A. M. J. Koonen, and C. M. Okonkwo, "Ultra-high-density spatial division multiplexing with a few-mode multicore fibre," Nat Photon **8**, 865-870 (2014).
39. C. Hnatovsky, R. S. Taylor, E. Simova, V. R. Bhardwaj, D. M. Rayner, and P. B. Corkum, "Polarization-selective etching in femtosecond laser-assisted microfluidic channel fabrication in fused silica," Opt. Lett. **30**, 1867-1869 (2005).
40. R. Vazquez, G. Cerullo, R. Ramponi, and R. Osellame, "Chapter 14 - Optofluidic Biochips," in *Femtosecond Laser Micromachining: Photonic and Microfluidic Devices in Transparent Materials*, R. Osellame, G. Cerullo, and R. Ramponi, eds. (Springer, Berlin Heidelberg, 2012), pp. 389-419.
41. A. Salehi-Reyhani, J. Kaplinsky, E. Burgin, M. Novakova, A. J. deMello, R. H. Templer, P. Parker, M. A. A. Neil, O. Ces, P. French, K. R. Willison, and D. Klug, "A first step towards practical single cell proteomics: a microfluidic antibody capture chip with TIRF detection," Lab on a Chip **11**, 1256-1261 (2011).
42. M. W. Toepke and D. J. Beebe, "PDMS absorption of small molecules and consequences in microfluidic applications," Lab on a Chip **6**, 1484-1486 (2006).
43. G. T. Roman, T. Hlaus, K. J. Bass, T. G. Seelhammer, and C. T. Culbertson, "Sol−Gel Modified Poly(dimethylsiloxane) Microfluidic Devices with High Electroosmotic Mobilities and Hydrophilic Channel Wall Characteristics," Analytical Chemistry **77**, 1414-1422 (2005).

44. D. Choudhury, W. T. Ramsay, R. Kiss, N. A. Willoughby, L. Paterson, and A. K. Kar, "A 3D mammalian cell separator biochip," Lab Chip **12**, 948-953 (2012).
45. V. K. Jagannadh, M. D. Mackenzie, P. Pal, A. K. Kar, and S. S. Gorthi, "Imaging Flow Cytometry With Femtosecond Laser-Micromachined Glass Microfluidic Channels," IEEE J. Sel. Top. Quantum Electron. **21**, 370-375 (2015).
46. R. Osellame, V. Maselli, R. M. Vazquez, R. Ramponi, and G. Cerullo, "Integration of optical waveguides and microfluidic channels both fabricated by femtosecond laser irradiation," Appl. Phys. Lett. **90**, 231118 (2007).
47. A. Keloth, L. Paterson, G. H. Markx, and A. K. Kar, "Three-dimensional optofluidic device for isolating microbes," Proc. SPIE 9320, (2015)
48. R. Osellame, S. Taccheo, M. Marangoni, R. Ramponi, P. Laporta, D. Polli, S. De Silvestri, and G. Cerullo, "Femtosecond writing of active optical waveguides with astigmatically shaped beams," J. Opt. Soc. Am. B **20**, 1559-1567 (2003).
49. S. Taccheo, G. Della Valle, R. Osellame, G. Cerullo, N. Chiodo, P. Laporta, O. Svelto, A. Killi, U. Morgner, M. Lederer, and D. Kopf, "Er:Yb-doped waveguide laser fabricated by femtosecond laser pulses," Optics Letters **29**, 2626-2628 (2004).
50. T. Calmano, J. Siebenmorgen, F. Reichert, M. Fechner, A.-G. Paschke, N.-O. Hansen, K. Petermann, and G. Huber, "Crystalline Pr:$SrAl_{12}O_{19}$ waveguide laser in the visible spectral region," Optics Letters **36**, 4620-4622 (2011).
51. A. Lancaster, G. Cook, S. A. McDaniel, J. Evans, P. A. Berry, J. D. Shephard, and A. K. Kar, "Mid-infrared laser emission from Fe:ZnSe cladding waveguides," Appl. Phys. Lett. **107**, 031108 (2015).
52. J. R. Macdonald, "Active and Passive Mid-infrared Photonic Devices in ZnSe Based Materials," PhD Thesis (Heriot-Watt University, 2013).
53. J. R. Macdonald, S. J. Beecher, A. Lancaster, P. A. Berry, K. L. Schepler, S. B. Mirov, and A. K. Kar, "Compact Cr:ZnS channel waveguide laser operating at 2333 nm," Opt. Express **22**, 7052-7057 (2014).
54. A. Okhrimchuk, V. Mezentsev, H. Schmitz, M. Dubov, and I. Bennion, "Cascaded nonlinear absorption of femtosecond laser pulses in dielectrics," Laser Physics **19**, 1415-1422 (2009).
55. J. R. Macdonald, P. A. Berry, K. L. Schelper, and A. Kar, "Directly Written Mid-Infrared Waveguides in Zinc Selenide," in *Advances in Optical Materials*, OSA Technical Digest (CD) (Optical Society of America, 2012), IF1A.3.

56. R. Mary, S. J. Beecher, G. Brown, R. R. Thomson, D. Jaque, S. Ohara, and A. K. Kar, "Compact, highly efficient ytterbium doped bismuthate glass waveguide laser," Opt. Lett. **37**, 1691-1693 (2012).

57. J. R. Macdonald, S. J. Beecher, P. A. Berry, K. L. Schepler, and A. K. Kar, "Compact mid-infrared Cr:ZnSe channel waveguide laser," Appl. Phys. Lett. **102**, 16110 (2013).

58. J. R. Macdonald, S. J. Beecher, P. A. Berry, G. Brown, K. L. Schepler, and A. K. Kar, "Efficient mid-infrared Cr:ZnSe channel waveguide laser operating at 2486 nm," Optics Letters **38**, 2194-2196 (2013).

59. U. Keller, "Recent developments in compact ultrafast lasers," Nature **424**, 831-838 (2003).

60. K. Petermann, "1 - Oxide laser crystals doped with rare earth and transition metal ions A2 - Denker, B," in *Handbook of Solid-State Lasers*, E. Shklovsky, ed. (Woodhead Publishing, 2013), pp. 3-27.

61. I. T. Sorokina and K. L. Vodopyanov, "Crystalline Mid-Infrared Lasers," in *Solid-State Mid-Infrared Laser Sources* (Springer, Verlag Berlin Heidelberg, 2003).

62. A. V. Podlipensky, V. G. Shcherbitsky, N. V. Kuleshov, V. I. Levchenko, V. N. Yakimovich, M. Mond, E. Heumann, G. Huber, H. Kretschmann, and S. Kück, "Efficient laser operation and continuous-wave diode pumping of Cr^{2+}:ZnSe single crystals," Appl. Phys. B **72**, 253-255 (2001).

63. H. A. Jahn and E. Teller, "Stability of Polyatomic Molecules in Degenerate Electronic States. I. Orbital Degeneracy," Proceedings of the Royal Society of London. Series A - Mathematical and Physical Sciences **161**, 220-235 (1937).

64. K. Ghiassi and R. J. Lancashire, "Jahn-Teller Distortions" (LibreTexts, 2016), retrieved 20/09/2016, http://chem.libretexts.org/Core/Inorganic_Chemistry/Coordination_Chemistry/Basics_of_Coordination_Chemistry/Coordination_Numbers_and_Geometry/Jahn-Teller_Distortions.

65. M. Kaminska, J. M. Baranowski, S. M. Uba, and J. T. Vallin, "Absorption and luminescence of Cr^{2+} (d^4) in II-VI compounds," Journal of Physics C: Solid State Physics **12**, 2197 (1979).

66. F. S. Ham, "The Jahn–Teller effect: a retrospective view," Journal of Luminescence **85**, 193-197 (2000).

67. J. W. Evans, "Iron-Doped Zinc Selenide: Spectroscopy and Laser Development," PhD Thesis (Air Force Instituite of Technology, 2014).
68. S. Mirov, V. Fedorov, I. Moskalev, M. Mirov, and D. Martyshkin, "Frontiers of mid-infrared lasers based on transition metal doped II–VI semiconductors," Journal of Luminescence **133**, 268-275 (2013).
69. S. A. McDaniel, P. A. Berry, K. L. Schepler, J. R. Macdonald, S. J. Beecher, and A. K. Kar, "Gain-switched operation of ultrafast laser inscribed waveguides in Cr:ZnSe," in 2015), 93420E-93420E-93428.
70. S. B. Mirov, V. V. Fedorov, D. Martyshkin, I. S. Moskalev, M. Mirov, and S. Vasilyev, "Progress in Mid-IR Lasers Based on Cr and Fe-Doped II-VI Chalcogenides," IEEE J. Sel. Top. Quant. Electon. **21**, 292-310 (2015).
71. L. Keldysh, "Ionization in the field of a strong electromagnetic wave," Soviet Physics JETP **20**(1964).
72. R. Osellame, G. Cerullo, and R. Ramponi, *Femtosecond Laser Micromachining - Photonic and Microfluidic Devices in Transparent Materials* (Springer, 2012), Vol. 123.
73. O. Caulier, D. Le Coq, L. Calvez, E. Bychkov, and P. Masselin, "Free carrier accumulation during direct laser writing in chalcogenide glass by light filamentation," Opt. Express **19**, 20088-20096 (2011).
74. K. Yamada, W. Watanabe, T. Toma, K. Itoh, and J. Nishii, "In situ observation of photoinduced refractive-index changes in filaments formed in glasses by femtosecond laser pulses," Optics Letters **26**, 19-21 (2001).
75. J. E. McCarthy, H. T. Bookey, N. D. Psaila, R. R. Thomson, and A. K. Kar, "Mid-infrared spectral broadening in an ultrafast laser inscribed gallium lanthanum sulphide waveguide," Opt. Express **20**, 1545-1551 (2012).
76. V. Zambon, R. Forest, N. McCarthy, and M. Piche, "Inscription of optical waveguides with ultrafast Bessel beams," in *2007 Conference on Lasers and Electro-Optics (CLEO)*, 2007), 1-2.
77. J. Lapointe, M. Gagné, M.-J. Li, and R. Kashyap, "Making smart phones smarter with photonics," Opt. Express **22**, 15473-15483 (2014).
78. R. R. Thomson, N. D. Psaila, H. T. Bookey, D. T. Reid, and A. K. Kar, "Chapter 5 - Controlling the Cross-section of Ultrafast Laser Inscribed Optical Waveguides," in *Femtosecond Laser Micromachining: Photonic and Microfluidic*

Devices in Transparent Materials, R. Osellame, G. Cerullo, and R. Ramponi, eds. (Springer, Berlin Heidelberg, 2012), pp. 93-125.

79. M. Ams, G. Marshall, D. Spence, and M. Withford, "Slit beam shaping method for femtosecond laser direct-write fabrication of symmetric waveguides in bulk glasses," Opt. Express **13**, 5676-5681 (2005).
80. R. R. Thomson, A. S. Bockelt, E. Ramsay, S. Beecher, A. H. Greenaway, A. K. Kar, and D. T. Reid, "Shaping ultrafast laser inscribed optical waveguides using a deformable mirror," Opt. Express **16**, 12786-12793 (2008).
81. Y. Nasu, M. Kohtoku, and Y. Hibino, "Low-loss waveguides written with a femtosecond laser for flexible interconnection in a planar light-wave circuit," Optics Letters **30**, 723-725 (2005).
82. A. Benayas, W. F. Silva, A. Ródenas, C. Jacinto, J. Vázquez de Aldana, F. Chen, Y. Tan, R. R. Thomsom, N. D. Psaila, D. T. Reid, G. A. Torchia, A. K. Kar, and D. Jaque, "Ultrafast laser writing of optical waveguides in ceramic Yb:YAG: a study of thermal and non-thermal regimes," Applied Physics A **104**, 301-309 (2011).
83. A. Rodenas, L. M. Maestro, M. O. Ramirez, G. A. Torchia, L. Roso, F. Chen, and D. Jaque, "Anisotropic lattice changes in femtosecond laser inscribed Nd^{3+}:MgO:$LiNbO_3$ optical waveguides," J. Appl. Phys. **106**, 013110-013116 (2009).
84. A. G. Okhrimchuk, A. V. Shestakov, I. Khrushchev, and J. Mitchell, "Depressed cladding, buried waveguide laser formed in a YAG:Nd^{3+} crystal by femtosecond laser writing," Opt. Lett. **30**, 2248-2250 (2005).
85. A. G. Okhrimchuk and P. A. Obraztsov, "11-GHz waveguide Nd:YAG laser CW mode-locked with single-layer graphene," Scientific Reports **5**, 11172 (2015).
86. D. G. Lancaster, S. Gross, H. Ebendorff-Heidepriem, K. Kuan, T. M. Monro, M. Ams, A. Fuerbach, and M. J. Withford, "Fifty percent internal slope efficiency femtosecond direct-written Tm^{3+}:ZBLAN waveguide laser," Opt. Lett. **36**, 1587-1589 (2011).
87. J. R. Macdonald, S. J. Beecher, P. A. Berry, K. L. Schepler, and A. K. Kar, "Compact mid-infrared Cr:ZnSe channel waveguide laser," Appl. Phys. Lett. **102**, 161110-161113 (2013).

88. S. J. Beecher, R. R. Thomson, D. T. Reid, N. D. Psaila, M. Ebrahim-Zadeh, and A. K. Kar, "Strain field manipulation in ultrafast laser inscribed BiB_3O_6 optical waveguides for nonlinear applications," Opt. Lett. **36**, 4548-4550 (2011).
89. J. Hu and C. R. Menyuk, "Understanding leaky modes: slab waveguide revisited," Adv. Opt. Photon. **1**, 58-106 (2009).
90. Y. Y. Ren, S. J. Beecher, G. Brown, A. Rodenas, A. Lancaster, F. Chen, and A. K. Kar, "Q-switched mode-locking of a mid-infrared Tm:YAG waveguide laser with graphene film," in *Lasers and Electro-Optics Pacific Rim (CLEO-PR), 2013 Conference on*, 2013), 1-2.
91. B. J. Eggleton, B. Luther-Davies, and K. Richardson, "Chalcogenide photonics," Nat Photon **5**, 141-148 (2011).
92. P. Berry, J. MacDonald, A. Kar, and K. Schepler, "Ultrafast Laser Inscription of Waveguide Structures in Cr^{2+}:ZnSe," in *Advances in Optical Materials*, OSA Technical Digest (CD) (Optical Society of America, 2011), AIFB5.
93. R. W. Boyd, "Chapter 4 - The Intenisty-Dependent Refractive Index," in *Nonlinear Optics* (Elsevier Science, 2003), pp. 189-236.
94. R. W. Boyd, "Chapter 7 - Processes Resulting from the Intenisty-Dependent Refractive Index," in *Nonlinear Optics* (Elsevier Science, 2003), pp. 311-356.
95. M. Balu, J. Hales, D. Hagan, and E. Van Stryland, "Dispersion of nonlinear refraction and two-photon absorption using a white-light continuum Z-scan," Opt. Express **13**, 3594-3599 (2005).
96. A. Couairon and A. Mysyrowicz, "Femtosecond filamentation in transparent media," Physics Reports **441**, 47-189 (2007).
97. M. Rosete-Aguilar, F. C. Estrada-Silva, N. C. Bruce, C. J. Román-Moreno, and R. Ortega-Martínez, "Calculation of temporal spreading of ultrashort pulses propagating through optical glasses," Revista Mexicana de Física **54**, 141-148 (2008).
98. B. Tatian, "Fitting refractive-index data with the Sellmeier dispersion formula," Appl. Optics **23**, 4477-4485 (1984).
99. Schott, "Optical Glass Data Sheets" (July, 2015), retrieved 07/09/2016, 2016, http://www.schott.com/advanced_optics/english/download/schott-optical-glass-collection-datasheets-july-2015-eng.pdf.
100. I. H. Malitson, "Interspecimen Comparison of the Refractive Index of Fused Silica," Journal of the Optical Society of America **55**, 1205-1209 (1965).

101. J. Connolly, B. diBenedetto, and R. Donadio, "Specifications Of Raytran Material," in 1979), 141-144.
102. A. Yariv and P. Yeh, "Chapter 7 - Chromatic Dispersion and Polarization Mode Dispersion in Fibers," in *Photonics: Optical Electronics in Modern Communications* (Oxford University Press, New York, 2006).
103. Y. Ren, S. J. Beecher, G. Brown, A. Rodenas, F. Chen, and A. K. Kar, "Near-IR to Mid-IR Multimode Waveguides in Rare-Earth doped YAG by Ultrafast Laser Inscription," in OSA Technical Digest (online) (Optical Society of America, 2012), CTU1J.3.
104. G. Salamu, F. Jipa, M. Zamfirescu, and N. Pavel, "Cladding waveguides realized in Nd:YAG ceramic by direct femtosecond-laser writing with a helical movement technique," Optical Materials Express **4**, 790-797 (2014).
105. J. R. Macdonald, S. J. Beecher, A. Lancaster, P. A. Berry, K. L. Schepler, and A. K. Kar, "Ultrabroad Mid-Infrared Tunable Cr:ZnSe Channel Waveguide Laser," IEEE J. Sel. Top. Quant. Electon. **21**, 375-379 (2015).
106. I. T. Sorokina and E. Sorokin, "Femtosecond Cr^{2+}-Based Lasers," IEEE J. Sel. Top. Quant. Electon. **21**, 273-291 (2015).
107. P. Zorabedian, "Chapter 8 - Tunable External-Cavity Semiconductor Lasers," in *Tunable Lasers Handbook*, F. J. Duarte, ed. (Academic Press Limited, London, 1995).
108. A. S. Arnold, J. S. Wilson, and M. G. Boshier, "A simple extended-cavity diode laser," Review of Scientific Instruments **69**, 1236-1239 (1998).
109. S. B. Mirov, V. V. Fedorov, I. S. Moskalev, and D. V. Martyshkin, "Recent Progress in Transition-Metal-Doped II-VI Mid-IR Lasers," IEEE J. Sel. Top. Quant. Electron. **13**, 810-822 (2007).
110. H. H. Li, "Refractive index of alkaline earth halides and its wavelength and temperature derivatives," Journal of Physical and Chemical Reference Data **9**, 161-290 (1980).
111. D. Chandler-Horowitz and P. M. Amirtharaj, "High-accuracy, midinfrared ($450cm{-}1\leqslant\omega\leqslant4000cm^{-1}$) refractive index values of silicon," J. Appl. Phys. **97**, 123526 (2005).
112. IPG Photonics, "Lasers" (2016), retrieved 13/10/2016, 2016, http://www.ipgphotonics.com/category/4/Lasers.

113. R. H. Page, J. A. Skidmore, K. I. Schaffers, R. J. Beach, S. A. Payne, W. F. E. D. P. C. Krupke, and W. Bosenberg, "Demonstrations of diode - pumped and grating - tuned ZnSe:Cr^{2+} lasers," in *Advanced Solid State Lasers*, OSA Trends in Optics and Photonics Series (Optical Society of America, 1997), LS6.

114. A. Sennaroglu, U. Demirbas, A. Kurt, and M. Somer, "Concentration dependence of fluorescence and lasing efficiency in Cr^{2+}:ZnSe lasers," Optical Materials **29**, 703-708 (2007).

115. J. R. Macdonald, S. J. Beecher, P. A. Berry, K. L. Schepler, and A. K. Kar, "Widely Tunable Cr:ZnSe Channel Waveguide Laser," in *Advanced Solid-State Lasers Congress*, OSA Technical Digest (online) (Optical Society of America, 2013), MW1C.5.

116. R. W. Stites, S. A. McDaniel, J. O. Barnes, D. M. Krein, J. H. Goldsmith, S. Guha, and G. Cook, "Hot isostatic pressing of transition metal ions into chalcogenide laser host crystals," Optical Materials Express **6**, 3339-3353 (2016).

117. H. Namba, H. Osaka, K. Kamon, and F. Higuchi, "Process for preparing ZnSe single crystal," (Google Patents, 1986).

118. J. Li, Z. Zhang, Z. Sun, H. Luo, Y. Liu, Z. Yan, C. Mou, L. Zhang, and S. K. Turitsyn, "All-fiber passively mode-locked Tm-doped NOLM-based oscillator operating at 2-μm in both soliton and noisy-pulse regimes," Opt. Express **22**, 7875-7882 (2014).

119. S. A. McDaniel, A. Lancaster, R. W. Stites, F. Thorburn, A. K. Kar, and G. Cook, "Cr:ZnSe guided wave lasers and materials," in *SPIE Photonics West/LASE*, 2017), paper 10082-10012.

120. I. T. Sorokina, V. V. Dvoyrin, N. Tolstik, and E. Sorokin, "Mid-IR Ultrashort Pulsed Fiber-Based Lasers," IEEE J. Sel. Top. Quant. Electon. **20**, 1-12 (2014).

121. M. Bo and W. Qi Jie, "Broadly tunable single-mode mid-infrared quantum cascade lasers," Journal of Optics **17**, 023001 (2015).

122. I. T. Sorokina and E. Sorokin, "Chirped-Mirror Dispersion Controlled Femtosecond Cr:ZnSe Laser," in *Advanced Solid-State Photonics*, OSA Technical Digest Series (CD) (Optical Society of America, 2007), WA7.

123. T. J. Carrig, G. J. Wagner, A. Sennaroglu, J. Y. Jeong, and C. R. Pollock, "Mode-locked Cr^{2+}:ZnSe laser," Optics Letters **25**, 168-170 (2000).

124. J. Ma, G. Xie, P. Lv, W. Gao, P. Yuan, L. Qian, U. Griebner, V. Petrov, H. Yu, H. Zhang, and J. Wang, "Wavelength-Versatile Graphene-Gold Film Saturable

Absorber Mirror for Ultra-Broadband Mode-Locking of Bulk Lasers," Scientific Reports **4**, 5016 (2014).

125. M. N. Cizmeciyan, H. Cankaya, A. Kurt, and A. Sennaroglu, "Operation of femtosecond Kerr-lens mode-locked Cr:ZnSe lasers with different dispersion compensation methods," Appl. Phys. B **106**, 887-892 (2012).
126. J. E. Williams, V. V. Fedorov, D. V. Martyshkin, I. S. Moskalev, R. P. Camata, and S. B. Mirov, "Mid-IR laser oscillation in Cr^{2+}:ZnSe planar waveguide," Opt. Express **18**, 25999-26006 (2010).
127. A. A. Lagatsky, A. Choudhary, P. Kannan, D. P. Shepherd, W. Sibbett, and C. T. A. Brown, "Fundamentally mode-locked, femtosecond waveguide oscillators with multi-gigahertz repetition frequencies up to 15 GHz," Opt. Express **21**, 19608-19614 (2013).
128. Y. Ren, G. Brown, R. Mary, G. Demetriou, D. Popa, F. Torrisi, A. C. Ferrari, F. Chen, and A. K. Kar, "7.8 GHz Graphene-based 2 μm Monolithic Waveguide Laser," IEEE J. Sel. Top. Quant. Electon. **PP**, 1-1 (2014).
129. F. X. Kartner, J. A. d. Au, and U. Keller, "Mode-locking with slow and fast saturable absorbers-what's the difference?," IEEE J. Sel. Top. Quantum Electron. **4**, 159-168 (1998).
130. H. A. Haus, "Mode-locking of lasers," IEEE J. Sel. Top. Quant. Electon. **6**, 1173-1185 (2000).
131. A. J. DeMaria, D. A. Stetser, and H. Heynau, "Self Mode-Locking of Lasers with Saturable Absorbers," Appl. Phys. Lett. **8**, 174-176 (1966).
132. R. Mary, G. Brown, S. J. Beecher, F. Torrisi, S. Milana, D. Popa, T. Hasan, Z. Sun, E. Lidorikis, S. Ohara, A. C. Ferrari, and A. K. Kar, "1.5 GHz picosecond pulse generation from a monolithic waveguide laser with a graphene-film saturable output coupler," Opt. Express **21**, 7943-7950 (2013).
133. A. Martinez and Z. Sun, "Nanotube and graphene saturable absorbers for fibre lasers," Nat Photon **7**, 842-845 (2013).
134. C. J. Saraceno, O. H. Heckl, C. R. E. Baer, C. Schriber, M. Golling, K. Beil, C. Kränkel, T. Südmeyer, G. Huber, and U. Keller, "Sub-100 femtosecond pulses from a SESAM modelocked thin disk laser," Appl. Phys. B **106**, 559-562 (2012).
135. W. Koechner, "Ch. 9. Mode Locking," in *Solid-State Laser Engineering* (Springer, New York, 2006), pp. 534-586.

136. F. Bonaccorso, Z. Sun, T. Hasan, and A. C. Ferrari, "Graphene photonics and optoelectronics," Nat Photon **4**, 611-622 (2010).
137. G. Demetriou, H. T. Bookey, F. Biancalana, E. Abraham, Y. Wang, W. Ji, and A. K. Kar, "Nonlinear optical properties of multilayer graphene in the infrared," Opt. Express **24**, 13033-13043 (2016).
138. B. W. Tilma, M. Mangold, C. A. Zaugg, S. M. Link, D. Waldburger, A. Klenner, A. S. Mayer, E. Gini, M. Golling, and U. Keller, "Recent advances in ultrafast semiconductor disk lasers," Light Sci Appl **4**, e310 (2015).
139. G. Demetriou, "Ultrafast Nonlinear Optics of Bulk and Two-Dimensional Materials for Infrared Applications," (Heriot-Watt University, 2016).
140. M. Rhodes, G. Steinmeyer, J. Ratner, and R. Trebino, "Pulse-shape instabilities and their measurement," Laser & Photonics Reviews **7**, 557--565 (2013).
141. D. Yuqiang, S. Qing, C. Shiying, Y. Jing, W. Ching-yue, and Z. Zhigang, "Accurate and automatic characterization of femtosecond optical pulses," Metrologia **49**, S39 (2012).
142. D. T. Reid, W. Sibbett, J. M. Dudley, L. P. Barry, B. Thomsen, and J. D. Harvey, "Commercial Semiconductor Devices for Two Photon Absorption Autocorrelation of Ultrashort Light Pulses," Appl. Optics **37**, 8142-8144 (1998).
143. ISOStandardscatalogue, "ISO 11146-1" (2005), retrieved 13th January, 2013, http://www.iso.org/iso/home/store/catalogue_tc/catalogue_detail.htm?csnumber=33625.
144. S. McDaniel, D. Hobbs, B. MacLeod, E. Sabatino, P. Berry, K. Schepler, W. Mitchell, and G. Cook, "Cr:ZnSe laser incorporating anti-reflection microstructures exhibiting low-loss, damage-resistant lasing at near quantum limit efficiency," Optical Materials Express **4**, 2225-2232 (2014).
145. I. S. Moskalev, V. V. Fedorov, and S. B. Mirov, "Tunable, single-frequency, and multi-watt continuous-wave Cr^{2+}:ZnSe lasers," Opt. Express **16**, 4145-4153 (2008).
146. M. N. Cizmeciyan, J. W. Kim, S. Bae, B. H. Hong, F. Rotermund, and A. Sennaroglu, "Graphene mode-locked femtosecond Cr:ZnSe laser at 2500 nm," Optics Letters **38**, 341-343 (2013).
147. M. N. Cizmeciyan, H. Cankaya, A. Kurt, and A. Sennaroglu, "Kerr-lens mode-locked femtosecond Cr^{2+}:ZnSe laser at 2420 nm," Opt. Lett. **34**, 3056-3058 (2009).

148. K. L. Schepler, R. D. Peterson, P. A. Berry, and J. B. McKay, "Thermal effects in Cr^{2+}:ZnSe thin disk lasers," IEEE J. Sel. Top. Quant. Electron. **11**, 713-720 (2005).

149. I. T. Sorokina, "Cr^{2+}-doped II–VI materials for lasers and nonlinear optics," Optical Materials **26**, 395-412 (2004).

150. Y. Sato and T. Taira, "Highly accurate interferometric evaluation of thermal expansion and dn/dT of optical materials," Optical Materials Express **4**, 876-888 (2014).

151. D. M. Simanovskii, H. A. Schwettman, H. Lee, and A. J. Welch, "Mid-infrared Optical Breakdown in Transparent Dielectrics," Physical Review Letters **91**, 107601 (2003).

152. M. Debenham, "Refractive indices of zinc sulfide in the 0.405–13 μm wavelength range," Appl. Optics **23**, 2238-2239 (1984).

153. D. E. Zelmon, D. L. Small, and R. Page, "Refractive-index measurements of undoped yttrium aluminum garnet from 0.4 to 5.0 μm," Appl. Optics **37**, 4933-4935 (1998).

154. W. Koechner, "Ch. 2. Properties of Solid-state Laser Materials," in *Solid-State Laser Engineering* (2006).

155. B. T. Do and A. V. Smith, "Bulk optical damage thresholds for doped and undoped, crystalline and ceramic yttrium aluminum garnet," Appl. Optics **48**, 3509-3514 (2009).

156. I. T. Sorokina, E. Sorokin, S. Mirov, V. Fedorov, V. Badikov, V. Panyutin, and K. I. Schaffers, "Broadly tunable compact continuous-wave Cr^{2+}:ZnS laser," Opt. Lett. **27**, 1040-1042 (2002).

157. I. S. Moskalev, V. V. Fedorov, and S. B. Mirov, "10-Watt, pure continuous-wave, polycrystalline Cr2+:ZnS laser," Opt. Express **17**, 2048-2056 (2009).

158. S. Vasilyev, M. Mirov, and V. Gapontsev, "Kerr-lens mode-locked femtosecond polycrystalline Cr2+:ZnS and Cr2+:ZnSe lasers," Opt. Express **22**, 5118-5123 (2014).

159. Y.-C. Jeong, A. J. Boyland, J. K. Sahu, S.-H. Chung, J. Nilsson, and D. N. Payne, "Multi-kilowatt Single-mode Ytterbium-doped Large-core Fiber Laser," J. Opt. Soc. Korea **13**, 416-422 (2009).

160. J. R. Macdonald, S. J. Beecher, P. A. Berry, K. L. Schepler, S. B. Mirov, and A. K. Kar, "Compact Cr:ZnS Channel Waveguide Laser Operating at 2360 nm," in

Advanced Solid-State Lasers Congress, OSA Technical Digest (online) (Optical Society of America, 2013), MW1C.3.

161. S. B. Mirov and V. V. Fedorov, "Mid-IR microchip laser: ZnS:Cr^{2+} laser with saturable absorber material," (Google Patents, 2014).

162. S. Mirov, V. Fedorov, I. Moskalev, D. Martyshkin, and C. Kim, "Progress in Cr^{2+} and Fe^{2+} doped mid-IR laser materials," Laser & Photonics Reviews **4**, 21-41 (2010).

163. D. Findlay and R. A. Clay, "The measurement of internal losses in 4-level lasers," Physics Letters **20**, 277-278 (1966).

164. W. Koechner, "Ch. 3. Laser Oscillator," in *Solid-State Laser Engineering* (Springer, New York, 2006), pp. 102-155.

165. S. B. Mirov, V. V. Fedorov, K. Graham, I. S. Moskalev, V. V. Badikov, and V. Panyutin, "Erbium fiber laser–pumped continuous-wave microchip Cr2+:ZnS and Cr^{2+}:ZnSe lasers," Optics Letters **27**, 909-911 (2002).

166. X. Zou, Y F. Dai, Y Y. Li, Y J. Dong, J. Du, and Y X. Leng, "Cr:ZnSe single crystal laser by pumping into the zero phonon line for efficiency enhancement," Laser Physics Letters **11**, 115810 (2014).

167. M. Ebrahim-Zadeh and I. T. Sorokina, *Mid-infrared Coherent Sources and Applications* (IOS Press, Amsterdam, 2005).

168. B. Jean and T. Bende, "Mid-IR Laser Applications in Medicine," in *Solid-State Mid-Infrared Laser Sources*, I. Sorokina and K. Vodopyanov, eds. (Springer Berlin Heidelberg, 2003), pp. 530-565.

169. N. S. Prasad, "Optical Communications in the mid-wave IR spectral band," in *Free-Space Laser Communications: Principles and Advances* (Springer New York, New York, NY, 2008), pp. 347-391.

170. J. J. Adams, C. Bibeau, R. H. Page, D. M. Krol, L. H. Furu, and S. A. Payne, "4.0-4.5-μm lasing of Fe:ZnSe below 180 K, a new mid-infrared laser material," Optics Letters **24**, 1720-1722 (1999).

171. G. A. Slack and B. M. O'Meara, "Infrared Luminescence of Fe^{2+} in ZnS," Physical Review **163**, 335-341 (1967).

172. V. Fedorov, D. Martyshkin, M. Mirov, I. S. Moskalev, S. Vasilyev, J. Peppers, S. B. Mirov, and V. P. Gapontsev, "Fe-doped II-VI Mid-Infrared Laser Materials for the 3 to 8 μm Region," in *CLEO: 2013*, OSA Technical Digest (online) (Optical Society of America, 2013), JM4K.2.

173. K. N. Firsov, E. M. Gavrishchuk, S. Y. Kazantsev, I. G. Kononov, and S. A. Rodin, "Increasing the radiation energy of ZnSe : Fe $^{2+}$ laser at room temperature," Laser Physics Letters **11**, 085001 (2014).

174. N. Myoung, V. V. Fedorov, S. B. Mirov, and L. E. Wenger, "Temperature and concentration quenching of mid-IR photoluminescence in iron doped ZnSe and ZnS laser crystals," Journal of Luminescence **132**, 600-606 (2012).

175. D. Jaque, N. D. Psaila, R. R. Thomson, F. Chen, L. M. Maestro, A. Ródenas, D. T. Reid, and A. K. Kar, "Ultrafast laser inscription of bistable and reversible waveguides in strontium barium niobate crystals," Appl. Phys. Lett. **96**, 191104 (2010).

176. G. Demetriou, J.-P. Bérubé, R. Vallée, Y. Messaddeq, C. R. Petersen, D. Jain, O. Bang, C. Craig, D. W. Hewak, and A. K. Kar, "Refractive index and dispersion control of ultrafast laser inscribed waveguides in gallium lanthanum sulphide for near and mid-infrared applications," Opt. Express **24**, 6350-6358 (2016).

177. R. R. Thomson, S. Campbell, I. J. Blewett, A. K. Kar, and D. T. Reid, "Optical waveguide fabrication in z-cut lithium niobate (LiNbO3) using femtosecond pulses in the low repetition rate regime," Appl. Phys. Lett. **88**, - (2006).

178. V. Z. Evgeny, V. I. Zhekov, L. A. Kulevskii, T. M. Murina, V. O. Vyacheslav, A. M. Prokhorov, A. D. Savel'ev, V. S. Valery, B. P. Starikov, and M. I. Timoshechkin, "Stimulated emission from Er 3+ ions in yttrium aluminum garnet crystals at $\lambda = 2.94$ μ," Soviet Journal of Quantum Electronics **4**, 1039 (1975).

179. A. A. Kaminskii, "Summary of the Properties of Activated Laser Crystals," in *Laser Crystals: Their Physics and Properties* (Springer Berlin Heidelberg, Berlin, Heidelberg, 1990), pp. 166-318.

180. J. W. Evans, P. A. Berry, and K. L. Schepler, "840 mW continuous-wave Fe:ZnSe laser operating at 4140 nm," Optics Letters **37**, 5021-5023 (2012).

181. D. V. Martyshkin, V. V. Fedorov, M. Mirov, I. Moskalev, S. Vasilyev, and S. B. Mirov, "High Average Power (35 W) Pulsed Fe:ZnSe laser tunable over 3.8-4.2 μm," in *CLEO: 2015*, OSA Technical Digest (online) (Optical Society of America, 2015), SF1F.2.

182. M. P. Frolov, Y. V. Korostelin, V. I. Kozlovsky, V. V. Mislavskii, Y. P. Podmar'kov, S. A. Savinova, and Y. K. Skasyrsky, "Study of a 2-J pulsed Fe:ZnSe 4-μm laser," Laser Physics Letters **10**, 125001 (2013).

183. Y. Okamura, S. Yoshinaka, and S. Yamamoto, "Measuring mode propagation losses of integrated optical waveguides: a simple method," Appl. Optics **22**, 3892-3894 (1983).

184. Q. An, Y. Ren, Y. Jia, J. R. Vázquez de Aldana, and F. Chen, "Mid-infrared waveguides in zinc sulfide crystal," Optical Materials Express **3**, 466-471 (2013).

185. S. Gross, N. Jovanovic, A. Sharp, M. Ireland, J. Lawrence, and M. J. Withford, "Low loss mid-infrared ZBLAN waveguides for future astronomical applications," Opt. Express **23**, 7946-7956 (2015).

186. V. V. Fedorov, S. B. Mirov, A. Gallian, D. V. Badikov, M. P. Frolov, Y. V. Korostelin, V. I. Kozlovsky, A. I. Landman, Y. P. Podmar'kov, V. A. Akimov, and A. A. Voronov, "3.77-5.05 μm tunable solid-state lasers based on Fe^{2+}-doped ZnSe crystals operating at low and room temperatures," IEEE J. Quant. Electron. **42**, 907-917 (2006).

187. J. W. Evans, P. A. Berry, and K. L. Schepler, "A Passively Q-Switched, CW-Pumped Fe:ZnSe Laser," IEEE J. Quantum Electron. **50**, 204-209 (2014).

188. A. Lancaster, G. Cook, S. McDaniel, J. Evans, P. Berry, J. Shephard, and A. Kar, "Fe:ZnSe Channel Waveguide Laser Operating at 4122 nm," in *CLEO: 2015*, OSA Technical Digest (online) (Optical Society of America, 2015), SM2F.5.

189. G. D. Marshall, M. Ams, and M. J. Withford, "Direct laser written waveguide-Bragg gratings in bulk fused silica," Opt. Lett. **31**, 2690-2691 (2006).

190. G. Brown, R. R. Thomson, A. K. Kar, N. D. Psaila, and H. T. Bookey, "Ultrafast laser inscription of Bragg-grating waveguides using the multiscan technique," Opt. Lett. **37**, 491-493 (2012).

191. D. Trivedi, P. Tayebati, and M. Tabat, "Measurement of large electro-optic coefficient in epitaxial thin films of strontium barium niobate (SBN:75)," in *Lasers and Electro-Optics Society Annual Meeting, 1996. LEOS 96., IEEE*, 1996), 18-19 vol.12.

192. A. Guarino, G. Poberaj, D. Rezzonico, R. Degl'Innocenti, and P. Gunter, "Electro-optically tunable microring resonators in lithium niobate," Nat Photon **1**, 407-410 (2007).

193. P. Gunter and J. Huignard, *Photorefractive Materials and Their Applications 1*, Photorefractive Materials and Their Applications (Springer, New York, 2006), Vol. 113.

194. N. Tolstik, E. Sorokin, and I. T. Sorokina, "Graphene mode-locked Cr:ZnS laser with 41 fs pulse duration," Opt. Express **22**, 5564-5571 (2014).

195. J. Kuhl and J. Heppner, "Compression of femtosecond optical pulses with dielectric multilayer interferometers," IEEE J. Quant. Electron. **22**, 182-185 (1986).

196. A. Lancaster, A. Choudhary, J. S. Nitin, R. Mary, D. P. Shepherd, and A. K. Kar, "1.94 GHz CW Modelocked Ytterbium-Doped Bismuthate Glass Waveguide Laser," in *Advanced Solid State Lasers*, OSA Technical Digest (online) (Optical Society of America, 2015), AM5A.22.

Appendix

1. ULI Waveguide Inscription in Strontium Barium Niobate

1.1. Introduction

Inscription parameters for the fabrication of depressed cladding waveguides were investigated at Heriot-Watt University in close collaboration with Dr. Gary Cook from WPAFB. Dr. Cook spent six weeks working in the laboratory at Heriot-Watt University with our research team developing the waveguides.

Strontium Barium Niobate (SBN) is in many ways an excellent material to use in photonics because of its nonlinear, electro optic and photorefractive properties. This investigation focused on its electro optic and photorefractive features. The main reason for developing waveguides in SBN is to develop non mechanical phase modulators and wavelength tuning elements for transition metal doped ZnSe waveguide lasers. SBN is available in different Strontium (Sr) and Barium (Ba) ratios: the two most common are $Sr_{0.61}Ba_{0.39}Nb_2O_6$ (SBN:61) and $Sr_{0.75}Ba_{0.25}Nb_2O_6$ (SBN:75). Both types are evaluated in this investigation to assess their suitability for wavelength tuning elements in Cr:ZnSe laser resonators. All the SBN:61 and SBN:75 used in this investigation was purchased from Altechna and fabricated using the Stepanov technique [1].

1.2. Waveguide Fabrication in SBN:61

Initially, ULI in SBN:61 was investigated with a range of single line modification elements. The SBN:61 samples were not poled before this test. The inscription beam was incident parallel to the c-axis of the SBN:61 crystal to allow access to the strongest electro optic coefficient, as shown in Figure 1:

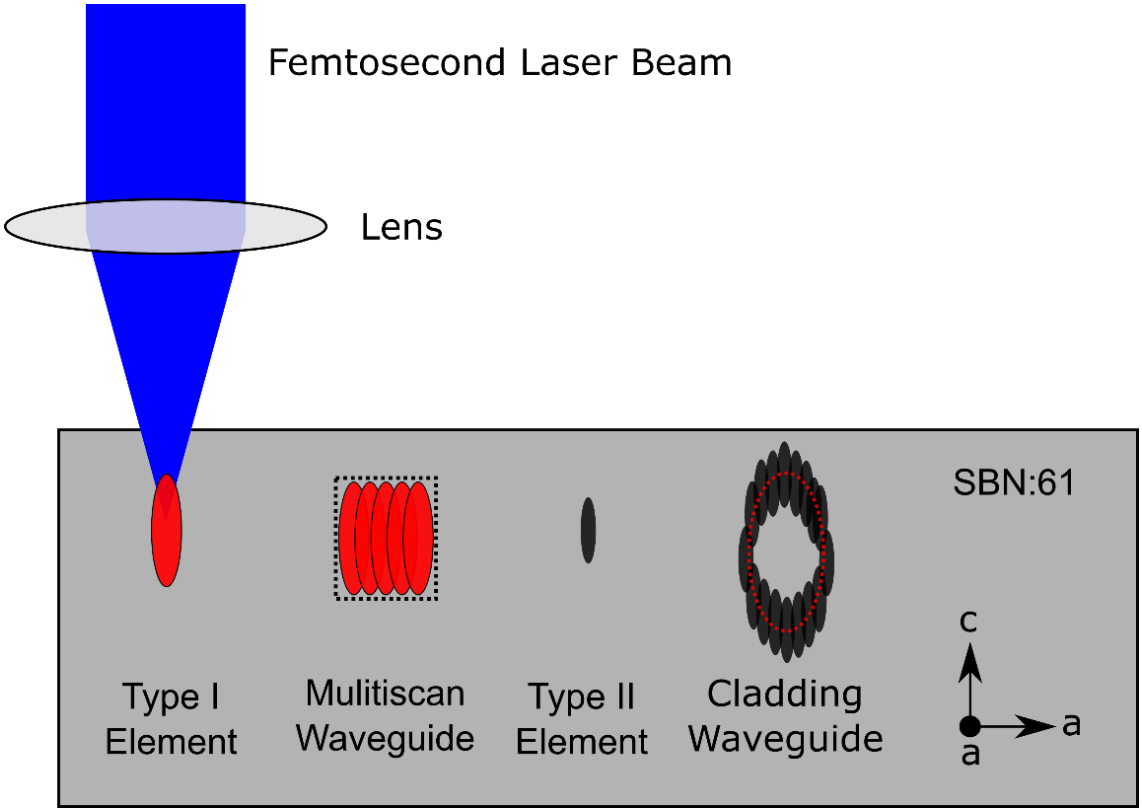

Figure 1: Schematic of multiscan and depressed cladding waveguides fabricated using ULI in SBN:61 with crystal axis given.

The range of inscription parameters investigated are given in Table 1.

SBN single element ULI modification parameter scan	
Inscription laser	IMRA 400 µJewel
Laser wavelength	1047 nm
Laser polarisation	Horizontal
Laser PRF & pulse width	100 kHz at 1.1 ps, 200 kHz at 447 fs, 500 kHz at 359 fs & 1 MHz at 373 fs
Pulse energy	0.05 to 2.5 µJ
Inscription lens	0.4 & 0.68 NA
Inscription depth below sample surface	200 µm
Sample translation speed	3, 5 & 10 $mm \cdot s^{-1}$

Table 1:Inscription parameters investigated in single scans of non-poled SBN:61 with inscription beam parallel to the c-axis.

Imaging the end facet of the sample with a transmission microscope can give a lot of information of the *delta n* induced by the inscription process, as shown in Figure 2.

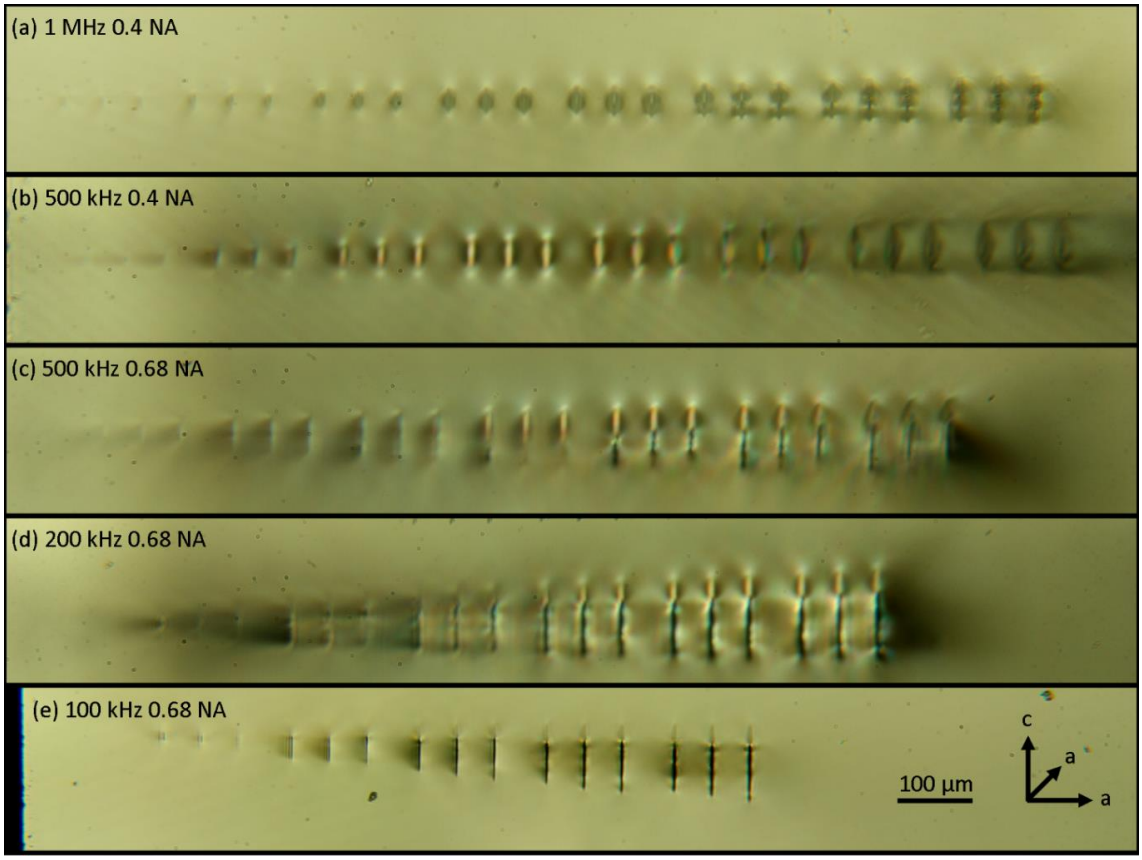

Figure 2:Transmission microscope image of single line modification elements in SBN:61 with a range of laser PRF and inscription lenses. (a) 1 MHz with 0.4 NA from left to right there are banks of 3 lines with 10, 5 and 3 mm·s^{-1} translation speeds respectively. The inscription pulse energy of each bank from left to right is 0.05 to 0.25 µJ increasing in 0.05 µJ steps. (b) 500 kHz with 0.4 NA using the same parameter pattern as (a), but with pulse energies of 0.1 to 0.8 µJ. (c) 500 kHz with 0.68 NA parameter pattern as (a) but with pulse energies of 0.2 to 0.8 µJ. (e) 100 kHz 0.68 NA parameter pattern same as (a), but with pulse energies of 0.25 to 1.75 µJ. (e) 200 kHz 0.68 NA parameter pattern same as (a), but with pulse energies of 0.5 to 2.5 µJ.

From Figure 2 (b), 500 kHz 0.4 NA, it can be seen that the modified regions are brighter than the surrounding unmodified region. This indicates that an increase in refractive index has been induced. This type of modification, Type I, can be used to build up a waveguide core with a square cross-section. This is achieved by passing the sample through the focus of the inscription beam multiple times with a small lateral offset to form a multiscan waveguide, as shown in Figure 1. The multiscan method has proven to be very effective in fused silica and Yb:Bismuthate glass because of its single mode operation with MFDs in the 5 - 10 µm range, which is well matched to SMF 28 fibre when guiding 1.5 µm light

[2]. Propagation losses at 1.5 μm of less than 1 dB/cm can be easily achieved with this method. The MFD of Type I waveguides, single element and multiscan, are often in the few to 20 μm range, which might not provide efficient coupling when compared with Cr:ZnSe waveguides, which are around 60 μm. From Figure 2 (e), 100 kHz 0.68 NA, the black lines show clear Type II modification, which is a localised reduction in refractive index. Using these elements and arranging multiple of them in an annular pattern may produce an effective depressed cladding waveguide. The parameters investigated in Figure 2 (c) & (b), 500 kHz and 200 kHz with 0.68 NA respectively, show the transition from Type I modification to Type II. This investigation has shown that SBN:61 is a promising material for both increased and decreased in Δn waveguides. This adaptability will be very useful for future applications.

From the promising single line scans, multiscan waveguide fabrication was investigated. However, before the inscription step the SBN:61 samples were electrically poled to create a single ferroelectric domain. The sample was heated in a pottery furnace from room temperature to 150 ^{0}C at a rate of 50 ^{0}C per hour. The furnace was then held at 150 ^{0}C for 15 minutes, during which a 1 kV DC electric field (5000 V/cm) was applied across the c-axis. The sample was then left to cool with the voltage still applied to force all the domains to be in the same direction.

From the single element modification investigation, no clear path for which type of waveguide to investigate was found. It was therefore decided to investigate multiscan waveguides and depressed cladding waveguides, as shown in Figure 1. The inscription parameters used for the depressed cladding waveguides are given below in Table 2:

SBN:61 depressed cladding waveguides ULI parameters	
Laser	IMRA 400 μJewel
Laser wavelength	1047 nm
Laser polarisation	Horizontal
Laser PRF & pulse width	100 kHz at 1.1 ps
Pulse energy	1 μJ
Inscription lens	0.68 NA
Inscription depth below sample surface	250 μm
Sample translation speed	10 mm·s^{-1}
Waveguide diameter	50 , 75 & 100 μm
Number of elements	Equal to the diameter in μm

Table 2: Inscription parameters used in investigation of SBN:61 depressed cladding waveguides.

The effect of inscription depth was investigated by inscribing the waveguides with the centre of the waveguide at 250 and 700 μm below the samples surface. Figure 3 below shows a transmission microscope image of the cladding waveguides inscribed at different depths:

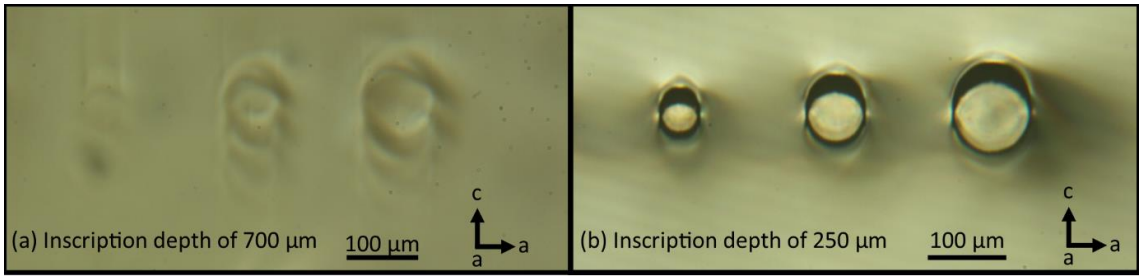

Figure 3: Pre-poled SBN:61 depressed cladding waveguides. The inscription laser was operated at 100 kHz with a pulse energy of 1 μJ, and a 0.68 NA lens was used to focus the light into the positive c-axis. (a) Inscription depth was 700 μm from surface of the sample. (b) Inscription depth was 250 μm from surface of the sample.

It's very clear from comparing Figure 3 (a) and (b) that there is a large modification dependence on inscription depth. The waveguides inscribed at 700 μm were barely visible. It's also worth noting that the modification at the top and bottom of the waveguide inscribed at a depth of 250 μm is different. This presents some challenges in creating a symmetrical waveguide in the vertical axis. Never the less, the 250 μm depth waveguides appeared viable for testing the guiding properties of SBN:61 cladding waveguides.

Multiscan waveguides were investigated using the parameters given in Table 3:

SBN:61 depressed cladding waveguides' ULI parameters	
Laser	IMRA 400 μJewel
Laser wavelength	1047 nm
Laser polarisation	Horizontal
Laser PRF & pulse width	500 kHz at 359 fs
Pulse energy	0.3 to 0.5 μJ in steps of 0.1 μJ
Inscription lens	0.40 NA
Inscription depth below sample surface	200 μm
Sample translation speed	10 $mm \cdot s^{-1}$
Number of elements	1 to 31 in steps of 10
Space between elements	1 μm

Table 3: ULI parameters used for the fabrication of multiscan waveguides in pro-poled SBN: 61. The inscription beam was parallel to the c-axis of the crystal.

A transmission microscope image of the multiscan waveguides inscribed using a pulse energy of 0.3 μJ is given in Figure 4:

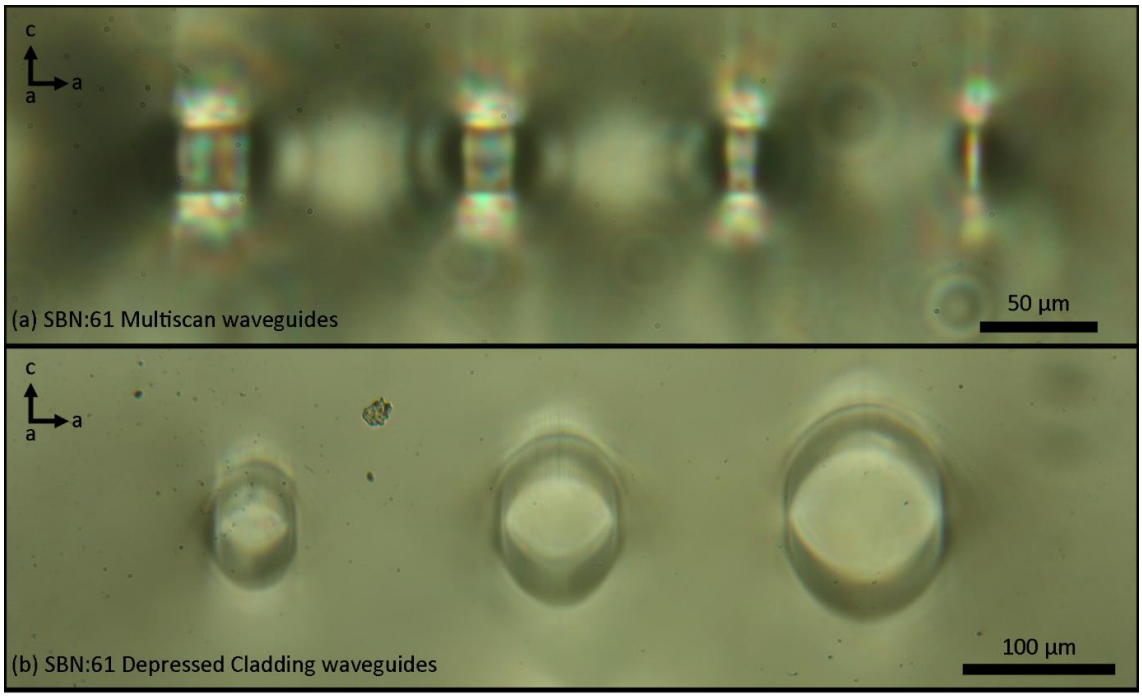

Figure 4: Transmission microscope image of SBN:61 waveguides. The inscription laser was operated at 500 kHz with a pulse energy of 0.3 μJ and the 0.4 NA lens was used to focus the laser beam on to the sample. (a) Multiscan waveguides with 31, 21, 11 and 1 elements respectively from left to right. The spacing between each element was 1 μm and the waveguides

were inscribed at a depth of 200 μm. (b) Depressed cladding waveguides with diameters 50, 75 and 100 μm respectively from left to right. The number of elements making up the cladding waveguides is equal to their diameter in μm.

From Figure 4, it can be seen that the waveguides guide light in the modified core which is expected for an increase in the refractive index. Interestingly, there is the gap between the waveguides and above each waveguide, which also appears to be guiding light. This would suggest that there is also a reduction in the refractive index by the laser. Similar results have been found with multiscan waveguides in GLS glass. This effect can be due to the moving of material in the modified region. With a densification of material in the modified area leading to an increase in refractive index and a reduction of refractive index from the surrounding region. To investigate this further, depressed cladding waveguides were inscribed using the same laser parameters as those of the multiscan waveguide. Figure 4 (b) shows depressed cladding waveguides fabricated using a laser PRF of 500 kHz, pulse width of 359 fs and a pulse energy of 0.3 μm. It can be seen from this figure that the cladding waveguides are guiding light in the central unmodified region, therefore a positive and negative change in refractive index is being induced with this set of inscription laser parameters.

1.3. Waveguide Fabrication in Ce Doped SBN:61

Doping SBN:61 with Ce greatly increases the photorefractive properties of SBN [3]. Photorefractive materials have been proposed for a number of different applications, most notably data storage because of the relatively long time scales involved in the process [4]. In this application, it could be used to form a Bragg grating in the waveguide by using two intersecting green laser beams. This would allow a tuneable Bragg grating to be created with the grating period proportional to the angle between the intersecting green laser beams. Figure 5, taken from Ref. [4], shows how this is implemented at 1550 nm:

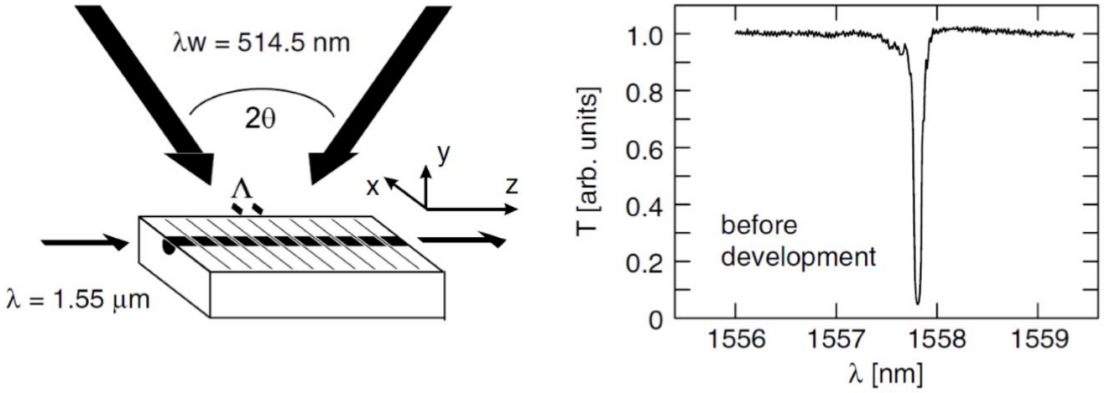

Figure 5: Holographically recorded reflection filters in $LiNbO_3$:Ti:Cu channel waveguides.(a) Geometry for recording and read-out of the grating, and (b) typical transmission spectrum T(λ) of a 15 mm-long filter. The c-axis referred to in the report is the z-axis in this schematic.

Cladding waveguides fabricated at 100 kHz with 0.68 NA were investigated using the parameters developed in SBN: 61, given in Table 2 . On inspection of the end facet with a transmission microscope, the waveguides were all found to be over exposed, caused by using too large a pulse energy, as shown in Figure 6:

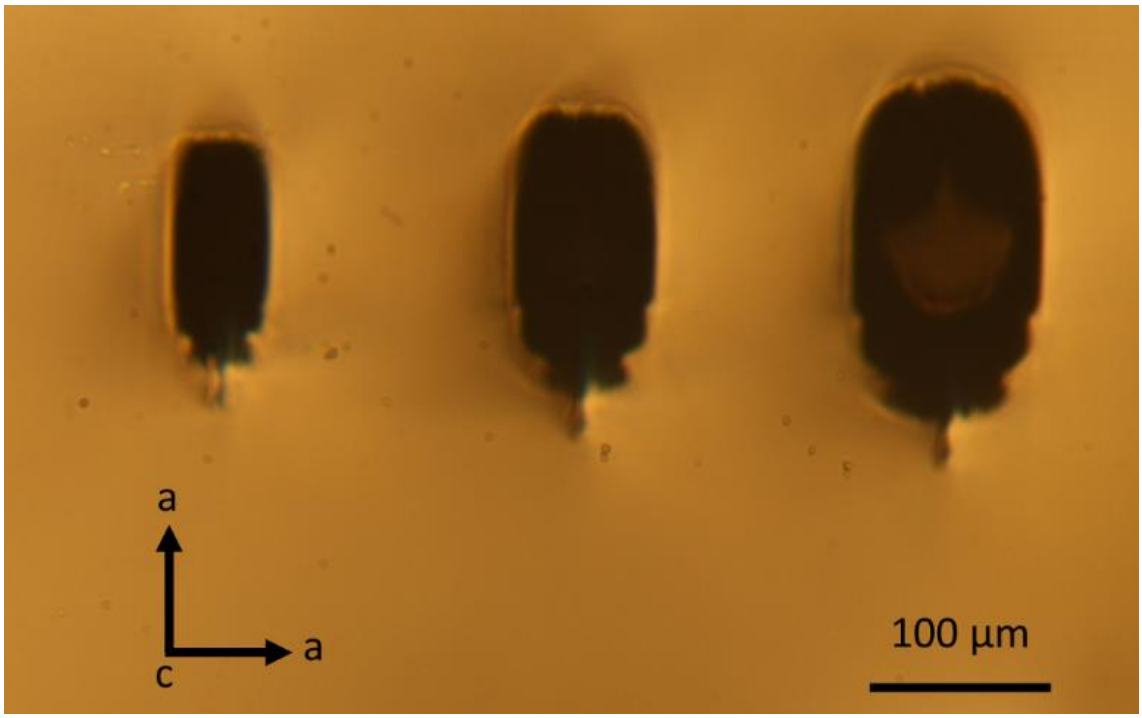

Figure 6: Ce:SBN61 depressed cladding waveguides inscribed using 100 kHz, 0.68 NA, 1 μJ and 10 mms^{-1}. Inscription beam was parallel to an a-axis of the crystal.

There are two initial thoughts as to what could be the reason for the discrepancy in inscription ‘recipes’ between SBN:61 and Ce:SBN:61. Cr dopant in ZnSe has been shown to drastically change the inscription ‘recipe’ of ZnSe [5]. The reason for this is that there is a small linear absorption of the Cr at 1047 nm which is the emission wavelength of the inscription laser. This absorption reduces the amount of modification for a given pulse energy which is not observed, thus it is not the Ce ions that are causing the difference in ULI parameters. A more likely reason for the increased inscription sensitivity is thought to be associated with the change in the effective polarisation properties of the inscription process with respect to the crystal c-axis. Previous inscriptions have been designed to produce waveguides where access to the r_{33} coefficient is possible (polarisation propagation issues aside). This meant we had to create waveguides with the crystal c-axis perpendicular to the waveguide direction. In order to minimise the external voltage needed to modulate the refractive index of the waveguides, the crystals were cut with the c-axis in the thinnest dimension, which, in turn, meant writing the waveguides through the crystal c-face. In this orientation, linearly polarised inscription light experiences progressive radial birefringence for all optical vectors in the a-c crystal plane with a resolved component along the c-axis. This creates a radially dependent progressive phase retardation for opposite segments of the focused light cone, while not introducing any phase delay for the remaining orthogonal segments of the focused inscription light. Figure 7 illustrates this concept. The presence of this type of radial and directionally dependent birefringence will cause the focal spot to become distorted, resulting in a reduction of the focused intensity compared with identically focused light in the absence of any such phase distortion. Conversely, the use of horizontally polarised light, where the polarisation vector is perpendicular to the crystal c-axis, does not create any radial dependent birefringence, and so the focal spot is likely to be much smaller than in the previous case, with a corresponding increase in the apparent inscription sensitivity.

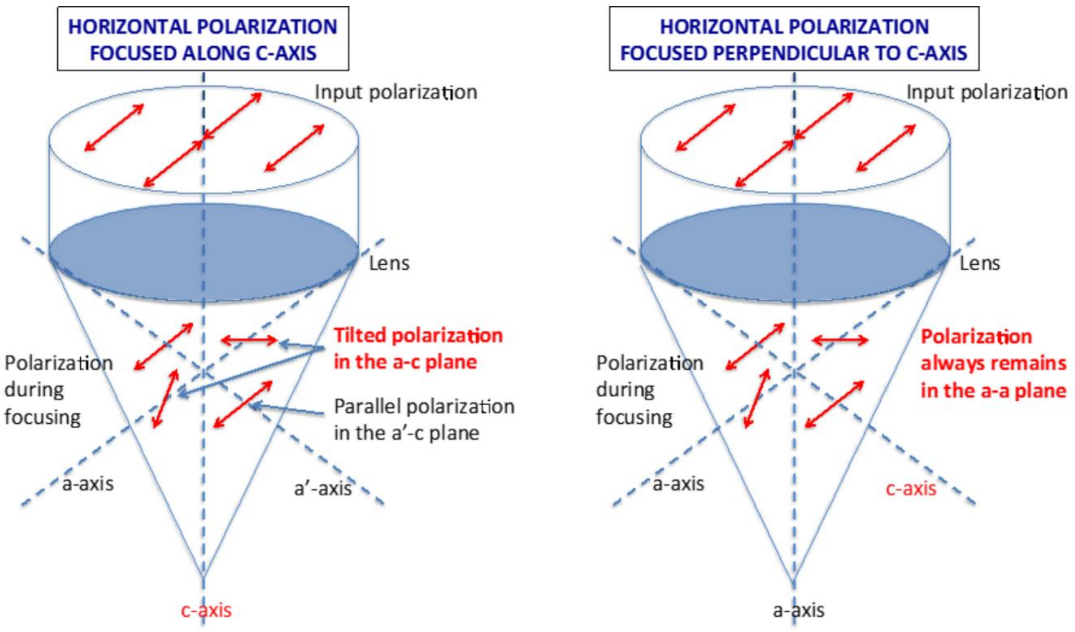

Figure 7: – Birefringence issues with focusing in SBN. Focusing along the c-axis causes tilting of the polarisation vector for light a-c plane (left), while the polarisation vector always remains in the a-a plane when focusing along the a-axis with the input polarisation perpendicular to the crystal c-axis (right). The two a-axes have been distinguished with a' symbol in the left-hand image, for clarity. This diagram has been provided by Dr. G. Cook.

The birefringence issue was confirmed by inscribing parallel to an a-axis of non-doped SBN:61. Inscription in parallel to the a-axis of SBN:61 was then used to optimise the inscription 'recipe' for Ce:SBN:61. The reason for using SBN:61 to develop the parameters was the higher cost and reduced availability of Ce:SBN:61. The parameter range found to give viable depressed cladding waveguides in Ce:SBN:61 is given in Table 4 below:

SBN:61 Depressed cladding waveguides' ULI parameters	
Laser	IMRA 400 µJewel
Laser wavelength	1047 nm
Laser polarisation	Horizontal
Laser PRF & pulse width	100 kHz at 1.1 ps
Pulse energy	0.3 to 0.35 µJ for top of waveguide 0.35 to 0.4 µJ for bottom of waveguide
Inscription lens	0.68 NA
Inscription depth below sample surface	250 µm
Sample translation speed	10 $mm \cdot s^{-1}$
Waveguide diameter	30, 40, 50 , 60 & 75 µm
Number of elements	Equal to the diameter in µm and it multiplied by 3/5

Table 4: Inscription parameters for Ce:SBN:61 depressed cladding waveguides. Note the change in modification with depth is compensated for by reducing the pulse energy for the top half of the waveguide.

To reduce the difference in modification element height with depth, the tops of the waveguides were inscribed with less pulse energy than the bottom of the waveguides, this is discussed further in the SBN:75 section of this report. A transmission microscope image of Ce:SBN:61 waveguides is given in Figure 8:

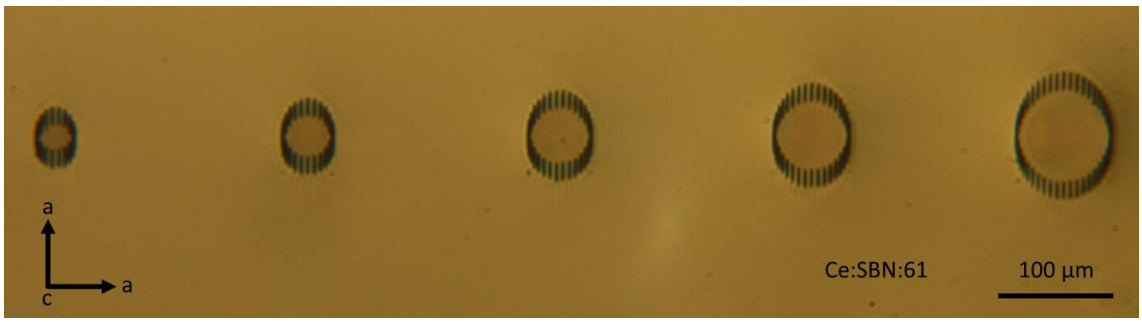

Figure 8: Transmission microscope image of depressed cladding waveguides in Ce:SBN:61. The inscription laser was parallel to the a-axis of the crystal. Inscription parameters were 100 kHz, 1.1 ps, 0.3 µJ for top half, 0.35 µJ for bottom half, a number of elements are equal in diameter in µm multiplied by 3/5 and 0.68 NA lens. The waveguides had a diameter of 30, 40, 50, 60 & 75 µm respectively, as seen from left to right in the figure.

Depressed cladding waveguides have been fabricated and are ready for use in applications. The first will be to insert the waveguide inside an extended cavity Cr:ZnSe laser resonator to use as a wavelength tuning element. This is achieved with a tuneable

Bragg grating created by interfering green laser beams inside the photorefractive Ce:SBN:61 waveguide. Our research group at Heriot-Watt University does not have a high power green laser with a long coherence length that is suitable, so the sample was sent to WPAFB for this experiment to be carried out there. This experiment is currently being set up by S. McDaniel and Dr. G. Cook with initial results expected in the near future.

1.4. Waveguide Fabrication in SBN:75

$Sr_{0.75}Ba_{0.25}Nb_2O_6$ (SBN:75) r_{33} electro optic coefficient is 1340 pm/V, which is ≈ 6 times that of SBN:61. However, SBN:75 has a low Curie temperature of 56 ^{0}C which might make it unsuitable for applications in warm environments. It's also more challenging to manufacture single crystal SBN:75 than SBN:61. This has a knock on effect in that our supplier (altechna.com) has a four to six week lead time for ordering SBN:75. That's why SBN:61 was investigated before starting this investigation. A summary of the material properties of SBN:75 and SBN:61 for comparison purposes is given in Table 5 below:

Strontium Barium Niobate Material Parameters		
Material parameters	SBN:61	SBN:75
Electro optic coefficients	r_{33} = 235 pm/V	r_{33} = 1340 pm/V
Curie temperature	80 ^{0}C	56 ^{0}C
Pyroelectric coefficient	0.065 μC per cm^{2}K	0.28 μC per cm^{2}K

Table 5: SBN Material properties (source Altechna.com).

The SBN:75 samples used in this investigation had dimensions of 10 x 10 x 2 mm with the c-axis along the 2 mm length. Before any laser inscription the samples were poled in the furnace at Heriot-Watt, the samples were heated to 100 ^{0}C at a rate of 50 ^{0}C/hour, then held at 100 ^{0} C for 30 minutes before being allowed to passively cool to room temperature. Once the sample reached 100 ^{0} C, a voltage of 1kV was applied across the c-axis to pole the ferroelectric domains. The voltage was left on until the sample returned to room temperature. The electrodes (silver paint) on the positive and negative c-axis surfaces were removed with acetone before inscription.

In order to access the strongest electro optic coefficient of SBN:75 (r_{33}), the inscription laser beam was incident on the sample parallel to the c-axis. This is the same geometry as discussed in the SBN:61 waveguide fabrication, Section 1.2 of this report, for which a schematic is give in Figure 1. Depressed cladding waveguides were fabricated in SBN:75

with the same parameters used in SBN:61, and given in Table 2. The ULI parameters used for cladding waveguides in SBN:61, 100 kHz PRF and 0.68 NA lens were found to induce larger amounts of modification than expected in SBN:75. Figure 9 (b) shows the modification induced using the same ULI parameters as SBN:61. In order to find more optimum inscription pulse energy for SBN:75, a set of 50 μm diameter depressed cladding waveguides were inscribed with a range of pulse energies, 0.2, 0.3 and 0.4 μJ, as shown in Figure 9 (c).

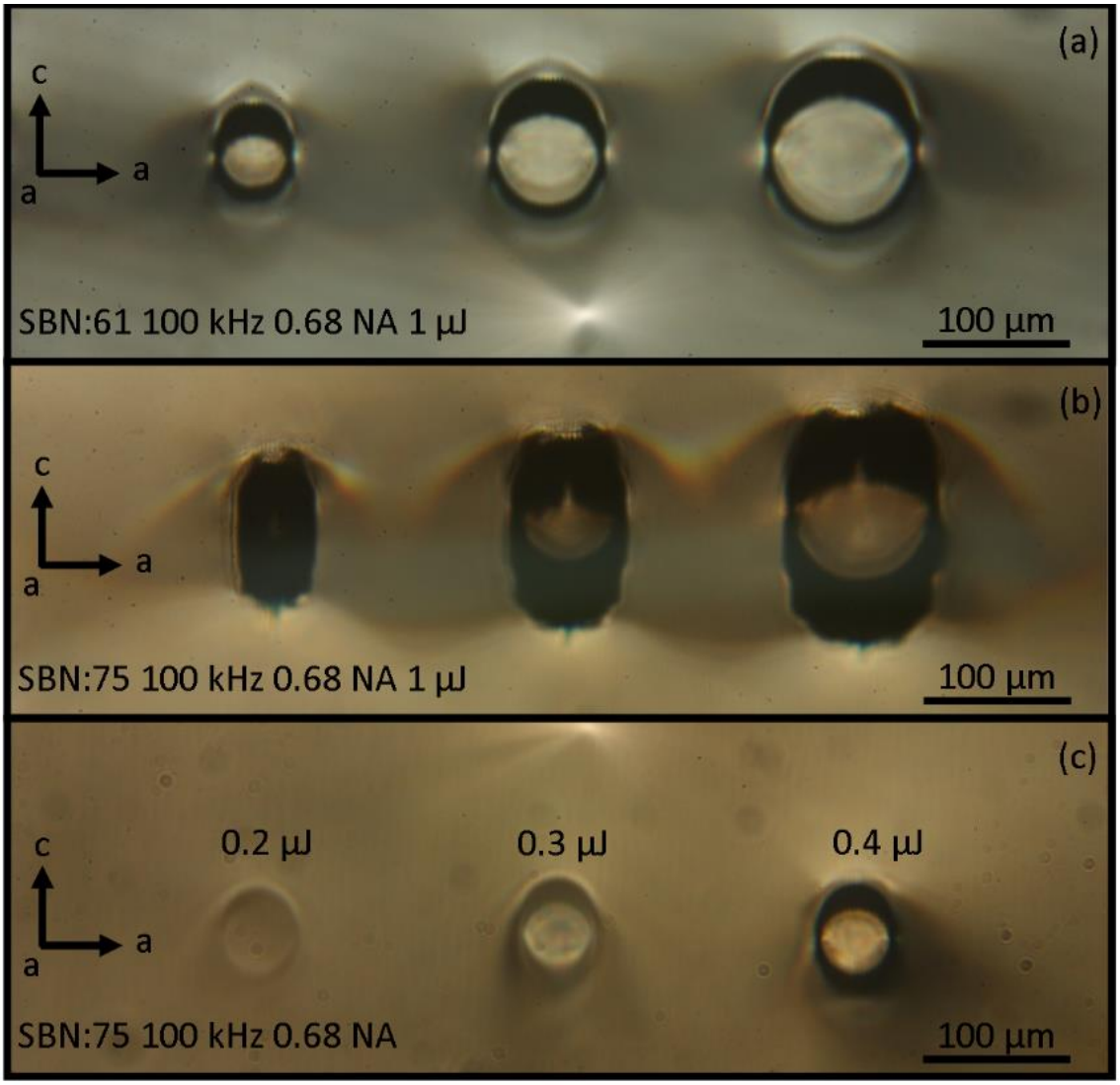

Figure 9: Transmission microscope images of SBN end facets. (a) SBN:61 with waveguides of diameters 50, 75 and 100 μm from left to right respectively. (b) SBN:75 with waveguides of diameter 50, 75 and 100 μm from left to right respectively.(c) SBN:75 with waveguides that are 50 μm in diameter. Pulses energy of 0.2, 0.3 and 0.4 μJ were used for inscription from left to right respectively.

From Figure 9 (c), it is clear that the optimum pulse energy needed for fabricating cladding waveguides in SBN:75 is between 0.3 and 0. 4 μJ. There is, however, still a clear difference in the waveguides between the modification at the top of the waveguide and the bottom. This is more apparent with the 100 μm waveguides, but is still visible in the 50 μm guides. To counter this effect, the pulse energy was reduced for the top half of the waveguide compared with the bottom elements. The exact amount of compensation needed was not known, so this was investigated with a parameter scan, as shown in Figure 10:

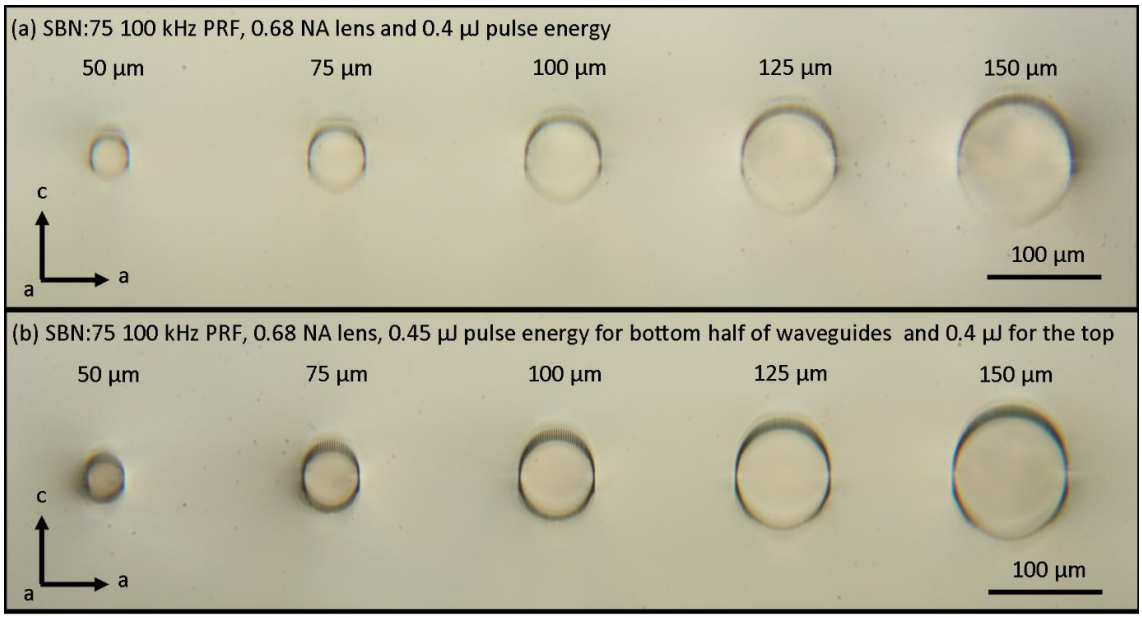

Figure 10: Depressed cladding waveguides fabricated at a depth of 250 μm in SBN:75 using a 100 kHz PRF, 1.1 ps pulse width,and a 0.68 NA lens. (a) 0.4 μJ of pulse energy is used to fabricate all elements that make up the waveguide. (b) 0.45 μJ pulse energies are used to fabricate the elements in the bottom half of the waveguides, and 0.4 μJ for the elements in the top half.

The laser parameters used, with the exception of pulse energy, were the same as for the 100 kHz depressed cladding waveguides inscribed in SBN:61, and given in Table 2. From our earlier work in SBN, it was clear that larger waveguides will need more compensation than smaller ones, thus a wider range of waveguide diameters was investigated. Figure 10 (a) shows depressed cladding waveguides, with diameters from 50 to 150 μm. All elements were inscribed with a pulse energy of 0.4 μJ. This run was used as a control sample to compare the compensated waveguides too. A range of pulse energies was investigated, the optimum of which, for the 75 μm waveguide, was 0.45 μJ for the bottom half of the waveguide and 0.4 μJ for the top half, as shown in Figure 10 (b). It can be noted that, for the 125 and 150 μm dimeter waveguides, a higher inscription energy is

needed for the bottom to make the modification more even. Nevertheless, compensating with different inscription powers appears to be an effective way of countering the depth dependence in the modification of SBN when inscribing along the c-axis of the crystal. The waveguide has now been sufficiently developed to investigate the guiding properties at different wavelengths.

1.5. Passive Guiding Properties of SBN at Telecoms Wavelengths

The passive guiding properties of the SBN:61 waveguides were investigated at 1550 nm. A 1550 nm fibre laser light was coupled into the waveguides by butt coupling a SMF-28 fibre to the end facet of the waveguide. The waveguide was found to guide 1550 nm fibre laser light, however it was difficult to couple the light into the waveguide, and there was a large difference in the amount of light exiting each waveguide. One reason for this could be a large numerical aperture (NA) mismatch between the fibre and the SBN:61 waveguides. To check this, the NA of the waveguides was measured at 1550 nm. The beam profiles of the SBN:61 waveguides in the far field and their corresponding NA are given in Figure 11:

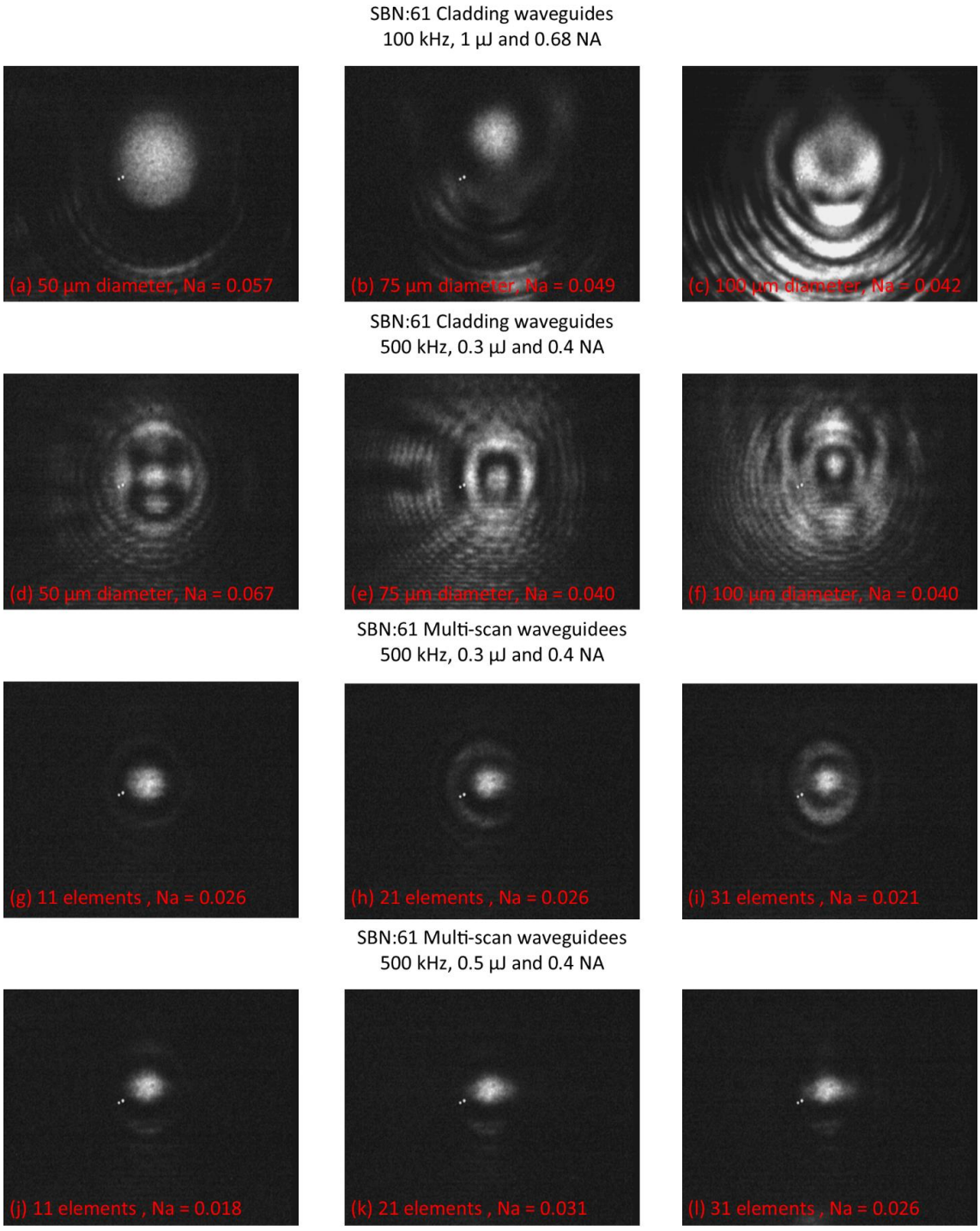

Figure 11: Far field images of SBN:61 ULI fabricated waveguides at 1550 nm. The cladding waveguides were inscribed with a laser repetition rate of 100 kHz, pulse energy of 1 µm and a lens with 0.68 NA.

The NA of SMF-28 at 1550 nm is 0.14, which is much larger than any of the SBN waveguides. To get an accurate loss measurement, the output of the SM-28 fibre was collimated with a 0.25 NA lens and focused on to the end facet of the waveguide with a 0.07 NA lens. This lens has a larger NA than the waveguides, but is more comparable

than the SMF-28. Using this method, the lowest loss of 0.08 dB/cm was measured with the 75 μm diameter depressed cladding waveguide inscribed with a laser at 100 kHz. A more typical value for the rest of the waveguides was found to be 0.3 dB/cm. This is a very impressive result for a ULI waveguide loss, which is typically around 1 dB/cm in ZnSe cladding waveguides [6, 7]. To confirm this measurement, we used a different method of propagation loss analysis. This method images the sample from above to directly detect the scattering loss. This method is a common technique used by Dr. G. Cook at AFRL and detailed for Fe:ZnSe in the paper by Lancaster et al. [8]. This method gives a typical loss of 2.5 dB/cm. The reason for the discrepancy was thought to be mode striping at the input of the waveguides. To remove this effect from the propagation loss calculation, the start of the waveguide was removed from the modelling, resulting in losses that agree with the first method. The waveguide loss being very low at 1550 nm is very promising for future work in the Mid-IR since the scattering loss is proportional to $1/\lambda^4$.

The guiding properties of SBN:75 depressed cladding waveguides fabricated with a modelocked laser operating at 100 kHz with a 0.68 NA lens, inscribed with reduced inscription pulse energy, were visually very similar to SBN:61. The waveguides were also very similar to the SBN:61 equivalent in terms of beam quality at 1550 nm. It was therefore surprising to learn that the SBN:75 cladding waveguides only propagated linearly polarised light that was parallel to the c-axis (i.e. vertically polarised light). The SBN:75 cladding waveguides did not support the propagation of horizontally polarised light. The scattering losses of the waveguides were investigated by imaging the scattering of the light as it propagates along the waveguide. At 1550 nm, no scattering was observed along the SBN:75 waveguides, suggesting a very low scattering loss. However, calculation of the propagation losses from this method needs some measurable loss above the noise floor to give accurate results. A comparison of 50 μm diameter cladding waveguides guiding 1550 nm light in SBN:61 and SBN:75 is shown in Figure 12:

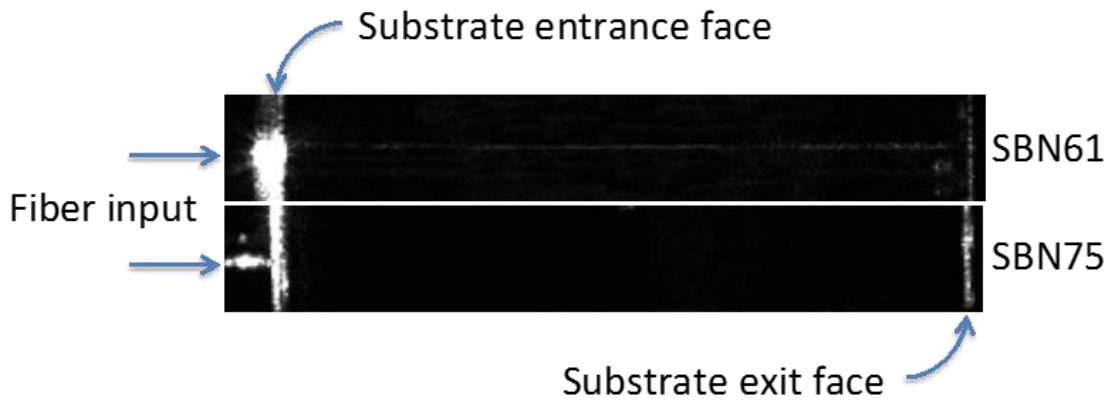

Figure 12: Exterior scattering comparison for SBN61 (top) and SBN75 (bottom) 50 µm waveguides at 1550 nm. Scattering is clearly visible for the SBN61 waveguide, but not in the equivalent waveguide in SBN75. This diagram was provided by Dr. G. Cook.

A graph showing the normalised scattering loss for each curve of each waveguide is given in Figure 13. This graph and the calculation of the losses from the images were completed by Sean McDaniel at AFRL.

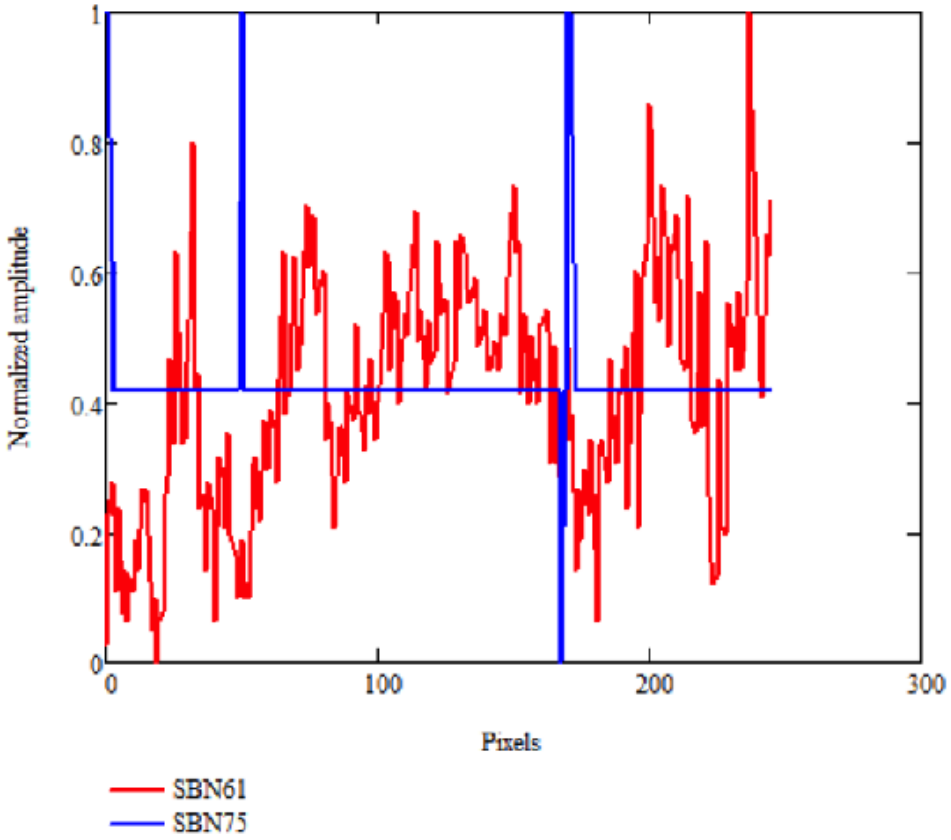

Figure 13: Local scattering intensity comparison for SBN61 and SBN75 50 µm waveguides at 1550 nm. Scattering is clearly negligible for SBN75 and no

discernible slope in the scattered light intensity with distance is apparent. This diagram was provided by S. McDaniel.

1.6. Effect of ULI on the Electro Optic Properties of SBN

The main reason for developing SBN waveguides is to use them as phase modulators and Mid-IR laser tuning elements. The effect of ULI on material properties is not fully understood because of the many different nonlinear processes involved. It cannot therefore be assumed that the electro optic properties of SBN will be retained in the modified region. To investigate this, one simple method is to insert the SBN waveguides into one arm of a Mach-Zender interferometer, as shown in Figure 14:

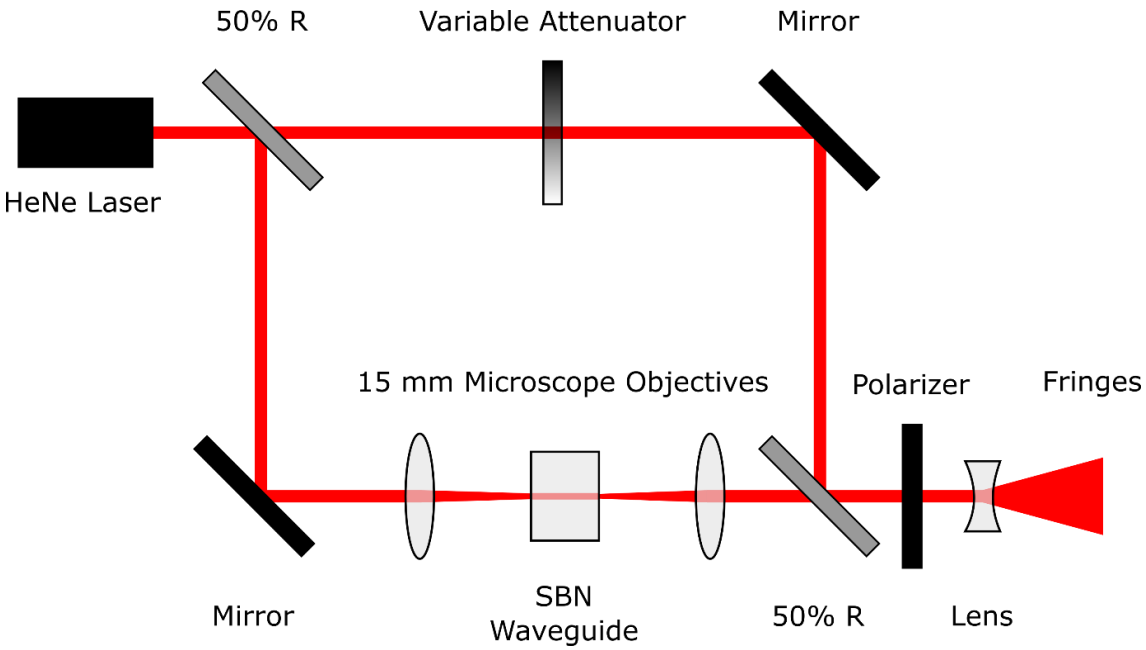

Figure 14: Mach-Zender interferometer with SBN waveguide forming a delay line in one of the arms.

The phase delay induced by applying an electric field to the SBN can be monitored by the change in the inference pattern at the output of the interferometer. To make monitoring the fringes by human eye possible, a HeNe laser, emitting 633 nm, was used.

The full wave voltage, corresponding to the field required to induce a 2π (whole fringe in the Mach-Zender interferometer) is given by Equation 1:

$$V_{2\pi} = \frac{2d}{L}\frac{\lambda}{r_{eff}n^3}$$

Equation 1

where *d* is the crystal thickness along the c-axis (2 mm), *L* is the optical path length (10 mm), λ is the laser wavelength (632.8 nm) and *n* is the refractive index (2.3103 for light polarised parallel to the crystal a-axis, 2.2817 for light polarised parallel to the crystal c-axis, both at 632.8 nm). r_{eff} is the effective electro optic coefficient, which depends on the crystal orientation, the direction of the applied electric field and the direction of the optical polarisation with respect to the crystal orientation. The effective electro optic coefficient is described by the tensor sum given in Equation 2:

$$r_{eff} = \dot{e}\,\ddot{\varepsilon}\,\dddot{r}\,\dot{E}$$

Equation 2

where *e* is the unit vector for the optical polarisation, ε is the dielectric permittivity tensor, *r* is the electro optic tensor and *E* is the applied field unit vector. The superscript dots represent the rank of the individual tensors, $\dot{}$ = vector, $\ddot{}$ = second rank tensor, $\dddot{}$ = third rank tensor. For waveguides along one of the a-axes with the applied electric field along the c-axis, the effective electro optic coefficients equate to $r_{eff} = \varepsilon_c r_{33}$ for light polarised parallel to the crystal c-axis, and to $r_{eff} = \varepsilon_a r_{23}$ for light polarised parallel to the crystal a-axis orthogonal to the waveguide direction. The electro optic coefficients for SBN61 ($Sr_{0.61}Ba_{0.39}Nb_2O_6$) are:

$$r_{13} = r_{23} = 55 \text{ pm/V}$$

$$r_{42} = r_{51} = 80 \text{ pm/V}$$

$$r_{33} = 225 \text{ pm/V}$$

This gives fullwave voltages, for a 2 mm thick c-axis orientation, of 95.13 V and 373.21 V for light polarised parallel to the c-axis and orthogonal to the c-axis, respectively.

Having established the linear electro optic r_{13} and r_{33} coefficients for our material, the electro optic properties of the three types of waveguides written in the same sample of SBN: 61 were measured. These are shown in figures 16 to 25, and the majority of these measurements were made by Dr. G. Cook. It was noted that Type I modification generated strong guiding immediately above and below the targeted inscription region, the electro optic properties of these regions were also measured, defined as Regions A and B, depicting the targeted inscription region and the adjacent guiding regions respectively. These are shown in Figure 15:

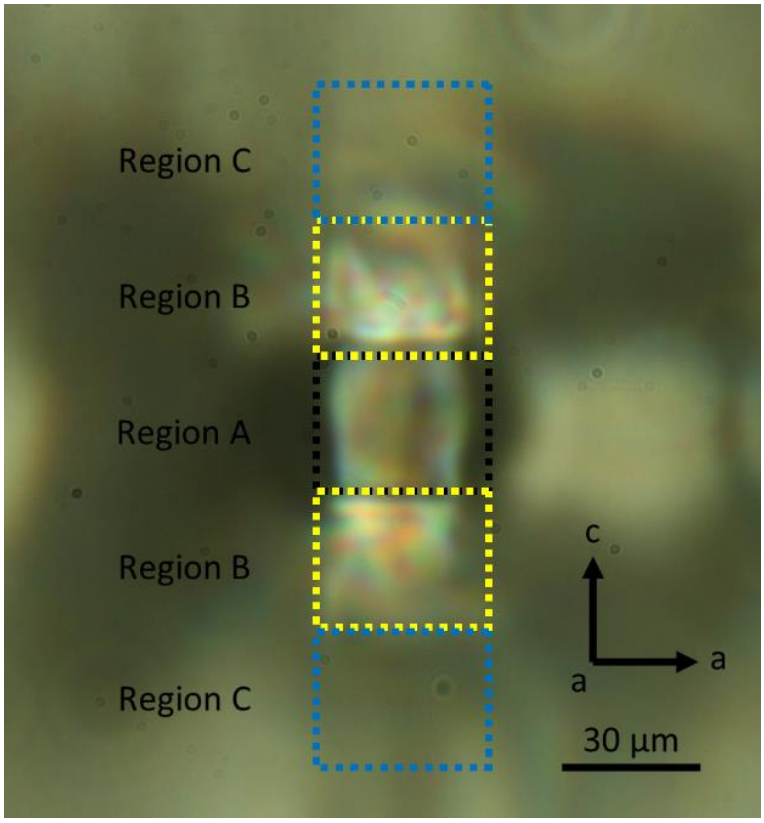

Figure 15: Defined regions for the Type I modification. Region A - targeted inscription region. Region B – induced guiding regions immediately above and below the targeted inscription region. Region C – area of induced photorefractivity.

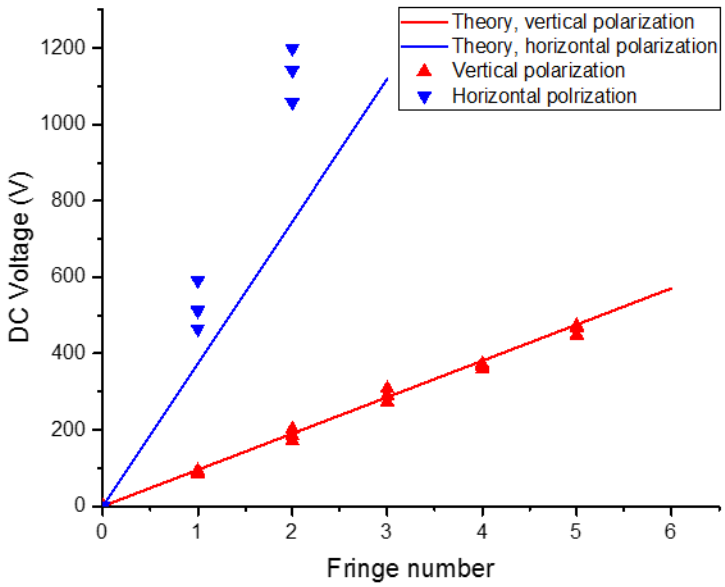

Figure 16: Measured linear electro optic response in bulk SBN:61. In this sample, vertical polarisation accesses the r_{33} coefficient, while horizontal polarisation accesses the r_{13} coefficient. The r_{42} coefficient is inaccessible for this geometry. Graph provided by Dr. G. Cook.

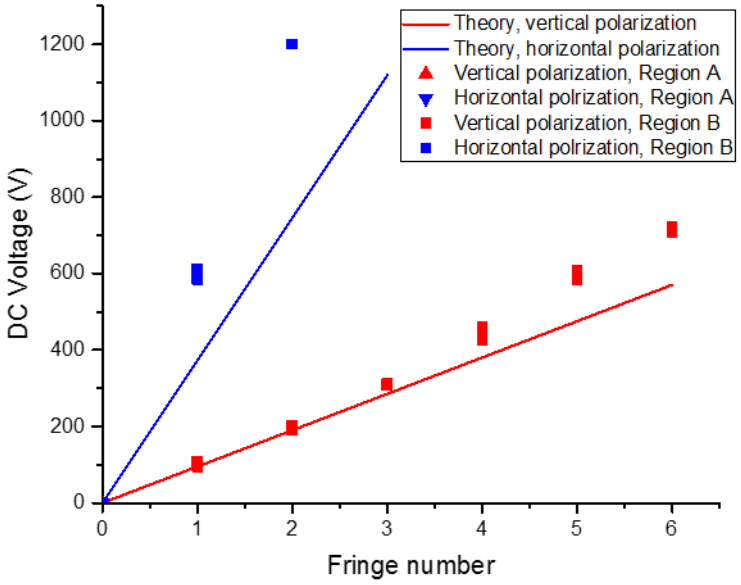

Figure 17: Measured linear electro optic response for single stripe Type I waveguides in SBN61. Graph provided by Dr. G. Cook.

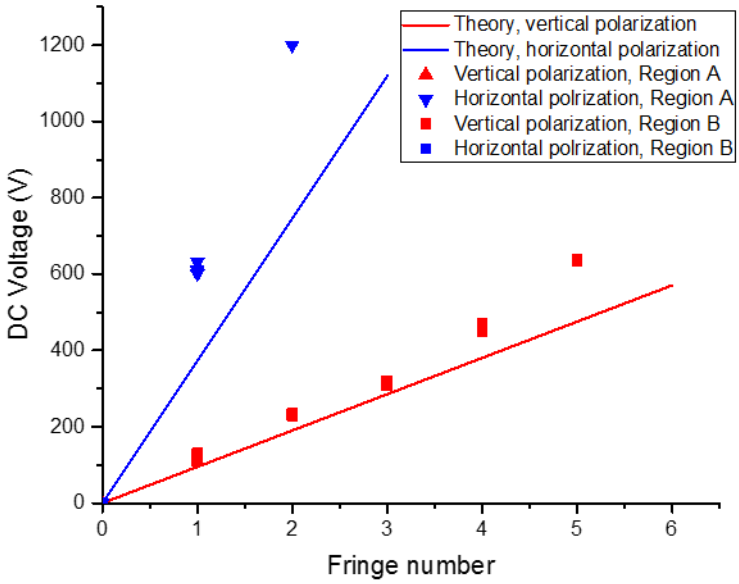

Figure 18: Measured linear electro optic response for 11 stripe Type I waveguides in SBN61. Graph provided by Dr. G. Cook.

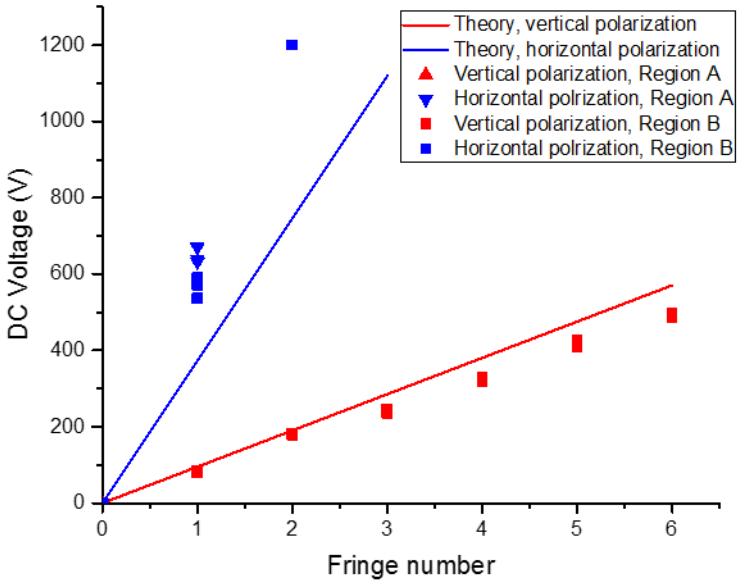

Figure 19: Measured linear electro optic response for 21 stripe Type I waveguides in SBN61. Graph provided by Dr. G. Cook.

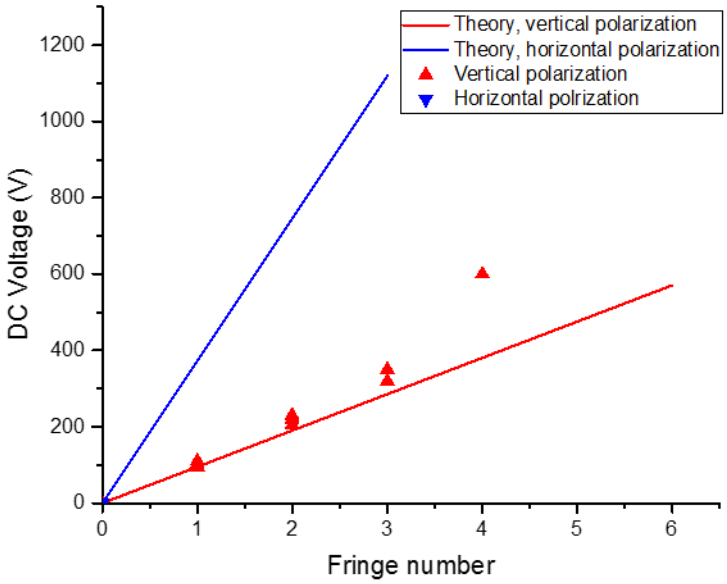

Figure 20: Measured linear electro optic response for 50 µm Type I cladding waveguides in SBN:61. Graph provided by Dr. G. Cook.

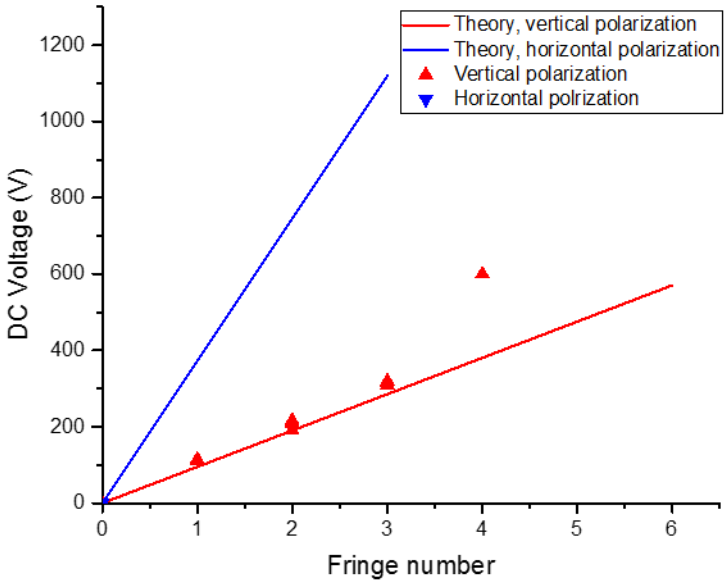

Figure 21: Measured linear electro optic response for 75 µm Type I cladding waveguides in SBN:61. Graph provided by Dr. G. Cook.

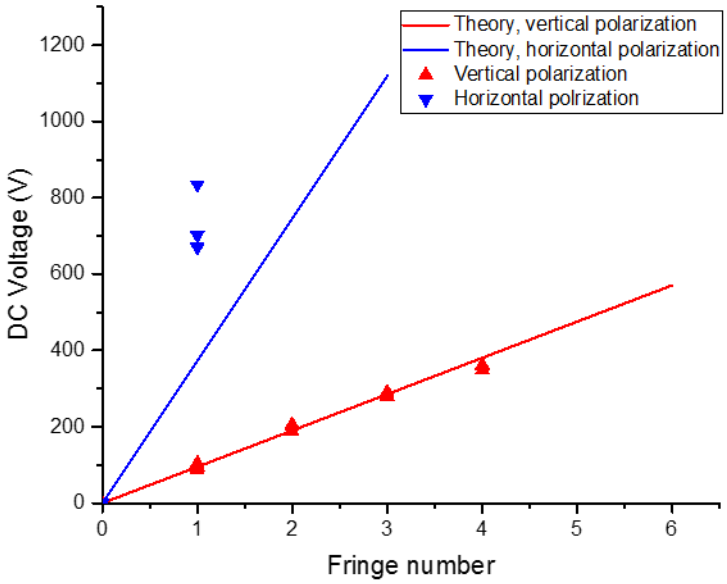

Figure 22: Measured linear electro optic response for 100 µm Type I cladding waveguides in SBN61. Graph provided by Dr. G. Cook.

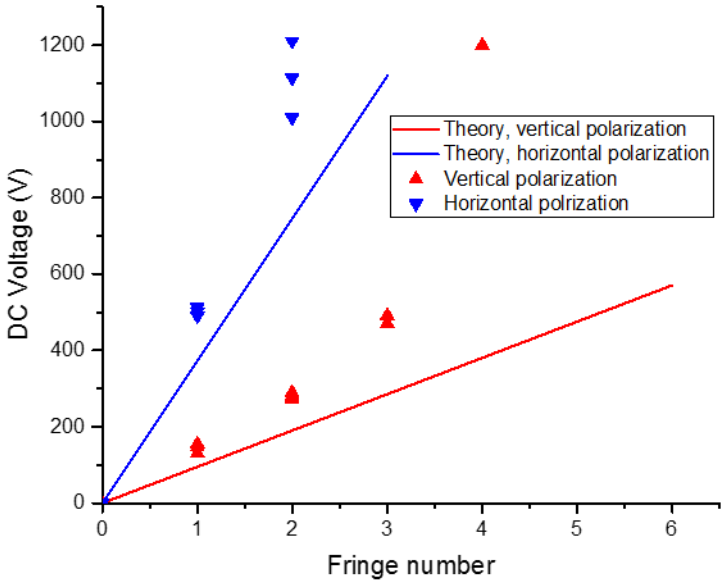

Figure 23: Measured linear electro optic response for 50 µm Type II cladding waveguides in SBN61. Graph provided by Dr. G. Cook.

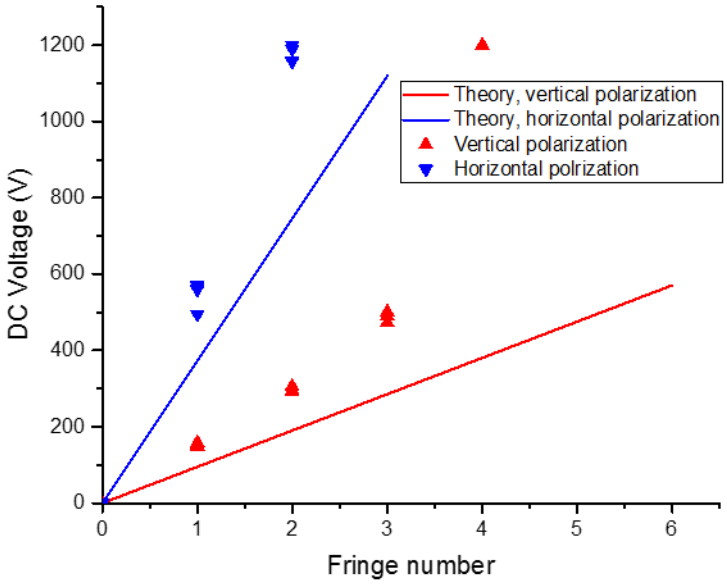

Figure 24: Measured linear electro optic response for 75 µm Type II cladding waveguides in SBN61. Graph provide by Dr. G. Cook.

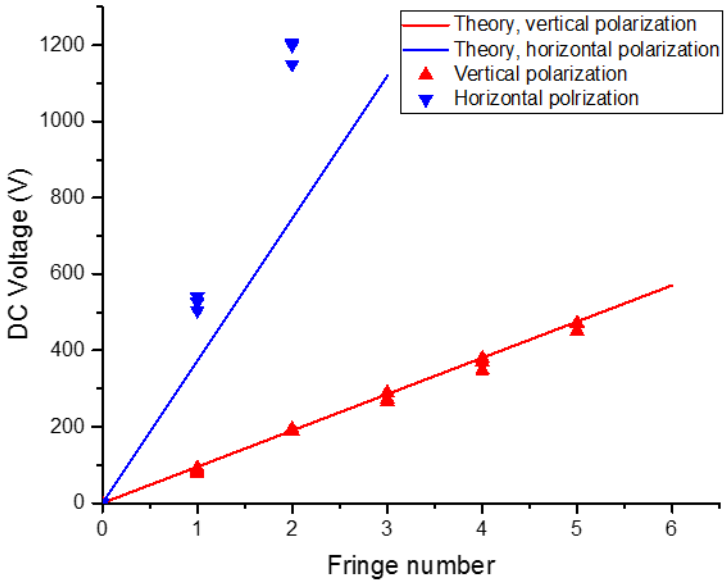

Figure 25: Measured linear electro optic response for 100 µm Type II cladding waveguides in SBN61. Graph provided by Dr. G. Cook.

Each of the three types of modification had distinct characteristics in terms of their polarisation properties. However, all of the inscription types, including the anomalous Type I Region B guides, demonstrated strong electro optic properties which generally followed the electro optic response noted earlier in bulk material. This was a very

important result, since it clearly demonstrated the ability of SBN:61 to retain its electro optic properties after the ULI procedure had been accomplished. The only caveat to this result is that the waveguides needed to be relatively large to match the electro optic response of the bulk crystal. If the guide regions were made too small, the electro optic response became progressively nonlinear with the applied field, as if the guide walls presented a physical boundary to the distortion of the electron orbitals that give rise to the linear electro optic effect. This was particular noticeable with the Type II cladding waveguides, which showed a progressive deviation compared with the bulk field induced birefringence. However, the 100 μm diameter Type II cladding waveguide behaved identically to bulk SBN:61. If small diameter waveguides were required, this might present a significant problem. However, since the waveguide numerical apertures are relatively large, the single mode diameter in the Mid-IR is likely to be around 100 μm diameter (or larger), meaning the electro optic properties of these waveguides are likely to be the same as the bulk material.

Although the electro optic properties seem to be suitable for device fabrication, care must be taken in selecting the appropriate waveguide type for the intended laser use. This is because the polarised light propagation properties of the waveguides vary considerably. Most of the SBN waveguides only propagate one linear polarisation state, which introduces two primary considerations. If the propagated polarisation does not correspond to the state required to access the largest electro optic coefficient, the device electro optic response will be small. Use of a polarisation dependent waveguides in a laser resonator that contains a non-polarization preserving waveguide element (including most Cr:ZnSe and Fe:ZnSe waveguides) will result in a 50% optical loss per round trip pass through the resonator, which is unacceptable. If a polarised SBN waveguide must be used, polarisation preserving waveguides need to be developed in Cr:ZnSe and Fe:ZnSe. This is not necessarily a challenge, but will require further development of the current technology.

Table 6 summarises the polarisation properties of the individual waveguide types:

Waveguide type	Polarisation guiding	Accessible EO coefficients
1, Region A	Guides horizontally polarised light only (polarised parallel to the c-axis).	r_{13} only.
1, Region B	Guides vertically polarised light only (polarised parallel to the c-axis).	r_{33} only.
1, Cladding	Guides only vertically polarised light (polarised parallel to the c-axis). Larger diameter guides may *weakly* guide horizontally polarised light.	r_{33} only.
2, Cladding	Vertical (polarised parallel to the c-axis) and horizontal (polarised parallel to the a-axis) guiding possible. Guide diameter needs to be ≥ 100 μm in diameter to avoid non linearity for EO effect for vertically polarised light. Horizontally polarised light appears to be unaffected by the guide diameter. Note: Although both polarisation states are guided, vertical input polarization is depolarised on exit, while horizontal polarisation is preserved.	r_{33} (light polarized long the c-axis); r_{13} (r_{23}) (light polarized along the a-axis). Note: in principal the r_{42} (r_{51}) coefficients are accessible if the field is applied along the crystal a-axis.

Table 6: Polarisation dependence of waveguides in SBN:61. For these characteristics, the crystal c-axis is perpendicular to the waveguides and the field is applied along the c-axis. Vertical polarisation is defined here as being parallel to the c-axis orientation, while horizontal polarisation is defined as being parallel to the a-axis orientation.

The Type II cladding waveguides seem to offer the greatest compatibility with existing Cr:ZnSe and Fe:ZnSe waveguide lasers. However, if a polarised laser is used, then Type I Region B waveguides would be preferred. Type II cladding could also be used with horizontally polarised light, since this is preserved on propagation through the waveguide, but this would give access only to the small r_{13} coefficient. It is interesting to note that the depolarisation of vertically polarised light on passage through the Type II waveguides does not seem to affect the apparent electro optic properties. This is unexpected, most likely the depolarisation occurs only towards the end of the waveguide, perhaps through a defect or local strain. Reversing the direction of the beam propagation through the

waveguide would provide a definitive confirmation, since the apparent electro optic properties may be different in each direction; if any depolarisation occurred first, then only part of the resulting optical field would be able to interact with the larger r_{33} coefficient.

The SBN:75 depressed cladding waveguides, inscribed at 100 kHz with a 0.68 NA lens, electro optic (EO) properties were also investigated. The SBM:75 was inserted into the Mach-Zender interferometer and then poled on the rig, with a standard hair dryer, at around 100 ^{o}C. Initial measurements of the EO properties were lower than expected, and so the waveguide was re-poled. The bulk EO properties were found to be r_{33} = 900 pm/V and r_{13} = 106 pm/V. The values are within the range normally expected for SBN:75 but with a slightly higher r_{13} coefficient. These results were constant throughout the sample inside and outside the waveguides. However, some of the higher power written waveguides had slightly lower EO properties than the bulk of around 10%. Unlike SBN61, no clamping of the EO coefficients was observed, even for the smallest waveguide. Both SBN substrates showed some degree of photorefractivity, but this was most noticeable within SBN:75, and caused disruption of the transmitted HeNe laser beam quality while also introducing significant cylindrical lensing in the bulk SBN75. Neither of these issues associated with photorefractivity was expected to be a problem in the IR since photorefractivity requires photoionisation of absorbing centres, which is unlikely with the relatively low photon energies encountered in the IR compared with using visible light [4].

It was found that ULI waveguides in SBN retain their electro optic properties. From an electro optic point of view, the ULI waveguide fabrication method is suitable for creating electro optic modulators in a non free space component format. Additionally, there is interest in the discovery of the photorefractive properties induced by the ULI process. This does not affect applications in the Mid-IR, but could be very useful for creating devices in the visible wavelength range.

1.7. Mid-IR Waveguides in SBN

The passive guiding properties of the SBN waveguides at 1550 nm and the electro optic properties at 633 nm have been discussed earlier in this report. Both of these investigations have shown SBN to be suitable for its desired application, but the waveguides. ability to support the Mid-IR wavelengths of a Cr:ZnSe laser has not yet

been demonstrated. In this section, the guiding properties of the SBN waveguides at 2.45 μm are discussed. A Cr:ZnSe waveguide laser was used as the signal source for this work. The Cr:ZnSe waveguide laser used had its emission peak at 2.45 μm. A 50 mm CaF_2 lens was used to couple the Cr:ZnSe laser beam into the SBN waveguides, and a Mid-IR camera was used to image the end facet of the waveguide. A schematic of the set up is given in Figure 26:

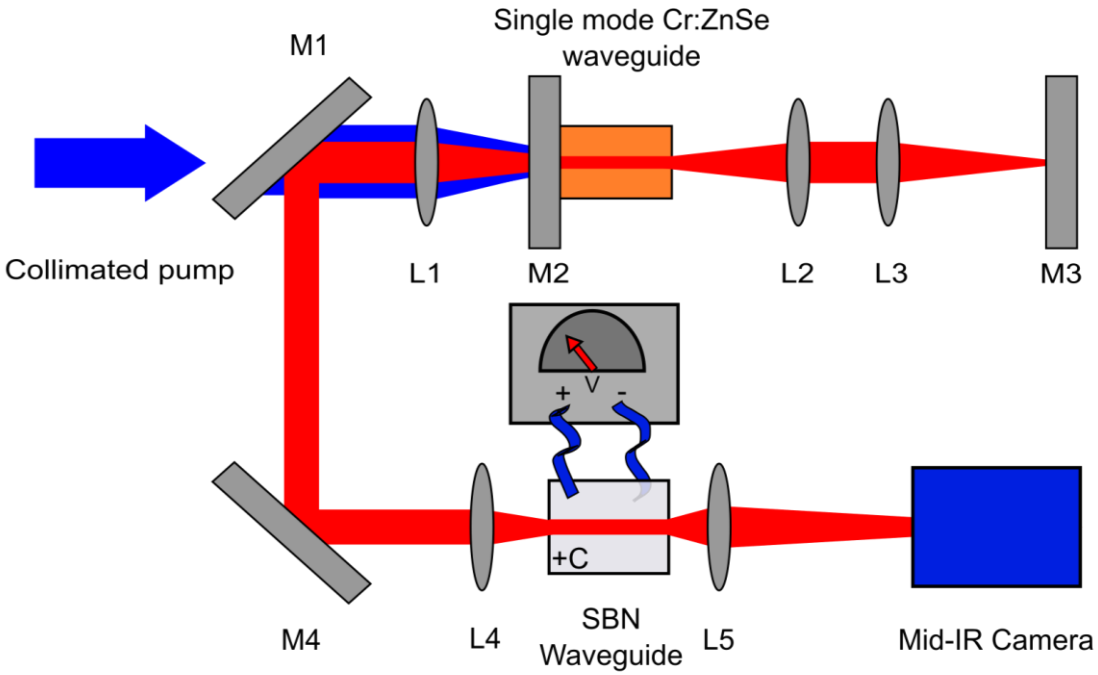

Figure 26: Schematic of experimental set up used to investigate the Mid-IR guiding properties of SBN waveguides with an applied electric field. L1-L4 are AR coated CaF_2 lenses with a focal length of 50 mm, L5 has a focal length of 20 mm. M1 is HR-coated for the Tm:fibre pump source and M3 is HR-coated for the signal output of a Cr:ZnSe laser. M4 is a gold mirror. Note the SBN was coated on the top and bottom surfaces with silver paint to act as electrical contacts.

The modified region of the multiscan waveguides inscribed at 500 kHz with 0.4 NA lens were not found to guide 2.45 μm light. The most likely reason for this is the mode field diameter of the waveguides was too small. The areas above and below the multiscan waveguide, Region B, Figure 15, were found to guide 2.45 μm light. However, on application of the electric field, the waveguide output was found to heavily distort and move. The reason for this is thought to be strain induced guiding created from the piezoelectric effect induced by the applied electric field. This makes Type I waveguides unlikely to be suitable for our intended future applications. It may be possible to

compensate for the strain effect by inscribing a ‘sandwich’ waveguide in which the ‘bread’ is multiscan and the ‘filling’ is unmodified material. This idea is supported in that the 500 kHz 0.4 NA cladding waveguide does guide the Mid-IR light of the Cr:ZnSe laser. The depressed cladding waveguides inscribed at 100 kHz with a 0.68 NA lens in SBN:61 are found to guide 2.45 μm light. Applying a positive electric field was found to increase the NA of the waveguide. As the electric field was further increased, it reached a point at which a single mode waveguide would become multimode. Mode images of the end facet of the SBN:61 cladding waveguide with and without an applied electric field are shown in Figure 27. The 75 μm diameter waveguide clearly shows the transition from single mode at V = 0 to Multimode at V = + 1400 V.

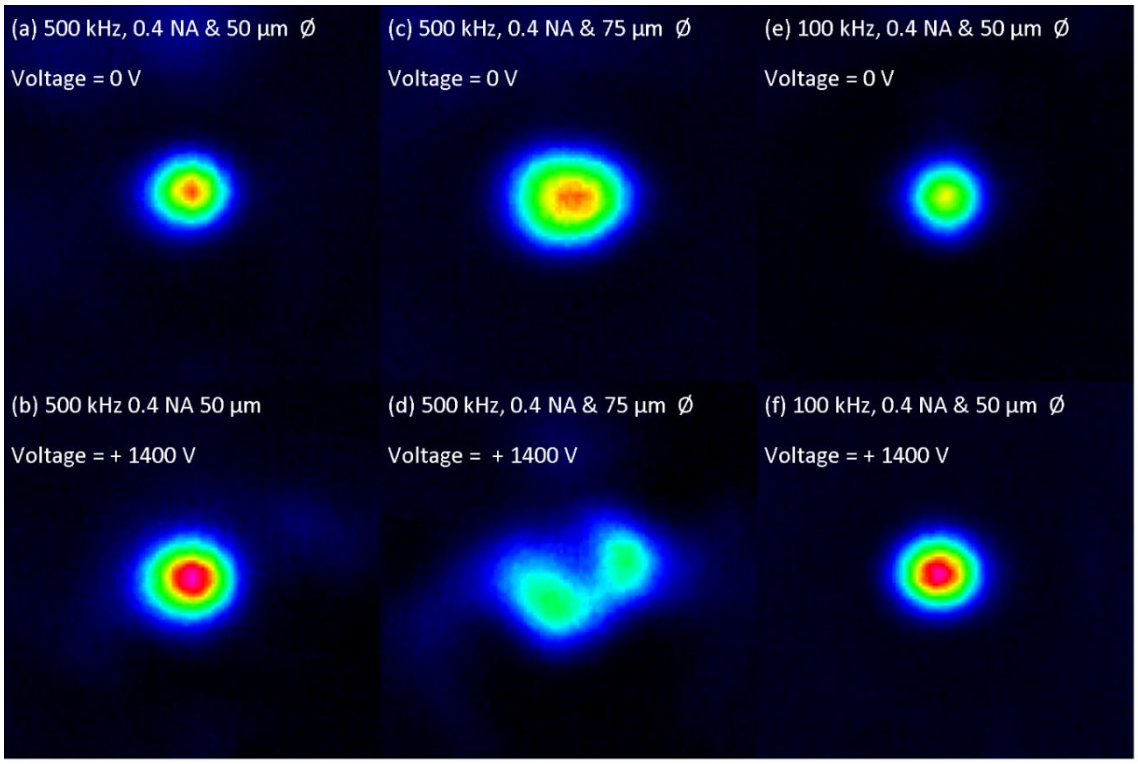

Figure 27: Electro optic mode control at 2.4 μm of cladding waveguides inscribed in SBN:61. The electric field is applied along the c-axis of the crystal.

The cladding waveguides were inscribed at 100 kHz with a 0.68 NA lens in SBN: 75 Mid-IR guiding properties were also investigated using the same methods as SBN:61. The waveguide did not propagate horizontally polarised light, and only propagated vertically polarised light (in the direction of the c-axis). This is in agreement with what was observed at 1550 nm. The effect of applying a positive electric field to the positive

c-axis face of the SBN:75 sample was found to be the same as SBN:61. Application of a negative field was also investigated. It was found that doing this reduced the NA of the waveguide and meant that a multimode waveguide could be changed to operate in single mode, as shown in Figure 28 with the 75 µm diameter waveguide.

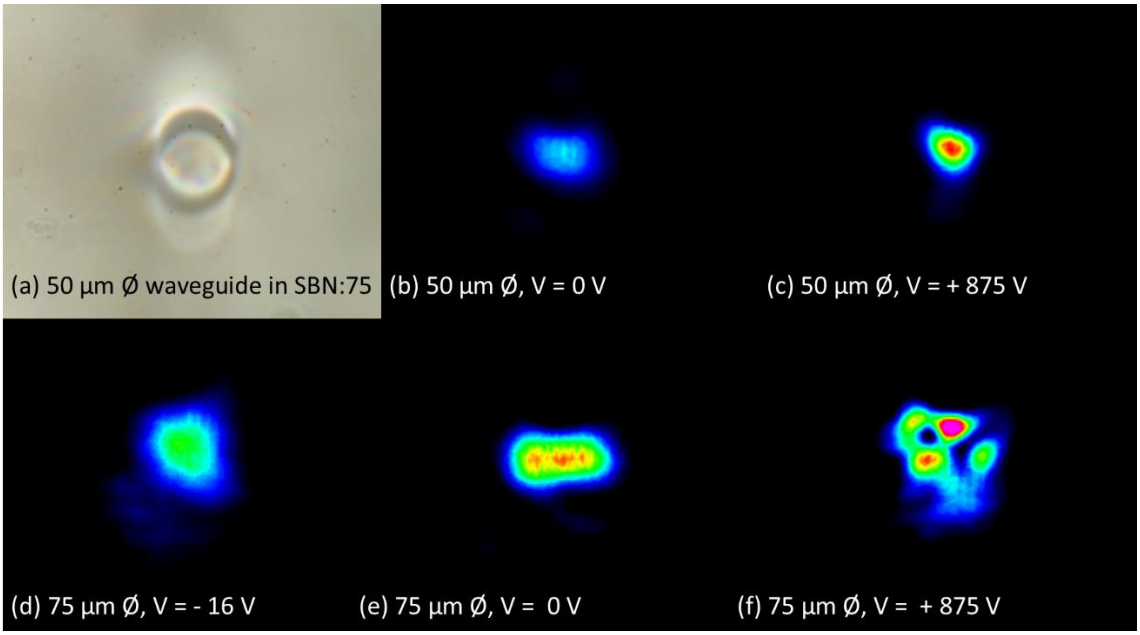

Figure 28:Electro optic mode control at 2.4 µm of cladding waveguides inscribed in SBN:75.(a) microscope image of 50 µm diameter waveguide inscribed in SBN:75 with a PRF of 100 kHz, 0.68 NA lens and a pulse energy of 0.3 µW.

These results mean that the refractive index of the modified elements are not changed with applied electric field. Applying a positive electric field increases the refractive index of the non-modified bulk SBN in the centre of the waveguide. The opposite is true of an application of a negative electric field. Initially, it was thought that applying a small electric field that does not induce a multimode operation could be used to improve coupling efficiency. The implication for inserting a SBN device, with ULI Bragg gratings inside the waveguide, into a Cr:ZnSe laser resonator is that it is likely to require a multimode operation to allow for reasonable wavelength tuning ranges. For applications requiring a single mode output, a MOPA system would be needed with a multimode wavelength tuneable oscillator and a single mode waveguide amplifier.

The ability to control the output mode of a waveguide could be very useful for many different applications. These include the ability to controllably couple light between a single mode waveguide and a cluster of single mode waveguides for phase-couple applications. It is also possible to extract information on the refractive index change the

ULI has induced in the SBN by examining the point at which different waveguide diameters change from single to multimode application. Measuring the refractive index change by ULI is often very difficult using other methods because of the small change induced, typically of order 10^{-3}. Repeating these results over a number of wavelengths will allow the extraction of the dispersion characteristics of the cladding. Knowing this could allow for accurate dispersion control in a modelocked Cr:ZnSe and Fe:ZnSe laser.

1.8. Conclusions

These results are a big step forward in the development of a non-free space component tuneable laser emitting in the atmospheric transition window. It has been found that fabrication of depressed cladding waveguides in SBN are capable of guiding Mid-IR light, something which has not previously been demonstrated. Initial measurements of propagation loss of SBN:75 cladding waveguides suggest the losses are much less than 1 dB/cm, which is suitable for inserting into Cr:ZnSe or Fe:ZnSe laser resonators. The electro optic properties of the bulk SBN are maintained after the inscription process, making the material suitable for its intended applications. The waveguide diameters and NA of the SBN depressed cladding waveguides are similar to those of ULI fabricated waveguides in Cr:ZnSe and Fe:ZnSe [6, 7]. This will facilitate efficient butt coupling between ZnSe and SBN waveguides inside a laser resonator, allowing for the creation of a compact tuneable laser system. An example of what such a cavity might look like is given in Figure 29:

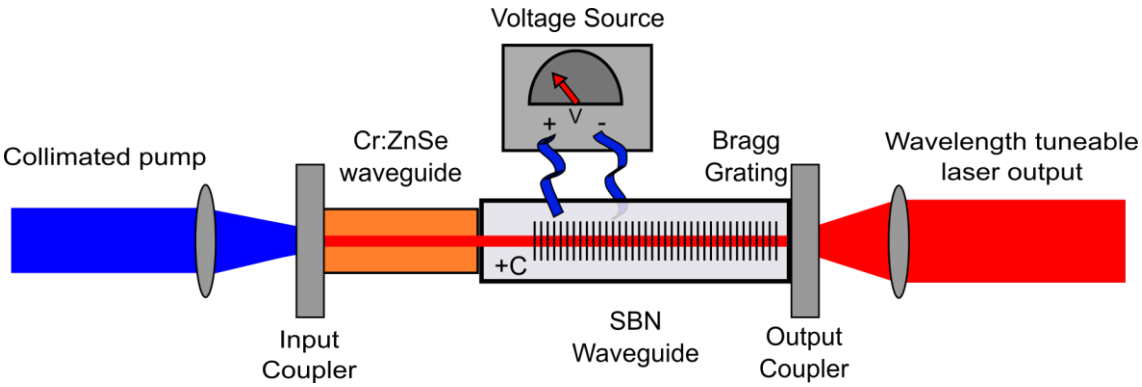

Figure 29: Schematic for Cr:ZnSe waveguide laser with SBN waveguide tuning element.

2.1. Calcium Fluoride Waveguide Fabrication

There had been no reports of ULI modification in CaF_2, so an initial laser parameter scan was performed. Polycrystalline CaF_2 was used in this investigation, specifically UV-polished grade, sourced from Crystran Ltd. In order to investigate the effect of femtosecond laser pulses on the refractive index of CaF_2, a range of single line scans with different laser parameters was used. The inscription parameters investigated are given in Table 7:

CaF_2 single line modification parameter range investigated	
Inscription laser	IMRA 400 μJewel
Laser wavelength	1047 nm
Laser polarisation	Horizontal, vertical and circular
Laser pulse width	370 fs
Laser PRF	500 kHz
Inscription lens	0.4 NA
Pulse energy	40 to 840 nJ
Sample translation speed	1 to 25 $mm \cdot s^{-1}$

Table 7: Ultrafast laser inscription parameters investigated in single-line modification of CaF2.

The end facet of the sample was imaged with a transmission microscope to get an indication of any permanent refractive index modification and whether it was Type I (increase in n) or Type II (reduction in n). A transmission microscope image of single line scan in CaF_2 is shown in Figure 30:

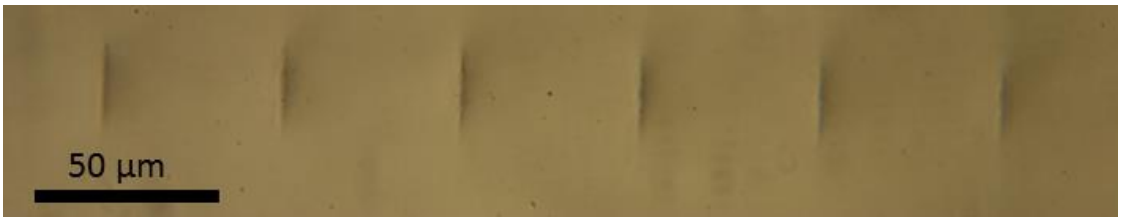

Figure 30: Transmission microscope image of end facet of single line scans in CaF_2. The modification elements shown were fabricated with pulse energies of 220 nJ.

From this figure it can be seen that the modification elements are anti guiding. thus could be suitable for Type II or depressed cladding waveguides [9]. The feasibility of depressed

cladding waveguides was investigated over that of Type II to facilitate effective integration with the current Cr:ZnS/ZnSe depressed cladding waveguide laser sources [6, 10]. A wide range of parameters was investigated for waveguide fabrication in CaF_2 waveguides at a depth of 250 μm below the surface of the sample. A list of the parameters investigated is given in Table 8:

CaF_2 Cladding Waveguides Inscription Parameters	
Laser	IMRA 400 μJewel
Laser wavelength	1047 nm
Laser polarisation	Horizontal
Laser pulse width	370 fs
Laser PRF	500 kHz
Inscription lens	0.4 NA
Pulse energy	40 to 300 nJ
Sample translation speed	10 to 25 $mm \cdot s^{-1}$
Waveguide diameter	20 to 120 μm
Number of elements per waveguide	20 to 90

Table 8: Range of inscription parameters investigated in the fabrication of CaF2 waveguides.

The pulse energy of the laser was reduced to below 220 nJ to stop the sample from cracking during the initial inscription step and the subsequent polishing stage. It was found that pulse energy of less than 140 nJ did not modify the CaF_2. From this, the waveguides parameters were optimised within this pulse energy envelope of 140 – 220 nJ. A transmission microscope image of CaF_2 depressed cladding waveguides is shown in Figure 31:

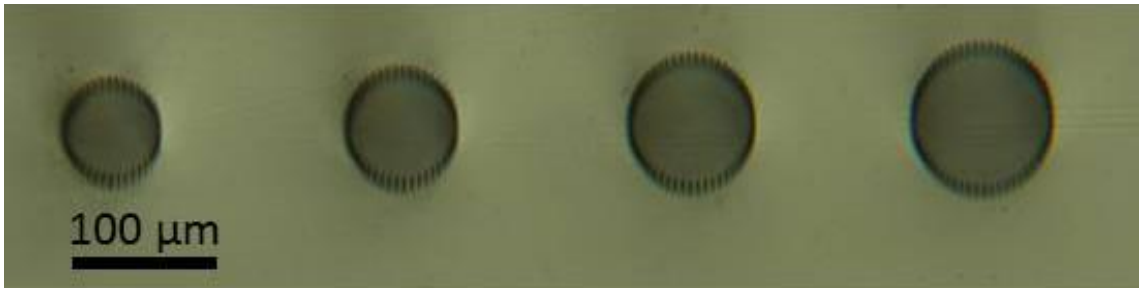

Figure 31: Transmission microscope image of CaF_2 cladding waveguides. The diameters of the waveguides from left to right are 65, 75, 85 and 95 μm.

2.2. Calcium Fluoride Waveguide Characterisation

These waveguides need to have efficient coupling with Cr:ZnSe waveguides, so a Cr:ZnSe waveguide laser was used to characterise the insertion losses of the CaF_2 waveguides. A schematic of the Cr:ZnSe waveguide laser signal source and the coupling setup used for testing the CaF_2 is shown in Figure 32:

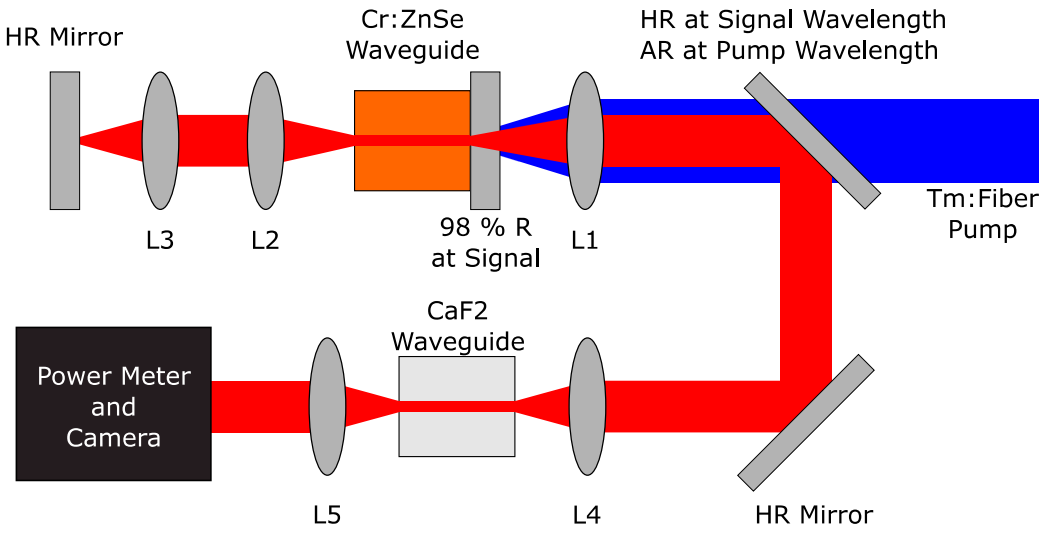

Figure 32: Schematic of CaF_2 waveguide characterisation setup used for insertion loss measurement with Cr:ZnSe as the signal source. L1 to L5 are AR-coated CaF_2 Lenses with 50 mm focal lengths.

The insertion loss measurement of the CaF_2 waveguides was found to give a result of < 1 dB/cm when tested at 2.45 µm. This is promising for future integration in a Cr:ZnSe resonator.

The output mode of the waveguides was imaged with a Flur Mid-IR camera. A typical mode image is shown in Figure 33. It was found that waveguides of 75 µm in diameter or less were single mode at 2.45 µm from near field imaging.

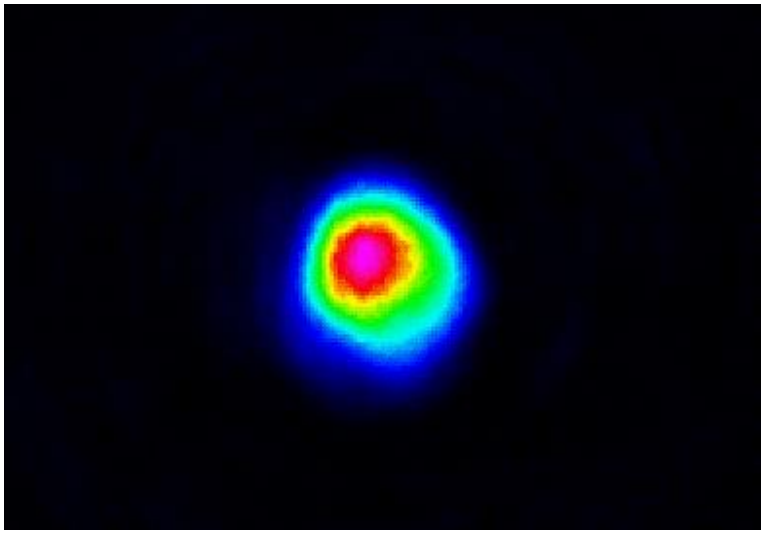

Figure 33: Mode image of CaF_2 waveguide laser guide the signal of the Cr:ZnSe waveguide laser emitting at 2.45 μm. The inscription parameters of the waveguide with diameter 75 μm, number of elements 45, inscription speed 10 $mm \cdot s^{-1}$, pulse energy 0.2 μJ, NA of inscription lens 0.68 and horizontal inscription laser polarisation.

2.3. Conclusion

The work in ULI fabricated waveguides in CaF_2 has been successful with low insertion loss and MFDs comparable to those of Cr:ZnSe waveguide lasers. The next stage for this work will be to insert the CaF_2 waveguides into a Cr:ZnSe laser resonator and investigate the effect on laser performance. Further investigation into the suitability for dispersion compensation in a modelocked Cr:ZnSe waveguide laser is needed.

3. Appendix Reference List

1. L. I. Ivleva, N. V. Bogodaev, N. M. Polozkov, and V. V. Osiko, "Growth of SBN single crystals by Stepanov technique for photorefractive applications," Optical Materials **4**, 168-173 (1995).

2. R. Mary, D. Choudhury, and A. K. Kar, "Applications of Fiber Lasers for the Development of Compact Photonic Devices," IEEE J. Sel. Top. Quant. Electon. **20**, 0902513 (2014).

3. G. Wood, W. Clark, M. Miller, E. Sharp, G. Salamo, and R. Neurgaonkar, "Broadband photorefractive properties and self-pumped phase conjugation in Ce-SBN:60," IEEE J. Quantum Electron. **23**, 2126-2135 (1987).

4. P. Gunter and J. Huignard, *Photorefractive Materials and Their Applications 1*, Photorefractive Materials and Their Applications (Springer, New York, 2006), Vol. 113.

5. S. A. McDaniel, A. Lancaster, J. W. Evans, A. K. Kar, and G. Cook, "Power scaling of ultrafast laser inscribed waveguide lasers in chromium and iron doped zinc selenide," Opt. Express **24**, 3502-3512 (2016).

6. J. R. Macdonald, S. J. Beecher, P. A. Berry, G. Brown, K. L. Schepler, and A. K. Kar, "Efficient mid-infrared Cr:ZnSe channel waveguide laser operating at 2486 nm," Optics Letters **38**, 2194-2196 (2013).

7. A. Lancaster, G. Cook, S. A. McDaniel, J. Evans, P. A. Berry, J. D. Shephard, and A. K. Kar, "Mid-infrared laser emission from Fe:ZnSe cladding waveguides," Appl. Phys. Lett. **107**, 031108 (2015).

8. A. Lancaster, G. Cook, S. McDaniel, J. Evans, P. Berry, J. Shephard, and A. Kar, "Fe:ZnSe Channel Waveguide Laser Operating at 4122 nm," in *CLEO: 2015*, OSA Technical Digest (online) (Optical Society of America, 2015), SM2F.5.

9. D. Choudhury, J. R. Macdonald, and A. K. Kar, "Ultrafast laser inscription: perspectives on future integrated applications," Laser & Photonics Reviews. **8** 827-846 (2014).

10. J. R. Macdonald, S. J. Beecher, A. Lancaster, P. A. Berry, K. L. Schepler, S. B. Mirov, and A. K. Kar, "Compact Cr:ZnS channel waveguide laser operating at 2333 nm," Opt. Express **22**, 7052-7057 (2014).